Fine structure of the Isovector Giant Dipole Resonance in neutron-rich calcium isotopes using the (p,p′) reaction at zero-degrees

Mouftahou Bakary Latif

A thesis submitted to the Faculty of Science,
University of the Witwatersrand, Johannesburg,
in fulfilment of the requirements for the degree of
Doctor of Philosophy.

Johannesburg, 2017.

Declaration

I, the undersigned, hereby declare that the work contained in this thesis is my own original work. It is being submitted for the Degree of Doctor of Philosophy in the University of the Witwatersrand, Johannesburg. It has not previously in its entirety or in part been submitted for any degree or examination in any other University.

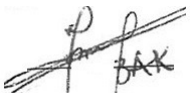

June 6, 2017

Signature *Date*

Abstract

In the present study, the fine structure of the IsoVector Giant Dipole Resonance (IVGDR) of stable neutron-rich isotopes of calcium, namely ^{42}Ca, ^{44}Ca and ^{48}Ca, has been investigated in a systematic way by including readily available data of ^{40}Ca.

Measurements were carried out at the cyclotron facility of iThemba Laboratory for Accelerator Based Sciences (iThemb LABS) which provided a high quality proton beam of 200 MeV, together with the state-of-the-art K600 magnetic spectrometer in zero-degree mode. Excellent energy-resolution of up to $\Delta E \approx 33$ keV was attained which allowed for a clear observation of fine structure in the excitation energy region of the IVGDR which lies between 11 and 25 MeV.

Double differential cross-sections were extracted from the experimental energy spectra and subsequently converted to equivalent photo-absorption cross-sections. The obtained results agree well with the photo-absorption cross-section data available in the literature, within limits of experimental errors. Centroid energies and widths of the IVGDR of the calcium isotopes were extracted by fitting the experimental data with both Lorentzian and Gaussian functions over the excitation energy range of 15 - 23 MeV. The obtained values of centroids and width agree well with the predictions of the theoretical macroscopic model.

Characteristic energy scales were extracted from the experimental spectra and compared to those of theoretical microscopic models of the Relativistic Quasi-particle Time Blocking Approximation (RQTBA), the Relativistic Quasi-particle Random Phase Approximation (RQRPA), the Random Phase Approximation

(RPA), the Quasi-particle RPA (QRPA), the Second RPA (SRPA) and the Continuum RPA (CRPA). The RQTBA was found to best describe the experimentally extracted energy scales.

The level density of the $J^{\pi} = 1^{-}$ states was also extracted from the high energy-resolution spectra and the results show a good agreement with the theoretical phenomenological models of the Back-shifted Fermi Gas in the excitation energy range of 13 and 20 MeV for all four calcium isotopes.

Dedication

This work is dedicated to the Latif's

Acknowledgements

All praise is due to the One by whom all things exist, the One without helper, the Worthy of praises, the Everliving who was and will always be while every other living being shall live for a fixed time. May His peace and benedictions be on the selected Men that came to guide humanity from darkness to light while promoting justice, love, unity and peaceful coexistence.

First of all, I would like to say a big "Thank You" to my WITS University principal supervisor, Dr Iyabo Usman, for all the guidance and support and for always lending me a listening ear every time I had queries. And I always had them .....

I would like to thank my WITS co-supervisor, Prof John Carter, for making me benefit from his wealth of knowledge and wisdom and for always creating time for me despite his very busy schedule then as the Head of School. I always remember his constant call for being meticulous as I later got to understand it is a key ingredient for success in my chosen field.

I specially want to thank my iThemba LABS-based co-supervisor, Dr Retief Neveling, for the incredible work put in towards the success of this project. His total commitment and devotion are well appreciated. I still remember those numerous nights of experiments during which he had to be present after working all day, to make sure all went well with the experiments. I wish to thank him for introducing me to the only operational magnetic spectrometer on the African con-

tinent (the K600) and for taking me through all the rudiments of its operational principles. I humbly say “Dankie”.

I also wish to express my sincere gratitude to Prof Elias Sideras-Haddad, a key member of the WITS nuclear structure group, for his support and assistance. He introduced me to the tandem accelerator of iThemba LABS Gauteng, housed on WITS campus. I appreciate the various scientific discussions we had. His passion for Physics struck me from my first meeting with him. He also introduced me to the most beautiful places in Cape Town. Together, we always drove to a new place in the coastal City every time we had a break with the experiments. His financial support is also well appreciated.

I hereby wish to express my sincere gratitude to Prof Daniel Joubert of the WITS School of Physics. As the postgraduate coordinator of the School, he assisted me in many various ways on administrative matters. I will forever remember the support letter he wrote me which fetched me the WITS Postgraduate Merit Award (PMA), “Dankie Professor. Aanvaar asseblief my opregte dank.”.

I hereby wish to acknowledge the assistance of Prof G. R. J. Cooper of the WITS School of Geosciences for guiding my first steps with the wavelet analysis technique of which I knew nothing before meeting with him.

My special appreciation goes to Prof Dr Peter von Neumann-Cosel of the Technische Universität Darmstadt, Germany, for his guidance with the interpretation of some of my results. The first meeting at iThemba LABS and the various skype discussions helped a long way in fostering my understanding of the phenomenon of Giant Resonances.

I also wish to thank Dr Vladimir Yu Ponomarev of the the Technische Universität

Darmstadt, Germany, for the various discussions we had during his visits to WITS and the numerous exchanges of emails. “Your efforts are well appreciated”.

I am indebted to Dr Panagiota Papakonstantinou of the Institute for Basic Science, Daejeon, South Korea and Dr Elena Litvinova of the Western Michigan University for providing the theoretical calculations used in this project and for providing detailed explanation on the various models. The countless exchanges of emails are appreciated. I will always be grateful.

I wish to express my sincere gratitude to the K600 group members for all the efforts put in during the experiments. Notably Dr F. D. Smit for providing some clarifications on the modes of operation of the K600. Also the Stellenbosch team led by Prof Paul Papka is well appreciated for their support during the experiments.

I would like to say a big “Merci” to my parents Alh.(Mr) and Alha (Mrs) Latif for being there and guiding my steps on the path of dignity and making me live by the principle of “only hard work pays off! A soul devoid of hard work is lifeless!”

My special gratitude goes to my soul mate, the honey of my life, Fatima Latif, for all the support and encouragements and most importantly for enduring my absence from home and being alone with our precious sprouts, the 3 A’s (Aisha, Asmaa, Ahmad) during the time of this programme. May your love continue to grow in my heart...As for you the 3A’s, you are the joy of my heart and the coldness of my eyes. I difficulty bore every night spent away from you. Always remember that DADDY LOVES YOU!

I also wish to acknowledge the support of the management of the Obafemi Awolwo University (OAU) for giving me the opportunity to go out and undertake this

PhD programme at WITS, South Africa. The following members of the Centre for Energy Research and Development (CERD), OAU are acknowledged: Prof M. K. Fasasi (my B.Sc.Hons. & Master's supervisor), Prof F. A. Balogun (my mentor), Prof. E. I. Obiajunwa (Director), Prof D. A. Pelemo (ex-Director), Prof G. A. Osinkolu and the following distinguished personalities still at the CERD, Profs J. Ajao, A. Y. Fasasi, W. Siyanbola, J-F. K. Akinbami, J. A. Akintunde, S. O. Olabanji, I. Obioh. Thank you all for the support and the guidance. Your pieces of advice went a long way in making me strong and eased my way to where I find myself today.

The financial supports that I enjoyed during the course of my PhD programme which came in the following forms are hereby acknowledged: the iThemba LABS topup funding, the WITS Postgraduate Merit Award (PMA), the WITS J.C. Carstens (2013), Bursary supplementation from Research funds of Dr Usman to pay my tuition fees during my first year (2013). I also wish to thank the National Research Foundation (WITS) for granting me the late 2015 award (Bursary Control) which helped clear my outstanding fees. I am and will always be grateful.

The management of the Abdul Salam International Centre for Theoretical Physics (ICTP), Trieste, Italy, is well acknowledged for providing me with financial assistance which covered half the travel and full subsistence expenses during my first visit to the ICTP for the SMR2575 from March 24-28, 2014 in Trieste, Italy.

This project would not have been a success without the hard work from behing the scene of the iThemba LABS target maker, Ms Yvonne Ntombizonke Kheswa. Thank you for providing details about the targets on my several requests. The exchanges of emails will be remembered. I am equally indebted to the iThemba LABS Accelerator team for providing high quality beam. The long hours of beam tuning to ensure my project becomes a success will forever be remembered. I also want to thank the Head of the iThemba Nuclear Physics Division, Dr. Rudolph

Nchodu for ensuring we had smooth running of the experiments. I say THANK YOU!

Lastly and definitely not the least, I wish to appreciate my brothers and sisters for their supports in all forms. Your brother will always remember you!

As a young scientist, I always found inspiration in the following quote:

"Only one who devotes himself
to a cause with his whole strength
and soul can be a true master.
For this reason mastery demands
all of a person."

—Albert Einstein

Contents

List of Figures

List of Tables

‘

Chapter 1

Introduction

Giant resonances were first observed in atomic nuclei in 1937 following the exposure of a series of target nuclei which included antimony, bromine, chromium, copper, gallium, indium, phosphorous, silver, tellurium, zinc, among others, to high energy γ-rays [Bot37]. At the time a number of questions were raised, such as whether or not it was a feature restricted to only certain nuclei. About a decade later, Baldwin and Klaiber made similar observations for uranium and thorium targets [Bal47] and then also in ^{12}C and ^{63}Cu [Bal48]. This resonance was first interpreted in terms of dipole vibrations by Migdal [Mig44]. A more comprehensive and widely accepted picture, which depicts it as two hydrodynamic fluids of protons and neutrons vibrating against each other, was later arrived at [Gol48,Ste50] and it was termed the IsoVector Giant Dipole Resonance (IVGDR). Other forms of giant resonances became known as more sophisticated light particle accelerators became operational. In 1971, Pittan and Walcher discovered the IsoScalar Giant Quadrupole Resonance (ISGQR) from inelastic electron scattering experiments (e,e$'$) [Pit71]. Shortly after in 1975, the IsoVector Giant Quadrupole Resonance (IVGQR) was also discovered from (e,e$'$) studies [Tor75], and in 1977 the IsoScalar Giant Monopole Resonance (ISGMR) was first clearly identified from inelastic alpha scattering (α, α') measurements [Har77]. The two types of isoscalar giant octupole resonances were discovered separately. The Low Energy Octupole Resonance (LEOR) was first observed in 1978 in (α, α') measurements [Mos78] while

the High Energy Octupole Resonance (HEOR) was only observed in 1996 in (e,e′) measurements [Cla96]. The IsoVector Giant Monopole Resonance (IVGMR) was discovered in pion exchange reactions in 1983 [Bow83] while the IsoScalar Giant Dipole Resonance (ISGDR) was not experimentally observed until 1997 in (α, α') experiments [Dav97]. In addition to the above mentioned types of giant resonances which are all electric in nature, spin-flip modes of giant resonances have also been found in nuclei. Their excitation is favoured by charge-exchange reactions which also greatly favours isospin excitation corresponding to isovector modes. The most prominent spin-flip modes are the magnetic isoscalar giant monopole resonance (M1) and the isovector giant monopole resonance, also known as the Gammow-Teller resonance [Har02].

In principle, charge-exchange reactions excite isovector modes while the (α, α') reaction excites isoscalar modes. The (e,e′) reaction excites both isoscalar and isovector modes. One of the setbacks associated with the (e,e′) reaction is that it poses the problem of disentanglement of the different GR modes that occur in the same excitation energy range as is the case for the electric ISGQR ($E2$) and the electric ISGMR ($E0$) modes. The proton inelastic scattering (p,p′) reaction also excites both isoscalar and isovector modes. The challenge of disentanglement of modes is overcome by selecting the appropriate kinematic conditions as suggested by the distorted wave Born approximation (DWBA) predictions.

Since giant resonances are highly damped with a width of only a few MeV, important information about their decay can be extracted from the total width of the resonance. This can be achieved with coincidence inelastic scattering experiments by analysing the excitation energies and angular distributions of all the reaction products. Such experiments, however, are very difficult to come by due to the sophistication of the setup they require and also their cost implication.

Three main factors contribute to the total width of a giant resonance. The first of them results from the coupling of correlated particle-hole $(p-h)$ configurations to uncorrelated $p-h$ configurations known as the Landau damping. The second term, called the escape width, results from the coupling of the correlated $1p-1h$ to the continuum. The third term which is associated with the mixing of the correlated $p-h$ states with more complex configurations, is known as the spreading width. Despite the remarkable success of the modern theoretical calculations in predicting the centroid energies, they fail to provide independently an acceptable description of the widths.

Over the years, significant progress has been made, from both the theoretical and experimental point of view, in the study of giant resonances. The recent discovery of fine structure as a fundamental feature of atomic nuclei, irrespective of the giant resonances mode [She04, Kal06, She09], has given a new impetus to this area of research. Modern theoretical calculations based on the shell model [Wil56] which introduced the concept of $1p-1h$ excitations [Tam45, Dan50], recorded huge successes in the interpretation of the IVGDR. They gave a more realistic picture and better predictions than the erstwhile hydrodynamic model [Era86].

The observation of fine structure in the excitation energy region of giant resonances provides an avenue for extracting important information about how they decay. The analysis of this fine structure by means of local scaling dimensions [Aib99] has been found to be a powerful means of extracting the characteristic energy scales from the experimental spectra [Aib03]. Besides, a number of other techniques has also been employed for analysing the fine structure of giant resonances and among them: the entropy index method [Lac00], the Fourier transform, the discrete wavelet transform (DWT) and the continuous wavelet transform (CWT) approaches [She08]. A direct comparison between the characteristic energy scales extracted from the fine structure of the experimental data and those of the microscopic theoretical calculations allows for the identification

of the dominant factors that contribute to the total width of the resonance. While the CWT is preferred for fine structure analysis in the giant resonance region, the DWT is efficient for estimating the background components of the spectra. On account of its very good resolution, the Morlet wavelet is preferred over other forms of wavelet basis [Pol14] for the analysis of the fine structure.

The present project seeks to investigate the fine structure of the IVGDR in the neutron-rich nuclei ^{42}Ca, ^{44}Ca and ^{48}Ca in a systematic way.

Photo-absorption cross-sections have been measured in ^{40}Ca, ^{42}Ca, ^{44}Ca and ^{48}Ca. The photo-neutron reaction in particular is a reliable tool for investigating the strength of the IVGDR in medium-heavy and heavy nuclei. This is owing to the fact that for such nuclei the Coulomb force becomes very important such that the decay of the IVGDR by proton emission is highly subdued [Har02]. Unlike the doubly-magic ^{40}Ca [Bag65] and ^{48}Ca [Pyw80], the semi-magic nuclei have broad-structured strength distributions. This is consistent with the predictions of Fallieros and Goulard [Gou67, Fal70] of isospin splitting as observed in ^{42}Ca [Ass81] and a clear splitting of the IVGDR strength into two components in ^{44}Ca [Har81].

Previous studies seeking to investigate the decay of the IVGDR in ^{40}Ca and ^{48}Ca were carried in coincidence experiments of inelastic electron scattering (e,e$'$) and inelastic proton scattering (p,p$'x$) reactions, where x stands for either a proton (p), a neutron (n) or an alpha particle (α), at finite angles [Cos94, Die94, Car01, Die01a, Die01b, Str00]. No such studies were performed for ^{42}Ca and ^{44}Ca. In those measurements, alongside the IVGDR, $E0$ and $E2$ modes were also excited within the excitation energy range of 8 to 26 MeV. The strength of each mode was resolved by multipole decomposition and angular correlations. One of the major setbacks of those measurements was that they gave no account of quasi-free reactions despite the relatively low two-particle emission threshold of those nuclei.

For example, the $2p$ emission threshold for ^{40}Ca is in the range of 15 MeV while the $2n$ emission threshold is around 18 MeV for ^{48}Ca. The extracted IVGDR strengths from those experiments were found to be significantly underestimated in comparison with the available gamma-absorption data [Cos94, Die94, Car01, Die01a, Die01b, Str00]. Consequently, tangible conclusions could not be drawn about the decay of the IVGDR.

In order to investigate the fine structure of the IVGDR of these isotopes, high energy-resolution zero-degrees ^{40,42,44,48}Ca(p,p$'$) measurements were carried out at the cyclotron facility of iThemba Laboratory for Accelerator Based Sciences (LABS), Cape Town, providing a 200 MeV proton beam together with the K600 magnetic spectrometer. As predicted by the DWBA calculations, nuclear response in zero-degrees (p,p$'$) reactions at intermediate energies is dominated by dipole excitations. Such measurements are now possible with the recently developed 0° facility of the K600 magnetic spectrometer of iThemba LABS [Nev11].

Equivalent photo-absorption cross-sections were obtained by conversion of the double differential cross-section extracted from the experimental data, by means of virtual photon production rates. Theoretical calculations within the framework of the Random Phase Approximation (RPA), the Second RPA (SRPA), the Quasi-particle RPA (QRPA) and the Continuum RPA (CRPA) have been performed. Similarly, theoretical calculations within the framework of the Relativistic QRPA (RQRPA) and Relativistic Quasi-particle Time Blocking Approximations (RQTBA) have also been performed. Level density of the $J^{\pi} = 1^{-}$ states has been extracted from the obtained experimental data using the fluctuation analysis method.

The experimental part of this project was approved by the iThemba LABS Programme Advisory Committee (PAC) in 2012 as project PR210. The project received beamtime for 3 weekends in October 2013 and 2 weekends in July 2014.

Measurements were carried out at the cyclotron facility of iThemba LABS, which provided a proton beam of 200 MeV, together with the K600 magnetic spectrometer in zero-degrees mode.

This thesis is structured as follows:

- Chapter 2 provides the theoretical background to the study of fine structure of the isovector giant dipole resonance. The chapter also gives an overview of; the proton inelastic scattering formalism, the virtual photon analysis method, the microscopic models used for the theoretical calculations and a comprehensive description of the techniques used for the extraction of the level density.

- Chapter 3 gives a description of the experimental procedure. An overview of the experimental setup and a detailed description of the various techniques employed for extracting the experimental spectra are presented.

- Chapter 4 deals with the results. Experimental and theoretical results are presented, compared and discussed.

- Chapter 5 deals with the conclusions and recommendations.

Chapter 2

Theoretical background to the study

This chapter is devoted to the theoretical concepts relevant to the study of fine structure of the isovector giant dipole resonance (IVGDR) in ^{42}Ca, ^{44}Ca and ^{48}Ca using the proton inelastic scattering reaction at zero-degrees. In Section 2.1, the theoretical concepts of giant resonances and their classification into various modes, with emphasis on the IsoVector Giant Dipole Resonance (IVGDR), are presented. Section 2.2 deals with the inelastic proton scattering formalism via the nucleon-nucleon and Coulomb interaction contributions. Section 2.3 focusses on the Coulomb excitation of the IVGDR. In Section 2.4, a description of the microscopic models used for the theoretical calculations is given while the tools of extraction of the characteristic energy scales of the IVGDR are presented in Section 2.5. This chapter ends with a description of the techniques employed for extracting the $J^{\pi} = 1^{-}$ level density, in Section 2.6.

2.1 Theory of giant resonances

Giant resonances (GR) are small-amplitude, high-frequency, coherent vibrations of nucleons against themselves. As compared to single-particle excitation resonances, GRs have larger strengths and widths. From a microscopic point of

view, GRs are commonly defined as a coherent superposition of $1p-1h$ excitations. Quantum-mechanically, a giant resonance (GR) state of the atomic nucleus, $\Psi^{\lambda,\sigma,\tau}$, is conceived as resulting from the transition from its ground state to some collective state characterised by a given set of quantum numbers, namely the angular momentum, λ, the spin, σ, and the isospin, τ, transfers. It is represented as:

$$|\Psi_{GR}^{\lambda,\sigma,\tau}\rangle = O^{\lambda,\sigma,\tau}|\Psi_{g.s}\rangle, \tag{2.1}$$

where $|\Psi_{g.s}\rangle$ and $|\Psi_{GR}^{\lambda,\sigma,\tau}\rangle$ are the wave functions describing the ground state and the giant resonance state, respectively and $O^{\lambda,\sigma,\tau}$ is the one-body operator acting on the ground state by exciting a specific λ, σ and τ, and is governed by the Pauli exclusion principle.

Giant resonances are effectively classified into various modes according to their macroscopic quantum numbers L, S and T which represent the angular momentum, the spin and the isospin, respectively. The angular momentum transfer also known as the multipolarity derives its name from the word *'multipole'* in which the prefix "multi" is substituted by the *Greek* adjective obtained from the number 2^L. Hence, the monopole, the dipole, the quadrupole, the octupole and the hexadecapole correspond to $L = 0$, 1, 2, 3 and 4, respectively. The mode is called magnetic when it involves some transfer of spin ($S = 1$) and electric when there is no spin transfer ($S = 0$). Also, it is termed isovector when there is some transfer of isospin ($T = 1$) during the course of the excitation, otherwise it is an isoscalar mode ($T = 0$).

The giant monopole resonance (GMR) also called the breathing mode is the one in which, according the hydrodynamic model, nucleons vibrate against themselves by successive compression and expansion about the equilibrium shape of the nucleus. One of the advantages of studying this mode is that it allows for the

determination of the nuclear compressibility of the nucleus. The giant dipole resonance (GDR) is characterised by a translational vibration of nucleons against themselves. The giant quadrupole resonance (GQR) and higher multipoles such as the giant octupole resonance (GOR) and the giant hexadecapole resonance (GHR) are modes in which the nuclear fluids assume very complex shapes with respect to the original shape of the nucleus.

The various possible modes of a giant resonance for $L = 0$, 1 and 2 are illustrated in Fig. 2.1 [Har02, Zeg99] where the modes are defined as follows:

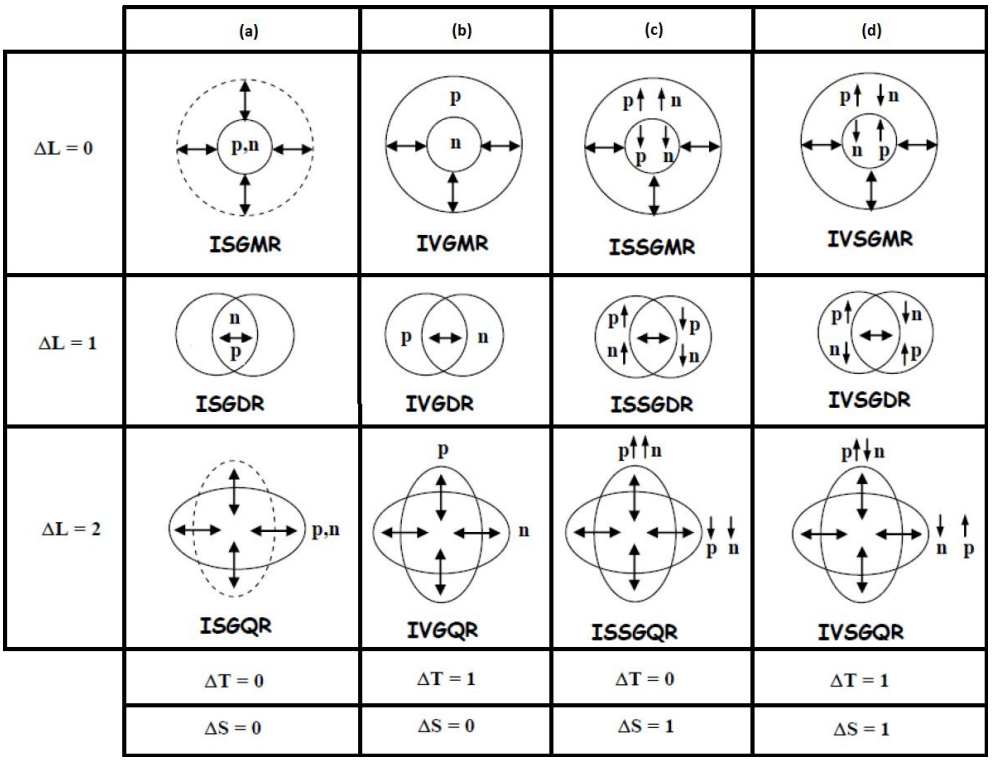

Figure 2.1: A schematic diagram of the various possible modes of giant resonance for $L = 0$, 1 and 2.

- For $\Delta L = 0$, *ISGMR*: IsoScalar Giant Monopole Resonance; *IVGMR*: IsoVector Giant Monopole Resonance; *ISSGMR*: IsoScalar Spin-flip Giant Monopole Resonance; and, *IVSGMR*: IsoVector Spin-flip Giant Monopole Resonance.

- For $\Delta L = 1$, *ISGDR*: IsoScalar Giant Dipole Resonance; *IVGDR*: IsoVector

Giant Dipole Resonance; *ISSGDR*: IsoScalar Spin-flip Giant Dipole Resonance; and, *IVSGDR*: IsoVector Spin-flip Giant Dipole Resonance.

- For $\Delta L = 2$, *ISGQR*: IsoScalar Giant Quadrupole Resonance; *IVGQR*: IsoVector Giant Quadrupole Resonance; *ISSGQR*: IsoScalar Spin-flip Giant Quadrupole Resonance; and, *IVSGQR*: IsoVector Spin-flip Giant Quadrupole Resonance.

2.1.1 Decay of giant resonances

Giant resonances in nuclei are located well above the particle emission threshold. They, therefore, mainly decay by particle emission. Significant information about the decay of GRs is contained in the width of the resonance. Coincidence experiments constitute a lucrative tool for investigating the width of GRs. Such experiments allow for the energy spectrum and angular distribution of all the reaction products to be determined simultaneously. However, the difficulty associated with the detection of inclusively all emitted particles, together with the cost implication of such set-ups have made such measurements very scarce. Meanwhile, recent experimental developments in inelastic hadron scattering with high energy-resolution set-ups have revealed that GRs carry fine structure irrespective of the modes. The observed fine structure provides valuable information about the factors that contribute to the decay of giant resonances. A practical way of determining the factors that dominate the decay of the GRs is by establishing a direct comparison between the energy scales extracted from the experimental spectra and those of applicable theoretical calculations.

2.1.1.1 The width of a giant resonance

The total experimental width, Γ of a GR is commonly described as consisting of three contributing factors [Har02]:

$$\Gamma = \Gamma_{\text{in}} + \Gamma^{\downarrow} + \Gamma^{\uparrow} \tag{2.2}$$

- The first term, Γ_{in}, is the inherent width also known as the Landau damping

which arises from the spreading in the excitation energy of the initial collective $1p-1h$ function. This width term occurs when non-collective $1p-1h$ configurations with same quantum numbers as the collective $1p-1h$ state have close energy.

- The second term, $\Gamma_{\downarrow}$, called the spreading width arises from the coupling of $1p-1h$ configurations to $2p-2h$ configurations. This is possible going by the fact that GRs occur in excitation energy ranges where $2p-2h$ configurations of same spin and parity as the collective $1p-1h$ configuration also occur. In the spreading width, there are possibilities of intermediate states $2p-2h$, $3p-3h$, etc, also decaying by particle emission yielding an intermediate width term, $\Gamma^{\downarrow\uparrow}$. This premise is built on the possible coupling of the $1p-1h$ to $3p-3h$ configurations and higher orders such that the energy spreads over all degrees of freedom. Similarly, if the overall system is considered to be at equilibrium, the decay will be that of a compound nucleus with the same excitation energy, spin and parity as the GR. Hence, this can lead to a partial width for equilibrium term, $\Gamma^{\downarrow\uparrow}$ and a statistical decay term of the compound nucleus, $\Gamma^{\downarrow\downarrow}$. The overall spreading width can then be written as:

$$\Gamma^{\downarrow} = \Gamma^{\downarrow\uparrow} + \Gamma^{\downarrow\downarrow}. \tag{2.3}$$

- The third term, $\Gamma^{\uparrow}$, called the escape width arises from particle emission as the collective $1p-1h$ occurs at excitation energies beyond the particle emission threshold. This term corresponds to the direct decay of the collective $1p-1h$ state of the original target nucleus, A, into a recoil nucleus, $(A-1)$, in which hole states are populated leading to the formation of a compound nucleus.

These various factors contributing to the width of a GR are schematically illustrated in Fig. 2.2.

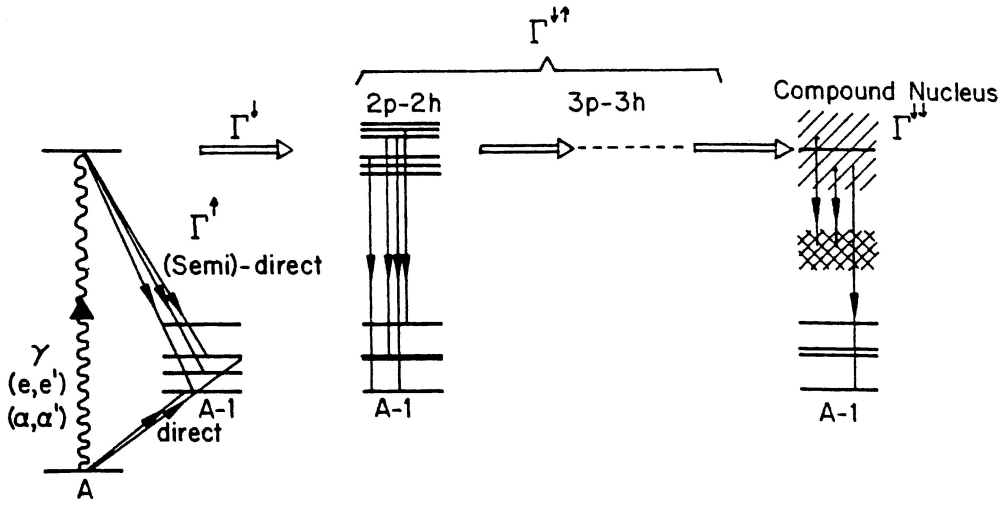

Figure 2.2: Schematic illustration of the various components contributing to the width of a GR (taken from Ref. [Har02]).

2.1.1.2 The doorway picture of giant resonances

The concept of doorway state in many-body nuclear reactions was first introduced by Block and Feshbach [Blo63] and subsequently generalised [Fes67, Fes74] and widely adopted for interpreting intermediate processes in nuclear reactions. This concept is also commonly adopted for interpreting the decay of GRs in terms of the spreading width but also gives a good account of the fine structure that occurs in the excitation energy region of GR in high energy-resolution experiments. It is built on the coupling of single states to the entrance channel such that more complex states, which are coupled to themselves, weakly couple to the continuum. For example, considering the damping of single-particle states due to collision processes among nucleons, a nucleon can transit from its initial state to a state above the Fermi energy level leaving behind an unpaired hole. This process is mostly effective at nuclear surfaces characterised by low level density. Since particle-particle correlation is weak in cold nuclei near close shells compared to particle-hole correlation [Har02], it is rather described by taking for the particle-hole state a low-lying correlated $1p-1h$ surface vibration. The states consisting of one nucleon and surface vibration are the doorway states [Ber83, Wam88]. The mechanism that describes them is schematically illustrated in Fig. 2.3 [Kal04,

Pol11].

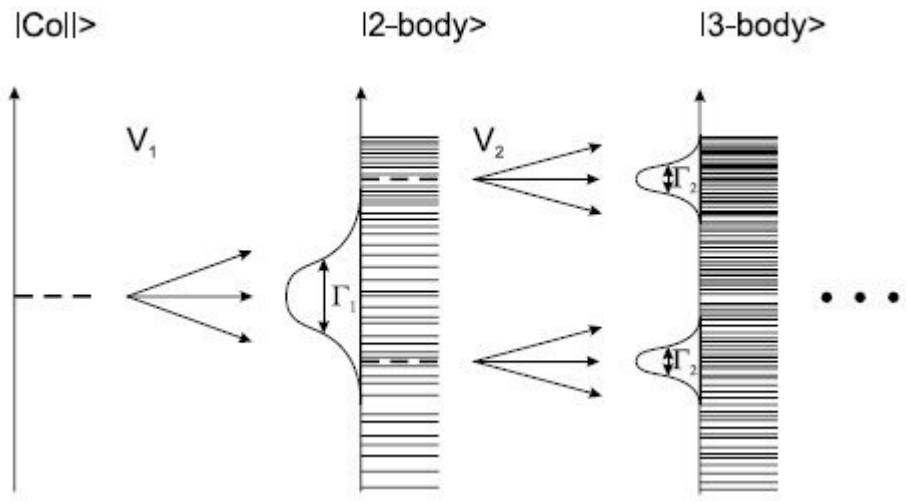

Figure 2.3: Schematic illustration of the doorway state. Here $|Coll\rangle$ denotes the doorway state, coupled to the entrance channel. It then couples to more and more complex states starting from the $2p-2h$ and then $3p-3h$ states, etc, and V_1, V_2, etc. are the residual interactions at each level of coupling.

2.1.2 The Isovector Giant Dipole Resonance (IVGDR)

The isovector giant dipole resonance (IVGDR) like any other type of GR results from the collective motion of nucleons. Its characteristic properties depend on the bulk structure of the nucleus. The IVGDR being the first type of GR to be known, has been extensively studied ever since its discovery. It has been found in virtually all nuclei across the periodic table from light nuclei in which its strength exhibits fragmentation through deformed nuclei in which it splits into two components to spherical nuclei where it is well reproduced with a Lorentzian function [Har02]. Reviews of the several years of investigations on the IVGDR have allowed for its systematic studies from which some of its main features have been understood and expressed as a function of the atomic mass and the excitation energy [Ber75, Ber77a, Ber83, Spe81].

The IVGDR like any other resonance is characterised by 3 main features namely

the resonance energy, the strength and the width of the resonance.

2.1.2.1 The resonance energy of the IVGDR

The resonance energy of the IVGDR has been found to be reproducible as a function of the atomic mass number, A, as [Ber75]:

$$E_{\mathrm{R}}(\mathrm{IVGDR}) = 47.9A^{-\frac{1}{4.27}} \quad (\mathrm{MeV}) \tag{2.4}$$

or

$$E_{\mathrm{R}}(\mathrm{IVGDR}) = 31.2A^{-\frac{1}{3}} + 20.6A^{-\frac{1}{6}} \quad (\mathrm{MeV}). \tag{2.5}$$

The $A^{-\frac{1}{3}}$ dependence of Eq. (2.5) was derived from the assumption that the nucleus can be considered as a spherical resonator with a fixed surface whose wavelength is directly proportional to the nuclear radius [Spe81]. On the other hand, the $A^{-\frac{1}{6}}$ dependence was arrived at considering the fact that the restoring force of the oscillation is directly related to the surface symmetry energy of the Myers and Swiatecki's extended mass formula [Mye69, Mye74].

A Plot of both expressions of the IVGDR resonance energy as a function of A, as illustrated in Fig. 2.4 shows excellent agreement for A ranging between 1 and 208.

2.1.2.2 The strength of the IVGDR

The strength of the IVGDR is generally expressed in terms of the Thomas-Reiche-Kuhn sum rule as:

$$\int_{E_{\mathrm{min}}}^{E_{\mathrm{max}}} \sigma_{\gamma}^{abs} dE = 60\frac{NZ}{A}(1+\kappa) \quad (\mathrm{MeV\ mb}), \tag{2.6}$$

where σ_{γ}^{abs} is the absolute photo-absorption cross-section, E_{min} and E_{max} are, respectively, the lower and the upper limits of the IVGDR excitation energy

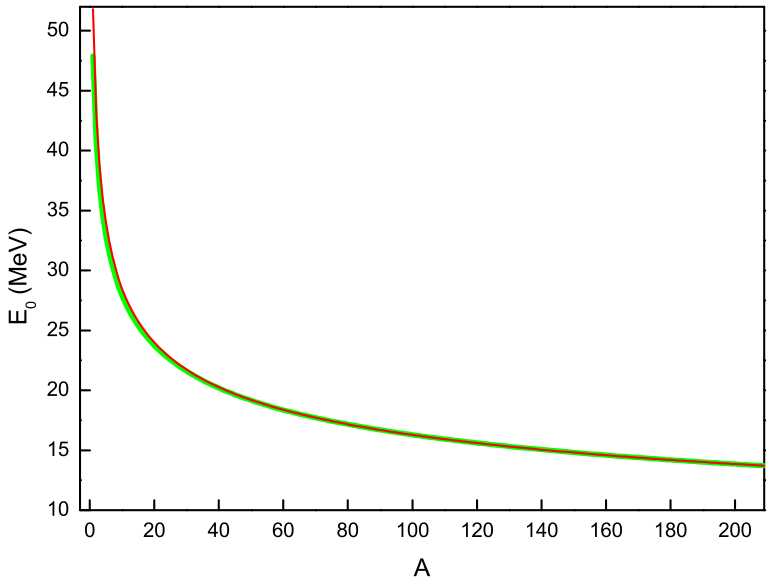

Figure 2.4: A plot of the IVGDR centroid energy, E_{R}, as a function of the atomic mass number, A, for all nuclei between A = 1 and A = 208 using Eqs. (2.4) (green line) and (2.5) (red line).

spectrum, N and Z are the neutron and proton numbers, respectively, and κ is the neutron-proton exchange factor which characterises all isovector modes.

2.1.2.3 The width of the IVGDR

The width of the IVGDR remains one of the least understood of its properties. There are however a few reports on its systematic studies and among such is the work of Auerbach and Yeverechyau [Aue75]. They concluded from photo-neutron yield measurements that the width of the IVGDR varies from around 4 MeV for heavy nuclei to 10 MeV for light nuclei. They also established that the IVGDR width could fairly be reproduced in terms of A as:

$$\Gamma = 2.3 + 14A^{-\frac{2}{3}} + 21A^{-\frac{1}{2}} \quad \text{MeV} \qquad \text{for} \qquad A < 90. \tag{2.7}$$

2.2 Proton inelastic scattering

The atomic nucleus is a complex A-nucleon system which, as yet, no exact wave function can successfully describe [Gle83]. The shell-model Hamiltonian of the nucleus is given as:

$$H_{\mathrm{A}} = \sum_{\mathrm{i}=1}^{A} (T_{\mathrm{i}} + U_{\mathrm{i}}) + \sum_{\mathrm{i}\neq\mathrm{j}} V_{\mathrm{ij}}, \tag{2.8}$$

where $U_{\mathrm{i}}(\mathrm{r})$ is the central potential acting on a single nucleon, $V_{\mathrm{ij}} = V(r_{\mathrm{i}} \text{ - } r_{\mathrm{j}})$ is a phenomenological 2-body potential that is well behaved and T_{i} is the kinetic energy operator defined as:

$$T_{\mathrm{i}} = -\frac{\hbar^2}{2m_{\mathrm{i}}} \bigtriangledown_i^2 \,. \tag{2.9}$$

Considering the proton inelastic scattering reaction:

$$p_{\mathrm{i}} + A_{\mathrm{i}} \rightarrow p_{\mathrm{f}} + A_{\mathrm{f}}, \tag{2.10}$$

where the subscripts i and f represent the entrance and exit channels, respectively, the Schrödinger equation of the entire system can be written as:

$$(H - E)\Psi = 0 \qquad \text{or} \qquad (E - H - T)\Psi = V\Psi. \tag{2.11}$$

Expressing H in terms of either partitions of the original system, one can write:

$$H = H_{\mathrm{i}} + T_{\mathrm{i}} + V_{\mathrm{i}} = H_{\mathrm{f}} + T_{\mathrm{f}} + V_{\mathrm{f}}. \tag{2.12}$$

Thus,

$$(E - H_{\mathrm{i}} - T_{\mathrm{i}})\Psi_{\mathrm{i}} = V_{\mathrm{i}}\Psi_{\mathrm{i}}. \tag{2.13}$$

For such reactions, the scattering amplitude is provided by the transition matrix, T, which is given as:

$$T_{\mathrm{fi}} = \langle \Psi_{\mathrm{f}}^{(-)} \mid V_{\mathrm{f}} \mid \Psi_{\mathrm{i}}^{(+)} \rangle, \tag{2.14}$$

where $\Psi^{(-)}$ and $\Psi^{(+)}$ denote the incoming and outgoing waves, respectively.

The differential cross-section of protons scattered into the direction θ, within a solid angle $d\Omega$ through the area $dA = r^2 d\Omega$ in channel f, for $r_{\rm f} \to \infty$, is given as:

$$\frac{d\sigma}{d\Omega} = \frac{m^2}{(2\pi\hbar^2)^2}\frac{k_{\rm f}}{k_{\rm i}} \mid T_{\rm fi} \mid^2 . \tag{2.15}$$

The scattering angle is defined as:

$$\theta \ = (k_{\rm i}, k_{\rm f}), \tag{2.16}$$

where $k_{\rm i}$ and $k_{\rm f}$ are the wavevectors of the incoming and outgoing waves, respectively.

2.2.1 Optical potential

The solution of Eq. (2.13) depends on $\Psi^{(+)}$ and consequently on $T_{\rm fi}$. Although no exact solution exists, a very good approximation is provided by the Distorted Wave Born Approximation (DWBA) [Gle65, Gle66, Mad83, Sat66, Joh66]. The central potential, U, of the shell model represents the average field of the nucleons on a particular nucleon and the corrections to this average are calculated by taking into account the residual interaction $V_{\rm ij}$. Thus, the central potential is chosen such that it depends only on relative coordinates between projectile and target. An optical potential component [Lev52, Fes54, Mel56, Woo54] is added in order to improve the description of the interaction. The central potential governing the scattering is built on the nucleon density which is fairly constant in the interior of the nucleus and vanishes beyond the nuclear radius. It is generally represented in a Woods-Saxon form [Woo54] as:

$$f(r) = \frac{1}{1 + exp(r - R)/a}, \tag{2.17}$$

where a is the diffuseness and R is the nuclear radius. Since a real potential conserves flux, the central potential, U, must be complex. It is thus represented

as:

$$U(r) = \frac{V}{1 + e^{(r-R_{\rm v})/a_{\rm v}}} + \frac{iW}{1 + e^{(r-R_{\rm w})/a_{\rm w}}}, \tag{2.18}$$

with

$$R_{\rm v,w} = r_{\rm v,w} A^{1/3}. \tag{2.19}$$

2.2.2 Coulomb and nuclear potentials

For charged particles scattering in general and proton in this case, a Coulomb potential term is added to the potential governing the scattering process. A good mathematical treatment on this can be found in Refs. [Mes62, Rod67]. In such a case, the scattering amplitude and consequently the cross-section consists of a pure Coulomb term and a nuclear potential term which are inextricably intertwined. The optical potential has the form [Sch82]:

$$\begin{aligned} U(r) = U_{\rm Coul}(r) - V f_0(r) - iW f_{\rm W}(r) \\ + \frac{2}{r} V_{\rm SO} \frac{d}{dr} f_{V_{\rm SO}}(r) \\ + iW_{\rm SO} \frac{d}{dr} f_{W_{\rm SO}}(r)] \vec{l}.\vec{\sigma}, \end{aligned} \tag{2.20}$$

where $f_{\rm x}(r_{\rm j},r_{\rm x},a_{\rm x})$ are Woods-Saxon form factors, $U_{\rm Coul}(r)$ is the Coulomb potential term, V and W are the real and imaginary terms of the nuclear potential, respectively, $V_{\rm SO}$ and $W_{\rm SO}$ are the real and imaginary terms of the spin-orbit potential, respectively, and $\vec{l}$ and $\vec{\sigma}$ are the angular momentum and spin operators, respectively.

Under zero-degrees kinematic conditions, proton inelastic scattering reaction responses at intermediate energies are dominated by Coulomb interaction as the nucleon-nucleon contribution in such situations is negligible. By way of example, the results of the DWBA calculations, using the code DWBA07 [Ray07], carried out on ^{48}Ca is shown in Fig. 2.5 [Pon14]. The nucleon-nucleon (NN) contribution,

the Coulomb contribution (Coul) and the sum response of both contributions (NN + Coul) are all illustrated. The overall response is predominantly due to Coulomb interaction. The optical potential in the DWBA07 calculations was computed from effective NN force based on Love-Franey parametrisations [Lov81, Fra85].

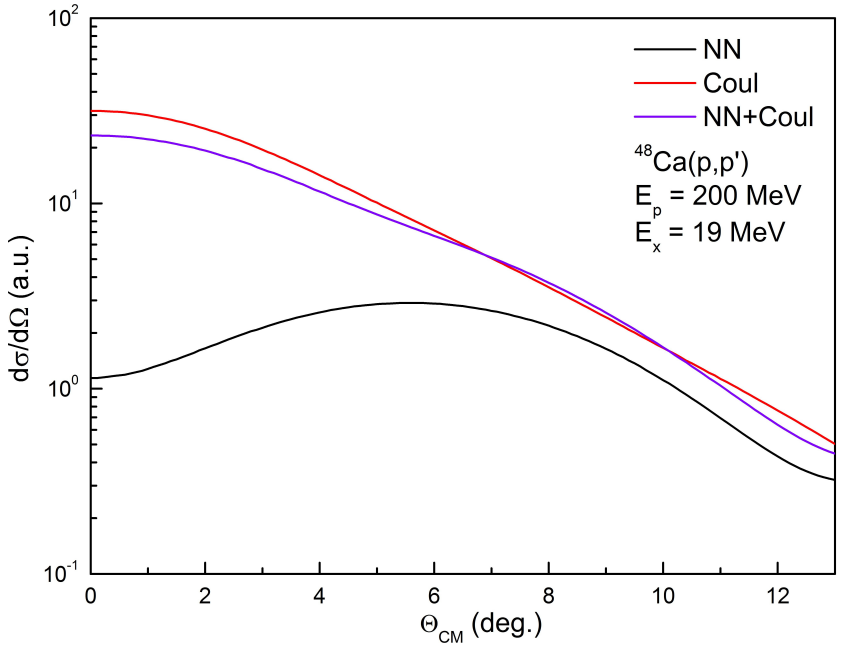

Figure 2.5: Result of the DWBA calculation of ^{48}Ca(p,p′) reaction at E_{p} = 200 MeV, $\theta_{\mathrm{Lab}} = 0$ and $E_{\mathrm{R}} = 19$ MeV. The NN contribution (black), the Coul contribution (red) and the sum [Coul + NN] (violet) are illustrated.

2.3 Coulomb excitation

As seen in Section 2.2.2, the IVGDR excitation in inelastic proton scattering reactions is predominantly due to the Coulomb interaction. In actual fact, there are no effective interactions between the incident projectile and the target nucleus at very forward angles. This is because the impact parameter in such reactions is generally greater than the radius of the combined projectile-target formed system. The interaction mechanism can be perceived in a semi-classical picture through the dynamic of projectile-target collision and also from the virtual photon production mechanism in a purely relativistic frame of reference.

2.3.1 The semi-classical picture

In a semi-classical regime, a projectile of mass m_p and relative velocity v_p moving along a straight path suffers deflection in the neighbourhood of a target nucleus due to the Coulomb interaction as illustrated in Fig. 2.6. In this picture, both particles are taken as point charges and the projectile is considered to move much faster than the target such that the latter is assumed stationary.

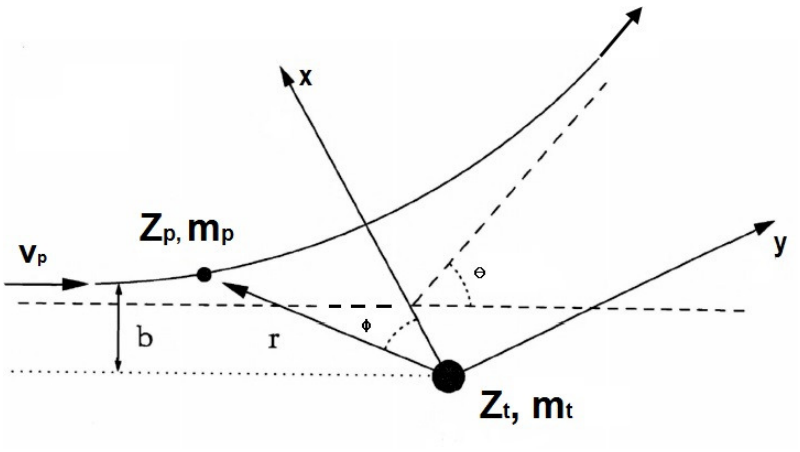

Figure 2.6: Inelastic scattering of a projectile under the influence of the Coulomb force in a semi-classical laboratory frame of reference.

The energy and momentum of the projectile are respectively given as:

$$E = \gamma m_{\mathrm{p}} c^2 \tag{2.21}$$

and

$$p = \gamma m v_{\mathrm{p}}, \tag{2.22}$$

where c is the speed of light in a vacuum.

The momentum impulse, Δp, can be expressed in terms of the transverse electric field, E_1, created by both particles as [Jac62]:

$$\Delta p = \int_{-\infty}^{\infty} eE_1(t)dt = \frac{2Z_t Z_{\mathrm{p}} e^2}{bv_{\mathrm{p}}}, \tag{2.23}$$

where b is the impact parameter and e is the elementary charge.

For small momentum transfers in which case the scattering angle, θ, is very small one can write:

$$\theta \simeq \frac{\Delta p}{p} = \frac{2Z_{\mathrm{p}}Z_{\mathrm{t}}e^2}{\gamma m_{\mathrm{p}} v_{\mathrm{p}}^2 b}. \tag{2.24}$$

The distance of closest approach is then given as:

$$b_{\mathrm{min}} = \frac{Z_{\mathrm{p}}Z_{\mathrm{t}}e^2}{\gamma m_{\mathrm{p}} v_{\mathrm{p}}^2}. \tag{2.25}$$

Assuming that the projectile is deflected through an orbit, the Rutherford differential cross-section can be written as:

$$\frac{d\sigma}{d\Omega} = \left(\frac{Z_{\mathrm{p}}Z_{\mathrm{t}}e^2}{4\pi\epsilon_0 4E}\right)^2 \frac{1}{\sin^4(\frac{\theta}{2})}, \tag{2.26}$$

where ϵ_0 is the permittivity of free space.

It is, however, important to note that in a relativistic regime, the projectile suffers no deflection rather it is the target that gets excited by the Coulomb field created. This is discussed in more details in the next subsection.

2.3.2 The virtual photon method

Independently developed by Weizsäcker [Wei34] and Williams [Wil34] in 1934, the virtual photon method which is an eikonal approximation method is built on the similarity between the fields of a fast moving charged projectile and the field of a pulse of radiation. It was arrived at by establishing a correlation between the effects of the projectile on the target and the interaction of radiation with the same target [Jac62]. In the scattering process, the perturbing fields of the

incident projectile are replaced with an equivalent radiation pulse which is employed to analyse the frequency spectrum of the virtual photons. The process is schematically illustrated in Fig. 2.7 [Ber88].

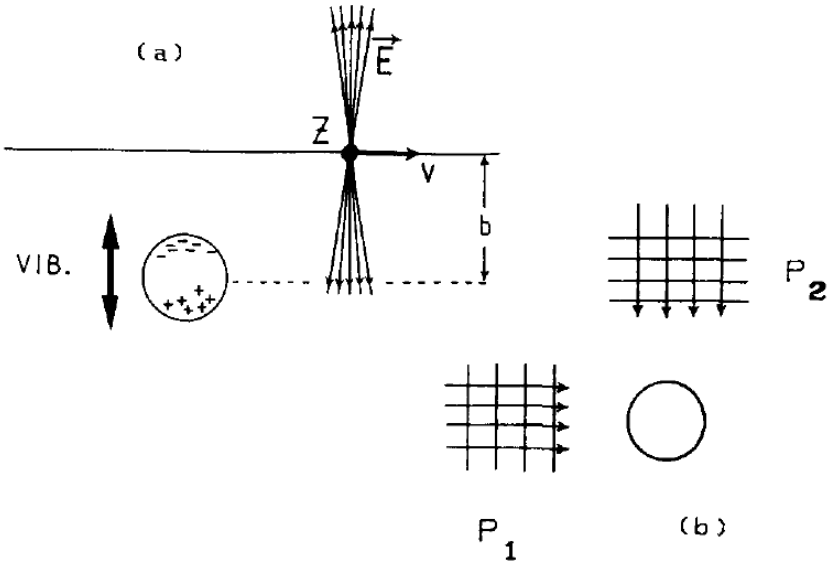

Figure 2.7: Principle of virtual photon production in the Coulomb excitation of the target nucleus. In (a): the relativistic projectile is incident on the target with an impact parameter large enough for the strong interaction to be negligible. A field is then created which induces vibration of the nucleus. In (b): The pulses (P_1) and (P_2) of plane wave of light produce similar effect on the target as the projectile in (a) (taken from Ref. [Ber88]).

Therefore, inelastic proton scattering reaction at and near zero-degrees, in principle, has an effect similar to photo-absorption reactions [Spe81] in the excitation of the isovector giant dipole resonance. The virtual photon spectrum is determined by the Fourier time-integral of the electromagnetic interaction [Gol84]. It can also be deduced from the total cross-section of the Coulomb excitation. This was first derived by Winther and Alder [Win79], and is given as [Ber85]:

$$\sigma(\hbar\omega) = (Z_{\rm p}\alpha)^2 \sum_{\pi lm} K^{2(l-1)} g_m(\xi) \mid G_{\pi {\rm lm}} \mid^2 B(\pi l)/e^2, \qquad (2.27)$$

where

$$g_m(\xi) = g_{-m}(\xi) = 2\pi(\omega/\gamma v)^2 \int_R^\infty \rho[K_m(\omega\rho/\gamma v)]^2 d\rho, \tag{2.28}$$

with α being the fine structure constant, π stands for either E (electric) or M (magnetic) excitation, K_m is the modified Bessel's function of order m and $G_{\pi\mathrm{lm}}$ are given in terms of the Legendre polynomials.

Integrating Eq. (2.27) over all possible final states of the target yields:

$$\sigma_\mathrm{c} = \sum_f \int \sigma(\epsilon)\rho_\mathrm{f}\ d\epsilon, \tag{2.29}$$

where $\rho_\mathrm{f}(\epsilon)$ is the density of final states of the target with energy ϵ.

Substituting Eq. (2.27) into Eq. (2.29), one gets:

$$\sigma_\mathrm{c} = \sum_f \int \{n_\mathrm{El}(\omega)\sigma_\mathrm{l}^\mathrm{E}(\omega) + n_\mathrm{Ml}(\omega)\sigma_\mathrm{l}^\mathrm{M}(\omega)\} d\omega/\omega, \tag{2.30}$$

where $\sigma_\mathrm{l}^\mathrm{E/M}$ are the photo-absorption cross-sections for a given multipolarity l.

Hence, the virtual photon numbers are deduced as:

$$n_{\pi\mathrm{l}}(\omega) = Z_\mathrm{p}^2\alpha \frac{l[(2l+1)!!]^2}{(2\pi)^3(l+1)} \sum_m \mid G_{\pi lm}(c/v) \mid^2 g_m(\xi). \tag{2.31}$$

A semi-classical virtual photon numbers expression for dipole excitation can also be obtained from Eq. (2.31) by adopting the Jäckle and Pilkuhn's approach [Jac75] as:

$$n_\mathrm{E1}(\omega) = Z_\mathrm{p}^2\alpha \frac{2}{\pi}\left(\frac{c}{v}\right)^2 [\xi K_0 K_1 - \frac{v^2\xi^2}{2c^2}(K_1^2 - K_0^2)], \tag{2.32}$$

where Z_p and v are the projectile atomic number and incident speed, respectively, γ is the Lorentz factor and ω is the angular frequency of the projectile.

The dimensionless quantity, ξ, is defined as:

$$\xi = \frac{\omega R}{\gamma v}, \tag{2.33}$$

where R is the nuclear radius defined as:

$$R = 1.25A^{\frac{1}{3}} \qquad \text{fm.} \tag{2.34}$$

The cut-off impact parameter, b_0, is given as:

$$b_0 = 1.25[1 + A^{\frac{1}{3}}] \qquad \text{fm.} \tag{2.35}$$

2.4 Microscopic models

In order to extract useful quantities that characterise the isovector giant dipole resonance (IVGDR) of the neutron-rich calcium isotopes understudy such as its strength as well its decay properties, a series of state-of-the-art theoretical calculations have been performed.

2.4.1 Random Phase Approximation (RPA)

First introduced by Bohm and Pines [Boh51], the RPA is an approximation method widely adopted in the study of many-body quantum systems such as in nuclear physics and condense matter physics. The RPA equation, for particle-hole ($\delta\overline{\rho}$: $X_{\rm ph} = \delta\overline{\rho}_{\rm ph}$) and hole-particle ($Y_{\rm hp} = \delta\overline{p}_{\rm hp}$) elements considered separately [Goe82], for the non-vanishing elements, can be written as [Tho61]:

$$\begin{pmatrix} A & B \\ -B^* & -A^* \end{pmatrix} \begin{pmatrix} X_{\rm ph} \\ Y_{\rm ph} \end{pmatrix} = \hbar\omega \begin{pmatrix} X_{\rm ph} \\ Y_{\rm ph} \end{pmatrix}, \tag{2.36}$$

where the matrices A and B are defined as :

$$A_{\rm php'h'} = (\epsilon_{\rm p} - \epsilon_{\rm h})\delta_{\rm pp'}\delta_{\rm hh'} - \left(\frac{\delta h_{\rm ph}}{\delta\rho_{\rm p'h'}}\right)_0 \tag{2.37}$$

and

$$B_{\mathrm{php'h'}} = \left(\frac{\delta h_{\mathrm{ph}}}{\delta \rho_{\mathrm{h'p'}}} \right)_0 , \tag{2.38}$$

with ϵ_{p} and ϵ_{h} being the particle and hole energies, respectively.

If a solution of Eq. (2.36) is denoted $|n\rangle$ where the correlated ground state is $|0\rangle$, then:

$$|n\rangle = \Omega_{\mathrm{n}}^{+}|0\rangle, \tag{2.39}$$

where Ω_{n}^{+} is the boson creation operator defined as:

$$\Omega_{\mathrm{n}}^{+} = \Sigma_{\mathrm{ph}}\{X_{\mathrm{ph}}^{(\mathrm{n})} a_{\mathrm{p}}^{+} a_{\mathrm{h}} - Y_{\mathrm{ph}}^{(\mathrm{n})} a_{\mathrm{h}}^{+} a_{\mathrm{p}}\} \tag{2.40}$$

such that $\Omega_{\mathrm{n}} \, |0\rangle = 0$ for all n, and the RPA amplitudes are:

$$X_{\mathrm{ph}}^{\mathrm{n}} = \langle n | a_{\mathrm{h}}^{+} a_{\mathrm{p}} | 0 \rangle \tag{2.41}$$

and

$$Y_{\mathrm{ph}}^{\mathrm{n}} = \langle n | a_{\mathrm{h}}^{+} a_{\mathrm{p}} | 0 \rangle. \tag{2.42}$$

The matrix elements of the transition operator, $O = \Sigma_{lk} O_{\mathrm{lk}} a_{\mathrm{l}}^{+} a_{\mathrm{k}}$, between the RPA state, $|n\rangle$, and the correlated ground state, $|0\rangle$, are given as:

$$|\langle n|O|0\rangle|^2 = \Sigma_{\mathrm{ph}} |O_{\mathrm{ph}}[X_{\mathrm{ph}}^{(\mathrm{n})} + Y_{\mathrm{ph}}^{(\mathrm{n})}]|^2. \tag{2.43}$$

Hence, the RPA is suitable for describing GR states which differ from the ground state by $1p-1h$ components as described in Eq. (2.1). Since RPA is limited to $1p-1h$ excitations, it gives a good account of the centroid energies and total transition probabilities. It, however, only accounts for Landau damping, and in the case of the CRPA (Sec. 2.4.5), for the escape width which is due to particle emission and does not account for the spreading width since coupling to higher orders such as $2p-2h$ are not included. The efforts of Brown and Bolsterli on simplifying the RPA calculations [Bro59] are well acknowledged. The outcome of their approximation is that all transition strengths are concentrated in one state which shifts to lower energy for attractive force (i.e. the isoscalar case) and to higher energy if the force is repulsive (i.e. the isovector case).

2.4.2 Second RPA (SRPA)

The second RPA (SRPA) is an extension of the RPA and was formulated by Yannouleas *et al.* [Yan83] following the Rowe's equation of motion method [Row68]. The SRPA is built on the simple RPA by adding $2p-2h$ couplings in addition to the $1p-1h$ couplings. It has successfully been applied to describe nuclear damping processes [Yan86] and in particular the spreading width in the decay of GRs [Dro86, Ada84]. In the SRPA, the excitation operator, O_ν^+, satisfies the following double-commutator equation:

$$\langle HF|[R,[H[O_\nu^+]]HF\rangle = \hbar\omega_\nu\langle HF|[R,O_\nu^+]|HF\rangle, \tag{2.44}$$

for any operator R, in the same space as O_ν^+, where:

- $\hbar\omega_\nu$ is the excitation energy,
- H is the exact many-body Hamiltonian and

- $|HF\rangle$ is the Hartree-Fock ground state of the nucleus.

The operator O_ν^+ is defined as:

$$\begin{aligned} O_\nu^+ = \Sigma_{mi}[X_{mi}(\omega_\nu)a_m^+ a_i - Y_{mi}(\omega_\nu)a_i^+ a_m] \\ +\Sigma_{m<n,i<j}[X_{mnij}(\omega_\nu)a_m^+ a_n^+ a_j a_i \\ -Y_{mnij}(\omega_\nu)a_i^+ a_j^+ a_n a_m]. \end{aligned} \tag{2.45}$$

In the latter equation, a^+ and a are fermion creation and annihilation operators, respectively, and X's and Y's are the forward and backward going amplitudes, respectively. The indices m, n, p, q indicate the particle state while i, j, k, l indicate the hole states.

Substituting Eq. (2.45) into Eq. (2.44), the matrix form of the SRPA equation reduces to:

$$\begin{pmatrix} A & B \\ -B^* & -A^* \end{pmatrix} \begin{pmatrix} X(\omega_\nu) \\ Y(\omega_\nu) \end{pmatrix} = \hbar\omega_v \begin{pmatrix} X(\omega_\nu) \\ Y(\omega_\nu) \end{pmatrix}, \tag{2.46}$$

where the matrices A, B, X and Y are defined as:

$$A = \begin{pmatrix} A_{mi,pk} & A_{mi,pqkl} \\ A_{mnij,pk} & A_{mnij,pqkl} \end{pmatrix}, \tag{2.47}$$

$$B = \begin{pmatrix} B_{mi,pk} & B_{mi,pqkl} \\ B_{mnij,pk} & B_{mnij,pqkl} \end{pmatrix}, \tag{2.48}$$

$$X(\omega_\nu) = \begin{pmatrix} X_{mi}(\omega_\nu) \\ X_{mnij}(\omega_\nu) \end{pmatrix} \tag{2.49}$$

and

$$Y(\omega_\nu) = \begin{pmatrix} Y_{mi}(\omega_\nu) \\ Y_{mnij}(\omega_\nu) \end{pmatrix}. \tag{2.50}$$

The elements of the matrices A, B, X and Y are as defined in Ref. [Yan87].

2.4.3 SRPA with the UCOM interaction

This method is also based on the SRPA as described in Section 2.4.2 in which a Unitary Correlation Operator Method potential (V_{UCOM}) derived from the Argonne V18 potential is used to describe the residual interactions [Rot05, Rot10, Usm11a]. In this case, only the two-body finite range interaction is used as the sole input for describing the residual couplings as well as the ground state. The UCOM provides effective nucleon-nucleon interactions (NNI) based on relativistic NNIs. The approach is formulated starting from a realistic NNI and treats explicitly short range correlations introduced. Hence, a softened phase shift equivalent NNI is derived. Some of the advantages of the SRPA with UCOM is that it is based on the SRPA which accomodates more interactions than the simple RPA and successfully describes long-range correlations (LRC) which are not embedded in UCOM by construction [Pap09]. A limitation of this method is that it is only efficient with closed-shell nuclei.

2.4.4 Quasi-particle RPA (QRPA) with the Gogny force D1S

Also built on the RPA, the quasi-particle random phase approximation (QRPA) allows one to treat the particle-particle ($p-p$), particle-hole ($p-h$) and hole-hole ($h-h$) excitations on the same footing. Unlike the SRPA, it is applicable to both close and open-shell nuclei. In this method, the quasi-boson operator representing nuclear excitations is defined as [Per08]:

$$O_n^+ = \frac{1}{2}\Sigma_{ij}(X_n^{ij} n_i^+ n_j^+ - Y_n^{ij} n_j n_i), \tag{2.51}$$

where n_i^+ and n_i are the quasi-particle (qp) creation and annihilation operators, respectively. X_n and Y_n are the amplitudes of the 2 qp's excitation.

The QRPA ground state, $|0\rangle$, and excited state, $|n\rangle$, satisfy the following equations:

$$O_n^+|0\rangle = |n\rangle \tag{2.52}$$

and

$$O_n|0\rangle = 0 \tag{2.53}$$

The QRPA equation built on the Gogny force D1S is given as:

$$\begin{pmatrix} A & B \\ B & A \end{pmatrix} \begin{pmatrix} X_n \\ Y_n \end{pmatrix} = \omega_n \begin{pmatrix} X_n \\ -Y_n \end{pmatrix}, \tag{2.54}$$

where ω_n is the energy of the QRPA excited state $|n\rangle$, while matrices A and B are real and symmetric. A and B are also built using the same Gogny D1S force in all $p-p$, $p-h$ and $h-h$ channels.

The solutions of Eq. (2.54) are provided in details in Ref. [Pap07].

2.4.5 Continuum RPA with the SLy4 interaction

The continuum random phase approximation (CRPA) formalism is built on the Green's functions [Tsa78] in coordinate space while the SLy4 interaction was obtained in Ref. [Cha98]. The polarisation propagator is derived by iteration over all possible $p-h$ and $h-p$ of the ground state excitation to all orders within the $1p-1h$ configuration. The transition densities are derived by solving the

CRPA version of the the Lippman-Schwinger equation [Jac02]:

$$\rho^{RPA} = \frac{1}{1 - RV}\rho^0, \tag{2.55}$$

where R and ρ^0 denote the unperturbed response function and transition densities, respectively and V is the residual interaction.

The algorithm of application of the CRPA with the SLy4 interaction can be summarised in the following steps:

- Solve the Skyrme-Hartree-Fock equation in order to determine the single-particle potentials and densities.
- Evaluate the unperturbed $p - h$ propagator.
- Evaluate the residual $p - h$ interaction, V_{res}, in matrix form with rows and columns corresponding to residual points on a mesh.

The RPA propagator is then evaluated from the following equation [Ber91,Kim15]:

$$G^{RPA} = (1 + G^0)^{-1} G^0. \tag{2.56}$$

The strength distribution is determined by polarisation diagram via Green's functions and the transition density matrix elements are obtained from the density operator [Kim15]:

$$d\rho^{\nu} = \langle \nu \mid \delta(r - r_i) \mid 0 \rangle. \tag{2.57}$$

2.4.6 Relativistic QRPA (RQRPA)

The relativistic quasi-particle random phase approximation (RQRPA) equation, using the finite range Gogny interaction in the pairing channel, can be derived

from the time-dependent relativistic Hartree-Bogoliubov model, for small amplitude oscillations [Paa03]. The generalised density matrix, $\mathcal{R}$ and the meson fields, ϕ_m are taken as independent variables. The time-dependent meson field is given as:

$$\phi_m = \phi_m^{(0)} + \delta\phi_m, \tag{2.58}$$

where $\phi_m^{(0)}$ is the meson field corresponding to the stationary ground state and $\delta\phi_m$ represents the small variations in the mean field near the stationary ground state.

The Klein-Gordon equation can be written as [Paa03]:

$$\left[-\Delta + U''(\phi_m^{(0)})\right] \delta\phi_m(\overrightarrow{r}) = \pm g_m \delta\rho_m(\overrightarrow{r}), \tag{2.59}$$

where $\delta\rho_m(\overrightarrow{r})$ represents the various currents and densities.

The propagator, $G_m(\overrightarrow{r}, \overrightarrow{r'})$, is related to $\delta\phi_m$ and $\delta\rho_m$ as:

$$\delta\phi_m(\overrightarrow{r}) = \pm g_m \int d^3r' G_m(\overrightarrow{r}\,\overrightarrow{r'})\rho_m(\overrightarrow{r'}). \tag{2.60}$$

The generalised Hamiltonian, $\mathcal{H}$, is expressed in terms of a functional of the generalised density, $\mathcal{R}$, which can be written as:

$$\mathcal{R} = \mathcal{R}_0 + \delta\mathcal{R}(t), \tag{2.61}$$

with $\mathcal{R}_0$ being the stationary ground state generalised density and $\delta\ \mathcal{R}(t)$ is the time-dependent variation.

For a linear order,

$$\mathcal{R}_0\delta\mathcal{R} + \delta\mathcal{R}\mathcal{R}_0 = \delta\mathcal{R}. \tag{2.62}$$

$\mathcal{R}_0$ and $\mathcal{H}(\mathcal{R}_0)$, in the quasi-particle basis, can be written as:

$$\mathcal{R}_0 = \begin{pmatrix} 0 & 0 \\ 0 & 1 \end{pmatrix} \tag{2.63}$$

and

$$\mathcal{H}_0 = \begin{pmatrix} E_n & 0 \\ 0 & -E_n \end{pmatrix}, \tag{2.64}$$

such that

$$\delta\mathcal{R} = \begin{pmatrix} 0 & \delta\mathcal{R} \\ -\delta\mathcal{R}^* & 0 \end{pmatrix}. \tag{2.65}$$

Hence, the linearised equation of motion becomes:

$$i\delta_t\mathcal{R} = [\mathcal{H}_0, \delta\mathcal{R}] + \left[\frac{\delta\mathcal{H}}{\mathcal{R}}\delta\mathcal{H}, \mathcal{R}_0\right]. \tag{2.66}$$

Considering an oscillatory solution, the RQRPA equation is obtained as:

$$\begin{pmatrix} A & B \\ -B^* & -A^* \end{pmatrix} \begin{pmatrix} X^\nu \\ Y^\nu \end{pmatrix} = \omega_\nu \begin{pmatrix} X^\nu \\ Y^\nu \end{pmatrix}. \tag{2.67}$$

The RQRPA matrix elements, A and B are expressed in terms of second derivatives of the energy functional with respect to the generalised densities $\mathcal{R}$. For

$k < k'$ and $l < l'$, they can be written as:

$$A_{kk'll'} = (E_k + E_{k'})\delta_{kl}\delta_{k'l'} + \frac{\delta^2 E}{\delta\mathcal{R}^*_{kk'}\delta\mathcal{R}_{ll'}} \tag{2.68}$$

and

$$B_{kk'll'} = \frac{\delta^2 E}{\delta\mathcal{R}^*_{kk'}\delta\mathcal{R}^*_{ll'}}. \tag{2.69}$$

The solutions of the equation embedded in Eq. (2.67) are obtained in the canonical basis where single particle density matrix, ρ is diagonal. The RQRPA transition density is given as [Paa03]:

$$\begin{aligned}\delta\rho^{\nu}_{j}(r) = \sum_{\kappa\kappa'} \Big\{ \langle \kappa \mid\mid Y_J \mid\mid \kappa' \rangle f_\kappa(r) f_{\kappa'}(r) + \langle \widehat{\kappa} \mid\mid Y_J \mid\mid \widehat{\kappa'} \rangle g_\kappa(r) g_{\kappa'}(r) \Big\} \\ \times (X^{\nu,J0}_{\kappa\kappa'} + (-1)^J Y^{\nu,J0}_{\kappa\kappa'})(u_\kappa v_{\kappa'} + (-1)^J v_\kappa u_{\kappa'}),\end{aligned} \tag{2.70}$$

where κ and $\widehat{\kappa}$ are the quantum numbers of the large and small components of the Dirac spinors, respectively and $f_\kappa(r)$ and $g_\kappa(r)$ are the corresponding radial components.

2.4.7 Relativistic Quasi-particle Time Blocking Approximation (RQTBA)

The relativistic quasi-particle time blocking approximation (RQTBA), developed in Refs. [Lit08,Lit09], is based on the covariant density functional theory (CDFT) with NL3 parametrisation [Lal97]. The approach is a self-consistent extension of the RQRPA (Section 2.4.6) in which quasi-particle vibration coupling is taken into account. In its formalism, the phonon space is truncated by the phonon

angular momentum and frequencies in a way that allows for decoupling of spurious translational modes by having a large enough 2-quasi-particle space. Within this framework, the response of the superfluid nucleus in a weak external field can be obtained using the Bethe-Salpeter equation (BSE) [Tse07] by extension to the relativistic case [Lit08].

Considering the time variable along with single particle quantum numbers in the double quasi-particle space, the BSE response function can be written as [Lit08]:

$$R(14,23) = G(1,3)G(4,2) - i\sum_{5678} G(1,5)G(6,2)V(58,67)R(74,83), \qquad (2.71)$$

where the summation over the number indices indicates integration over the respective time variables.The function G is the exact single-quasi-particle Green's function and V is the amplitude of the effective interaction irreducible in the $p-h$ channel.

Combining the non-relativistic [Tse07] and the relativistic [Lit07] quasi-particle time blocking approximation, the response function for the $p-h$ channel can be written as [Lit08]:

$$\begin{aligned} R^{\eta\eta'}_{k_1k_4,k_2k_3}(\omega) = \tilde{R}^{(0)\eta}_{k_1k_2}(\omega)\delta_{k_1k_3}\delta_{k_2k_4}\delta_{\eta\eta'} + \tilde{R}^{(0)\eta}_{k_1k_2}(\omega) \\ \times \sum_{k_5k_6k_7k_8}\sum_{\eta''} \bar{W}^{\eta\eta''}_{k_5k_8,k_6k_7}(\omega) R^{\eta''\eta'}_{k_7k_4,k_8k_3}(\omega), \end{aligned} \qquad (2.72)$$

where

$$R^{\eta\eta'}_{k_1k_4,k_2k_3}(\omega) = R^{\eta,-\eta',-\eta,\eta'}_{k_1k_4,k_2k_3}(\omega), \qquad (2.73)$$

$$R^{\eta_1,\eta_4,\eta_2\eta_3}_{k_1k_4,k_2k_3}(\omega) = -i\int_{-\infty}^{\infty} dt_1dt_2dt_3dt_4\delta(t_1-t_2)\delta(t_3-t_4)\times\delta(t_4)e^{i\omega t_{13}}R(14,23) \qquad (2.74)$$

and

$$\bar{W}^{\eta\eta'}_{k_1k_4,k_2k_3}(\omega) = \tilde{V}^{\eta\eta'}_{k_1k_4,k_2k_3} + (\Phi^{\eta}_{k_1k_4,k_2k_3}(\omega) - \Phi^{\eta}_{k_1k_4,k_2k_3}(0))\delta_{\eta\eta'}. \tag{2.75}$$

In the latter equation, Φ is the dynamical part of the interaction amplitude which is responsible for particle-phonon coupling with the backward component (η = -1) and the forward component ($\eta = 1$). More details about the formalism of this model can be found in Ref. [Ego16].

2.5 Extraction of the characteristic energy scales

High energy-resolution inelastic proton scattering experiments at zero-degrees offer a unique avenue for fine structure to be observed in the IVGDR excitation energy region. This is important as there exists a direct connection between the observed fine structure and the dominant mechanisms that characterise the decay of the IVGDR. In order to extract the scales that characterise the fine structure, wavelet analysis which is described in the following subsection can be applied to the experimental spectra.

2.5.1 Wavelet transform

In general, signals and spectra are analysed in order to extract fundamental physical quantities such as the amplitude, the period, the frequency, etc. The wavelet analysis is a well established technique used for analysing signals and spectra. It involves using a wavelet that is localised in both time and frequency domains. The wavelet transform can be used to analyse among others: periodic, abrupt, continuous and discrete signals, and can provide localised information about the analysed signal. It finds application in diverse areas including data

compression, image processing [Dau92], accelerator physics [Fed99], fingerprint recording and identification [Sif09], etc.

By definition, a wavelet is a small wave that decays fast. Wavelets are generated from a basic vector $\Psi(t)$ called the "mother wavelet" through scaling and translation, and can generally be represented as:

$$\Psi_{s,\tau}(t) = \frac{1}{\sqrt{s}}\Psi\left(\frac{t-\tau}{s}\right), \tag{2.76}$$

where s is the scale factor used to shrink or expand the mother wavelet function and τ is the translation factor. Some of the commonly used wavelet functions are shown in Fig. 2.8.

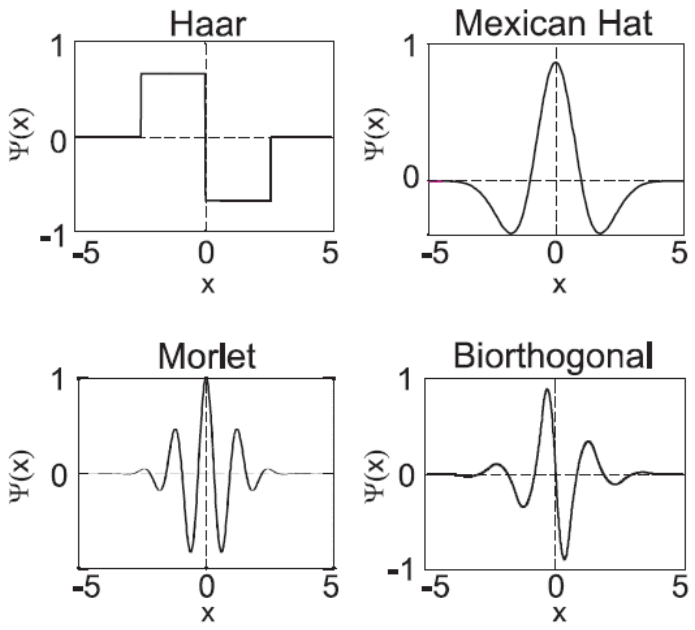

Figure 2.8: Examples of wavelet functions commonly used as mother wavelets. *Top-left:* the Haar wavelet; *Top-right:* the Mexican Hat wavelet; *Bottom-left:* the Morlet wavelet; and, *Bottom-right:* the Biorthogonal 6.8.

Wavelets have 3 very important properties: the admissibility, the regularity and the condition of vanishing moments.

- Admissibility: requires that the Fourier transform, $\Psi(\omega)$ of the mother wavelet be square-integrable as:

$$\int \frac{|\Psi(\omega)|^2}{|\omega|} d\omega < \infty, \tag{2.77}$$

This implies that $\Psi(\omega)$ vanishes at zero-frequency:

$$|\Psi(\omega)|^2_{\omega=0} = 0. \tag{2.78}$$

Therefore, the mother wavelet, $\Psi(t)$ must be oscillatory.

- Regularity: is the property of the wavelet transform that makes it decrease quickly with decreasing scale, s. This is an important property as the time-bandwidth product of a wavelet transform is the square of the input signal. Therefore, the regularity conditions require that the wavelet function be smooth and concentrated in both time and frequency domains.

- Vanishing moments: Considering a wavelet transform:

$$\gamma(s,\tau) = \int f(t)\Psi^*_{s,\tau} dt, \tag{2.79}$$

where $\Psi^*_{s,\tau}$ is the complex conjugate of $\Psi_{s,\tau}$, the expansion of $\gamma(s,\tau)$ into Taylor series at $t = 0$ up to order n, assuming $\tau = 0$, gives [She96]:

$$\gamma(s,0) = \frac{1}{\sqrt{s}} \left[\sum_{p=0}^{n} f^{(n)}(0) \int \frac{t^p}{p!} \Psi\left(\frac{t}{s}\right) dt + O(n+1) \right], \tag{2.80}$$

with $f^{(p)}$ being the p^{th} order derivative of f while $O(n+1)$ represents the higher terms of the expansion.

The vanishing moment of the wavelet is defined as [Cal98]:

$$M_P = \int t^p \Psi(t) dt. \tag{2.81}$$

Hence, further expansion of Eq. (2.80) gives:

$$\gamma(s,0) = \left[f(0) M_0 s + \frac{f^{(1)}(0)}{1!} M_1 s^2 + \frac{f^{(2)}(0)}{2!} M_2 s^3 + ... + \frac{f^{(n)}(0)}{n!} M_n s^{n+1} \right]. \tag{2.82}$$

The admissibility condition requires that $M_0 = 0$. If for other terms M_n is also 0 then, $\gamma(s,0)$ will decay as fast as s^{n+1} for a smooth signal.

2.5.1.1 Continuous Wavelet Transform (CWT)

The CWT is an excellent tool for analysing non-stationary signals with no need for choosing a time window nor fixing the time-frequency resolution of the signal. It is typically in the form of Eq. (2.79). For the purpose of energy scales extraction, it is rather represented as [She08]:

$$\gamma(\delta E, E_x) = \frac{1}{\sqrt{\delta E}} \int \sigma(E) \Psi^* \left(\frac{E_x - E}{\delta E} \right) dE, \tag{2.83}$$

where the subscript x denotes a position over the excitation energy spectrum and δE is the energy scale.

The analysis is made easier when scales and positions are chosen on powers of 2 [Mal99] in which case, adjacent scales can be related as:

$$\delta E_i = \delta E_0 2^{\frac{i}{q}}, \tag{2.84}$$

where δE_0 is the smallest scale considered to be equal to the energy bin size of the spectrum and q divides each factor of 2 into subintervals.

The power spectrum of the CWT is defined as [She08]:

$$P(\delta E) = \frac{1}{N} \sum_{i=i_1}^{i_2} |C_i(\delta E) C_i^*(\delta E)|, \tag{2.85}$$

where $C_i(\delta E)$ is the CWT coefficient and $C_i^*(\delta E)$ its complex conjugate, and N is the number of energy bins in the range considered.

2.5.1.2 Discrete Wavelet Transform (DWT)

This method presents a more efficient algorithm for practical application to signal analysis and is preferred over the CWT for compression and filtering of signal data. Unlike the CWT, the DWT is scaled and translated in discrete steps. This can be realised by modifying Eq. (2.76) to :

$$\Psi_{j,\tau}(t) = \frac{1}{\sqrt{s_0^j}} \Psi \left(\frac{t - k\tau_0 s_0^j}{s_0^j} \right), \tag{2.86}$$

where j and k are integers and $s_0 > 1$ is a fixed dilation step.

The time-scale space is sampled at discrete intervals. In order to make the frequency sampling dyadic, s_0 is chosen to be 2 such that one obtains:

$$\delta E_k = 2^j \Delta \tag{2.87}$$

and

$$E_{xk} = k\delta E_k, \qquad k = 1, 2, 3..., \tag{2.88}$$

where k indicates the number of sinusoidal oscillations within a given Gaussian window.

The DWT can be applied as a low-pass filter (for large scale δE) and high-pass filter (for low scale δE) on a spectrum by decomposing it into approximation (A_j) and details (D_j) components. This process is schematically illustrated in Fig. 2.9. By means of a reconstruction process, the original spectrum can be recovered by summing up the approximation and detail components at each level, starting from the smallest scale ($j = 1$).

2.6 Level density extraction

The nuclear level density is a characteristic of the atomic nucleus. It is defined as the amount of levels in the nucleus per unit energy within a given range of excitation energy. A microscopic description depicts a level density as the different ways in which individual nucleons can be arranged in different single-particle orbitals, for a given excitation energy range. Level density is an important parameter of the nucleus as it allows for the estimation of the nuclear reaction cross-sections. It also finds applications in nuclear photosynthesis where it can be used to determine the thermonuclear rates. It is also a key ingredient in nuclear reactors design. The evaluation of level densities in atomic nuclei not only allows for microscopic and phenomenological nuclear structure models to be tested, it also constitutes an important factor of pre-equilibrium and statistical models of nuclear reactions [Hil98].

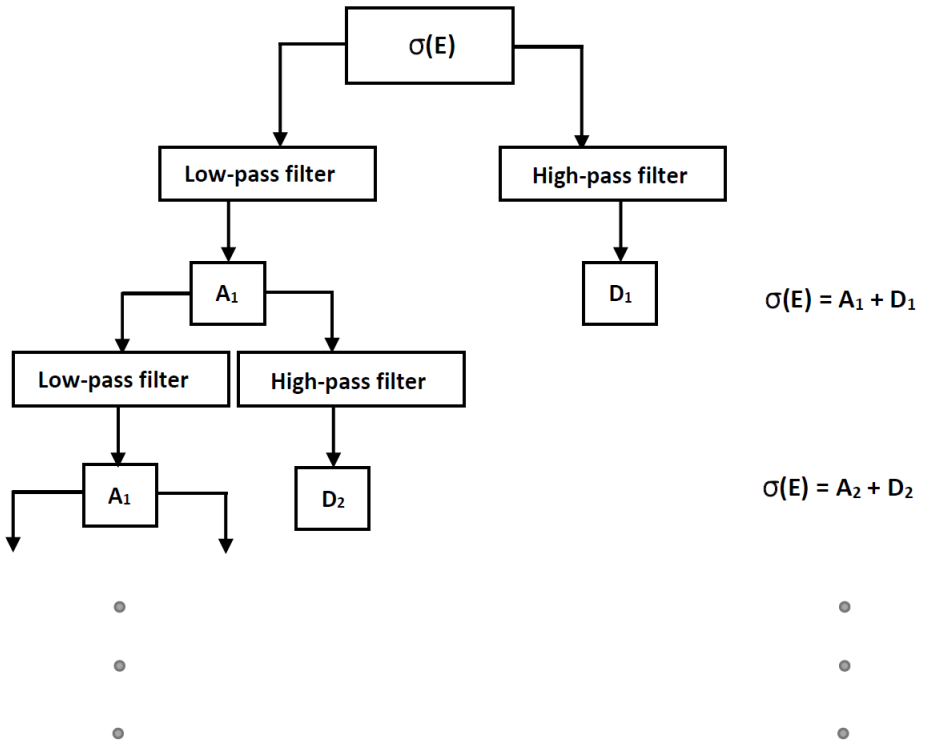

Figure 2.9: Illustration of scheme of decomposition of a signal into approximation (A_j) and detail (D_j) components.

Nuclear levels are well separated at low excitation energies. However, these levels are more difficulty resolved as the excitation energy increases. In fact, the increase in nuclear level with increasing excitation energy, E_{x}, is best described with an exponential function in E_{x} [Hil00]. The need for estimating level densities at higher excitation energies was borne out of its geometric increase with E_{x}. In addition to this, there are no readily available data on the level density of every nucleus over a wide range of E_{x} and angular momentum [Mis94].

Some of the factors that influence the accurate estimation of the level density include the following:

- Pairing effects: according to the pairing correlations, fermions are coupled in pairs. This implies that for a given excitation energy within a small

change of mass range, the level density of even-even nuclei will be lower than that of even-odd nuclei which will be, in turn, lower than that of odd-odd nuclei. This is due to the fact that part of the energy is used for breaking the pairings between nucleons before they get excited.

- Vibrational effects of nuclei: the vibration of the nucleus around its equilibrium shape leads to vibrational levels and this occurs in all nuclei. This is a form of coherent excitation of the nucleus which obeys the Bose-Einstein statistics and is well described with a partition function without restrictions on occupational number [Hil00]. The level density in such case is enhanced when the vibrational levels are taken into account. The effects of this, however, fades with increasing excitation energy.

- Rotational effects of nuclei: most nuclei, except nuclei with nucleon numbers near closed shells exhibit more or less some deformation in their ground state. The effect of rotational energy bands exhibited by such nuclei impacts on the evaluation of the level density.

Some of the existing models used for evaluating nuclear level density are described below.

2.6.1 Independent Particle Model (IPM)

The IPM is built on the assumption that protons and neutrons can only occupy states with definite excitation energies, spin projections and parities, forming what is known as single particle level schemes [Hil97, Hil00]. The model assumes that nucleons can only occupy the Fermi level and levels below it in the ground state of the nucleus such that states above the Fermi level are totally empty. For every nucleon of individual excitation energy $\epsilon_i(j)$, in the single-particle state i, with occupation number $n_i(j)$, the total number of nucleons is given as:

$$n = \sum_i n_i(j), \tag{2.89}$$

where j indicates the excited state.

The excitation energy can be written as the sum of single-particle state energies as:

$$E_j(n) = \sum_i n_i(j)\epsilon_i(n). \tag{2.90}$$

In this model, a good description of the level density can be derived at low E_x. However, a view of the atomic nucleon independently, as assumed here, does not well represent the excitation of the nucleus as a whole. Rather, a holistic view with all nucleons involved is more appropriate.

2.6.2 Fermi Gas Model (FGM)

The FGM is an extension of the IPM with less complications. This model assumes that single particle states are equally distributed in the nucleus. The over simplicity of the latter assumption makes the model one that is far from being realistic.

The density of single particle states with A fermions, which are assumed to be equally distributed, is given as [Lyn68]:

$$g = \frac{3A}{2\epsilon_f}, \tag{2.91}$$

where ϵ_f is the Fermi energy level given by:

$$\epsilon_f = \left(\frac{9\pi}{8}\right)^{\frac{2}{3}} \frac{\hbar^2}{2mr_0^2}, \tag{2.92}$$

in which m and r_0 are the rest mass and radius of the nucleon, respectively.

The density of state can then be written as [Hil00, Boh98]:

$$\rho(A, E) = \frac{exp\left(2\sqrt{aE}\right)}{4\sqrt{3}E}, \tag{2.93}$$

where E is the energy and a is the level density parameter defined as:

$$a = \frac{\pi^2}{6} g. \tag{2.94}$$

2.6.3 Back-shifted Fermi Gas Model (BSFGM)

This model is also based on the FGM. It was first suggested [Dil73] by Newton and Cameron [New56]. In this model, the pairing effect is accounted for by some energy shift. The excitation energy is measured from a fictive ground state. This ground state is assumed to correspond to the ground state of odd nuclei which will be shifted forward by a factor equal to the pairing energy of the even nuclei. The fictive ground state is then determined by experimental mass difference [Nem62, Kum66, Gil65]. The level density parameter, a, then becomes the only parameter to be adjusted in the model. It is determined in such a way to match the experimental conditions.

2.6.4 Fluctuation analysis

The method of fluctuation analysis is an efficient tool for estimating the density of levels of excited nuclei especially in excitation region where they strongly overlap. Such a region corresponds to the high excitation energy region where several

inelastic decay channels of the compound nucleus can compete. The interference between levels is random in nature [Eri63], therefore, a statistical analysis remains a reliable means of evaluating the level density in such circumstances. The technique relies on the use of an autocorrelation function which allows for obtaining a gauge of the fluctuation in the cross-section with respect to a stationary mean value.

The fluctuation analysis method can be applied in an excitation energy region where the experimental energy resolution (ΔE) is greater than the average distance ($\langle D \rangle$) between levels. If $\langle \Gamma \rangle$ denotes the mean level width, two cases may arise:

(i) $\langle \Gamma \rangle \leq \langle D \rangle$ and fluctuations are due to the density and incoherent overlap of levels and

(ii) $\langle \Gamma \rangle > \langle D \rangle$, in this case the fluctuations are classified as Ericson fluctuations which results from the coherent overlap of levels [Eri60].

In the latter case, the fluctuation analysis can in principle also be applied so long sufficient statistics is available.

In order to apply this technique, the following two assumptions are made:

(i) For highly excited nuclei with a strong fluctuation configuration mixing of levels of same spin and parity, the probability of a given nuclear level spacing is provided by the Wigner distribution, $P_{\mathrm{W}}(s)$ as [Wig65]:

$$P_{\mathrm{W}}(s) = \frac{\pi s}{2} exp\left(-\frac{\pi s^2}{4}\right), \tag{2.95}$$

where s is defined in terms of the resonances spacing, D, as:

$$s = \frac{D}{\langle D \rangle}. \tag{2.96}$$

(ii) The ground state decay widths or the transition strengths are governed by the Porter-Thomas distribution, $P_{\rm PT}$, given as:

$$P_{\rm PT}(s) = \frac{1}{\sqrt{2\pi s}} exp\left(-\frac{s}{2}\right), \tag{2.97}$$

where s is related to the width of the resonance, Γ, as:

$$s = \frac{\Gamma}{\langle\Gamma\rangle}. \tag{2.98}$$

Eq. (2.97) favours weak transitions.

2.6.4.1 Application of fluctuation analysis

The procedure of applying the fluctuation analysis is outlined as follows:

- the background-subtracted experimental spectrum, $S(E_{\rm x})$, is first smoothed with a Gaussian function of width $\sigma_{>}$, which must be greater than ΔE by at least a factor of 2. The obtained spectrum is then labelled $g_{>}(E_{\rm x})$.
- $S(E_x)$ is also folded with a Gaussian function of width (σ) smaller than ΔE. This is done with a view to eliminating the effects of fluctuations due to counting statistics. The obtained spectrum is labelled $g(E_{\rm x})$.
- thereafter, we define the stationary spectrum, $\langle d(E_x)\rangle$, as:

$$d(E_{\rm x}) = \frac{g_{>}(E_{\rm x})}{g(E_{\rm x})}, \tag{2.99}$$

which has a mean value of $\langle dE_{\rm x}\rangle = 1$.

If ϵ is the energy shift between spectra, $C(\epsilon = 0)$ denotes the autocorrelation function and $C(\epsilon = 0) - 1$ is the variance of $d(E_{\rm x})$ given as:

$$C(\epsilon = 0) - 1 = \frac{\langle d^2 E_x \rangle - \langle dE_{\rm x} \rangle^2}{\langle dE_{\rm x} \rangle^2}. \tag{2.100}$$

An approximation of the experimental autocorrelation function is given as [Jon76]:

$$\begin{aligned} C(\epsilon) = 1 + \frac{\alpha \langle D \rangle}{2\Delta E \sqrt{\pi}} \Bigg[exp\left(\frac{-\epsilon^2}{4\Delta E^2}\right) + \frac{1}{y} exp\left(\frac{-\epsilon^2}{4\Delta E^2 y^2}\right) \\ - \frac{2\sqrt{2}}{\sqrt{y^2+1}} exp\left(\frac{-\epsilon^2}{2\Delta E^2 (1+y^2)}\right) \Bigg], \end{aligned} \tag{2.101}$$

where $y = \frac{\sigma_>}{\sigma}$, and α is the sum of the normalised variances of the assumed spacing and transition width distributions given as:

$$\alpha = \alpha_{\rm D} + \alpha_{\rm PT} = 0.273 + 2.0. \tag{2.102}$$

Equation (2.102) holds if only states of same J^π values are present in the spectrum. Otherwise, the variance of the distribution of each J^π state in the overlapping region must be defined separately.

The nuclear level density, ρ, is then defined as the inverse of the mean level spacing as:

$$\rho(\epsilon) = \frac{1}{\langle D \rangle}. \tag{2.103}$$

Chapter 3

Experimental procedure

The fine structure of the isovector giant dipole resonance (IVGDR) has been investigated in the present study. The Separated-Sector Cyclotron (SSC) of the iThemba Laboratory for Accelerator Based Science (iThemba LABS) was used to deliver high quality beams of 200 MeV protons to the K600 magnetic spectrometer scattering chamber. In this chapter a brief description of the facilities used will be given starting with a general overview of the SSC in Section 3.1 and a comprehensive description of the K600 magnetic spectrometer in Section 3.2. A brief description and relevant techniques involved in zero-degrees inelastic proton scattering measurements will be the focus of Section 3.3. While Section 3.4 will be dedicated to providing useful information about the selected isotopes of calcium under investigation, the general experimental procedure and data extraction will be discussed in Sections 3.5 and 3.6, respectively.

3.1 Separated-Sector Cyclotron (SSC)

The separated-sector cyclotron (SSC) constitutes the main accelerator of the iThemba Laboratory for Accelerator Based Sciences (iThemba LABS) [Jon85]. It is used to deliver 66 - 200 MeV proton beams to the radiotherapy vaults [Con02, Mla06], for the sake of cancer treatment, and also to the isotope production vault [Ste13]. These constitute the activities of the cyclotron accelerator

during the week while it is used over the weekends (starting from Friday afternoon to Monday morning) for nuclear physics studies. In this case, proton beams or sometimes other charged particle beams (spanning over a wide range of atomic mass) are accelerated and transported to either the AFRican Omnipurpose Detector for Innovative Techniques and Experiments (AFRODITE) vault [Hla05], the K600 magnetic spectrometer vault [Nev11], the D-line quasi-monoenergetic neutron vault or the huge A-line scattering chamber. The main components of the SSC are four sector magnets denoted by SM1, SM2, SM3 and SM4, each weighing approximately 350 tons and subtending a central angle of 34°. Other key components are the vacuum chambers and the resonators. More details about the physical properties of the facility can be found in Ref. [Vil06]. A sectional view of the SSC showing the 4 sector magnets and other key components is illustrated in Fig. 3.1.

Charged particles are first pre-accelerated to 8 MeV by either of the two solid-pole injector cyclotrons (SPC's) denoted SPC1 and SPC2, before injection into the SSC where they are accelerated to the maximum desired energy up to 200 MeV. SPC1 has an internal Penny Ionisation Gauge (PIG) [Abo02] ion source which produces intense proton beams while SPC2 pre-accelerates charged particles produced from one of the 2 external ion sources connected to it namely the Electron Cyclotron Resonance (ECR) [Con10] ion source and the polarised ion source. The high energy ion beam produced through the SSC is carefully transported through designated beam lines and delivered to the various vaults mentioned above. The layout of the accelerator infrastructure of iThemba LABS showing the three accelerators, the vaults and the various beam lines is illustrated in Fig. 3.2.

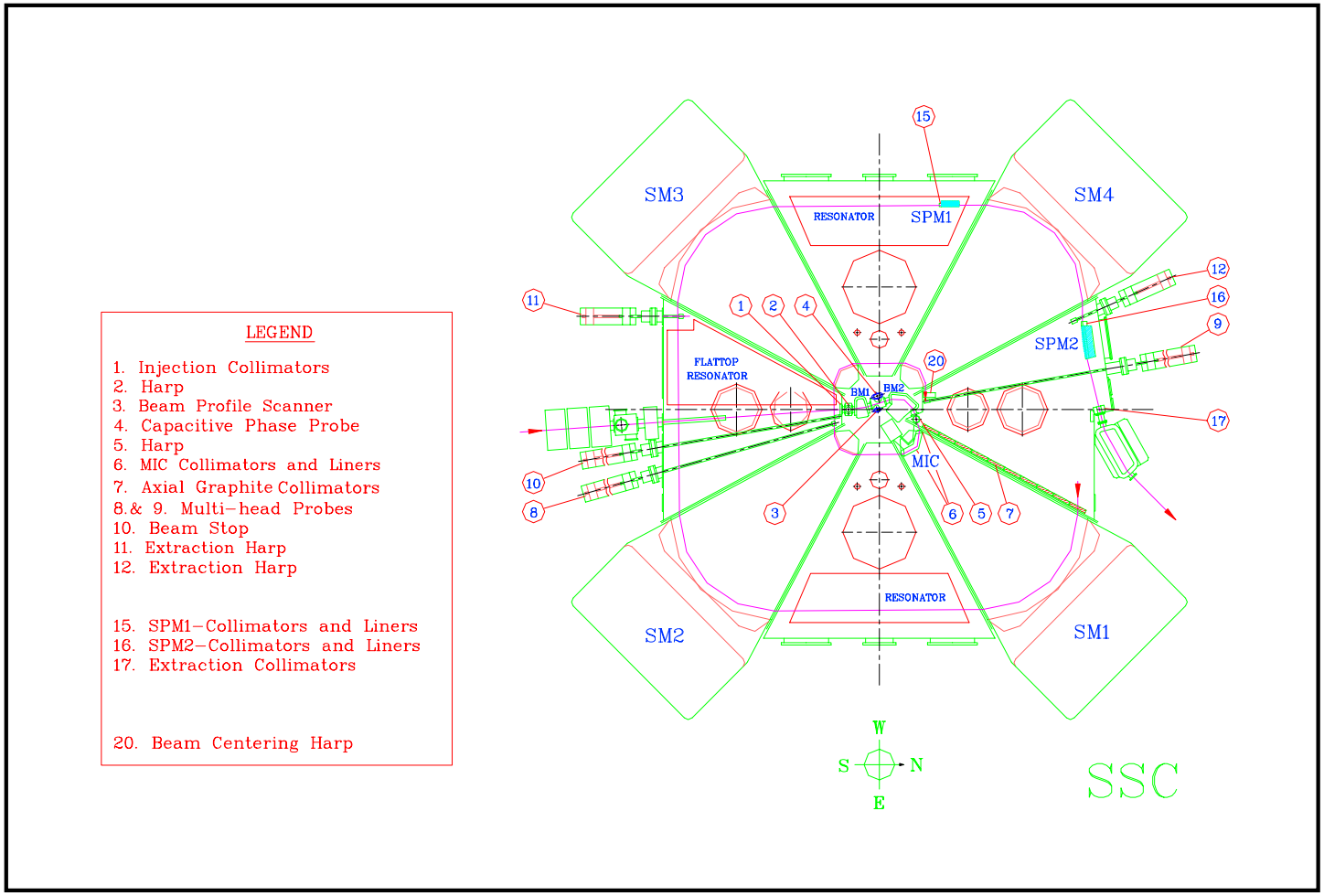

Figure 3.1: A sectional view of the SSC showing its four sector magnets together with other components.

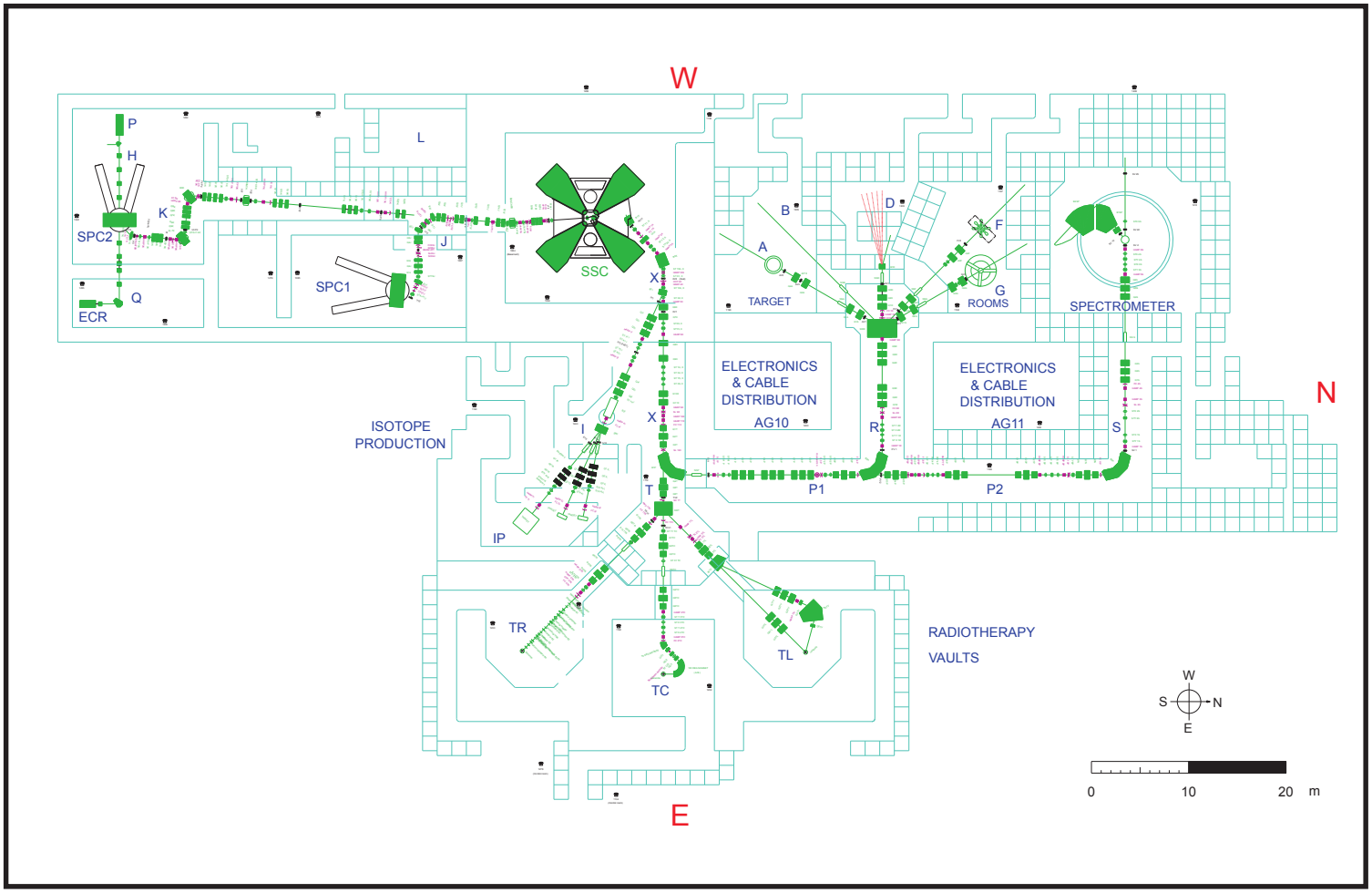

Figure 3.2: Layout of the accelerator infrastructure of iThemba LABS.

3.2 K600 magnetic spectrometer

The K600 magnetic spectrometer of iThemba LABS is one of only a few currently operational hadron spectrometers where high energy-resolution (Δ E $\leq$ 50 keV) can be achieved at medium energies (50 - 200 MeV). First commissioned in October 1991 [Nat91], it is a Quadrupole-Dipole-Dipole (QDD) type spectrometer and a copy of the K600 magnetic spectrometer of the Indiana University Cyclotron Facility [Fri89] which ceased to be operational in 1999. The quadrupole (Q) is located at the entrance of the spectrometer followed by the first dipole (D1) and then the second dipole (D2). Inside each dipole is a pole face current winding. The H-coil is located inside D1 and the K-coil is located inside D2. They are used to achieve final focussing of the charged particles before reaching the focal plane [Nev14]. Other key components of the spectrometer include the scattering chamber and the collimator carousel. Each of these components will be discussed in the following subsections. A schematic diagram of the K600 magnetic spectrometer of iThemba LABS is illustrated in Fig. 3.3. An overview of the technical specifications of the K600 magnetic spectrometer is summarised in Table 3.1.

3.2.1 Scattering chamber

The cylindrical scattering chamber of the K600 has an outer diameter of 524 mm. It is made of aluminium and has two sliding seals made of stainless steel. The chamber sits on a base connected to the spectrometer. A turntable inside the scattering chamber can be used to mount a detector or a beamstop. The said beamstop is primarily used during experiments at spectrometer angles $\theta_{K600} \gg 0^o$ and $\theta_{K600} \ll 21^\circ$. It is also used during 0° beam tuning to prevent the beam from entering the K600 while optimising beam spot, size and shape. At the centre of the chamber, a target ladder mechanism is mounted which can accommodate a maximum of six (6) targets at a time. The selected target is at the beam height which is 1.5 m above the ground. A top view of the scattering chamber of the K600 depicting its main components is shown in the picture in Fig. 3.4.

Table 3.1: Technical specifications of the K600 magnetic spectrometer for the high-dispersion focal plane.

Property	value
Nominal bend radius	2.1 m
Nominal bend angle	115°
Dipole field ratio (R=D1/D2)	1.49
Maximum dipole field	1.64 Tesla
Maximum magnetic rigidity	3.60 Tm
Momentum dispersion (x| $\frac{\Delta P}{P}$)	-10.9 cm /%
Energy dispersion for 200 MeV proton setting	31 keV/mm at 200 MeV
Momentum range (P_{max}/P_{min})	1.048
Resolving power, $\frac{P}{\delta P}$ (for an object width of 0.6mm)	28000
Horizontal magnification at P_{max}	-0.74
Vertical magnification at P_{max}	-7.05
focal plane tilt angle (with respect to central ray)	39.75°
Distance: target $\leftrightarrow$ back of collimator	735.5 mm
Collimator maximum diameter	55 mm
Maximum solid angle ($\Delta\theta\Delta\phi$)	4.39 msr
Maximum horizontal acceptance ($\Delta\theta$)	$\pm$ 37.4 mrad or $\pm$ 2.14°
Maximum vertical acceptance ($\Delta\phi$)	$\pm$ 37.4 mrad or $\pm$ 2.14°

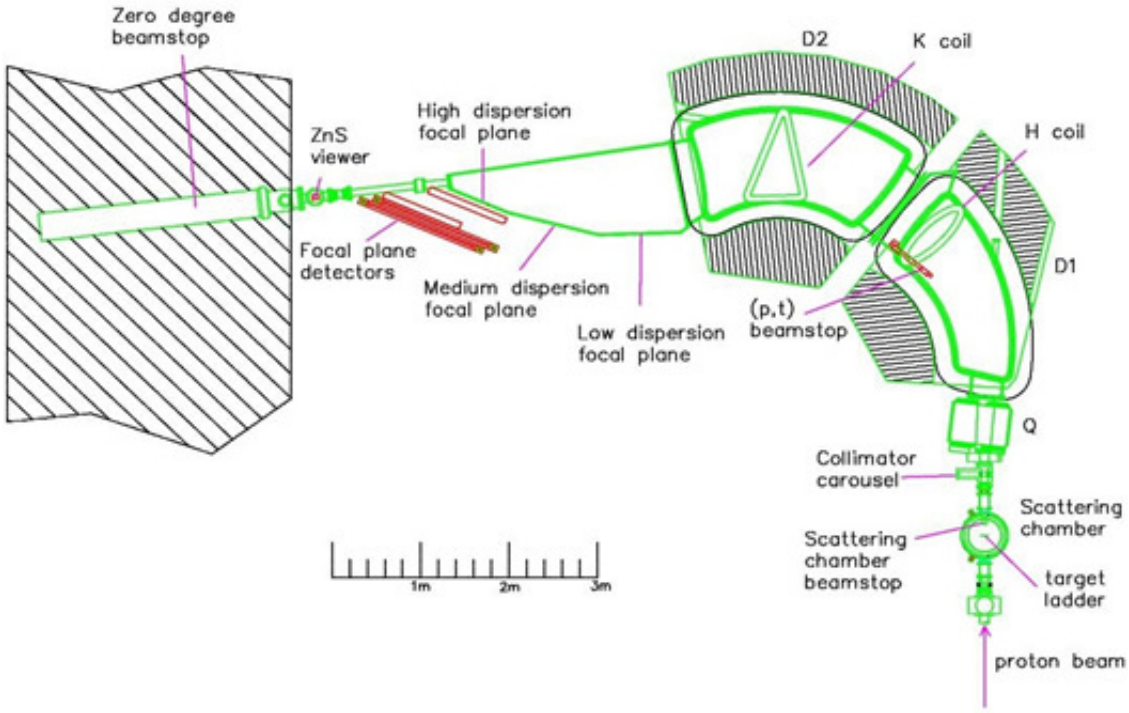

Figure 3.3: Layout of the K600 magnetic spectrometer of iThemba LABS in the Zero-degree mode.

3.2.2 Collimator carousel

The collimator carousel is located 735.5 mm away from the target position and right before the hexapole magnet. It houses 6 collimators which are used to determine the solid angle to be subtended by the K600. The carousel is remote controlled from the dataroom such that the desired collimator can be selected at convenience. The available collimators have circular openings of various inner diameters ranging between 22 mm and 63 mm. They are all made of brass. In addition, there are other types of collimators such as the blank collimator, which constitutes an integral part of the Zero-Degree interlock and used to protect the K600 focal plane, the multi-slot collimators and the pepper-pot collimator. The latter is used for angular calibration of the spectrometer. Some of the collimators commonly used are illustrated in Fig. 3.5. The maximum solid angle of the spectrometer, its maximum vertical acceptance and maximum horizontal acceptance are listed in Table 3.1.

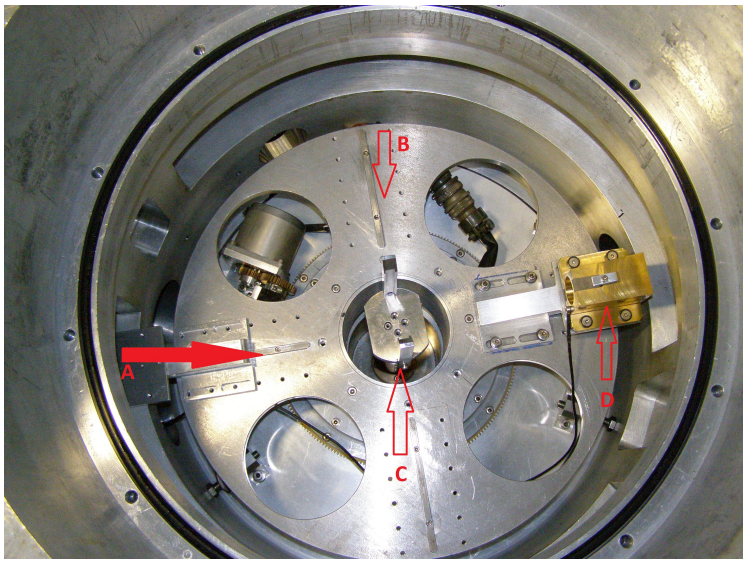

Figure 3.4: A top view of the scattering chamber of the K600 magnetic spectrometer used for the measurements. The solid arrow (A) represents the beam inlet into the scattering chamber, B represents the turntable, C is the target ladder and D is the internal beamstop.

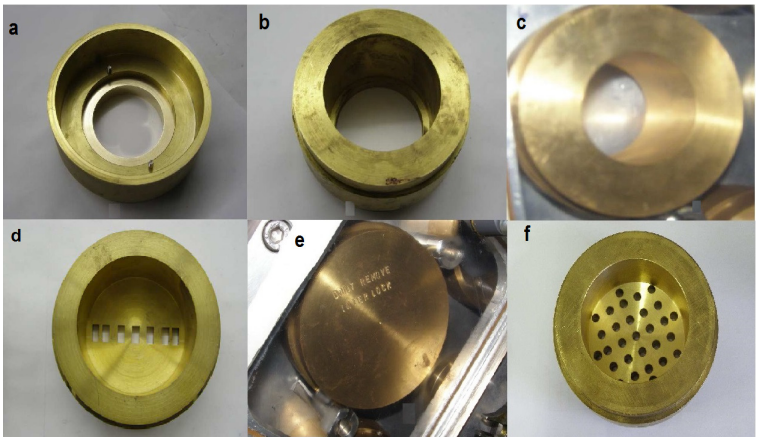

Figure 3.5: Some of the collimators used in the K600 experiments [Nev14]. (a): A 63 mm diameter 39 mm thick collimator (type A_1 or A_2), the insert has a 49 mm diameter and is 11 mm thick; (b): A 63 mm diameter 51 mm thick collimator (type B_1); (c): A 49 mm diameter 51 mm thick collimator (type C); (d): the multislot collimator; (e): the blank collimator in the carousel; and (f): the pepper-pot collimator which is 15 mm thick and has a central-region diameter of 63.5 mm.

3.2.3 Magnets

The magnetic elements of the K600 are the quadrupole magnet (Q), the two dipoles magnets (D1 and D2) and the two coil windings (H and K). There is an hexapole (S) magnet right in front of the Q magnet. However, it is not active and has not been used in the last decade.

3.2.3.1 Quadrupole magnet (Q)

The Q-magnet of the K600 is used to achieve vertical focussing of the charged particles onto the focal plane.

3.2.3.2 Dipole magnets

The two dipoles sit next to each other and in-between them is a turbo pump. The entrance to the first dipole (D1) is adjacent to the quadrupole magnet while the end of the second dipole (D2) is adjacent to the focal plane. The latter is slightly larger in size compared to the former as illustrated in Fig. 3.3. Together, they guide charged particles scattered in the spectrometer onto the focal plane. A range of different momentum dispersions can be achieved by varying the ratio of the fields in the 2 dipoles. The field of each of the magnetic elements of the spectrometer is set by selecting current settings in the dataroom on a designated personal computer (PC). The programme SPEXCIT [Nev14] can be used to determine the current in each magnet when the following parameters are supplied: the ejectile particle type, its charge and kinetic energy. With the use of a macro command called the 'superknob' which features on the K600 magnet control page, it has become more efficient to change magnet settings. The superknob allows for the current settings of the other magnets to be fixed with a pre-defined ratio relative to the current value of D1. Hence, only D1 can be modified in order to change all magnetic field values in the spectrometer.

3.2.3.3 Coil windings H and K

The H and K coil windings are pole-face current windings embedded in the two dipoles, D1 and D2, respectively. The coil winding H has an elliptic shape while the K-coil has a triangular shape as seen in Fig. 3.3. These two coils are adjusted such that particle position within the middle of the focal plane is independent of the scattering angle. The K-coil introduces dipole and quadrupole components which correct for first order $(x \mid \theta)$ aberration while the H-coil introduces dipole and hexapole components which correct for second order $(x \mid \theta^2)$ aberrations.

3.2.4 Focal plane detector package

3.2.4.1 Drift chambers

A pair of identical vertical drift chambers (VDC) is used to determine the position of the particles in the focal plane as well as the scattering angle with a high degree of accuracy. Each drift chamber has 198 vertical signal wires, and are collectively referred to as the X-wireplane. Each of these X-wires has a diameter of 20 μm and is made from gold-plated tungsten. This makes them strong enough to withstand tension, highly conductive and also resistant to oxidation and corrosion. These wires are arranged 4 mm apart in a plane perpendicular to the scattering plane. There are also 143 signal wires in each VDC that are spaced 4 mm apart and are oriented at 50° with respect to the scattering plane. This is known as the U-wireplane. The two VDCs are placed in the focal plane 18.3 cm apart and each of them has a vertical acceptance of 10 cm and a horizontal acceptance of 78 cm. A schematic of the 2 VDCs showing their geometry, the wireplane arrangements and their relative position to incident particles is provided in Fig. 3.6.

The 2 wireplanes (X and U) are sandwiched between 3 cathode planes 16 mm apart and each of which is connected to a high negative voltage ($\sim$ -3700V) while the signal wires are kept at zero potential. An electric field is then created at both sides of the signal wireplanes and oriented towards the cathode planes. Gold-

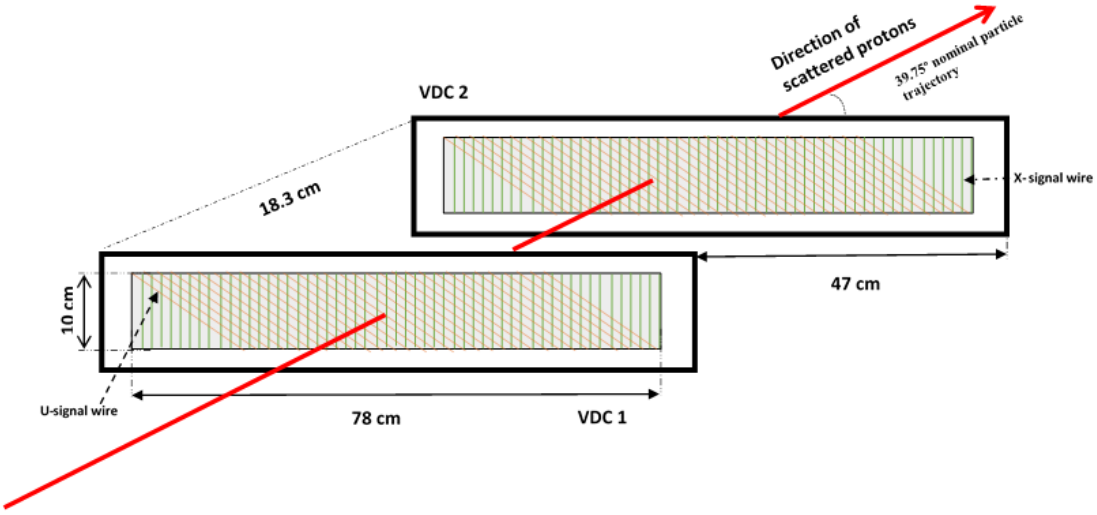

Figure 3.6: A schematic of the pair of vertical drift chambers used for the measurements.

plated guard wires with a 50 μm-diameter are placed in-between successive anode wires as well as at the 2 edges of the wireplanes in order to create drift cells. The guard wires are connected to a negative potential of -500V. Each drift chamber is filled with a gas mixture of Ar (90%) and CO_2 (10%) [But90]. When the scattered particles enter the drift chambers, they ionise the gas molecules. The created free electrons drift towards the anode planes [New96]. The position of the scattered particles in the focal plane is determined by translating the electron drift time information into spatial information through the use of a lookup table. More details on the operational principle of drift chambers can be found in Refs. [Blu08, Ber77b]. A sectional view of a VDC showing its inner dimensions and the electron drift mechanism when scattered particles cross the chamber is illustrated in Fig. 3.7.

3.2.4.2 Scintillation detectors

The pair of scintillators represents the other component of the focal plane detector package that are essential for particle identification and for providing a fast timing trigger. These detectors are also referred to as 'paddles' as an indication of their shapes. The dimensions of each of them are given as: 1219.2 × 101.6 × 12.7 mm^3 for the first paddle and 1219.2 × 101.6 × 6.175 mm^3 for the second paddle.

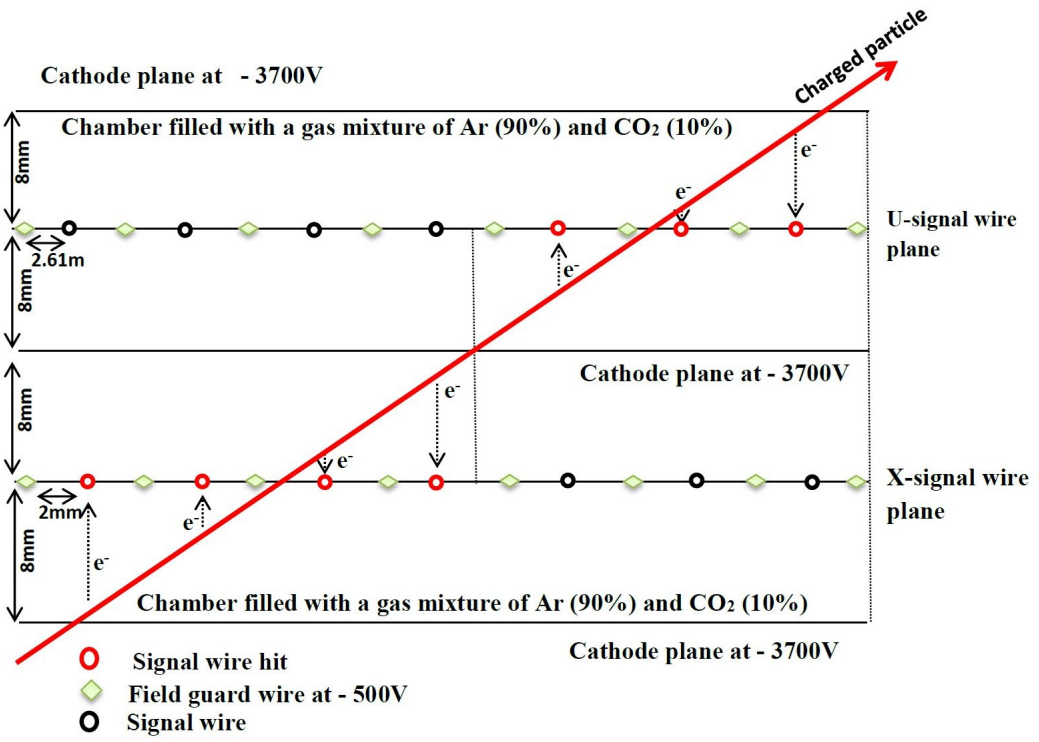

Figure 3.7: A sectional view of a vertical drift chamber illustrating its operational principle. The geometry and relative position of scattered particles are also shown.

They are made of Polyvinyltoluene and Organic Fluors ($C_{10}H_{11}$) manufactured by Saint-Gobain Crystals [Sai15]. A Hamamatsu R329-02 type photomultiplier tube with a Hamamatsu E-934 base is coupled with each of them to record the light emitted when the scattered particles cross them. Typically a good scintillation material converts the energy deposited by charged particles into detectable light with a good scintillation efficiency [Kno99]. A good scintillator is required to have a linear response between incident particles energy transfer and amount of light output, should be transparent to its own wavelength, have a very short decay time and have good optical properties with a refractive index near that of glass ($\sim$ n = 1.5), among others. In principle, when the scattered particles interact with the scintillation material they lose part of their energy to it through ionisation and excitation of the organic molecules giving rise to a fluorescence process which results from the de-excitation of the free electrons created by the particles [Kno99]. The photomultiplier tube, which is enclosed in a light-proof

box, records and converts the light detected into electrical pulses. Generally, the surfaces of the scintillator are polished to ensure better internal reflection and thus light collection efficiency.

3.2.5 Data acquisition electronics and trigger system

The data acquisition (DAQ) system of the spectrometer constitutes the interface between the user and the detectors. It comprises a hardware component (i.e. the DAQ electronics) and a software component. The trigger electronics used for the measurements consists of Nuclear Instrumentation Modules (NIM) electronics while the signal generated in the detectors were digitised with the use of Versa Module Europa (VME) electronics. A total of 10 VME modules were used for the experiments:

- 1 CAEN V792 Charge-to-Digital Converter (QDC),
- 7 CAEN V1190 Time-to-Digital Converters (TDC) and
- 2 CAEN V830 Scalar Modules.

The CAEN V792 is a 1-unit wide 6U VME module housing 32 QDC channels with current integrating negative inputs (50 Ohm impedance). For each channel, the input charge (0 - 400 pC) is converted to a voltage level by a charge-to-amplitude conversion section [CAE10]. Each of the CAEN V1190 modules is a 1-unit wide 6U VME module that contains 128 independent multi-hit/multi-event TDC channels [CAE12]. The CAEN V830 is a 1-unit wide 6U latching scalar and multievent latching scalar module which houses 32 independent counting channels each of which has a 32-bit counting depth [CAE02]. When the scattered particles cross the paddles the signals produced are amplified by the photomuliplier tubes (PMT) at each end of the paddles. A mean-timer is used to compute the average arrival time of the 2 input signals received from a particular paddle. A logical AND gate is then used to select events for which both mean-timers simultaneously produce valid mean-time pulses. Such an output signal serves as the QDC gate which effectively triggers the DAQ. The signal is also used to estimate the relative

time-of-flight (TOF) between the cyclotron radio-frequency and the paddle trigger signal. A description of the trigger electronics for the data acquisition system is given in Fig. 3.8. The Maximum Integrated Data Acquisition System (MIDAS) [MID15] is employed to address the software aspect of the K600 data acquisition through an event-by-event construction and analysis scheme with a ROOT-based application [Bru97].

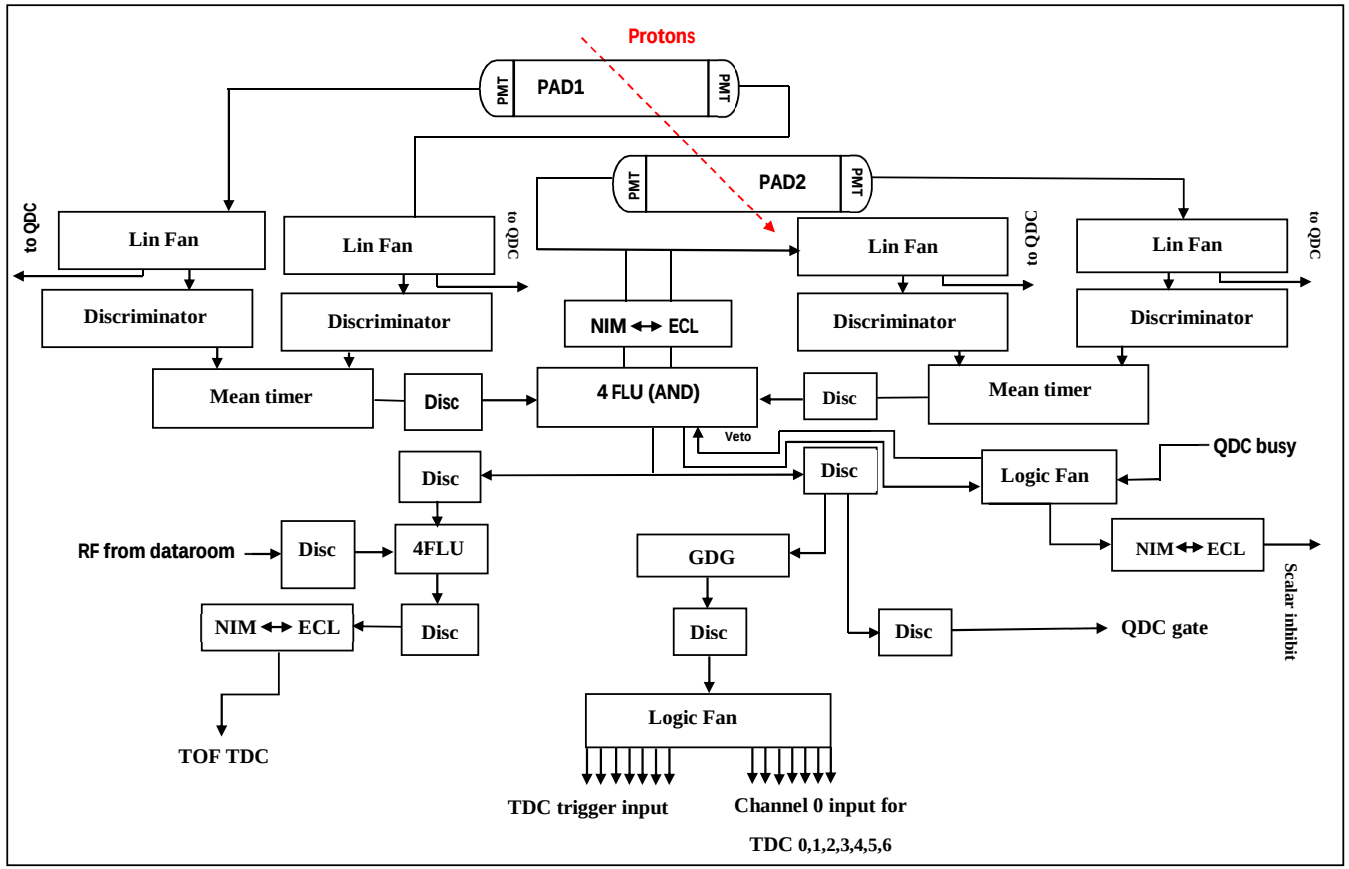

Figure 3.8: Block diagram representing the trigger electronics employed during the experiments.

3.3 Zero-degree inelastic proton scattering measurements

Zero-degrees inelastic proton scattering measurements begin by ensuring the characteristics of the beam is optimised. The exercise is aimed at having a background count rate of 100 Hz or less for a 1 nA beam current. When this is achieved dispersion matching techniques can be applied using the faint beam method, which will be described in the next subsection.

3.3.1 Dispersion matching techniques

First suggested by Cohen in 1959 [Coh59], the concept of dispersion matching involves matching the dispersion of the incident beamline with the capabilities of the spectrometer in order to have a spectral resolution better than the momentum spread of the beam, within the limit of the resolving power of the spectrometer [Wak02]. The technique was later tested and confirmed by Blosser and colleagues [Blo71] and subsequently became widely adopted and implemented [Wak02, Mar83, Ber93b, Ike80] and is also successfully realised at the iThemba LABS magnetic spectrometer facility [Nev11].

In principle, setting up an achromatic beam requires that the spatial and angular coordinates of the protons at the target be independent of their incident momentum, P. This is mathematically expressed as [Eng81]:

$$(x \mid \frac{\delta P}{P}) = 0 \qquad and \qquad (\theta \mid \frac{\delta P}{P}) = 0, \tag{3.1}$$

where δP is the fractional momentum.

Under these conditions, the momentum spread in the beam limits the energy resolution of the analysing spectrometer. To address this, the beam transport to

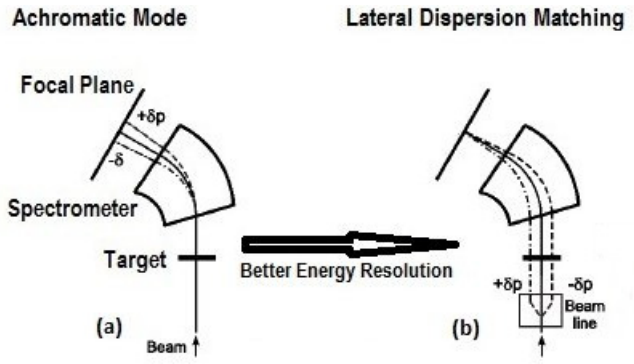

Figure 3.9: A schematic illustration of beam trajectories for different beam transport conditions (after Ref. [Fuj02]). In (a) is shown an achromatic beam transport, in (b) is shown dispersive beam transport (i.e. lateral dispersion matching realised).

the target is changed such that protons of lower momentum are to the left of the centre of the beam spot on target while protons of higher momentum are to the right of the centre of the beam spot on target. The overall effect is achromatic focus at the focal plane of the spectrometer. The process is schematically illustrated in Fig. 3.9 starting from an achromatic beam set-up in (a) to a spatially matched beam in (b) [Fuj02].

3.3.2 Faint-beam method

Dispersion matching of the beamline to the spectrometer at zero-degrees is achieved through the so-called faint-beam method. The method relies on attenuating the beam intensity by a factor of 10^6 without altering the beam profile. The low intensity beam is then directly viewed with the spectrometer focal plane detectors. Such a low beam intensity (of the order of a few hundred protons per second) cannot cause damage to the detectors. Beam intensity attenuation is realised with the use of 3 meshes made of thin copper plates with tiny holes through which the beam passes. The meshes are located between the ECR ion source and SPC2 (see Fig. 3.2). It is important to note that this level of beam attenuation is not possible in case SPC1 is employed to provide the pre-accelerated beam to the main cyclotron as it has an internal ion source which does not provide room

Table 3.2: Calculated ion-optical properties of the K600 magnetic spectrometer in vertical focus mode near the central momentum of the medium and high-dispersion focal planes using the ray-tracing code TRACK [Vra14].

Matrix element	Medium dispersion (R = 1)	High dispersion (R = 1.49)
(x | x)	-0.52	-0.74
(θ | θ)	-1.89	-1.37
(y | y)	-5.45	-7.05
(ϕ | ϕ)	-0.20	-0.13
(x | $\frac{\Delta P}{P}$)	-8.4 cm/%	-10.9 cm/%
(P_{max}/P_{min})	1.097	1.048

for attenuation meshes to be installed. For this reason, SPC2 is always preferred for zero-degree measurements.

3.3.3 Ion-optical and beam transport properties of the K600 magnetic spectrometer

The ion-optical properties of the K600 magnetic spectrometer were computed, using the TRACK ray tracing program [Vra14], near the central momentum of the medium and high-dispersion focal planes. These properties are summarised in Table 3.2.

The particle transport from the point of interaction at the target to the focal plane is also illustrated in Fig. 3.10. In a zero-degree experiment, a precise determination of the scattering angle, Θ_{scat} in the focal plane requires accurate estimation of its horizontal, θ_{scat}, and vertical, ϕ_{scat}, components and is given as [Nev11]:

$$\Theta_{scat} = \sqrt{\theta_{scat}^2 + \phi_{scat}^2} \tag{3.2}$$

The Q-magnet is responsible for the vertical focussing of the scattered protons

onto the focal plane. The top-panel of Fig. 3.10 shows the vertical trajectory of protons in focus mode in the high dispersion focal plane (R = 1.49). However, depending on the requirements of the experiments, an underfocus mode or an overfocus mode (see Ref. [Fuj02] for detailed descriptions of these modes) characterised by $(y \mid \phi) < 0$ or $(y \mid \phi) > 0$, respectively could also be adopted by changing the Q-magnet field settings. For the present study, all measurements were taken in vertical focus mode.

The beam transport in the last part of the beamline is monitored at 3 critical stages in every zero-degree experiment. Three beam viewers made of scintillating ZnS are used for this purpose. The first of them is placed right behind the QS6 quadrupole magnet which is the last beamline magnet before the K600, and is called the Hatanaka mesh. It is named after Professor Hatanaka[1] who donated it to iThemba LABS. The Hatanaka mesh allows for the relative position of the beam, its shape and size to be determined. The second viewer is placed inside the scattering chamber to allow for monitoring of the beam position on target. The last viewer is placed right before the zero-degree beam dump (see Fig. 3.3). The latter viewer is used to ensure proper beam transport to the beamdump.

[1]Professor Kichiji Hatanaka, Accelerator Physics Group, Physics Department, Osaka University, Osaka, Japan

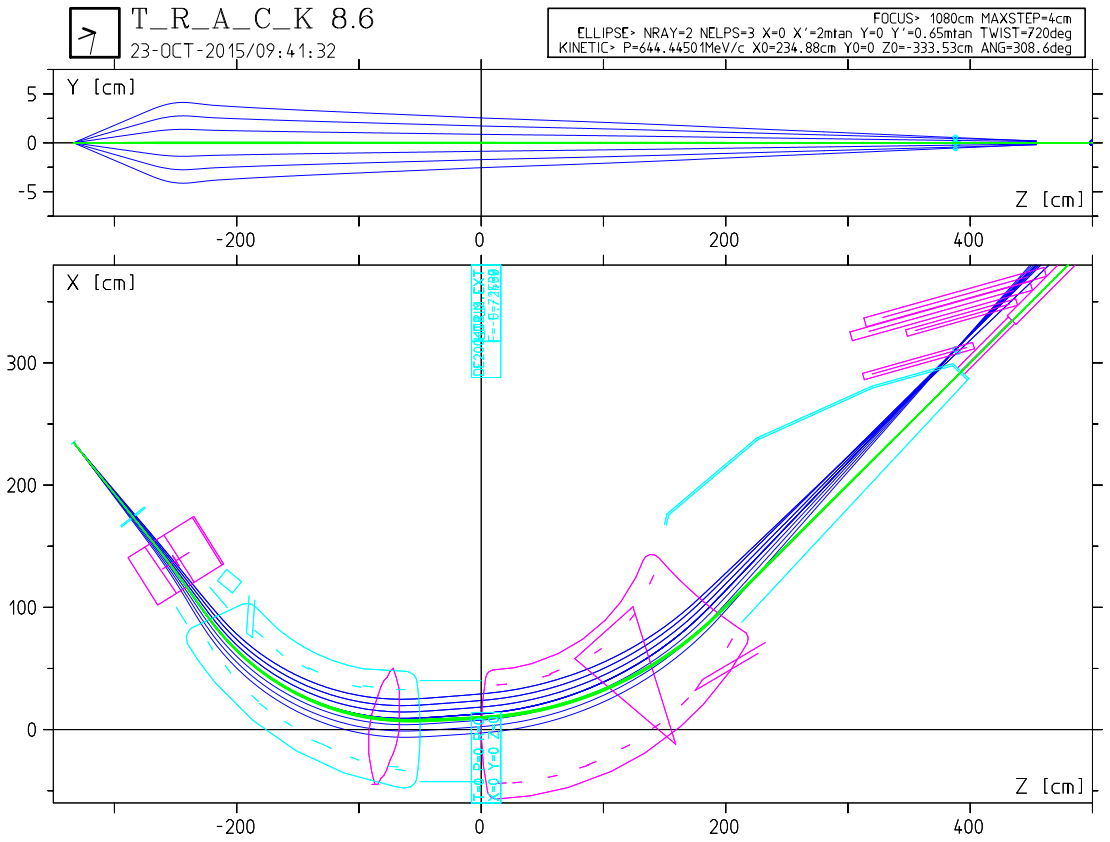

Figure 3.10: Particle transport through the K600 magnetic spectrometer computed with the computer code TRACK [Vra14] for a 200 MeV incident proton beam (green) and the 190 MeV scattered protons (blue) for full angular acceptance of $\pm$ 1.91^o. The top panel shows the vertical beam trajectory in focus mode.

3.4 Calcium targets

Calcium occurs in nature mostly as ^{40}Ca. It is a soft gray alkaline earth metal and is considered the fifth most abundant element by mass in the Earth's crust. First discovered in 1808 by Sir Humphry Davy [Kni98], it has the atomic number $Z = 20$ and therefore is the twentieth element of the periodic table. Some of its most important physical properties are listed in Table 3.3a [Wol14]. Calcium has 25 known isotopes from ^{34}Ca through ^{58}Ca of which only ^{40,42,43,44,46}Ca and ^{48}Ca are considered stable [Nud14]. The nuclear properties of these stable isotopes of calcium are summarised in Table 3.3b.

The calcium isotopes selected for the present study are ^{42}Ca, ^{44}Ca and ^{48}Ca. These isotopes were selected with the aim to investigate the fine structure of the isovector giant dipole resonance in the stable neutron-rich isotopes of calcium with ground state (g.s) $J^{\pi} = 0^{+}$. Consequently, ^{43}Ca was left out for not satisfying the second requirement ((g.s.) $J^{\pi} = 0^{+}$) and similar investigations have just been completed for ^{40}Ca [Jin14], therefore the measurement was not repeated. The non-inclusion of ^{46}Ca is due to financial constraints owing to its very low natural abundance as seen in Table 3.3b.

3.4.1 Target preparation

The metal pieces of ^{42}Ca, ^{44}Ca and ^{48}Ca, as shown in Fig. 3.11, were used for the manufacturing of the targets and were supplied by Oak Ridge National Laboratory [Oak15]. The targets were prepared in the Nuclear Physics target laboratory of iThemba LABS. Special caution was required considering the very reactive nature of calcium with moisture, acids and air. The manufacture process, which required rolling of the metal pieces down to the required thickness, took place inside a glove box using stainless steel plates as carriers. A detailed description of how calcium targets are prepared at iThemba LABS has already been reported (see Ref. [Khe10]). An areal thickness of 1.5 mg cm^{-2} was requested for each of

Table 3.3: Physical and nuclear properties of calcium isotopes

(a) Physical properties

Name	Calcium
Symbol	Ca
Phase at Standard Temperature and Pressure (STP)	Solid
Atomic Number (Z)	20
Atomic Weight	40.078
Density	1.55 g/cm^3
Melting Point	842°C
Specific Heat	631 J/(kg.°K)
Thermal Conductivity	200 W/(m.°K)
Crystal Structure	Face-Centered-Cubic (fcc)

(b) Nuclear properties of the stable isotopes of calcium

Isotopes	Ground state spin (J^π)	Half-Life ($T_{1/2}$)	Relative Abundance (%)
^{40}Ca	0^+	STABLE	96.94
^{42}Ca	0^+	STABLE	0.647
^{43}Ca	$7/2^-$	STABLE	0.135
^{44}Ca	0^+	STABLE	2.09
^{46}Ca	0^+	STABLE	0.004
^{48}Ca	0^+	STABLE	0.187

Figure 3.11: The metal pieces of ^{42}Ca, ^{44}Ca and ^{48}Ca (from left to right) prior the rolling.

the targets. This thickness was achieved for all targets within reasonable limits. The properties of the final targets are summarised in Table 3.4 while a picture of all targets mounted on the target ladder within the target storage box is shown in Fig. 3.12.

Table 3.4: Properties of prepared targets for the experiments.

Target isotopes	Areal thickness (mg/cm^2)	isotopic enrichment (%)
^{24}Mg	2.10 ± 0.2	99.9
^{42}Ca	1.48 ± 0.1	98.68
^{44}Ca	1.50 ± 0.1	93.71
^{48}Ca	1.49 ± 0.1	90.04

As seen from Fig. 3.12, in the first target slot of the target ladder is the beam viewer which allows for monitoring the beam position in the scattering chamber.

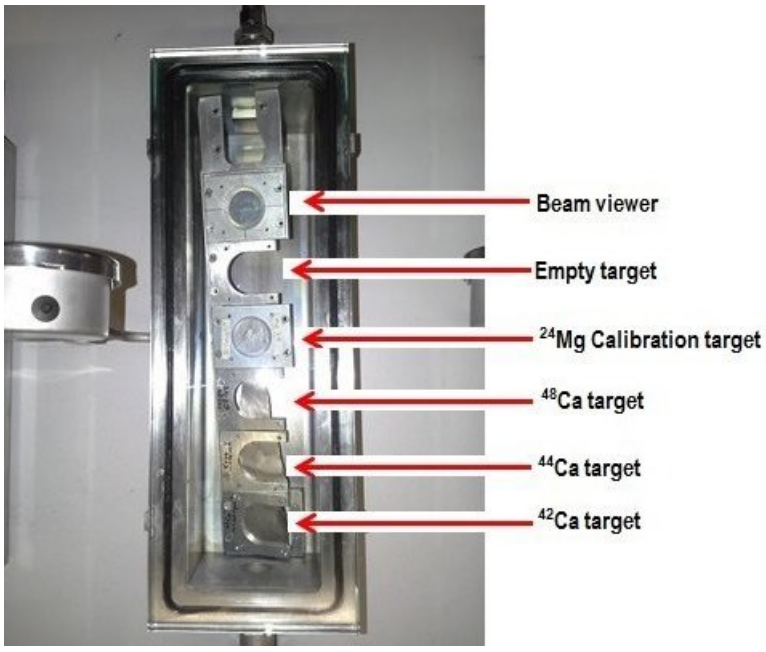

Figure 3.12: The prepared targets of ^{42}Ca, ^{44}Ca and ^{48}Ca together with the ^{24}Mg calibration target mounted on the target ladder inside the target storage box.

In the second slot is the empty target which is selected periodically for monitoring the background contribution to the data collection process. As mentioned in section 3.3, a typical count rate of 100 Hz or less is desired for a 1nA beam in proton inelastic scattering zero-degree measurements. In the third target slot is a ^{24}Mg target which is used for the energy calibration owing to its numerous distinct and well known states lying around the region of the isovector giant dipole resonance. The target slots 4, 5 and 6 are occupied by ^{48}Ca, ^{44}Ca and ^{42}Ca, respectively.

3.5 Experimental procedure

The target ladder shown in Fig. 3.12 was carefully mounted inside the scattering chamber and the spectrometer was positioned at an angle of 0°. A proton beam of 200 MeV was used to bombard the respective target nuclei. The schedule for the experimental project is summarised in Table 3.5.

Table 3.5: Beam-time schedule for the experimental project PR210.

Original Experiment Schedule	Period
Weekend 1	11 - 14 October, 2013
Weekend 2	18 - 21 October, 2013
Weekend 3	25 - 28 October, 2013
Additional Experiment Schedule	Period
Weekend 4	4 - 7 July, 2014
Weekend 5	11 - 14 July, 2014

After the beam interacts with the target, the unscattered protons go to the beam-dump. The scattered protons are directed to the focal plane where they interact with the detectors and data is acquired through the trigger system provided by the scintillation paddles in the data acquisition set-up as described in section 3.2.5. A certain routine was adopted in the data acquisition process and was maintained until sufficient data was acquired for each isotope. After beam tuning, data was first acquired for the ^{24}Mg calibration target for about 30 minutes and then the beam halo was characterised by running the empty target for about 20 minutes before data was acquired for the calcium isotopes for about 1 hour. This allowed for frequent monitoring of the beam halo so that corrective action could be requested from the beam operators whenever the background counts was found to be above 100 Hz for 1nA beam current. Data were acquired for the project over a total period of 5 weekends spanning from Friday afternoons to the early hours of Monday mornings. The project was initially scheduled for beam-time over 3 weekends devoted to ^{44}Ca, ^{42}Ca and ^{48}Ca, respectively. In spite of the minor challenges encountered during the first weekend of the experiments, measurements were successfully completed. On the other hand, the second and third weekends were marred by a lot of difficulties as summarised below:

(i) The preamplifier cards on the drift chambers were exceedingly sensitive to electronic noise causing frequent output signal oscillation in the 50 MHz

range. This resulted in instabilities in the VME DAQ and consequently causing the DAQ to crash frequently;

(ii) Beam halo conditions never stabilised especially during the second weekend. A lot of available beamtime was taken up by repeated halo and dispersion matching tuning due to beam instabilities.

The additional measurements performed in 2014 were very successful and sufficient data could be acquired for ^{42}Ca and ^{48}Ca during that period. The obtained data on ^{44}Ca was acquired during Weekend 1.

3.6 Data extraction

Event-by-event data acquired by means of the VME electronics are packaged into data files by means of the MIDAS data acquisition system. The raw datafiles are then analysed, populating ROOT histograms and TTree structures [Bru97]. The analysis software contains 4 files of interest to the user: f-plane.c, adc.c, qdc.c and scalar.c. In our case, adc.c was not used as the experiments did not involve any other detection systems apart from the spectrometer. While qdc.c extracts the accumulated charge in the paddle PMT's for each event, f-plane.c is the principal code used to analyse all raw data acquired in the focal plane. The function of scalar.c is to extract scalar outputs from the raw datafiles, such as rates for the clock, pulser, trigger, current integrator as well as the count rates in the Bergoz beam loss monitors which consist of two PIN-photodiodes mounted to detect charge particles along the beamline, due to beam halo [Wit00]. During the course of data analysis, all drift times are converted into drift distances in individual drift cells through a lookup table (LUT). For accurate position determination in the focal plane, it is imperative that all drift times are measured relative to the same starting point. However, time measurements depend on the slightly varying response time among preamplifiers and the slightly varying length of the signal cables linking each pre-amplifier to the corresponding TDC channel. This

is addressed by adopting a process termed 'the cablelength offsetting' which refers to the alignment of the TDC channels as shown in Fig. 3.13. This is effected in f-plane.c.

The setting up of an appropriate lookup table is advisable for every experiment. This is because key parameters of the spectrometer and its detectors, such as the VDC high voltage setting, the gas mixture, the beam particles and energy may vary for different experiments. In order to generate a suitable lookup table, the electron drift time-drift distance relationship in the VDC is established at the beginning of the experiment. The lookup table then is derived as follows [Ber77b, Fis01].

Assuming dN is the number of protons trajectories crossing the element of distance dx in a drift cell of the VDC, then a linear relationship can be established between dN and dx. The number of events per time bin in that drift cell is given as dN/dt which can be mathematically expressed as:

$$\frac{dN}{dt} = \frac{dN}{dx}\frac{dx}{dt}, \tag{3.3}$$

where $\frac{dN}{dx}$ is the linear density of tracks along dx and $\frac{dx}{dt}$ is the mean drift velocity towards the signal wire.

Rearranging and integrating with respect to drift time, one obtains:

$$x(t) = \frac{\int_0^t \frac{dN}{dt'}dt'}{\frac{dN}{dx}}. \tag{3.4}$$

The denominator of the right-hand side of Eq. (3.4) is selected such that the width of the drift distance distribution is the geometric maximum for the drift cell considered. Hence Eq. (3.4) corresponds to the lookup table for each time bin. More often than not, after creating the lookup table for each wire plane, an offset is required for each of them. After applying the offset, the drift length spectrum as a function of the drift distance changes as illustrated in Fig. 3.14. This also translates into a smooth locus horizontally across the spectrum for each of the wire planes as illustrated in Fig. 3.15.

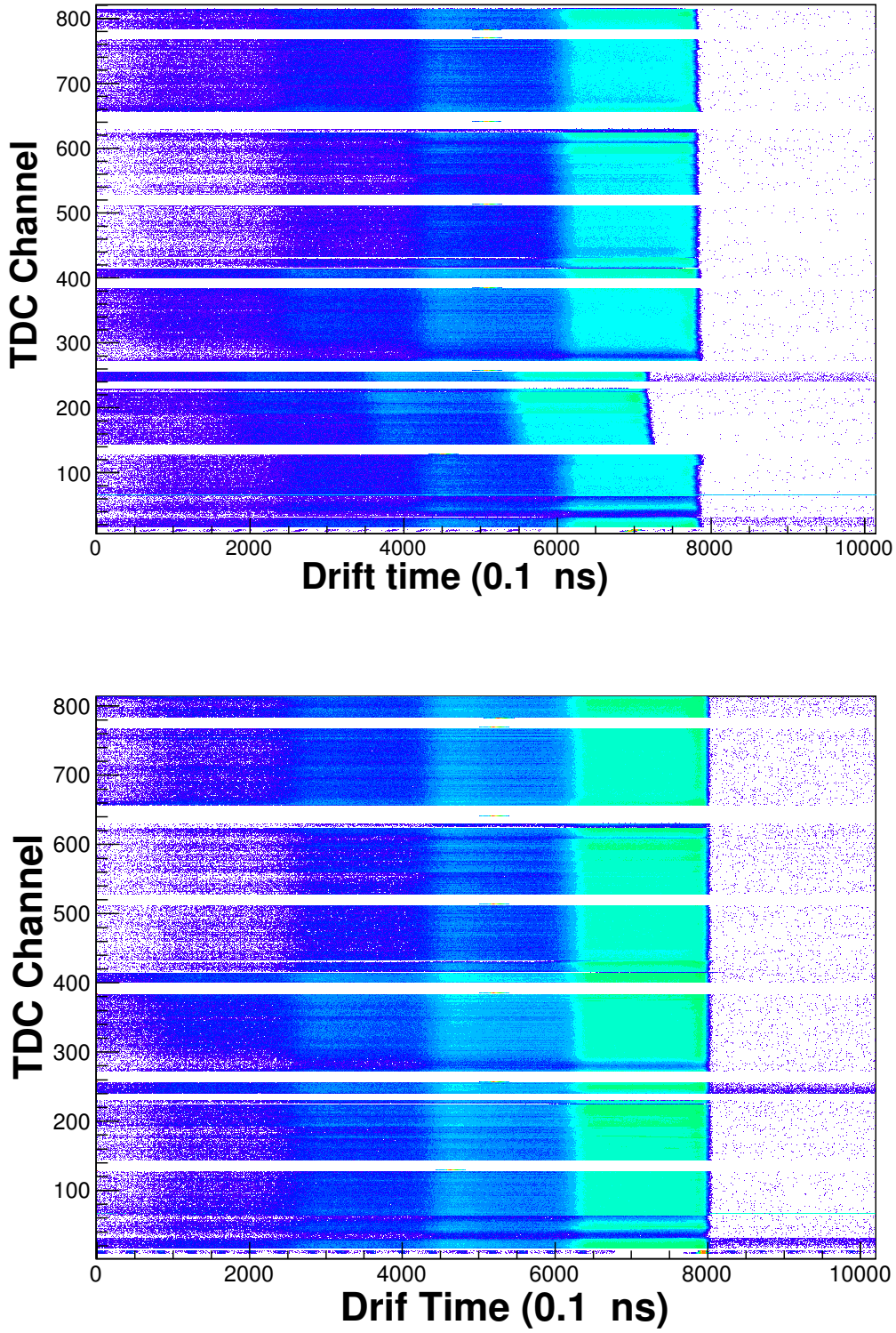

Figure 3.13: TDC Channels as a function of electron drift time. *Top panel*: before cablelength offset was applied. The TDC channels fail to properly align. *Bottom panel*: after the cablelength offset was applied. TDC channels align properly.

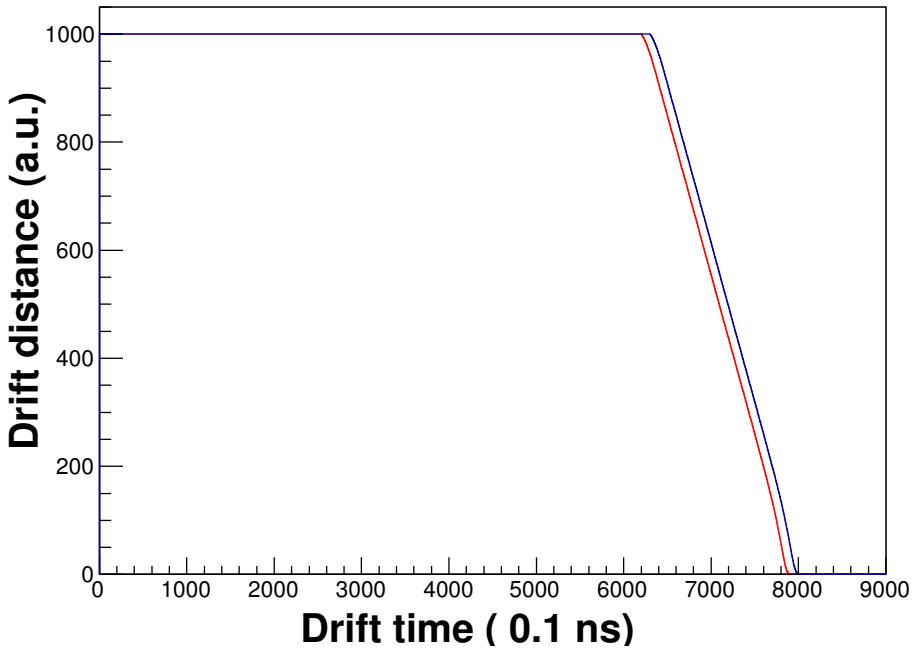

Figure 3.14: Drift length as a function of drift time for one of the wire planes before (blue) and after (red) applying the lookup table offset.

3.6.1 Particle Identification (PID)

A careful identification of the particles of interest is key to a successful experimental data extraction. The spectrometer selects particles to be seen in the focal plane according to rigidity. The magnetic rigidity is a function of the dipole field and the radius of gyration of the particle under the influence of the magnetic field. It is also expressed as the ratio of the momentum of the particle to its charge as:

$$R = B\rho = \frac{p}{q}. \tag{3.5}$$

The relative time-of-flight with respect to the cyclotron radio-frequency (RF) allows for estimation of the time during which the scattered particles travel through the spectrometer to the focal plane thereby providing a measure of their velocity. Another important parameter for identifying charged particles in the present type of measurement is by their ionisation energy loss. This corresponds to the amount of energy the protons lose to the paddles by crossing them. The average energy loss per unit track length is indirectly proportional to the square of the

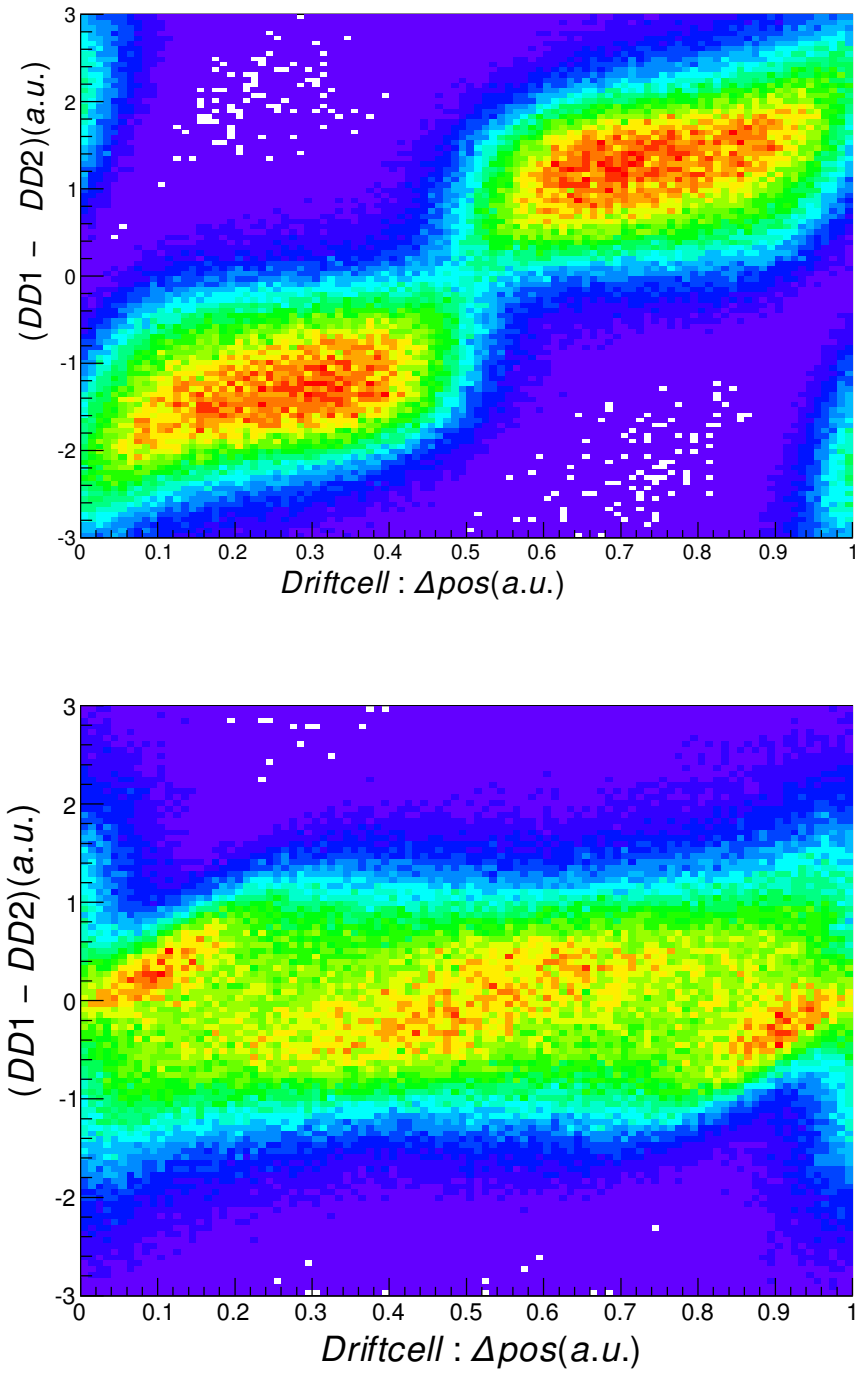

Figure 3.15: A resolution plot for the lookup table (LUT) for one of the wire-planes. *Top panel*: before LUT offset was applied.*Bottom panel*: after LUT offset was applied. (DD1-DD2) is the difference between the minimum estimated drift distance (DD1) and the actual drift distance (DD2) and Δpos is the difference between the actual focal plane position and the nearest wire position.

particle velocity as [Blu08]:

$$-\frac{dE}{dx} \propto \frac{q^2c^2}{v^2} ln\gamma. \tag{3.6}$$

For the selection of the physics events, 4 different histograms are plotted and their respective software gates are created. These gates are then applied in order to eliminate the unwanted background events mainly due to beam halo. There are, however, other background contributions which emanate from physics events other than the (p,p′) reaction. Examples of these include (p,2p) and (p,np) reactions as well as target-related background which cannot be removed by only applying these software gates.

The histograms are:

- hpad1vstof: this histogram plots the energy deposited by the protons that pass through the first scintillation paddle (pad1) as a function of their relative time of flight (TOF). An illustration of such scatterplots for a Ca target and an empty target are given in Fig. 3.16 where the physics events are selected with the software gate indicated by the dashed contour line.

- hpad2vstof: this histogram plots the energy deposited by the protons that cross the second scintillation paddle as a function of their relative time of flight similar to hpad1vstof (Fig. 3.16).

- hpad1pad2: this histogram plots the energy deposited by the protons in the first paddle as a function of the energy deposited by them in the second paddle. The software gate created is indicated by the dashed contour line in Fig. 3.17. Results for a Ca target and an empty target are shown.

- htofX1: this histogram plots the relative time of flight of the scattered protons as a function of their horizontal position in the focal plane. Background events due to beam halo are distinguished by their corresponding time of flight. A plot of this histogram showing the region of the physics events as indicated by the software gate selection is illustrated in the top panel of Fig. 3.18. In the bottom panel, the software gate is applied and

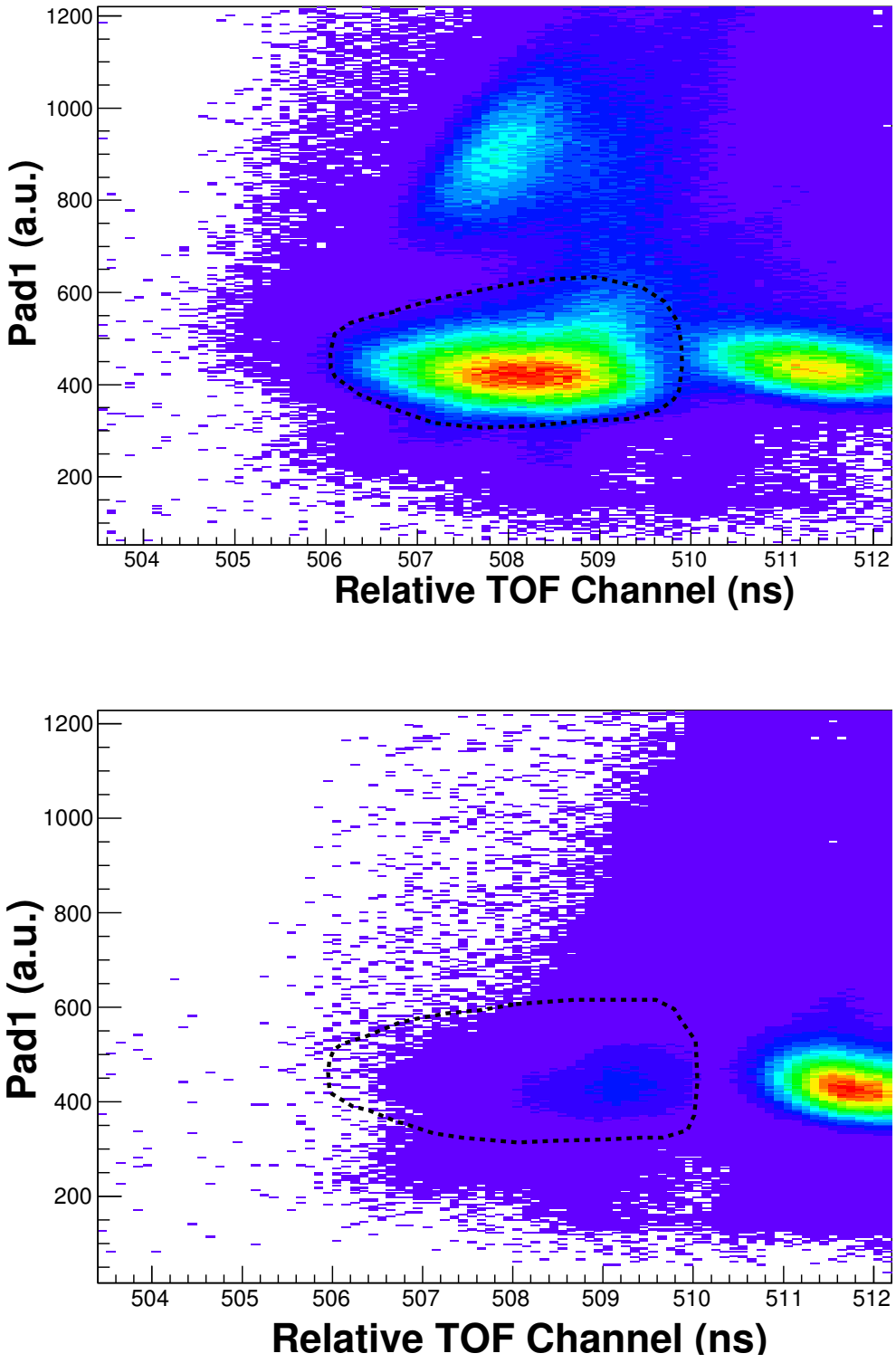

Figure 3.16: A plot of the energy deposited in pad1 as a function of the relative time of flight. *Top panel*: ^{44}Ca target. The software gate is indicated by the dashed contour line. *Bottom panel*: empty target. The region of the physics events is indicated by the dashed contour line.

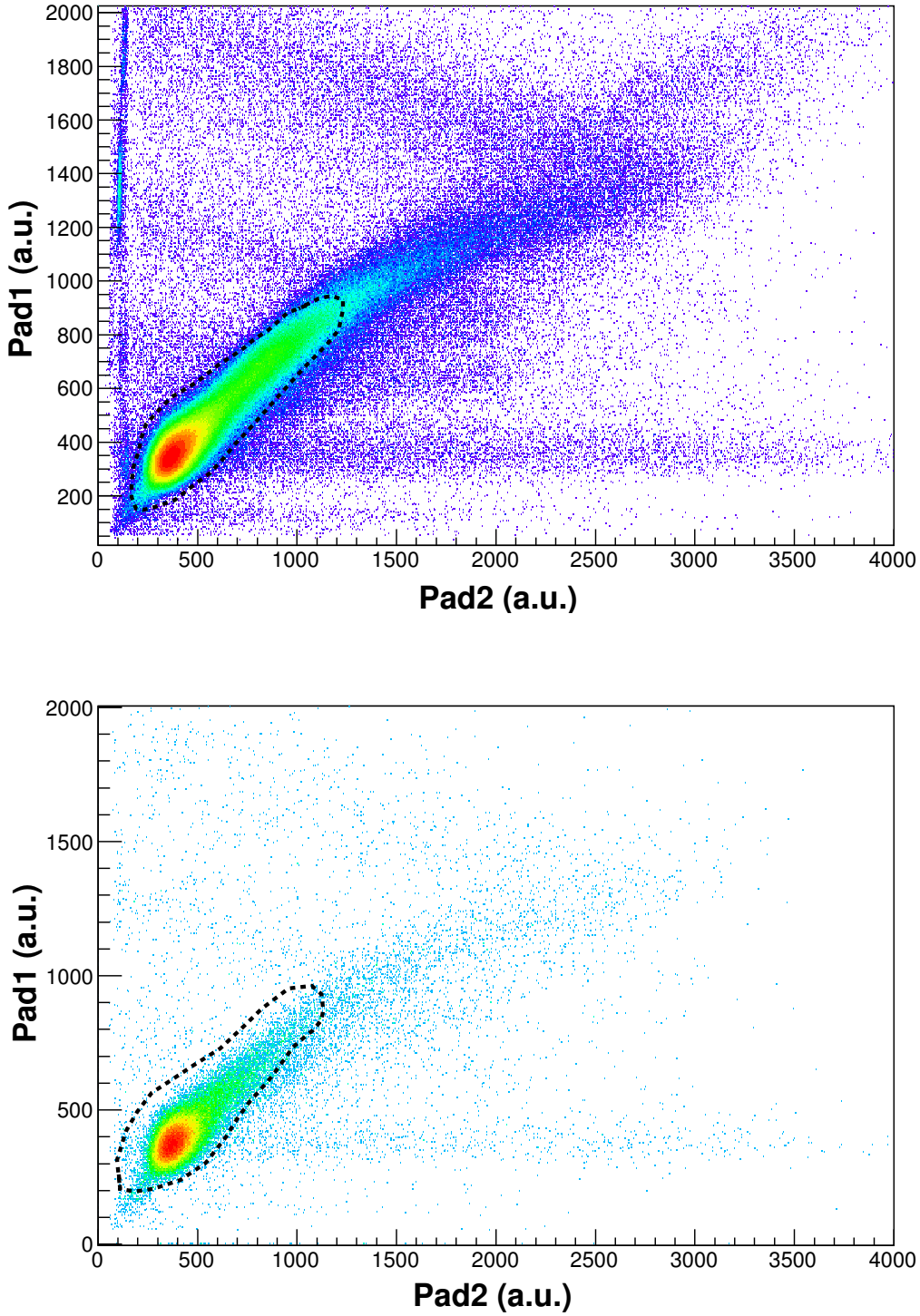

Figure 3.17: A scatterplot of the energy deposited in the first paddle as a function of the energy deposited in the second paddle. *Top panel*: ^{44}Ca target. The software gate is indicated by the dashed contour line. *Bottom panel*: empty target. The region of the physics events is indicated by the dashed contour line.

all background due to beam halo are removed showing only the region of physics events.

A combination of these four software gates, when applied, allows for the physics events to be effectively selected.

3.6.2 Horizontal angular calibration

As discussed in subsection 3.3.3, an effective angular calibration is crucial in a zero-degree measurement. The procedure of horizontal angular calibration is carried out in the achromatic mode at a finite angle with the pepperpot collimator (see Fig. 3.5). In the present investigation, calibration measurements were made at 6.9° using the ^{44}Ca(p,p′) reaction at 3 different energies: 216.3 MeV, 222.3 MeV and 228.3 MeV. The corresponding runs were numbered 132, 133, and 134 while the detector separation parameters, z_{x1x2} and x_{x1x2}, were set at 285 mm and 515 mm, respectively. These parameters are crucial to obtain realistic focal plane scattering angles (θ_{FP}). The measurements were taken in vertical focus mode. In the process, the elastic peak of ^{44}Ca was swept through the focal plane from 305 mm to 650 mm by changing the K600 magnetic field, being careful to keep constant ratios between the different individual magnetic elements. The transformation from the focal plane angle (θ_{FP}) to the the scattering angle (θ_{SCAT}) is achieved using a designated script. The script outputs the fit parameters of the horizontal focal-plane angle. These parameters are then used as input to determine the scattering angle relative to the angle of the spectrometer, using the equation:

$$\theta_{SCAT} = (a_0 + a_1 X_{FP})\theta_{FP} + (b_0 + b_1 X_{FP}), \tag{3.7}$$

where X_{FP} is the particle horizontal coordinate in the focal plane.
The obtained fit parameters are as summarised in Table 3.6.

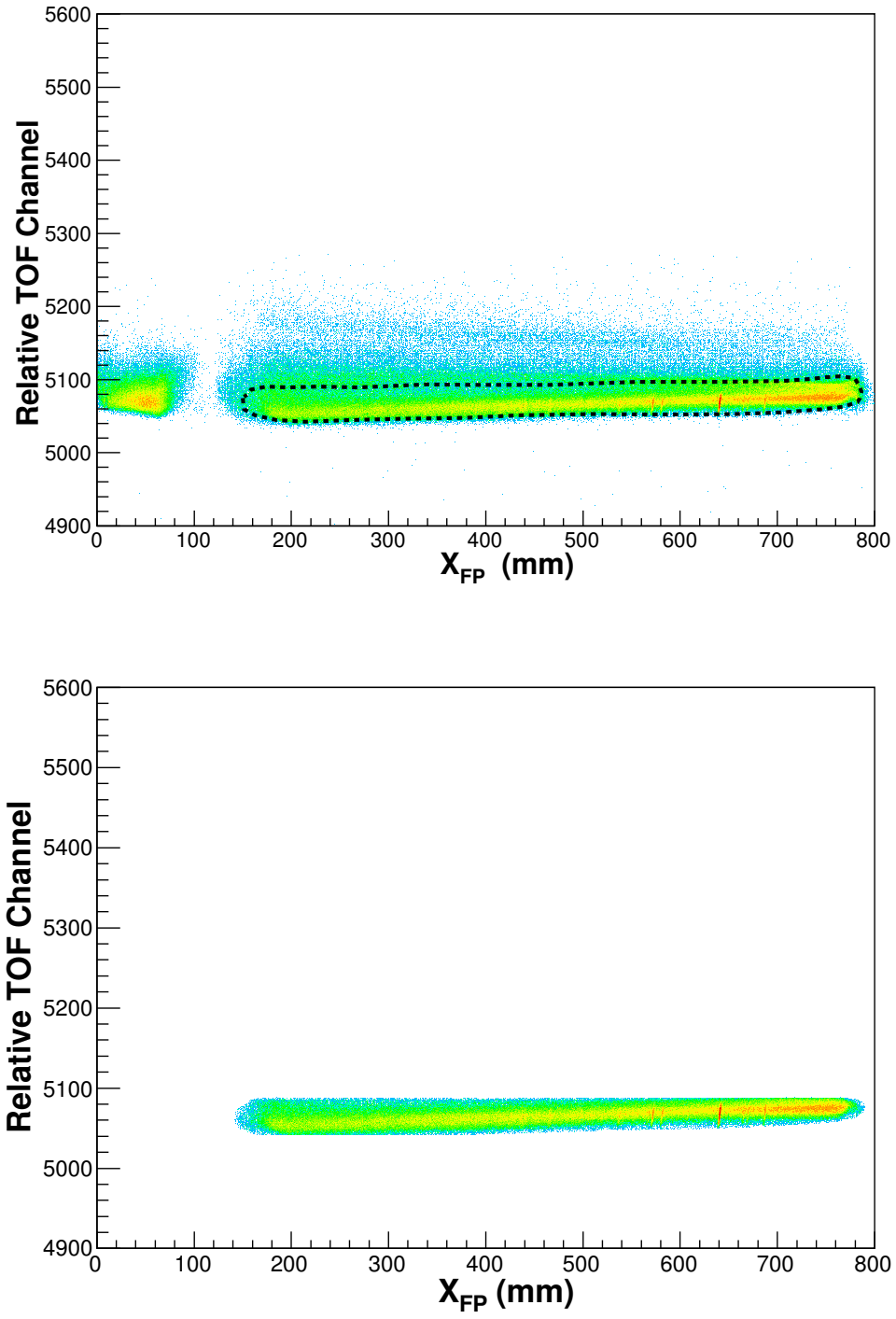

Figure 3.18: A scatterplot of the relative time of flight as a function of the focal plane horizontal position. *Top Panel*: TOF vs X1 plot of ^{24}Mg target acquired at E_p = 200 MeV at zero-degrees. The selected region within the black contour corresponds to the physics events. *Bottom Panel*: TOF vs X1 for the same target after applying the software gate. Here only physics events are seen.

Table 3.6: Horizontal angular calibration parameters for the experiments

Parameter	Value
a_0	-1.01703
a_1	-6.25653e-05
b_0	33.6679
b_1	-0.0025703

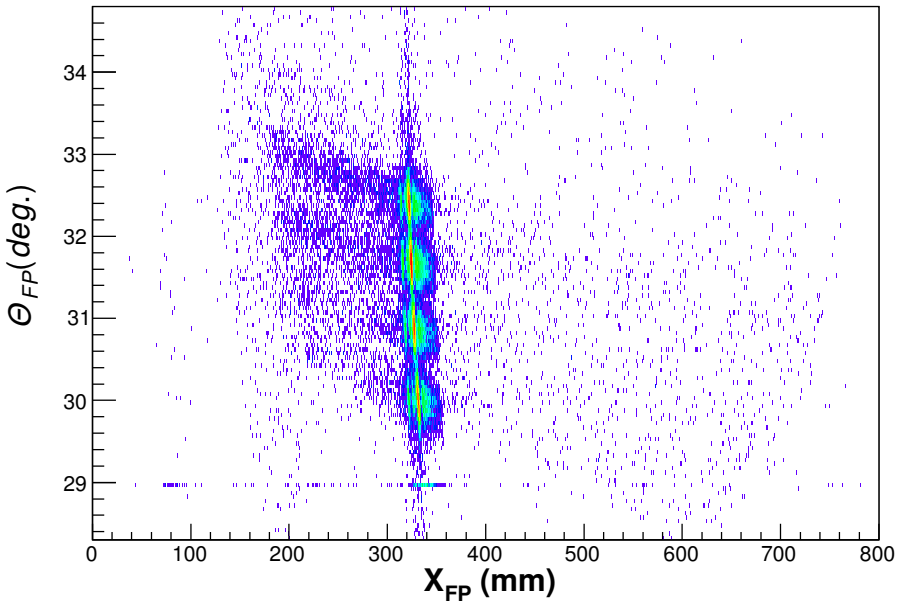

Figure 3.19: A plot of the focal plane angle, θ_{FP} as a function of the focal plane horizontal position, X_{FP} after angular calibration.

A typical pepperpot plot as used during the angle calibration exercise is illustrated in Fig. 3.19.

3.6.3 Line shape and position correction

The next step in the analysis procedure is to look at the corrections to the position determination prior to the excitation energy calibration of the focal plane.

3.6.3.1 Line shape correction

The procedure consists of correcting for the tilt in the plot of the scattering angle, θ_{SCAT}, and the vertical focal plane position, Y_{FP}, against the horizontal position, X_{FP} in the focal plane. This is done with a view to having the prominent states observed in those plots forming perfect straight lines perpendicular to the X-axis. To achieve this, the observed most prominent state is fit with a second order polynomial in θ_{SCAT} or at times up to a third order and a first order polynomial fit in Y_{FP} or at times up to a second order, depending on the initial shape of the spectrum. This process is aimed at optimising the position resolution in the spectrum.

3.6.3.2 Peak position correction

This refers to the correction of the peak position from run to run. This is due to small but measurable change in beam energy following beam tuning which is quite a recurrent exercise in these measurements. Peak correction is a necessary step as several runs are summed up to get the final spectrum with an optimised position resolution. This correction in peak position is achieved by selecting the prominent peaks in the position spectrum of the calibration target and identify its exact position in the focal plane for one of the runs taken as reference run. Then for each of the other calibration runs an offset in position is determined with respect to the reference run and corrected for. A slight drift in the magnetic field of the K600 can also partially contribute towards this problem. Such variations can in principle be introduced due to small temperature variations of the magnet cooling water temperature. The line shape and position corrections are illustrated in Figs. 3.20 and 3.21 which show some of the prominent states of ^{24}Mg resulting from the (p,p$'$) reaction at $E_{\mathrm{p}} = 200$ MeV. The top panels show the states before the line shape and position corrections were effected and the bottom panels show the same states after the corrections were effected. It can be seen from these figures that the resolution is significantly improved after line shape and peak position corrections were applied.

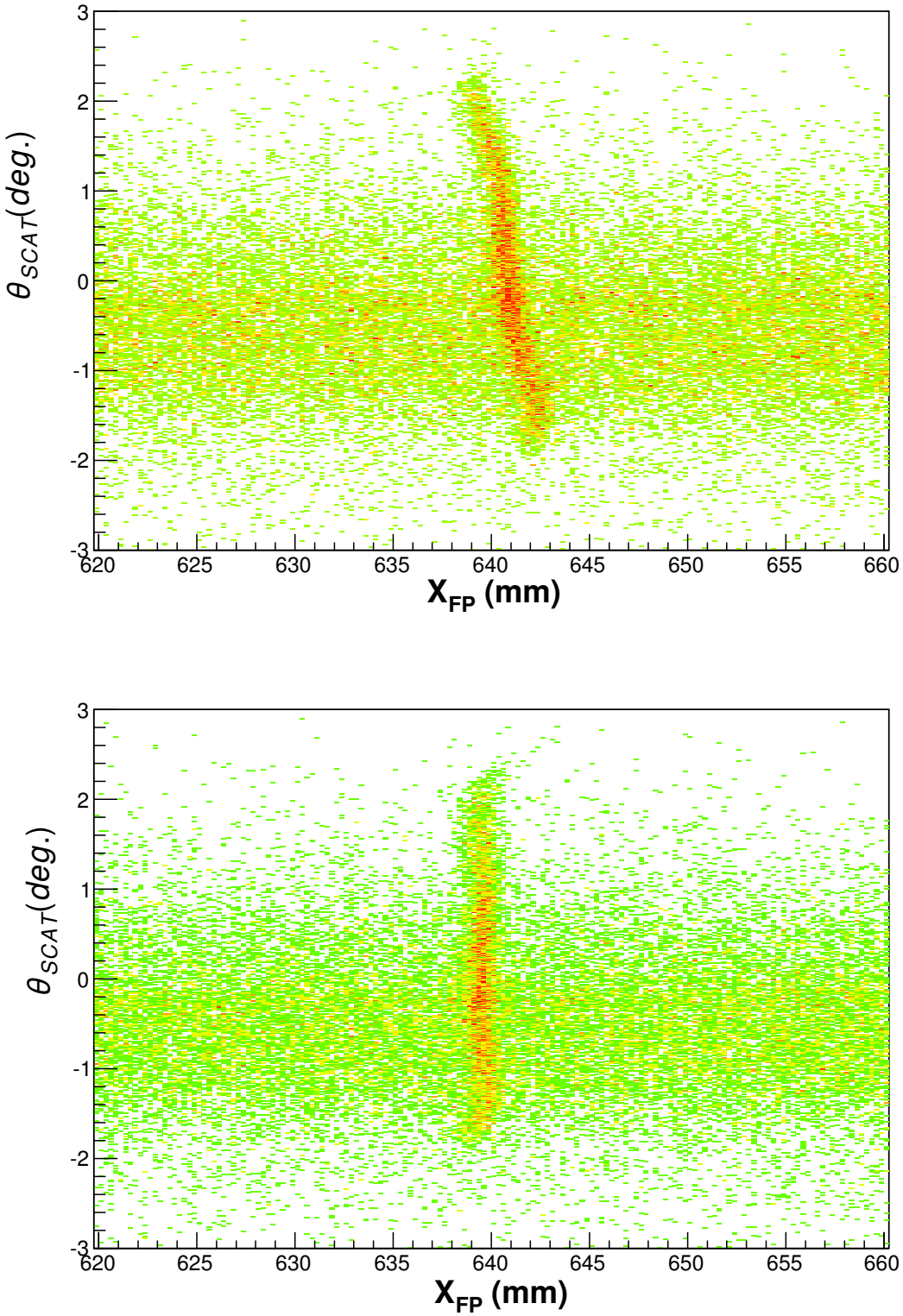

Figure 3.20: A histogram plot of the scattering angle in the focal plane, (θ_{FP}) against the horizontal coordinate (X_{FP}) for the ^{24}Mg(p,p′) reaction at E_p = 200 MeV and $\theta_{k600} = 0 \pm 1.91°$ showing the prominent 1^+ occurring at 10.71 MeV before (*top panel*) and after (*bottom panel*) line shape corrections.

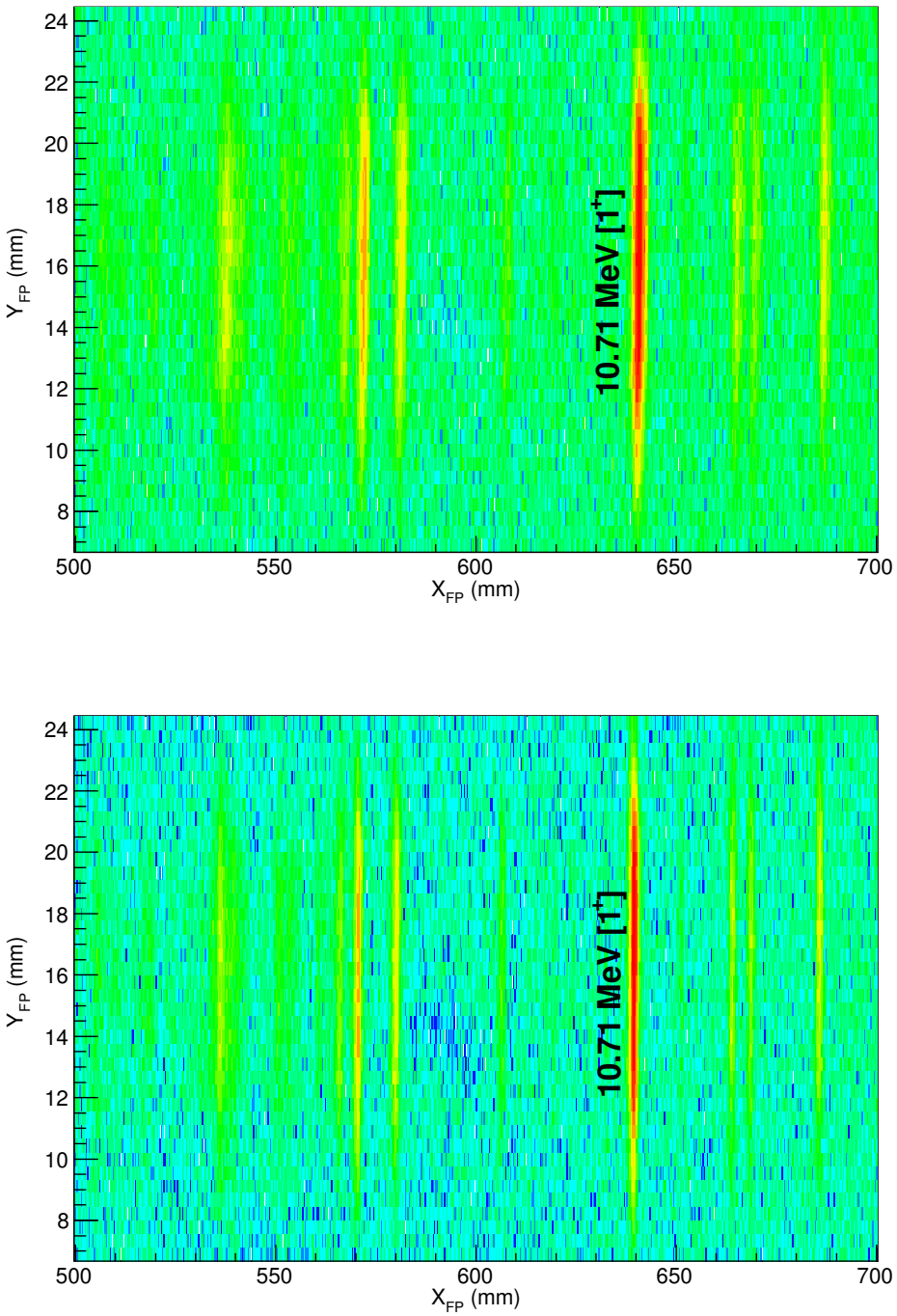

Figure 3.21: A histogram plot of the focal plane vertical coordinate (Y_{FP}) against the horizontal coordinate (X_{FP}) for the ^{24}Mg(p,p′) reaction at $E_p = 200$ MeV and $\theta_{k600} = 0 \pm 1.91°$. The most prominent 1^+ state is identified. *Top panel*: before line shape and peak position corrections. *Bottom panel*: after line shape and peak position corrections. It can be seen from the prominent 10.71 MeV $[1^+]$ state that the resolution is improved after line shape correction.

3.6.4 Energy calibration

After proper angular and lineshape corrections, a careful energy calibration is also very important in the data extraction procedure. In the present study, ^{24}Mg was used as our calibration target. Seven of its well known peaks with energies 9.31 MeV (0^+), 9.83 MeV (1^+), 9.97 MeV (1^+), 10.71 MeV (1^+), 12.53 MeV (1^+), 12.82 MeV (1^+) and 13.88 MeV (1^+) were used for the energy calibration. These states cover the low lying excitation region as well as the IVGDR excitation energy region which is the main purpose of the present campaign. The energy calibration procedure can be realised successfully using two different approaches which are the direct fit approach and the proper excitation energy calibration which is based on a momentum calibration.

3.6.4.1 Direct fit approach

In this approach a direct relationship is established between the position spectrum of the calibration target and its excitation energy spectrum through a quadratic fit. The position spectrum is generated using a 1-dimensional histogram called hX1pos after carefully selecting the physics events of interest by applying the various gates. Peak positions are estimated using a Gaussian fit approach in ROOT which provides position values accurate to within ~ 0.01 mm. A fit to the main peak of ^{24}Mg which occurs around 10.71 MeV is schematically illustrated in Fig. 3.22. This is done for all peaks to be used for the calibration whose excitation energies are known. Then a second order polynomial fit of the excitation energy as a function of the focal plane position is generated as:

$$E_x = aX_{FP}^2 + bX_{FP} + c, \tag{3.8}$$

where a, b and c are the fit parameters to be determined.

For the seven prominent states of the ^{24}Mg calibration target, the fit parameters

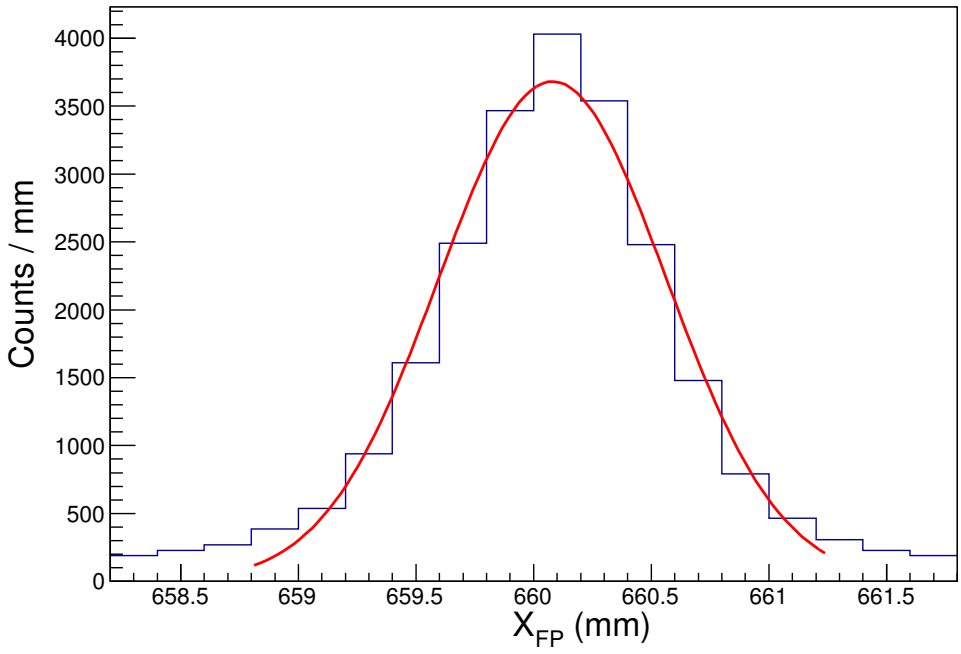

Figure 3.22: Gaussian fit of the dominant 10.71 MeV [1^+] state in ^{24}Mg obtained from ^{24}Mg(p,p$'$) reaction at E_p = 200 MeV. The energy resolution full width at half maximum (FWHM) is $\sim$ 33 keV for an energy dispersion of $\sim$ 31 keV/mm.

are listed in Table 3.7. It is important, however, to note that this method gives account of the excitation energy for ^{24}Mg but cannot be extended to the calcium isotopes.

Table 3.7: Excitation energy calibration parameters for ^{24}Mg target using equation 3.8.

Weekend of experiment	a	b	c
Weekend 1	1.504436 $\times 10^{-6}$	- 0.03227	31.35459
Weekend 4	3.023 $\times 10^{-6}$	- 0.03437	31.31833
Weekend 5	2.224516 $\times 10^{-6}$	- 0.03327	31.08404

3.6.4.2 Proper excitation energy calibration

In this approach, the excitation energies of the selected states are converted to momentum and a position-momentum calibration is performed. The projectile

(proton in this case) of mass m_0 arrives at the stationary target with a kinetic energy KE_0 and momentum p_0. After interaction with the target of mass m_1, the ejectile is scattered at an angle θ with a momentum p_2 while the recoil target is scattered at angle ϕ with a momentum p_3. The scattering reaction is illustrated in Fig. 3.23.

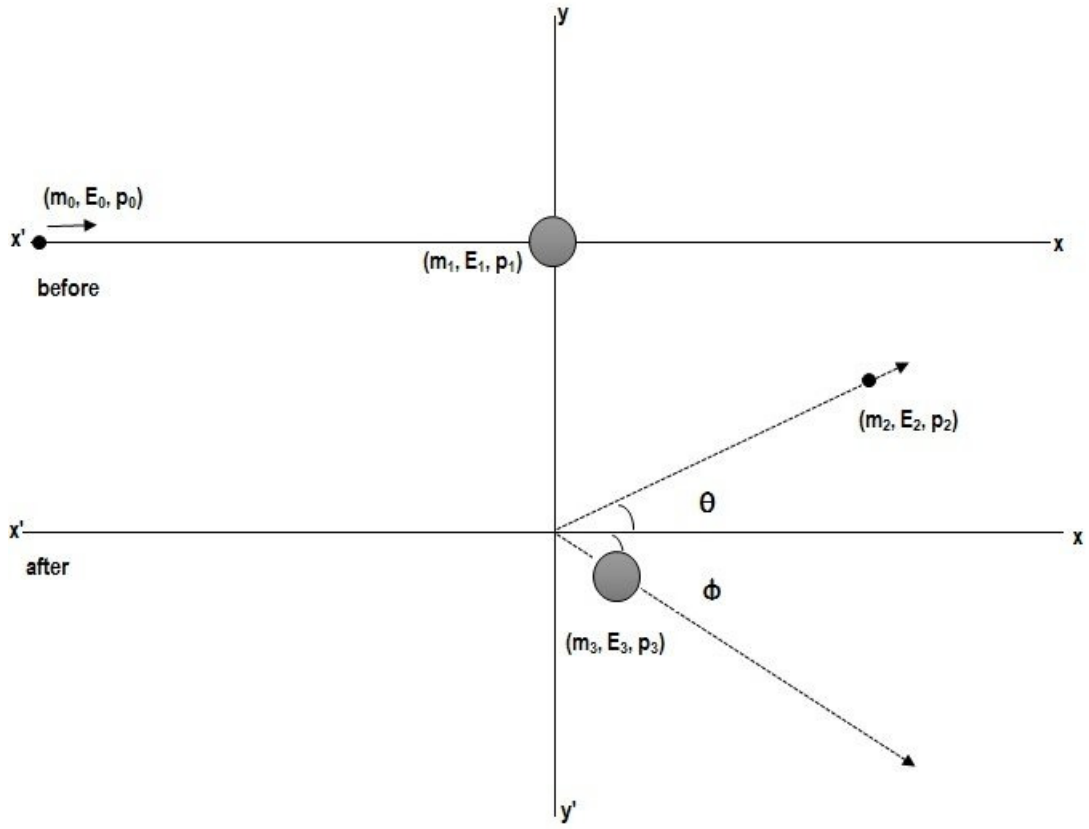

Figure 3.23: Illustration of two-body scattering in the laboratory frame of reference.

From the principle of conservation of momentum:

$$\vec{p_0} + \vec{0} = \vec{p_2} + \vec{p_3} \tag{3.9}$$

projecting Eq. (3.9) on the x-axis,

$$p_0 = p_2 cos\theta + p_3 cos\phi \tag{3.10}$$

$$\therefore p_0 - p_2 cos\theta = p_3 cos\phi. \tag{3.11}$$

Likewise, projecting Eq. (3.9) on the y-axis,

$$0 + 0 = p_2 sin\theta - p_3 sin\phi, \tag{3.12}$$

which can be arranged as:

$$p_2 sin\theta = p_3 sin\phi. \tag{3.13}$$

Squaring both sides of Eqs. (3.11) and (3.13) and adding side by side yields:

$$(p_0 - p_2 cos\theta)^2 + p_2^2 sin^2\theta = p_3^2(cos_\phi^2 + sin_\phi^2) \tag{3.14}$$

$$\therefore p_0^2 - 2p_0 p_2 cos\theta + p_2^2 = p_3^2. \tag{3.15}$$

From the principle of conservation of energy, if follows that:

$$E_0 + E_1 + Q = E_2 + E_3 + E_X, \tag{3.16}$$

where E_i is the total energy of particle i and Q is the energy released by the reaction, defined as:

$$Q = (m_0 + m_1 - m_2 - m_3)c^2. \tag{3.17}$$

Being a scattering reaction in which there is no mass transfer, in other words $m_0 = m_2$ and $m_1 = m_3$, the value of $Q = 0$.

Since the kinetic energy of the incident proton is in the range of 200 MeV which has an equivalent Lorentz factor of $\gamma = \sim 1.213$, a relativistic treatment is incumbent. Hence, Eq. (3.16) can be rewritten as:

$$(KE_0 + m_0c^2) + (0 + m_1c^2) + 0 = E_2 + E_3 + E_X. \tag{3.18}$$

Also, using the relativistic expression of energy as a function of momentum,

$$E_i = \sqrt{m_i^2c^4 + p_i^2}, \tag{3.19}$$

Equation (3.18) can then be rewritten as:

$$KE_0 + m_0c^2 + m_1c^2 = \sqrt{m_0^2c^4 + p_2^2} + \sqrt{m_1^2c^4 + p_3^2} + E_X. \tag{3.20}$$

Substituting Eq. (3.15) into Eq. (3.20), one obtains

$$KE_0 + m_0c^2 + m_1c^2 = \sqrt{m_0^2c^4 + p_2^2} + \sqrt{m_1^2c^4 + (p_0^2 - 2p_0p_2cos\theta + p_2^2)} + E_X. \tag{3.21}$$

Hence, the excitation energy can be derived from the latter equation as:

$$E_X = KE_0 + m_0c^2 + m_1c^2 - \sqrt{m_0^2c^4 + p_2^2} - \sqrt{m_1^2c^4 + (p_0^2 - 2p_0p_2cos\theta + p_2^2)} \tag{3.22}$$

In this last expression, only p_2 is unknown on the right hand side. It represents the momentum of the ejectile which can be expressed as a function of the focal plane position, X_{FP}. In order to achieve this, for each of the known excited states of the calibration target the corresponding kinetic energy of the ejectile is derived using a standard two-body relativistic kinematics code [Dro08]. The code requires as input the type of reaction (e.g. ^{24}Mg(p,p$'$)), the energy of the incident projectile, the number of excited states with their corresponding energy values and the scattering angle. The code then calculates the kinetic energy of the scattered ejectile for each of those levels. From the obtained values of kinetic energies, the corresponding momenta can be derived.

Using the expression of total energy,

$$E_0 = KE_0 + m_0 = \sqrt{m_0^2 + p_0^2}, \tag{3.23}$$

the momentum can then be derived as:

$$p_0 = \sqrt{(KE_0 + m_0)^2 - m_0^2}. \tag{3.24}$$

It has been established from the study of the ion-optical properties of the K600 magnetic spectrometer that the relationship between measured momentum of the scattered particles and their corresponding position in the focal plane is best represented with a second order polynomial regression [Nev01] as:

$$p_2 = \alpha X_{FP}^2 + \beta X_{FP} + \gamma, \tag{3.25}$$

where α, β and γ are the fit parameters to be determined. The obtained parameters for the seven prominent states of ^{24}Mg are as listed in Table 3.8.

Table 3.8: Momentum fit calibration parameters derived for each of the weekends of experiments

Weekend of experiment	α	β	γ
Weekend 1	-5.432827 $\times 10^{-6}$	0.0617	587.474
Weekend 4	-9.096155 $\times 10^{-6}$	0.0667	583.651
Weekend 5	-8.486751 $\times 10^{-6}$	0.0659	581.691

All physical constant values used for the calibration procedures are as provided by the most recent update of the National Institute of Standard and Technology (NIST), Physical Reference Data [Moh12]. The calibration curves obtained using both the direct fit and the momentum fit are both illustrated in Fig 3.24 for each of the weekends of experiments.

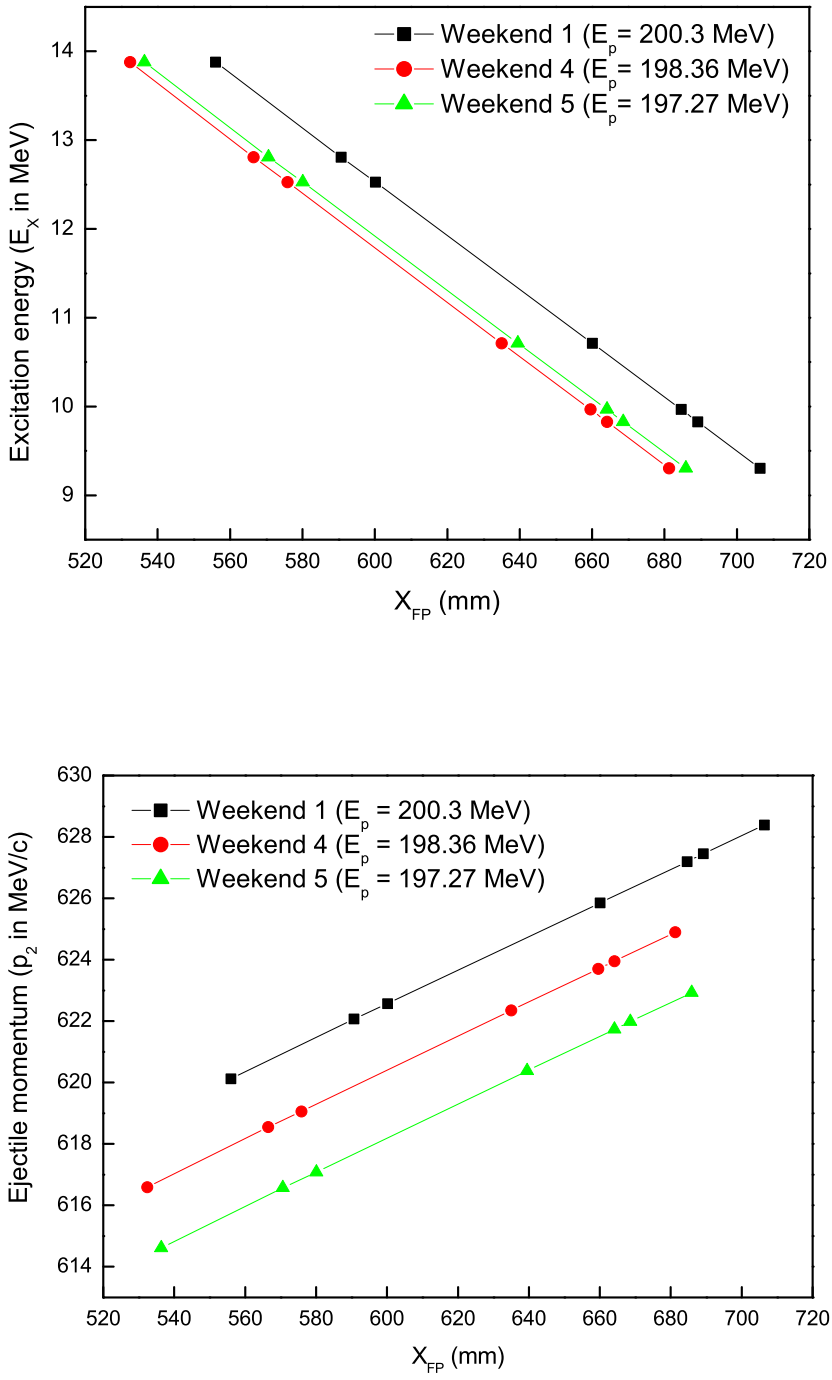

Figure 3.24: Excitation energy calibration curves for the 3 weeks of experiment characterised by slightly varying field values. *Top panel*: the calibration curve was generated using the direct-fit approach using the parameters in Table 3.7. *Bottom panel*: proper excitation energy calibration using the parameters in Table 3.8.

Two different sources were consulted for providing reference values of energy levels in ^{24}Mg. Those are the Table Of Isotopes (TOI) CD ROM edition [Fir95] and the database of the National Nuclear Data Center (NNDC) Brookhaven National Laboratory (BNL) [Bro14]. Although both sources provide values matching to within < 1 keV, NNDC values were prefered since they are up-to-date. After calibration using both methods described above, it has been observed that both techniques reproduced the excitation energy of ^{24}Mg quite well to within < 10 keV for 6 out of the 7 states. For the sixth state the difference between the measured value and the reference value was < 15 keV in both cases. The residual plot of the measured excitation energy with respect to the reference values provided by [Bro14] for all three weekends is illustrated in Fig. 3.25. The associated error bars are the estimated standard deviation of the mean [Bev03].

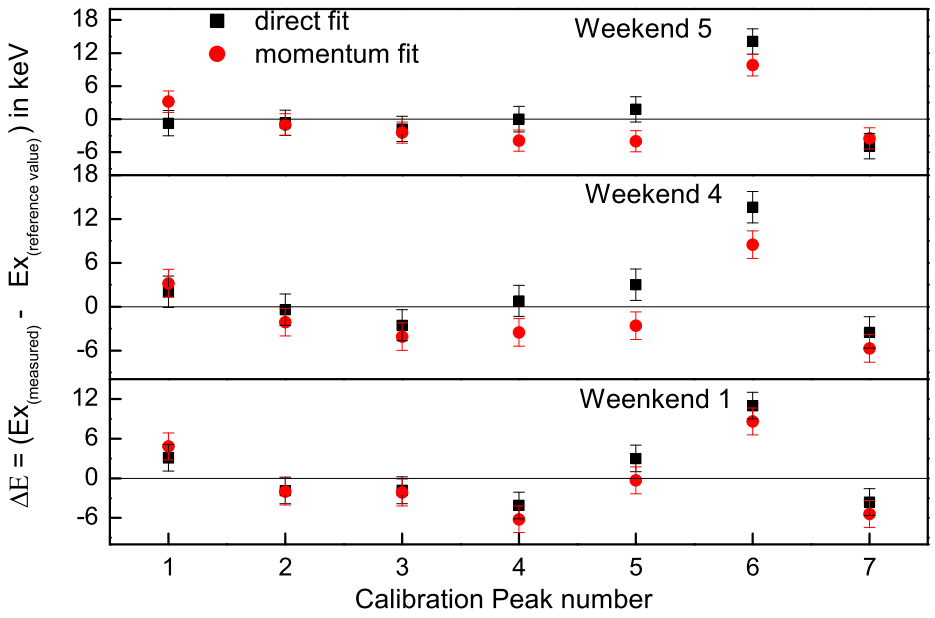

Figure 3.25: The residual plot of the measured excitation energy using both methods with respect to the reference values provided by the NNDC [Bro14] for all three weekends of experiments. Error bars are estimated as the standard deviation of the mean. There is a good agreement between both techniques. It can also be observed that the residual follows no specific pattern.

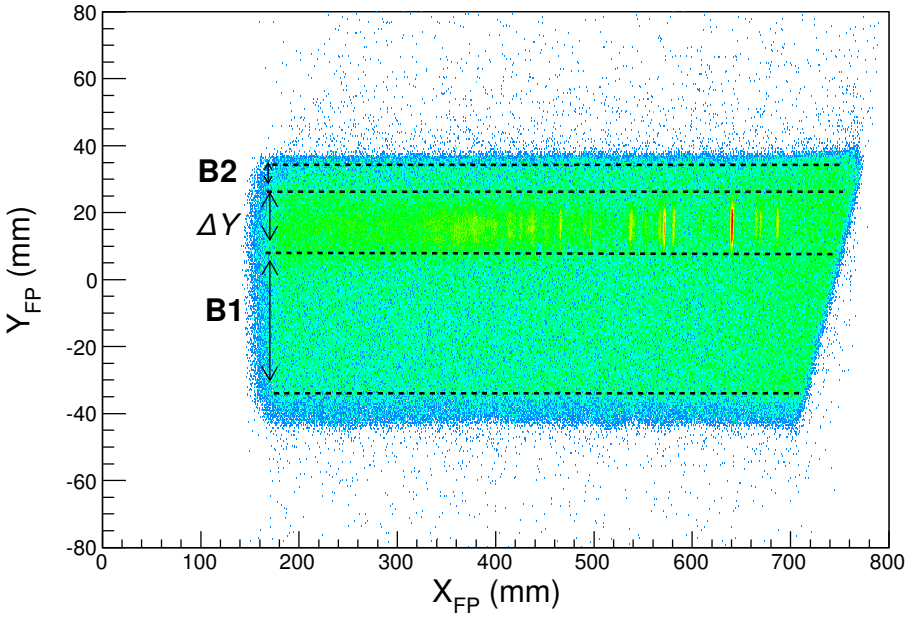

Figure 3.26: A histogram plot Y_{FP} as a function of X_{FP} showing background contributions in $B1$ and $B2$. The middle locus (ΔY) contains the good events and both background contribution ($B1$ + $B2$).

3.6.5 Background subtraction

After a successful selection of the physics events, an optimum background subtraction process is also crucial. Background subtraction is quite a tasking exercise in zero-degree experiments. After applying the software gates, the background contribution from the beam halo is mostly removed. However, background due to halo and other physics events are not completely removed as the reaction products of such events have a time of flight similar to that of the scattered protons of interest. This background contribution can easily be seen and then subtracted from the data by plotting the vertical position of the scattered particles as a function of their horizontal position in the focal plane. This is possible because the data was acquired in focus mode. As seen in Fig. 3.26, the background contributions are represented as $B1$ (below) and $B2$ (above) the central locus, ΔY. The position spectra of $B1$ and $B2$ were normalised to half of ΔY.

The central locus represents the scattered protons of interest together with both

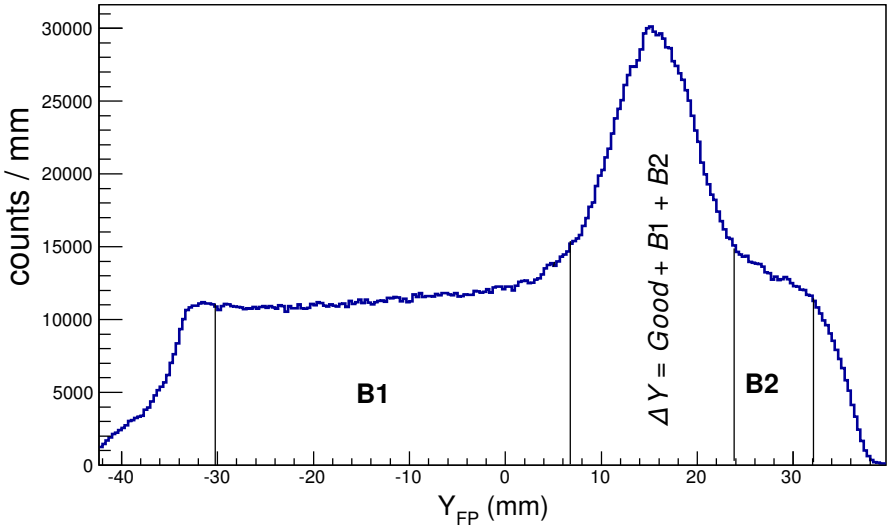

Figure 3.27: A plot of Y_{FP} showing background contributions in $B1$ and $B2$. The middle locus (ΔY) contains the good events and a background contribution.

background contributions. A histogram plot of $Y1$, as seen in Fig. 3.27 shows the two background contributions $B1$ (left) and $B2$ (right) and a cone-shape spectrum in the middle representing ΔY.

An energy spectrum of ^{24}Mg(p,p$'$) acquired at $E_p = 200$ MeV and $\theta_{K600} = 0^\circ$ with both background components illustrating the background subtraction procedure is shown in Fig. 3.28. The same spectrum after the background subtraction procedure is illustrated in Fig. 3.29.

3.7 Extraction of experimental cross-section

The cross-section is a fundamental quantity derived from extracted data in nuclear physics experiments. Its effective extraction from the obtained experimental data requires a good account of some properties of the detectors which include the deadtime and the efficiency.

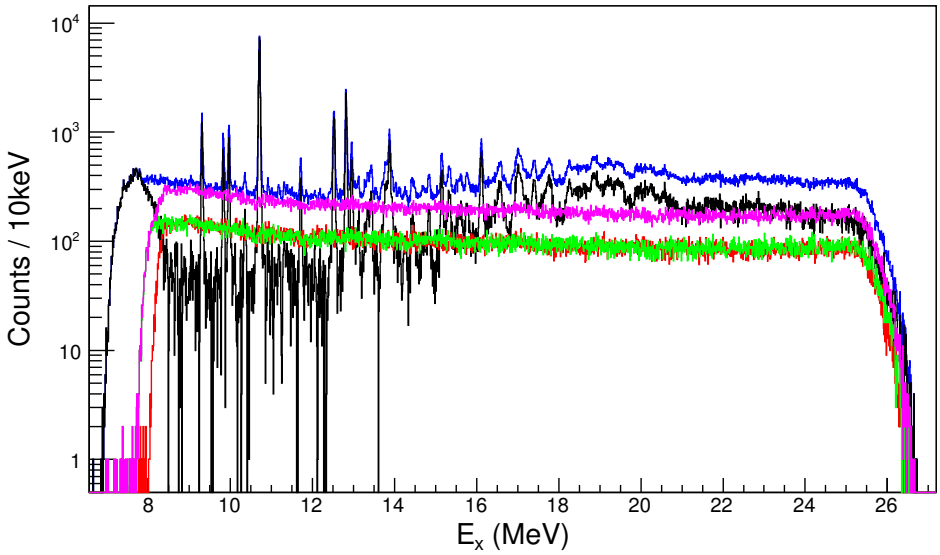

Figure 3.28: Background subtraction procedure illustrated with a ^{24}Mg excitation energy spectrum obtained from the the ^{24}Mg(p,p$'$) at $E_p = 200$ MeV and $\theta_{K600} = 0^o$. The blue spectrum is the spectrum before the background subtraction. The green and red spectra are the first ($B1$) and second ($B2$) components of the background contribution. The pink is the sum of both background contributions and the black is the background subtracted spectrum.

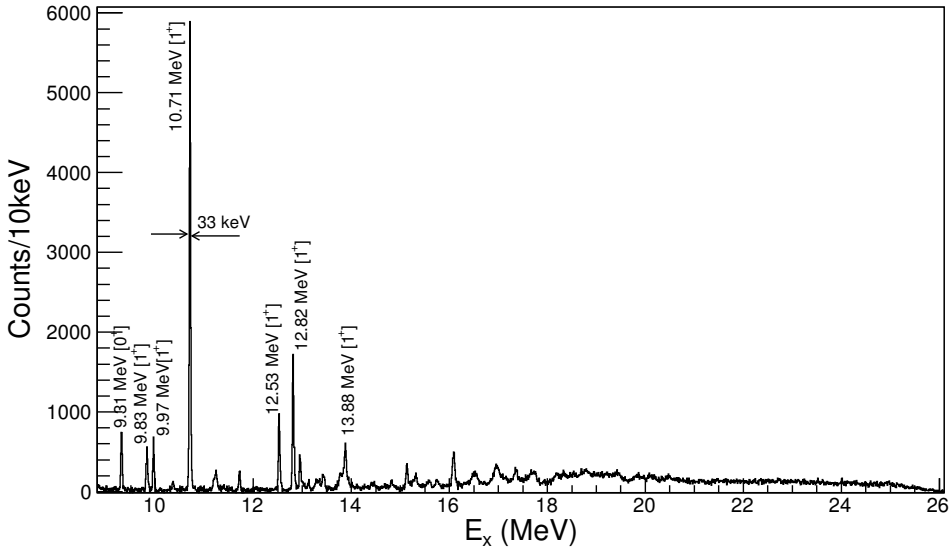

Figure 3.29: Excitation energy spectra of ^{24}Mg acquired from the ^{24}Mg(p,p$'$) reaction at $E_{\mathrm{p}} = 200$ MeV and $\theta_{\mathrm{K600}} = 0^{o}$ after background subtraction. The energy resolution (FWHM) is 33 keV. The identified states are those used for the energy calibration.

3.7.1 Deadtime factor and efficiency of the detectors

3.7.1.1 Deadtime correction

The dead-time, τ_D, of a detector system is the short time interval spanning between two consecutive recordings of events for which the detector or electronics does not detect any particle. It varies from as low as 1 ns for Cherenkov counters to as high as 1 ms in Geiger-Muller tubes [Gru08]. If C is the event rate, the detector will be insensitive to $C\tau_D$ events per unit time such that the true count rate becomes C' given as [Gru08]:

$$C' = \frac{C}{1 - C\tau_D}. \tag{3.26}$$

For the K600 magnetic spectrometer, the dead-time per event is overshadowed by the 6 μs derived from the conversion time of the QDC [Nev14]. For a detected count rate of 1000 Hz the actual count rate, C$'$, would be 1006 Hz.

For our measurements, the dead-time correction factor is defined as:

$$D = \frac{CII}{CIU}, \tag{3.27}$$

where CII is the current integrator inhibited and CIU is the current integrator uninhibited.

The inhibited scalar was vetoed by the QDC busy signal. A typical value of D in our measurement was in the range of 0.99.

3.7.1.2 Efficiency

We assume 100 % efficiency for the paddles. We then have to calculate the efficiency of the VDC's. The efficiency of a detector is the probability that a particle passing through it is detected. The events for which the VDC efficiencies are computed are defined by the PID locus of the paddle versus TOF as described in section 3.6.1. The following define specific types of events in the VDC:

N_{max}: all events for which more than 8 wires are hit;

N_{min}: all events for which less than 3 wires are hit;

N_{out}: all events for which the drift time falls outside the valid range;

N_{no}: all events for which no 3-wire group could be found in otherwise valid event; and,

All: is the total number of PID selected events.

The total number of valid events denoted $True$ is defined as:

$$True = All - (N_{max} - N_{min} - N_{out} - N_{no}). \tag{3.28}$$

For the 4 wire-planes in the drift chambers, a 100% geometric efficiency is assumed. Therefore, the efficiency of the ith wire plane is defined as:

$$\epsilon_i = \frac{True}{All}, \tag{3.29}$$

If all 4 wire-planes, $U1$, $X1$, $U2$ and $X2$, are used in the data analysis, the overall efficiency is given as:

$$\epsilon_{all} = \epsilon_{U1}.\epsilon_{X1}.\epsilon_{U2}.\epsilon_{X2}. \tag{3.30}$$

Since several runs are added up to arrive at the final spectrum, the efficiency in this case is the weighted average efficiency of all the runs in all wire-planes. A typical overall efficiency in the range of 77 % was achieved in our measurements.

After interacting with the target, the protons are scattered into the spectrometer at some radial angle, θ, and azimuthal angle, ϕ, within a solid angle, Ω. The number of particles scattered into the direction (θ, ϕ) per unit time per unit solid angle divided by the flux of the incident particles is the differential cross-section. The experimental double differential cross-section is given as:

$$\frac{d^2\sigma}{d\Omega dE} = \frac{N.10^{27}}{\epsilon.\eta.\Omega.\Delta E.D.\rho.I_f} \quad \text{(mb sr}^{-1}\text{ MeV}^{-1}\text{)}, \tag{3.31}$$

where the various parameters are defined as below:

- N is the corrected count from the background subtracted energy spectrum;

- ϵ is the weighted average efficiency of all wire planes of the drift chambers used in the experiment;

- η is the isotopic enrichment factor of the target as listed in Table 3.4 divided by 100;

- ρ is the area density of target atoms (in atoms/cm^2) and given as:

$$\rho = \frac{t_{\mathrm{A}}.N_{\mathrm{A}}}{A}, \tag{3.32}$$

where t_{A} is the areal thickness of the target (in g/cm^2), N_{A} is the Avogradro's constant and A is the atomic mass number of the target (in g/mol);

- Ω is the solid angle and has a value of 3.48 msr for the collimator used;

- ΔE is the energy bin size (in MeV) ; and,

- I_{f} is the total number of incident protons defined as:

$$I_f = \frac{CI.R.10^{-12}}{e}, \tag{3.33}$$

where:

- CI is the scalar read-out of the current integrator;

- R is the selected current integrator range (in nA) which represents 1000 counts/s for a full range current; and,

- e is the elementary charge which has a value of 1.602 176 6208 x 10^{-19} C.

For a zero-degrees measurement as shown in Fig. 3.26, the background subtracted count, N is given in terms of the background terms B_1 and B_2 as:

$$N = A - B_1 - B_2, \tag{3.34}$$

where A is the count in the central Y region. The simplest assumption for total error in this case is:

$$\Delta N^2 = \Delta A^2 + \Delta B_1^2 + \Delta B_2^2, \tag{3.35}$$

assuming zero covariances. For $\Delta A = \Delta B_1 = \Delta B_2$, the statistical error in the double differential cross section can be written as:

$$\Delta\left(\frac{d^2\sigma}{d\Omega dE}\right) = \sqrt{\frac{3}{N}}\frac{d^2\sigma}{d\Omega dE} \tag{3.36}$$

Chapter 4

Results and discussion

In this chapter, the experimental results are presented and discussed. They are compared with theoretical model calculations described in Chapter 2. Section 4.1 is devoted to the analysis of the experimental energy spectra via the extraction of the double differential cross-sections and their conversion into equivalent photo-absorption cross-sections. For the sake of a systematic investigation, ^{40}Ca data acquired under similar experimental conditions, taken from Ref. [Jin14], was included in the present study. Section 4.2 deals with the extraction of the centroid energies and the width of the isovector giant dipole resonance (IVGDR) in the calcium isotopes. In Section 4.3 the electric dipole strength distributions estimated with the various theoretical microscopic models are compared with the experimental spectra while the characteristic energy scales are extracted and discussed in Section 4.4. This chapter ends with the extraction of the $J^{\pi} = 1^{-}$ states level density from the acquired high energy resolution data and the comparison with existing theoretical microscopic and phenomenological models of level density, as presented in Section 4.5.

4.1 Experimental spectra analysis

The experimental excitation energy spectra acquired from the ^{42,44,48}Ca(p,p$'$) reaction measured at proton incident energy of $E_{\mathrm{p}} = 200$ MeV and laboratory angle

of $\theta_{\mathrm{Lab}} = 0^{\circ} \pm 1.91^{\circ}$ are shown in Fig. 4.1. For these energy spectra, the energy resolution of $\Delta E = 33$ keV Full Width Half Maximum (FWHM) was achieved for ^{44}Ca and $\Delta E = 40$ keV was achieved for ^{42,48}Ca using the most prominent peak of the ^{24}Mg calibration target which occurs at 10.712 MeV and corresponds to a 1^{+} state. Fine structure is clearly exhibited in the excitation energy spectra of all three isotopes in the region of the Isovector Giant Dipole Resonance (IVGDR), which lies between 11 - 25 MeV. In the excitation energy region below the IVGDR, some states have successfully been identified as shown in Fig. 4.2. For ^{48}Ca, a total of 6 states were identified as seen in the top panel of Fig. 4.2: two 2^{+} states occurring at 9.295 MeV and 10.73 MeV; two 1^{-} states at 9.545 MeV and 10.13 MeV, and two 1^{+} states occurring at 10.22MeV and 10.33 MeV. The former 1^{+} state is the most prominent peak in the ^{48}Ca(p,p$'$) spectrum and has an energy resolution similar to that of the calibration target ($\sim$ 40 keV). For ^{44}Ca, three 1^{-} states were identified in the low-lying region which occur at 9.317 MeV, 9.665 MeV and 9.814 MeV. In the case of ^{42}Ca, three states were also identified: one 2^{+} state at 9.750 MeV, one 1^{+} state at 11.235 MeV and one 0^{+} state at 11.47 MeV. Besides, there are a number of unidentified states in the ^{42,44}Ca(p,p$'$) spectra. There is the need for identification of these states and establish their multipolarity with subsequent measurements as they might be pygmy dipole resonance states.

A contaminant peak was observed in the ^{44}Ca(p,p$'$) spectrum and is indicated in red (Fig. 4.1). This contaminant peak observed at around 15 MeV was identified as the 1^{+} state of ^{12}C which occurs at 15.11 MeV. The said carbon contamination which is likely to originate from the manufacture of the target was not seen in the ^{42,48}Ca(p,p$'$) spectra which were carbon-free. Since the contamination occurs within the IVGDR excitation energy region where only 1^{-} states are expected to be present, there is a compelling need to remove and replace the contaminant peak with a white spectrum of similar fluctuation as the original spectrum before further analysis is carried out.

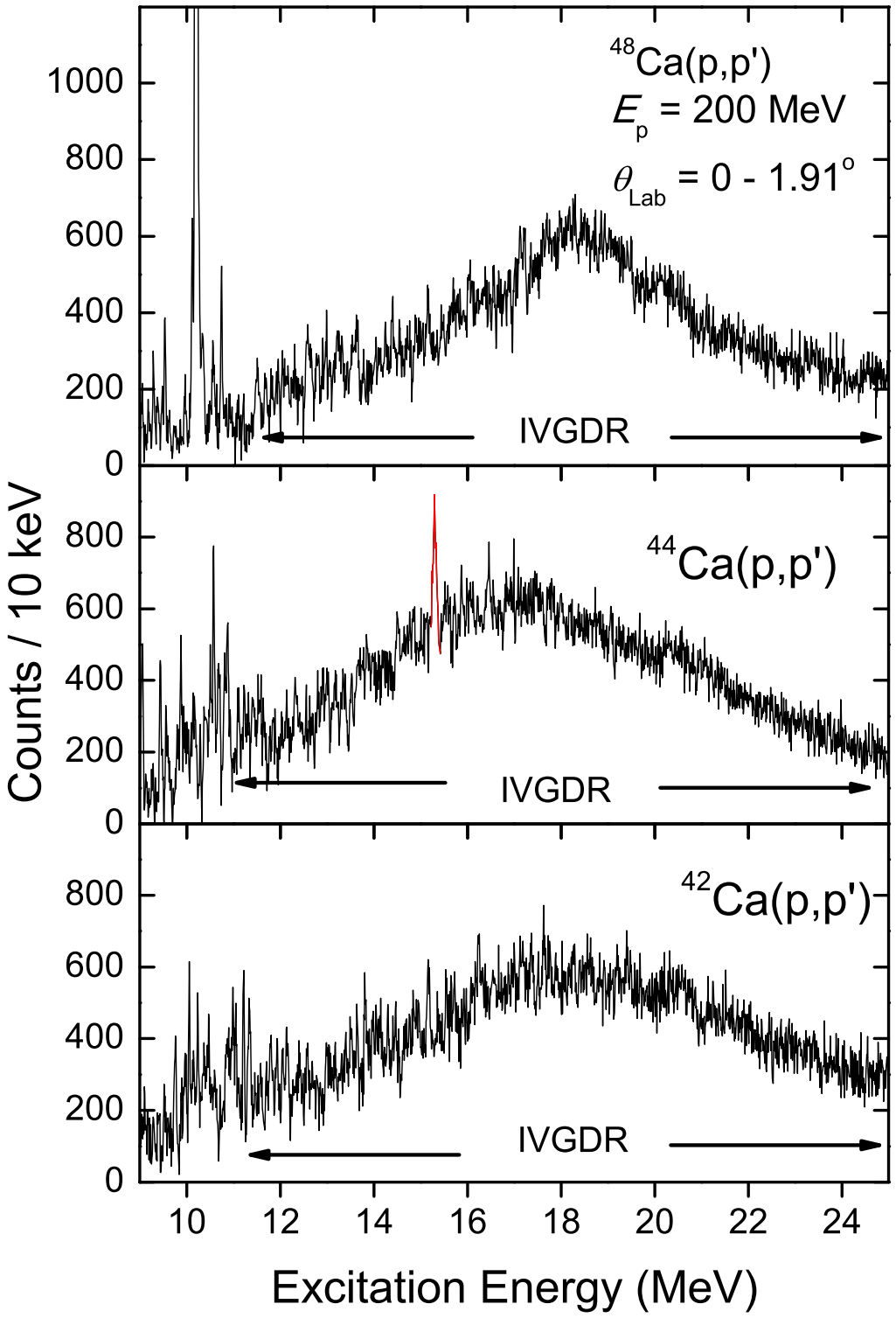

Figure 4.1: Excitation energy spectra from the ^{42,44,48}Ca(p,p′) reaction measured at $E_{\mathrm{p}} = 200$ MeV and $\theta_{\mathrm{Lab}} = 0 \pm 1.91°$. A contaminant peak identified in the ^{44}Ca(p,p′) spectrum is illustrated in red colour as seen in the middle panel.

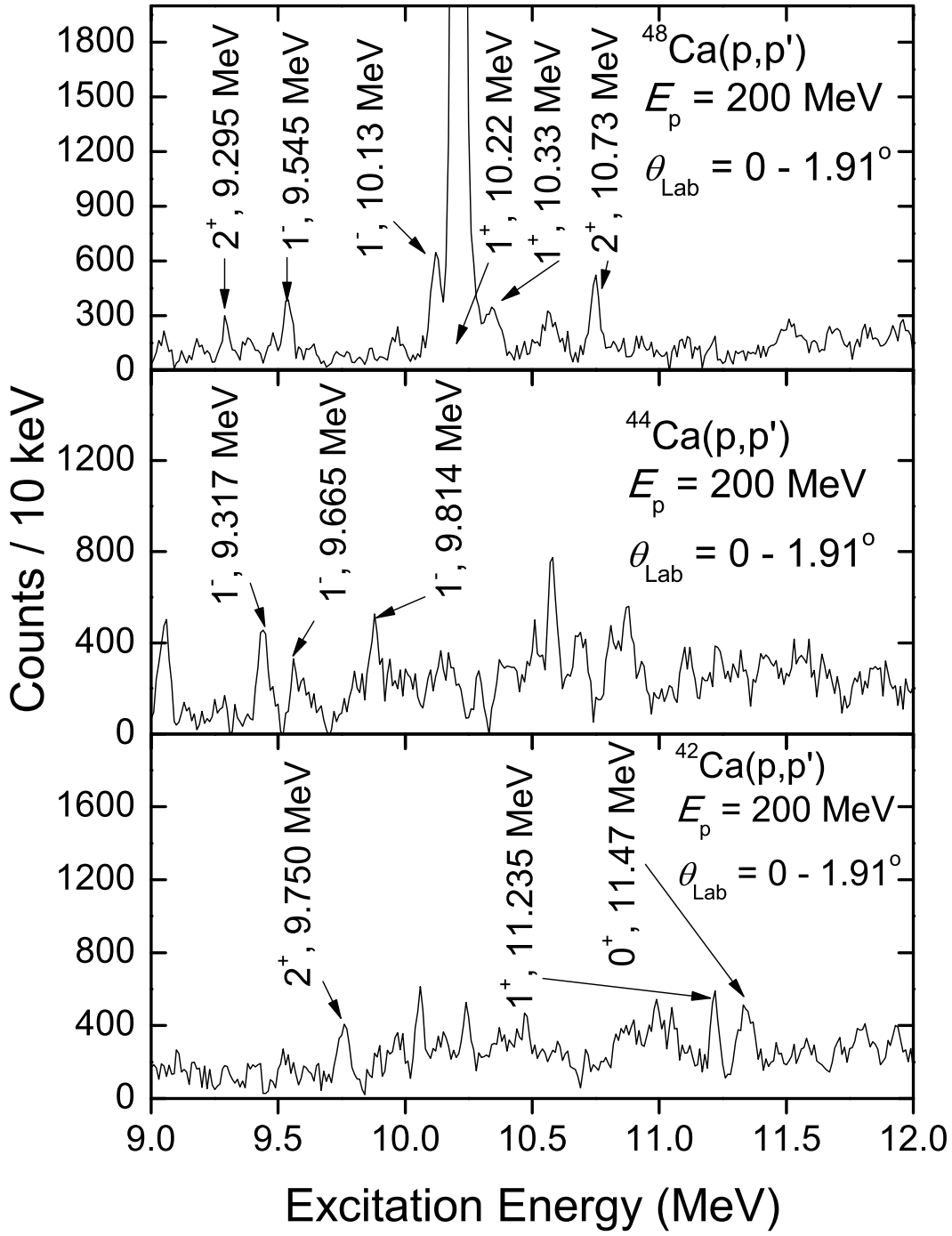

Figure 4.2: Low-lying states identified in the ^{42,44,48}Ca(p,p′) excitation energy spectra acquired at $E_{\mathrm{p}} = 200$ MeV and $\theta_{\mathrm{Lab}} = 0 \pm 1.91°$.

4.1.1 Removal of contaminant peaks

Important information about the decay of GRs can be derived from the fine structure by means of Wavelet analysis. The presence of a contamination signal in the acquired spectra can influence the thereof extracted information. Therefore, the contaminant signal must be removed from the observed fine structure spectrum in the GR region. In signal analysis, the algorithm adopted for the removal of the contamination depends on the field of application and the method used.

In order to remove a contaminant signal from a GR spectrum, the algorithm to adopt can be summarised as follows:

- First identify the contaminant peak. Select a region R comprising the contaminant peak, over which the white spectrum is computed.
- Fit the experimental data (original spectrum) with a Lorentzian or a Gaussian function, by way of example see 4.2 (Fig. 4.9 or Fig. 4.10). The latter fit is then made to pass through the points to be replaced with the white spectrum. In order to achieve this, a shift of the Lorentzian or Gaussian fit towards higher or lower excitation energy depending on the situation, may be necessary.
- The fit function and the original spectrum must have the same energy bin size.
- Subtract every y value (counts) of the Lorentzian or Gaussian fit from the corresponding y value (counts) of the original spectrum over R. A set of positive and negative numbers are then obtained whose total number N is equal to the number of data points present in the region R of the original experimental spectrum.
- The mean, $\overline{y}$, and standard deviation, σ of the N positive and negative

numbers are then computed as:

$$\overline{y} = \frac{1}{N}\sum_{i}^{N}\Delta y_i \qquad \text{and} \qquad \sigma = \sqrt{\frac{1}{N}\sum_{i}^{N}(y_i - \overline{y_i})}. \tag{4.1}$$

- Then, N random deviates of mean $\overline{y}$ and standard deviation σ are generated from a Gaussian distribution using the Box-Muller transform [Box58].

- The obtained random normal deviates are then added to the Lorentzian or Gaussian fit to form the white spectrum. The latter spectrum is then used to replace the contaminated region in the original experimental spectrum. The random normal deviates may be generated a number of times and tried on the spectrum until a set that best matches the original spectrum is obtained.

The process of generating random normal deviates can easily be achieved through an online platform [Haa10]. It requires as inputs the computed mean and standard deviation described above. For the ^{44}Ca spectrum, a total of 101 points were selected as region R corresponding to the excitation energy range of 14.8 - 15.8 MeV, over which the white spectrum was generated. However, only the contaminated region corresponding to the excitation energy range of 15.20 - 15.42 MeV was replaced with the white spectrum as illustrated in Fig. 4.3. A mathematical description of the Box-Muller method is given in Appendix A.

4.1.2 Cross-section evaluation

Double differential cross-sections were evaluated from the excitation energy spectra of ^{42}Ca, ^{44}Ca and ^{48}Ca using Eq. (3.31) while that of ^{40}Ca was taken from [Jin14] in which case the energy resolution is $\Delta E = 47$ keV. The obtained double differential cross-section spectra for all four calcium isotopes are shown in Fig. 4.4.

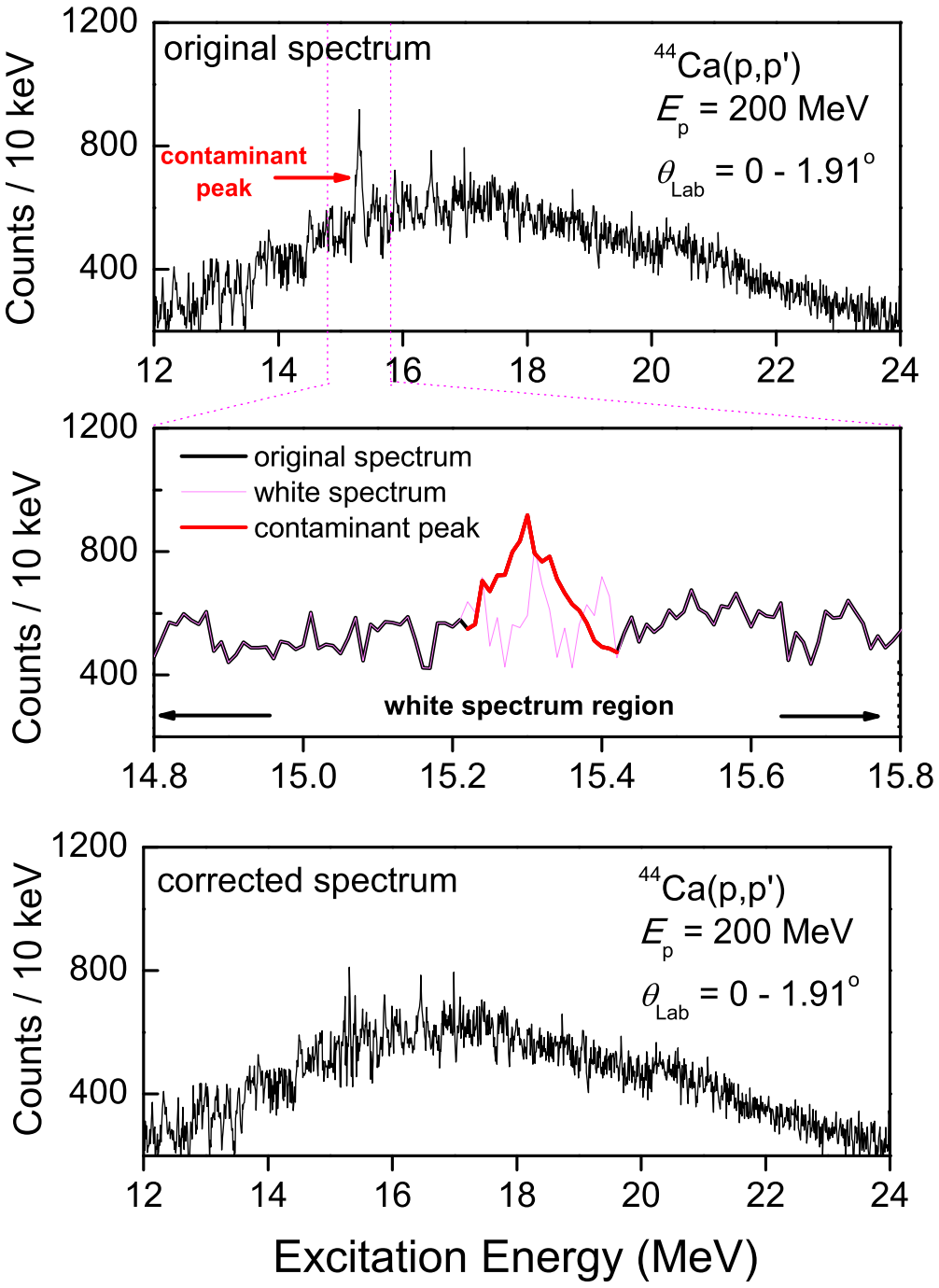

Figure 4.3: An illustration of the removal process of the contamination from the ^{44}Ca(p,p′) spectrum shown in Fig. 4.1. From top to bottom: the original spectrum; the selected region for white spectrum region of similar fluctuation as the original spectrum, and the corrected spectrum. Only the region of 15.20 - 15.42 MeV is replaced with the generated white spectrum.

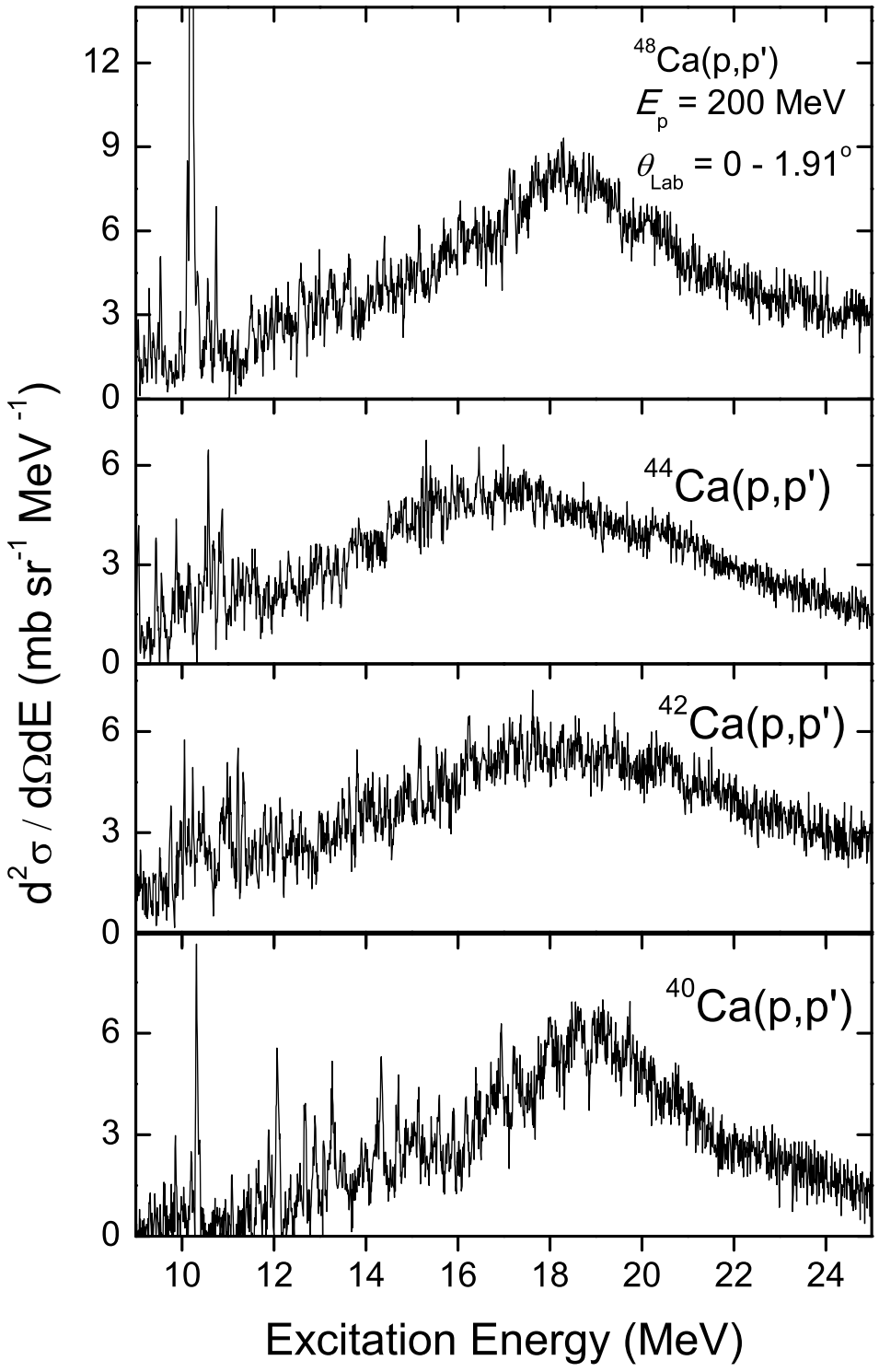

Figure 4.4: Double differential cross-section of ^{48}Ca, ^{44}Ca, ^{42}Ca and ^{40}Ca extracted from the ^{40,42,44,48}Ca(p,p′) reaction at $E_{\mathrm{p}} = 200$ MeV and $\theta_{\mathrm{Lab}} = 0 \pm 1.91°$.

4.1.2.1 Subtraction of the nuclear background in the IVGDR energy region

As discussed in Section 2.3 and illustrated with the DWBA calculations in Fig. 2.5, the excitation of the $E1$ mode from the proton inelastic scattering reaction at and near zero degree is predominantly due to the Coulomb interaction. The reaction also yields some nuclear background which results from the excitation of other giant resonance modes and quasi-free scatterings. As observed from previous studies on ^{208}Pb(p,p$'$) [Jin14, Pol11], the giant resonance modes which are expected to contribute to the nuclear background are the IsoScalar Giant Quadrupole Resonance (ISGQR) whose centroid is located around $63A^{-1/3}$ MeV and has a width of $\Gamma \approx 16A^{-1/3}$, and the IsoVector Giant Quadrupole Resonance (IVGQR) whose centroid is located around $130A^{-1/3}$ MeV with a width of ~ 15 MeV in the case of ^{40}Ca [Har02].

In order to subtract from the experimental spectra the nuclear background contribution, the following assumptions were made:

(i) The nuclear background is dominated by quasi-free scattering which can be estimated with the Discrete Wavelet Transform (DWT), the properties of which are described in Section 2.5.1.2. Here, the Biorthogonal 6.8 (Bio6.8) was used as Wavelet basis owing to its significant number of vanishing moments. This is an established method for removing non-resonant background from experimental spectra and has successfully been applied in experimental nuclear level density extraction [Pol14, Usm11b]. A more detailed description of this procedure is given in Section 4.5.1.

(ii) The ISGQR whose centroid occurs around $E_{\mathrm{x}} = 17$ MeV across the calcium isotope chain has a negligible contribution to the nuclear background as compared to the quasi-free scatterings contribution.

(iii) The IVGQR whose centroid occurs outside the IVGDR region ($E_{\mathrm{x}} \sim 37$ MeV across the calcium isotope chain) has no significant contribution to

the nuclear background unlike in the case of ^{208}Pb.

The experimental ^{40,42,44,48}Ca(p,p$'$) double differential cross-section spectra together with the DWT background and the background subtracted spectra are illustrated in Figs. 4.5 and 4.6 for 10 keV bin and larger energy bin, respectively. As seen in these figures, the shape of the DWT background is internally consistent across the calcium isotope chain. This procedure is entirely consistent with the shape and strength of the calculated quasi-free scattering cross-section for ^{48}Ca(p,p$'$) at $E_{\mathrm{x}} = 295$ MeV in Ref. [Bir16]. It can also be noted that the ratio of the cross-section with the calculated background at the centroid of the IVGDR is smaller in the cases of the doubly-magic nuclei ^{40,48}Ca being more tightly bound with similar widths as against ^{42,44}Ca which are broader being between the two extremes.

4.1.3 Equivalent photo-absorption cross-section

The background subtracted double-differential cross-sections computed from the (p,p$'$) spectra (blue histogram of Fig.4.6) can be converted into equivalent photo-absorption cross-sections (σ_{γ}^{E1}) using the following expression [Ber93a]:

$$\frac{d^2\sigma}{d\Omega dE} = \frac{1}{E}\frac{dN_{E1}}{d\Omega}\sigma_{\gamma}^{E1}, \tag{4.2}$$

where $\frac{1}{E}\frac{dN_{E1}}{d\Omega}$ is the differential virtual photon number per unit energy.

In the present work, the virtual photon number was computed using the eikonal approximation and a FORTRAN code developed by C. Bertulani [Ber14]. The code requires as input the atomic numbers of the projectile and the target, their respective mass numbers, the incident projectile energy, the scattering angle and the excitation energy range.

A plot of the virtual photon number, n_{E1} which is the integral of $\frac{1}{E}\frac{dN_{E1}}{d\Omega}$ over E, as a function of the excitation energy, for all four isotopes of calcium, is given in

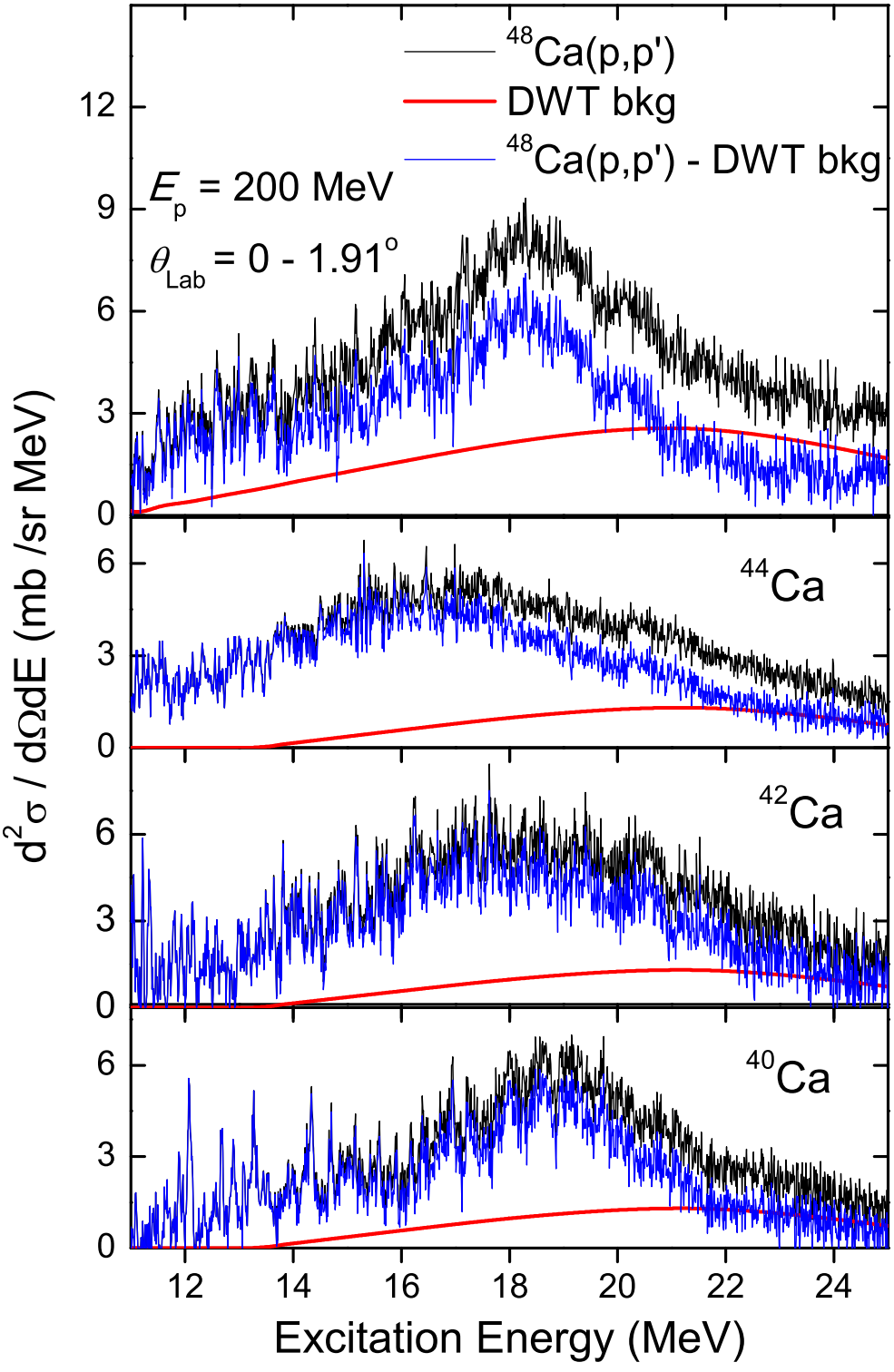

Figure 4.5: Double differential cross-section of ^{40,42,44,48}Ca(p,p′) acquired at E_p = 200 MeV and $\theta_{Lab} = 0 \pm 1.91°$ (black histogram); theDiscrete Wavelet Transform background (DWT bkg) (red line) and the background subtracted double differential cross-section (blue histogram), all in 10 keV bin.

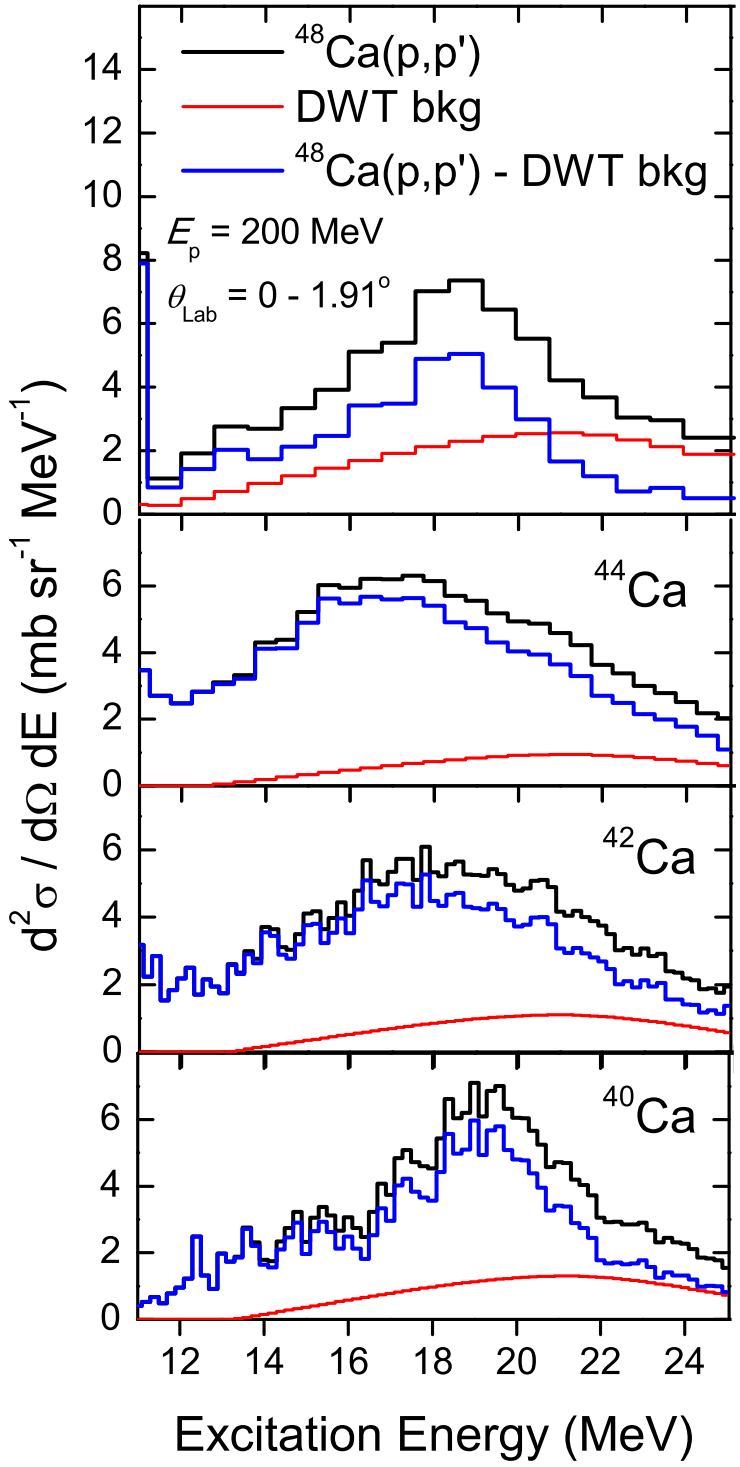

Figure 4.6: Same as Fig.4.5 except for the energy bin size. Here, the ^{40,42}Ca(p,p′) histograms are presented in 200 keV bin while ^{44}Ca(p,p′) and ^{48}Ca(p,p′) histograms are in 500 keV and 796 keV, respectively, for comparison later with measured photo-absorption cross-sections.

Fig. 4.7. As seen in the figure, there are no significant differences in the virtual photon numbers. The slight differences in the virtual photon spectra are due to differences in the impact parameters which are function of the nuclear radii. The equivalent photo-absorption cross-section can then be derived from the double differential cross-section by substituting the obtained virtual photon number in Eq. (4.2). The normalisation factors of 0.31, 0.23, 0.29 and 0.32 were applied to the obtained equivalent photo-absorption cross-sections for ^{40}Ca, ^{42}Ca, ^{44}Ca and ^{48}Ca, respectively. Although the obtained factor of 0.23 in the case of ^{42}Ca is slightly lower than those of the other isotopes, it yields a good agreement with the photo-absorption cross-section data.

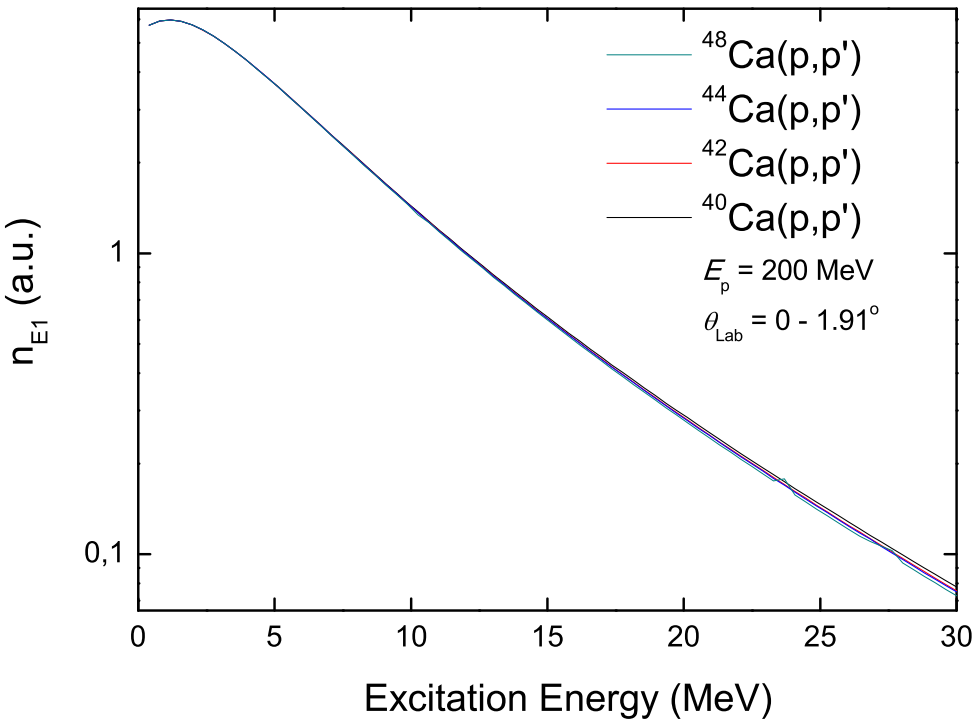

Figure 4.7: Virtual photon numbers of ^{40}Ca, ^{42}Ca, ^{44}Ca and ^{48}Ca as a function of the excitation energy for $E_{\mathrm{p}} = 200$ MeV and $\theta_{\mathrm{Lab}} = 0 \pm 1.91°$.

A comparative plot of the equivalent photo-absorption cross-section derived in the present study and the photo-absorption data for ^{40}Ca of Ref. [Ahr75], ^{42,44}Ca

of Ref. [Ero03] and ^{48}Ca of Ref. [Str00] are shown in Fig. 4.8.

As seen in Fig. 4.8 there is a good agreement between the equivalent photo-absorption cross-section derived in the present study and the available photo-absorption data. It can also be clearly observed that the IVGDR exhibits an overall compact shape for ^{40,48}Ca and a broader shape for ^{42,44}Ca. Also, the resonance shape in ^{44}Ca tends to split into 2 distinct components whose centroid energies are around 17 MeV and 20 MeV.

4.2 Extraction of the IVGDR centroids and widths

In this section, the properties of the IVGDR have been extracted from the experimentally obtained spectra and compared to the predicted values. So far, the known properties of the IVGDR were derived from photo-nuclear reaction measurements which selectively excite the electric dipole resonance across the periodic table. The (p,p$'_{\gamma-\mathrm{corr}}$) spectra were fitted with a Lorentzian function and also with a Gaussian function in order to extract the centroids and widths of the IVGDR of the calcium isotopes.

The obtained values of widths and centroids are compared with the theoretically predicted values based on the macroscopic model in which each of these parameters is expressed as a function of the atomic mass number. It is important to point out that the selected excitation energy range influences significantly the fit parameters derived. In this case, the selection of the excitation energy range was first based on the region in which the (p,p$'_{\gamma-\mathrm{corr}}$) spectra all maintain Lorentzian or Gaussian shapes. The excitation energy range of 15 - 23 MeV was selected for all four spectra. The fitting was done with the computer package Origin 6.1. The Lorentzian fits of the spectra are shown in Fig. 4.9 while the Gaussian fits of the same spectra are shown in Fig. 4.10.

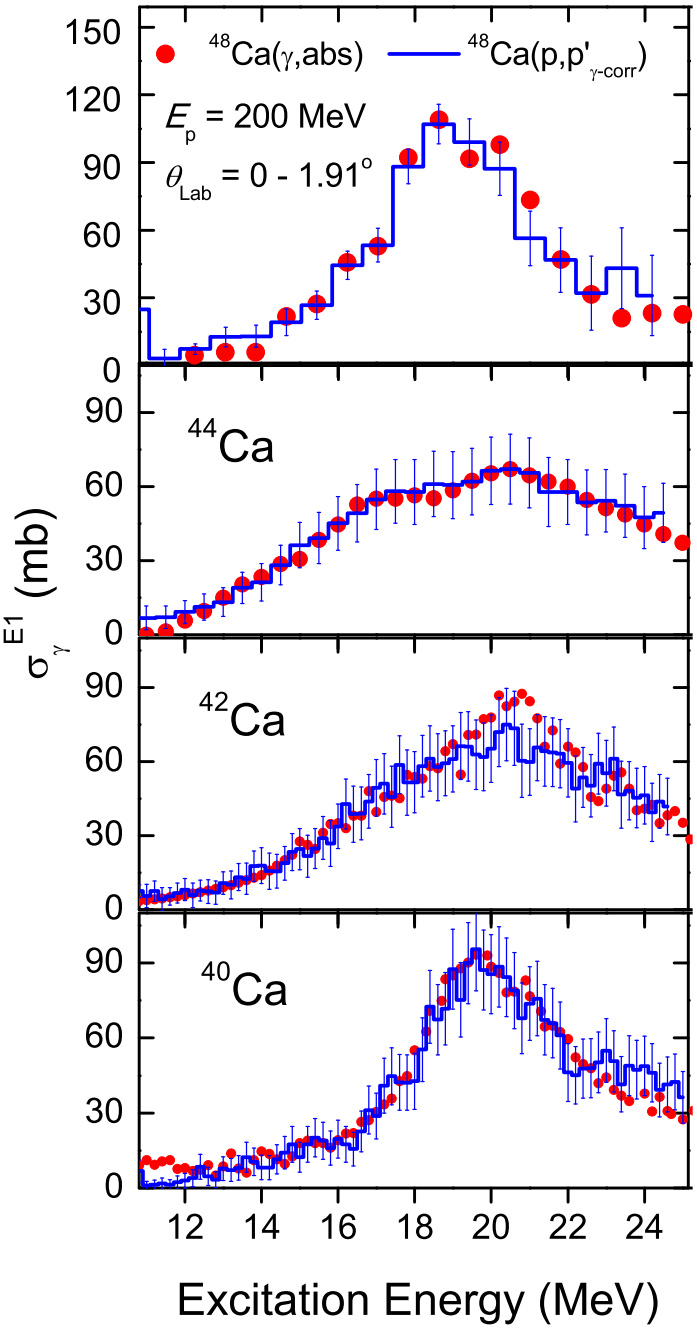

Figure 4.8: Comparative plot of the equivalent photo-absorption cross-sections derived from the ^{40,42,44,48}Ca(p,p′) double differential cross-section (blue histogram of Fig.4.6) and the photo-absorption cross-section data (red circles) of Ref. [Ahr75] (^{40}Ca), Ref. [Ero03](^{42,44}Ca) and Ref. [Str00] (^{48}Ca). The normalisation factors of 0.31, 0.23, 0.29 and 0.32 were applied to ^{40,42,44,48}Ca(p,p′$_{\gamma-\text{corr}}$), respectively. The data in red circle are presented in 200 keV for ^{40,42}Ca, 500 keV for ^{44}Ca and 796 keV bin for ^{48}Ca.

Table 4.1: Extracted values of widths (W) and centroids (C) (in MeV) of the IVGDR using Lorentzian fits (W_L, C_L) and Gaussian fits (W_G, C_G) are compared to the theoretically predicted values (W_T, C_T) for the four isotopes of calcium. W_L values are reported for ^{40,48}Ca and W_G are reported for ^{42,44}Ca

Ca-isotope	W	W_T	C_L	C_G	C_T
^{48}Ca	5.80 ± 0.37	6.39	19.24 ± 0.03	19.24 ± 0.03	19.39
^{44}Ca	8.69 ± 1.95	6.59	19.67 ± 0.05	19.64 ± 0.05	19.80
^{42}Ca	7.86 ± 1.09	6.69	20.11 ± 0.05	20.10 ± 0.05	20.02
^{40}Ca	5.22 ± 0.27	6.81	19.58 ± 0.03	19.58 ± 0.03	20.26

The obtained centroid energies and widths are summarised in Table 4.1 together with the theoretically predicted values using Eqs. (2.4) or (2.5) for the centroids and (2.7) for the widths. The reported values of widths are those obtained from either the Lorentzian fit (^{40,48}Ca) or the Gaussian fit (^{40,48}Ca) as they were in better agreement with the theoretically predicted values.

It can be observed from the values listed in Table 4.1 that the centroid energies obtained from both Lorentzian and Gaussian fits agree well with the theoretically predicted values. The extracted width values of the IVGDR are also in very good agreement with the theoretical values within limits of error bars.

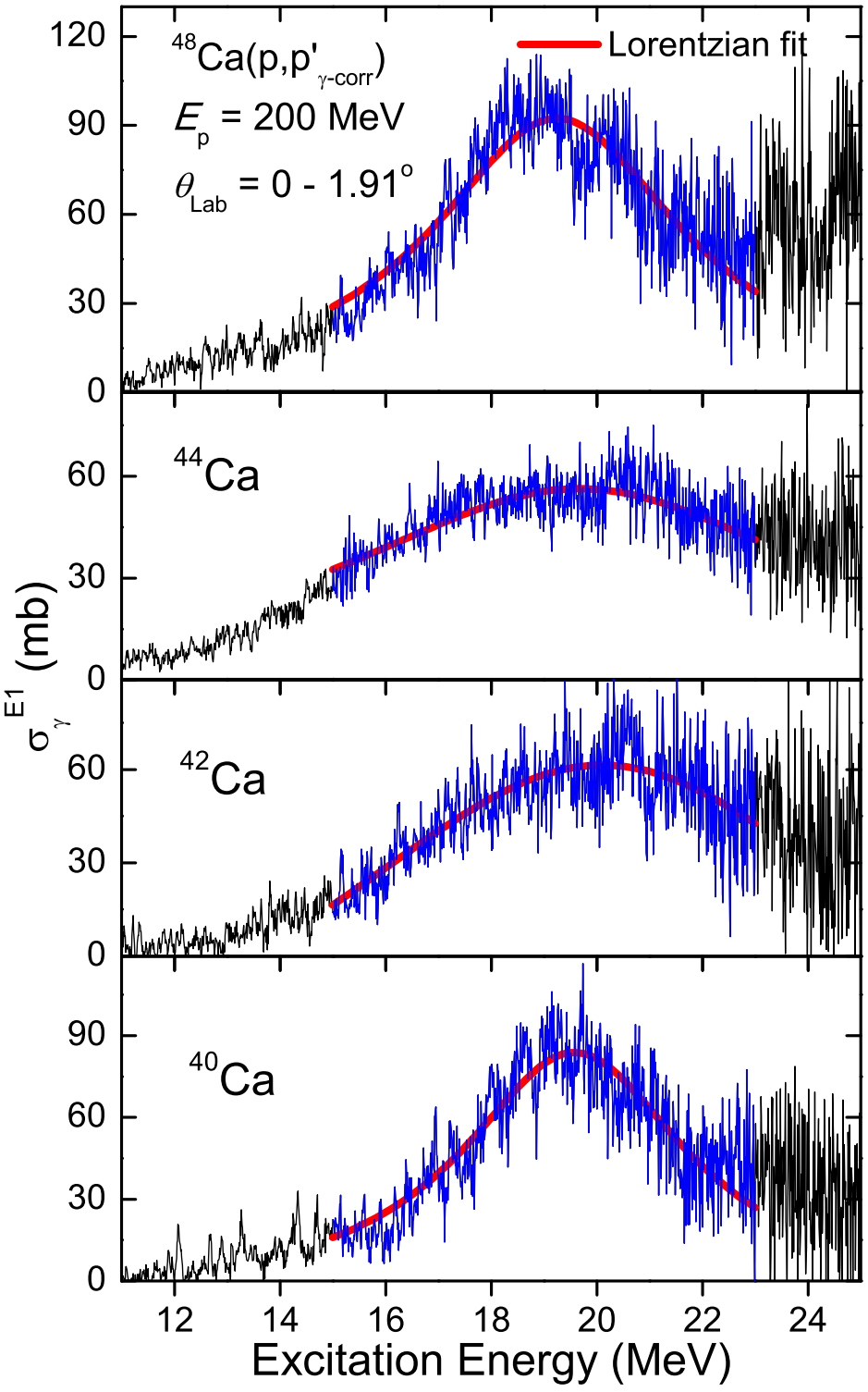

Figure 4.9: ^{40,42,44,48}Ca(p,p$'_{\gamma-\mathrm{corr}}$) spectra fit with a Lorentzian function. The excitation energy range of 15 - 23 MeV selected for the fit is indicated in blue (spectrum) while the fitting Lorentzian curve is indicated in red line.

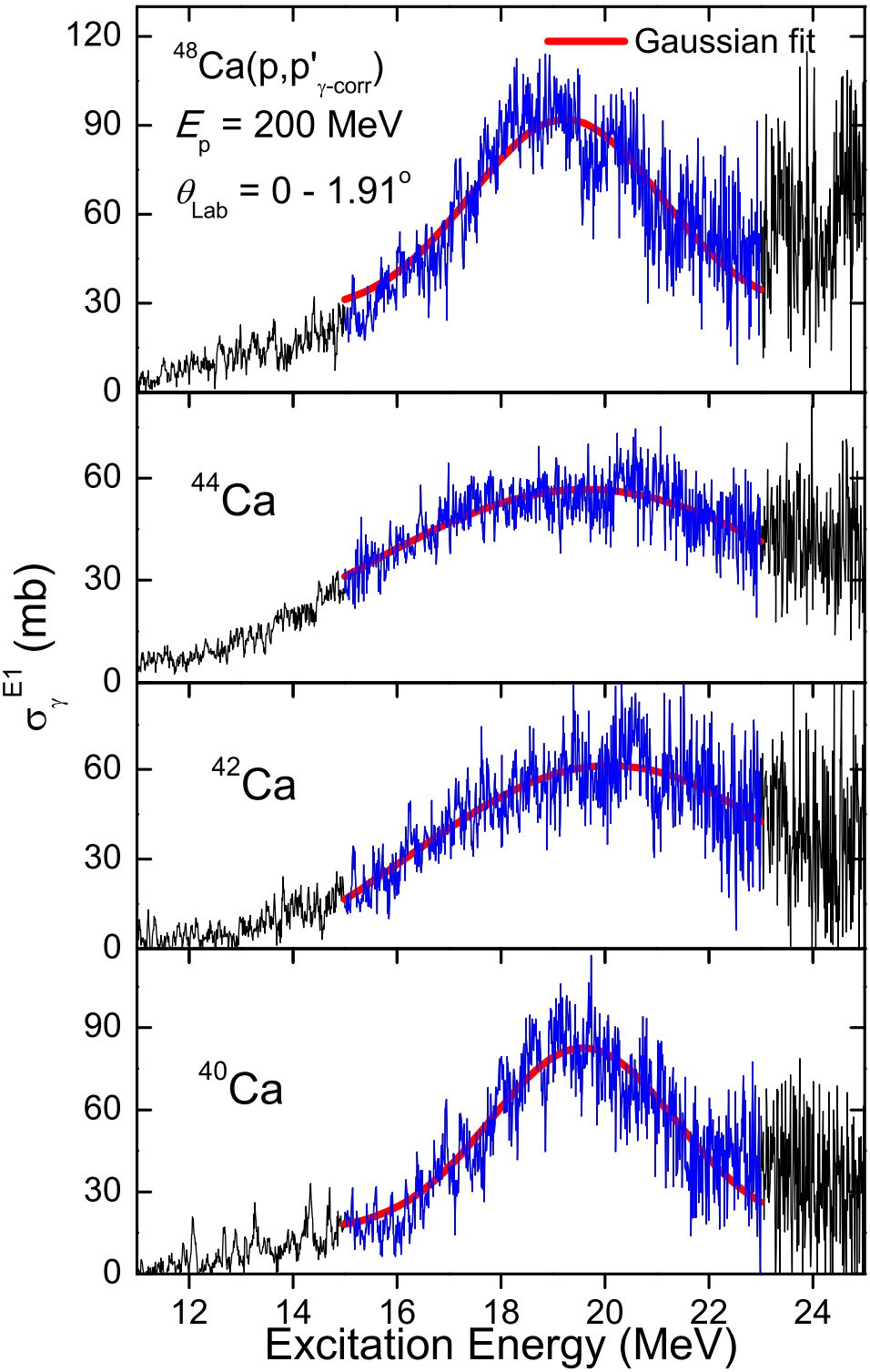

Figure 4.10: ^{40,42,44,48}Ca(p,p$'_{\gamma-\text{corr}}$) spectra fit with a Gaussian function. The excitation energy range of 15 - 23 MeV selected for the fit is indicated in blue (spectrum) while the fitting Gaussian curve is indicated in red line.

4.3 Electric dipole strength distribution of the calcium isotopes

Investigating the decay of giant resonances provides an avenue for having a better understanding, from a microscopic point of view, of the various mechanisms that contribute to the total width of the resonance. Such an investigation is of paramount importance as GRs are strongly damped with a width of only a few MeV. The physical nature of the characteristic energy scales extracted from the fine structure observed in the experimental spectra serves as basis for interpreting these scales in terms of the various factors that contribute to the total width. Thus, by studying the fine structure one can study the decay mechanisms. As yet, these scales cannot independently be interpreted. Rather, their interpretation is based on scales extracted from microscopic model calculations of known interaction types in the pairing channels and degrees of freedom, to which they are compared.

For the semi-magic nuclei of ^{42}Ca and ^{44}Ca, microscopic model calculations have been carried out within the framework of the Quasi-particle Random Phase Approximation (QRPA) with the Gogny D1S interaction (Section 2.4.4), the Relativistic Quasi-particle Random Phase Approximation (RQRPA) also with the Gogny interaction (Section 2.4.6) and the Relativistic Quasi-particle Time Blocking Approximation (RQTBA) with an energy dependent two-quasi-particle interaction (Section 2.4.7). For the doubly-magic nuclei of ^{40}Ca and ^{48}Ca, in addition to the above mentioned models, there are also microscopic model calculations within the framework of the Random Phase Approximation (RPA) with the GLSG interaction (Section 2.4.1), the Second Random Phase Approximation (SRPA) with the UCOM interaction (Section 2.4.3) and the continuum random phase approximation (CRPA) with the SLy4 interaction (Section 2.4.5).

Within a microscopic picture the RPA, in which only $1p-1h$ transitions are considered, gives a good account of some gross features of the resonance such as the total transition strength and the centroid energies. It, however, fails to give a good prediction of the width.

Understanding from a theoretical point of view, the connection between the observed fine structure from the experimental spectra and the total width of the resonance requires that the $1p-1h$ couples with $2p-2h$ through spreading [Goe82]. The mixing of the $1p-1h$ and the $2p-2h$ configurations by the residual interaction accounts for the spreading width which constitutes the major component of the total width.

Comparative plots of the IVGDR strength distribution functions for the experimental data (top panels) and theoretical calculations within the framework of the RQTBA (second panels), the RQRPA (third panels) and the QRPA (fourth panels) for ^{48}Ca, ^{44}Ca, ^{42}Ca and ^{40}Ca are illustrated in Figs. 4.11 - 4.14, respectively.

It can be observed from the strength distribution functions, as illustrated in the different figures, that the RQTBA best represents the experimental data in terms of the amount of fine structure exhibited, compared with the other models. It also gives a reasonably good prediction of the centroid energies for all four calcium isotopes. Furthermore, this model is observed to exhibit more high energy strengths with increasing neutron number from ^{40}Ca to ^{48}Ca. A smoothing of the RQTBA strength function of all four calcium isotopes with a sufficiently wide Gaussian function allows for a better comparison of the overall shape of the resonance with the experimental results as shown in Fig. 4.15. In this case, the RQTBA spectra were smoothed with a 4 MeV-width Gaussian function. As seen in the figure, the overall shape of the resonance between the RQTBA and the $(\mathrm{p},\mathrm{p}'_{\gamma-\mathrm{corr}})$ spectra are roughly in agreement.

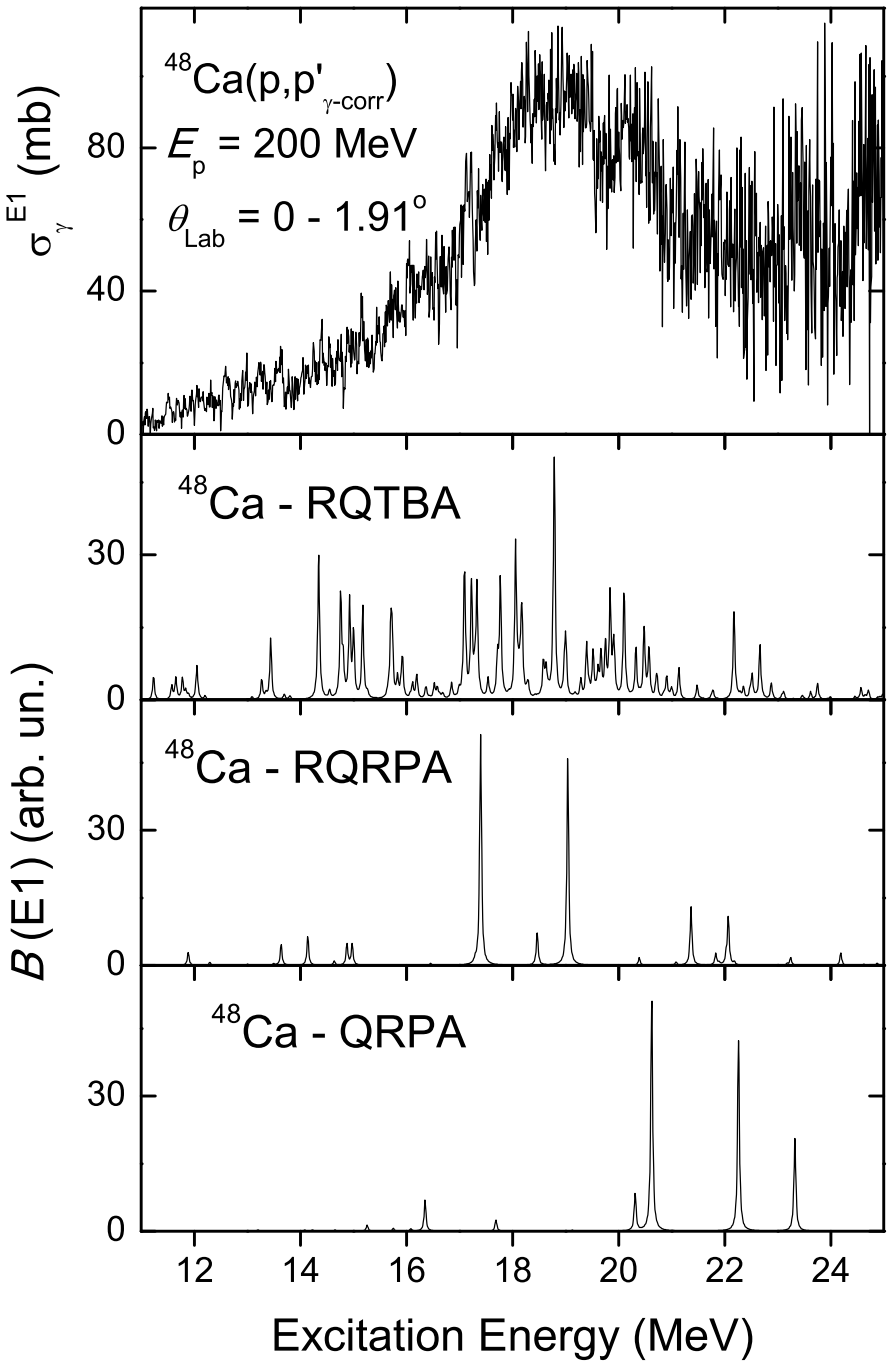

Figure 4.11: From top to bottom: the ^{48}Ca(p,p$'_{\gamma-\mathrm{corr}}$) spectrum acquired at E_p = 200 MeV and $\theta_\mathrm{Lab} = 0 \pm 1.91°$; strength distribution functions within the framework of the Relativistic Quasi-particle Time Blocking Approximation (RQTBA) (Section 2.4.7) ; the Relativistic Quasi-particle Random Phase Approximation (RQRPA) (Section 2.4.6), and the Quasi-particle Random Phase Approximation (QRPA) (Section 2.4.4)

.

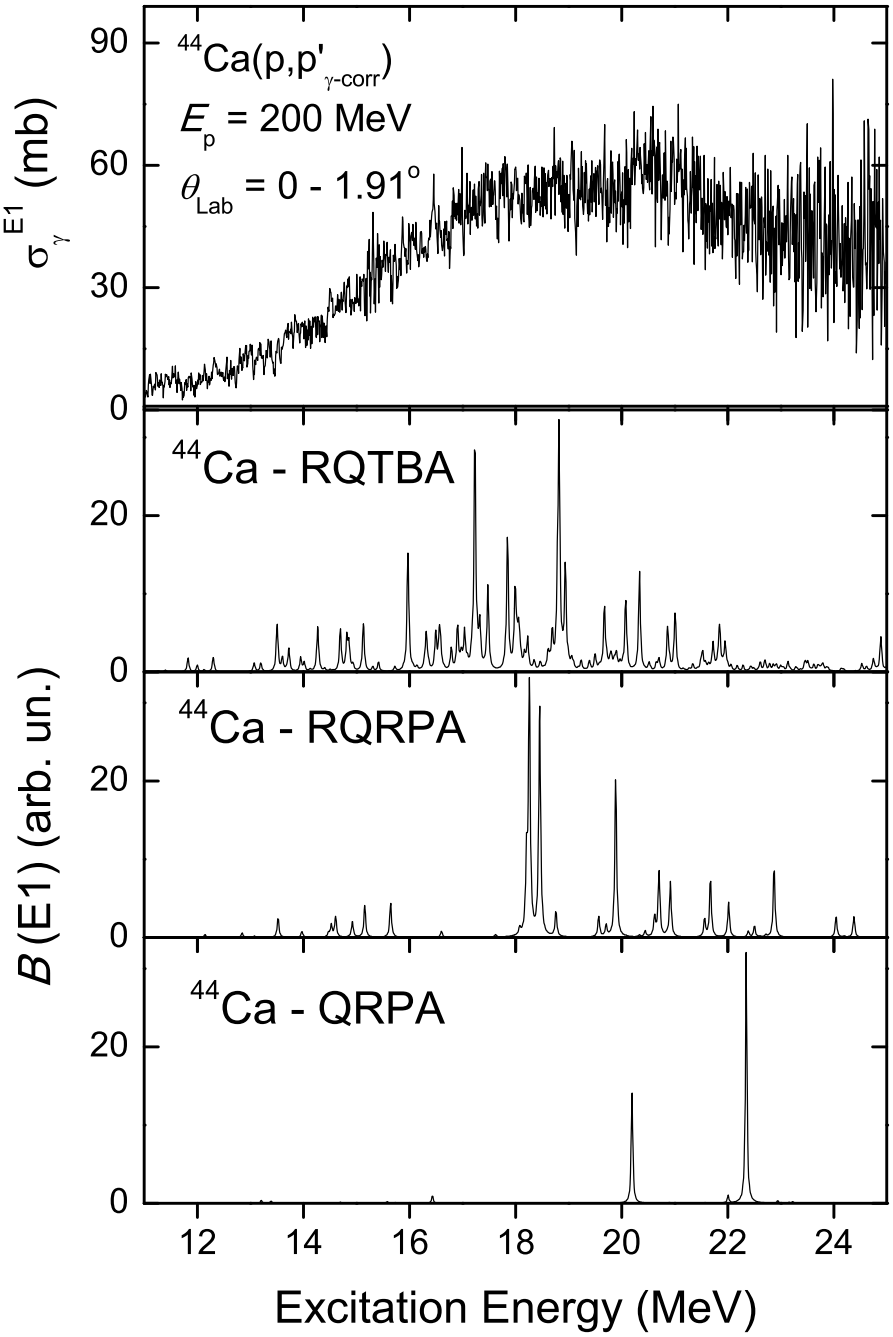

Figure 4.12: From top to bottom: the ^{44}Ca(p,p$'_{\gamma-\mathrm{corr}}$) spectrum acquired at E_p = 200 MeV and $\theta_\mathrm{Lab} = 0 \pm 1.91°$; strength distribution functions within the framework of the relativistic quasi-particle time blocking approximation (RQTBA) (Section 2.4.7); the relativistic quasi-particle random phase approximation (RQRPA) (Section 2.4.6), and the quasi-particle random phase approximation (QRPA) (Section 2.4.4).

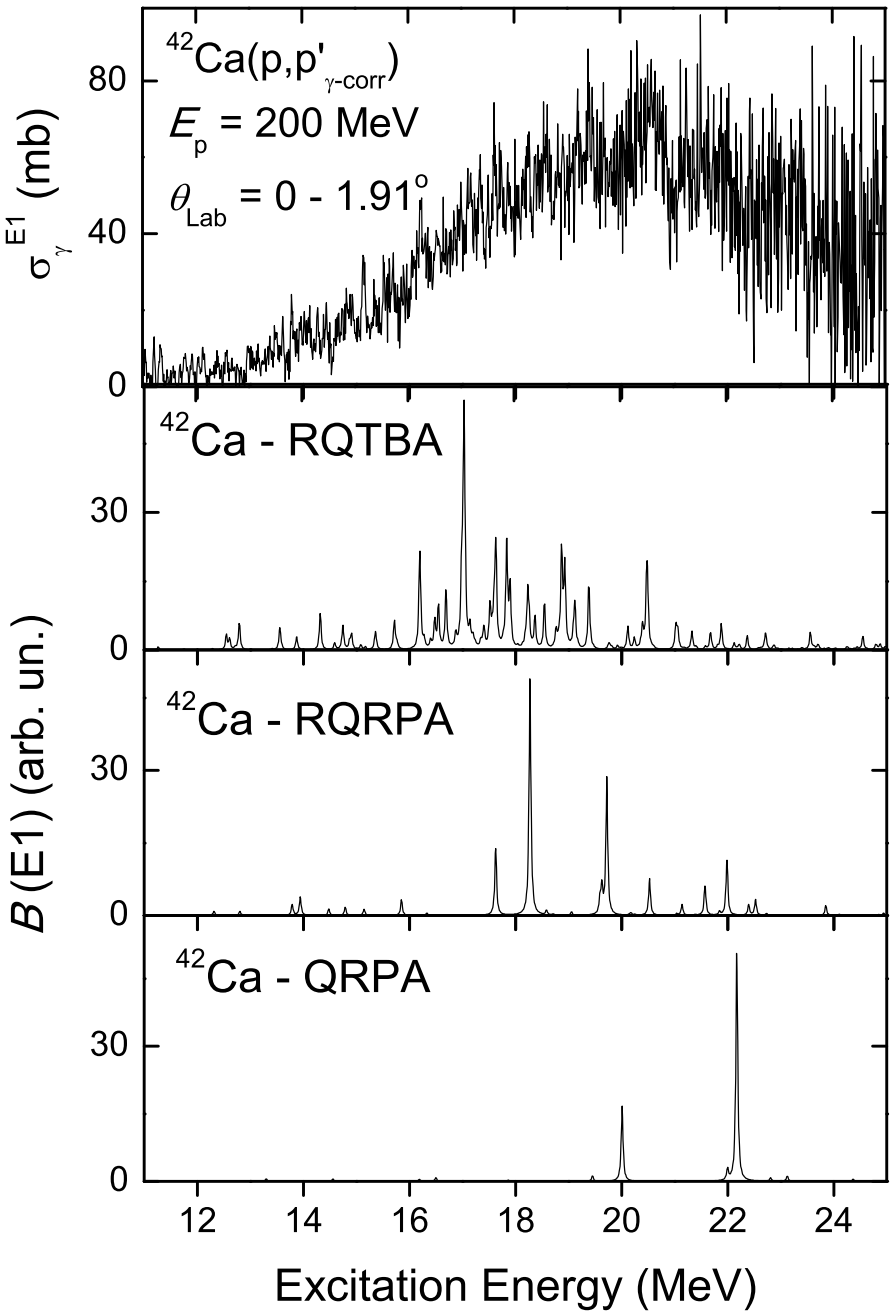

Figure 4.13: From top to bottom: the ^{42}Ca(p,p$'_{\gamma-\text{corr}}$) spectrum acquired at E_p = 200 MeV and θ_Lab = 0 ± 1.91°; strength distribution functions within the framework of the relativistic quasi-particle time blocking approximation (RQTBA) (Section 2.4.7); the relativistic quasi-particle random phase approximation (RQRPA) (Section 2.4.6), and the quasi-particle random phase approximation (QRPA) (Section 2.4.4).

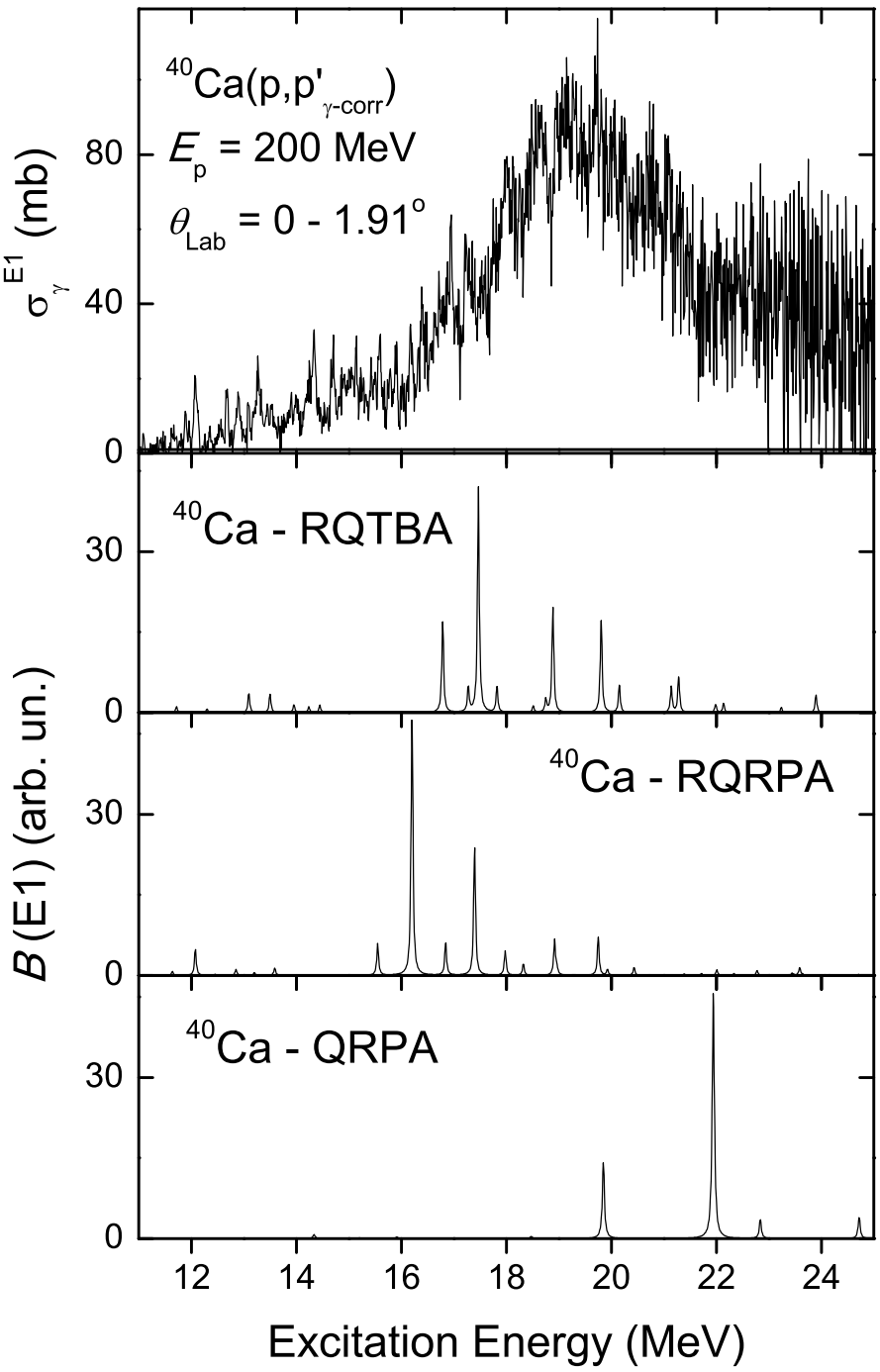

Figure 4.14: From top to bottom: the ^{40}Ca(p,p$'_{\gamma-\text{corr}}$) spectrum acquired at E_p = 200 MeV and $\theta_\text{Lab} = 0 \pm 1.91°$; strength distribution functions within the framework of the relativistic quasi-particle time blocking approximation (RQTBA) (Section 2.4.7); the relativistic quasi-particle random phase approximation (RQRPA) (Section 2.4.6), and the quasi-particle random phase approximation (QRPA) (Section 2.4.4).

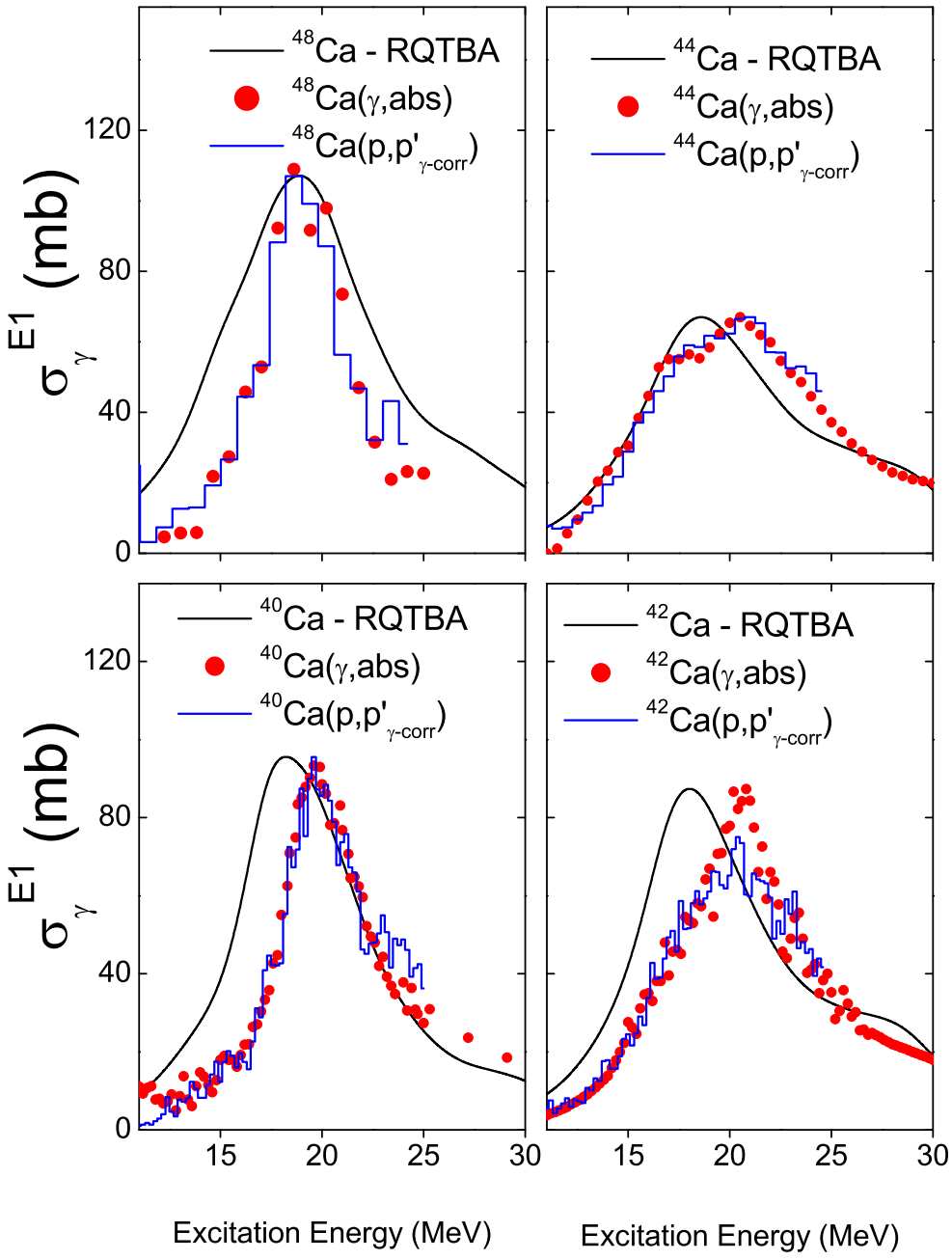

Figure 4.15: Comparative plots of the ^{48,44,42,40}Ca(p,p$'_{\gamma-\mathrm{corr}}$) spectra with smoothed RQTBA strength distribution functions. The RQTBA spectra were smoothed with a 4 MeV-width Gaussian function which allows for a better appreciation of the overall shape of the resonance.

The RQRPA also exhibits significant amount of fine structure although less than the RQTBA. It also gives a good prediction of the centroid energies. The QRPA, on the other hand, exhibits much less fine structure and significantly overestimates the centroid energies for all four isotopes. This can be attributed to the Thomas-Reiche-Kuhn enhancement factor, κ, which was taken to be 0.6 for the Gogny D1S interaction used in these calculations.

In the same vein, a comparative plot of the theoretical model calculations performed within the framework of the SRPA (second panels), CRPA (third panels) and RPA (bottom panels) together with the experimental data (top panels) for ^{48}Ca and ^{40}Ca are shown in Fig. 4.16 and Fig. 4.17, respectively.

In the results of strength distributions based on the RPA calculations with the GLSG interaction (RPA-GLSG) the centroid energies are severely overestimated for both doubly-magic nuclei of calcium. Consequently, no significant amount of fine structure is seen in the energy range of 11 - 25 MeV for which experimental data to which they are compared, was acquired. In case of ^{48}Ca for example, a single state is observed in that energy region. In the case of ^{40}Ca, however, more fine structure is seen in the IVGDR energy region. The overestimation of the centroids in the RPA-GLSG can be attributed to the low nucleon effective mass and is corrected for in the SRPA with the UCOM interaction (SRPA-UCOM) (second panels) in which a better estimation of the centroid energies is observed with reasonable amount of fine structure compared with the ^{48}Ca - RPA. More details on this can be found in Refs. [Pap09] and [Usm11a].

It can then be inferred from the comparison of the strength functions, as seen in Figs. 4.16 and 4.17 (second panels), that the SRPA-UCOM gives a better estimation of the centroid energies compared with the RPA although a bit underestimated in the case of ^{48}Ca with less significant amount of fine structure in the high excitation energy region. The strength distribution functions from

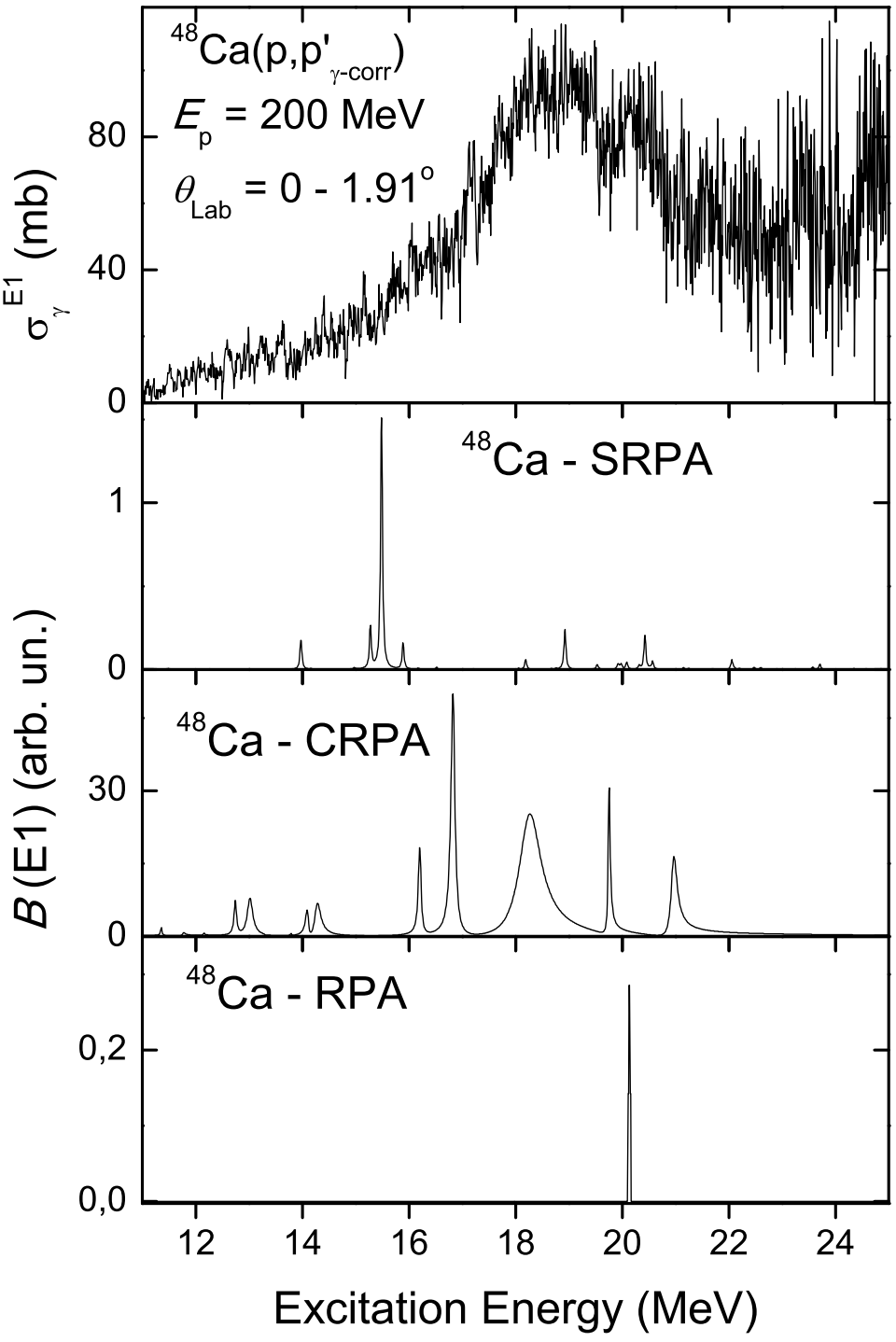

Figure 4.16: From top to bottom: the experimental ^{48}Ca(p,p$'_{\gamma-\mathrm{corr}}$) spectrum; strength distribution functions within the framework of the relativistic second random phase approximation (SRPA) (Section 2.4.3); the continuum random phase approximation (CRPA) (Section 2.4.5), and the random phase approximation (RPA) (Section 2.4.1).

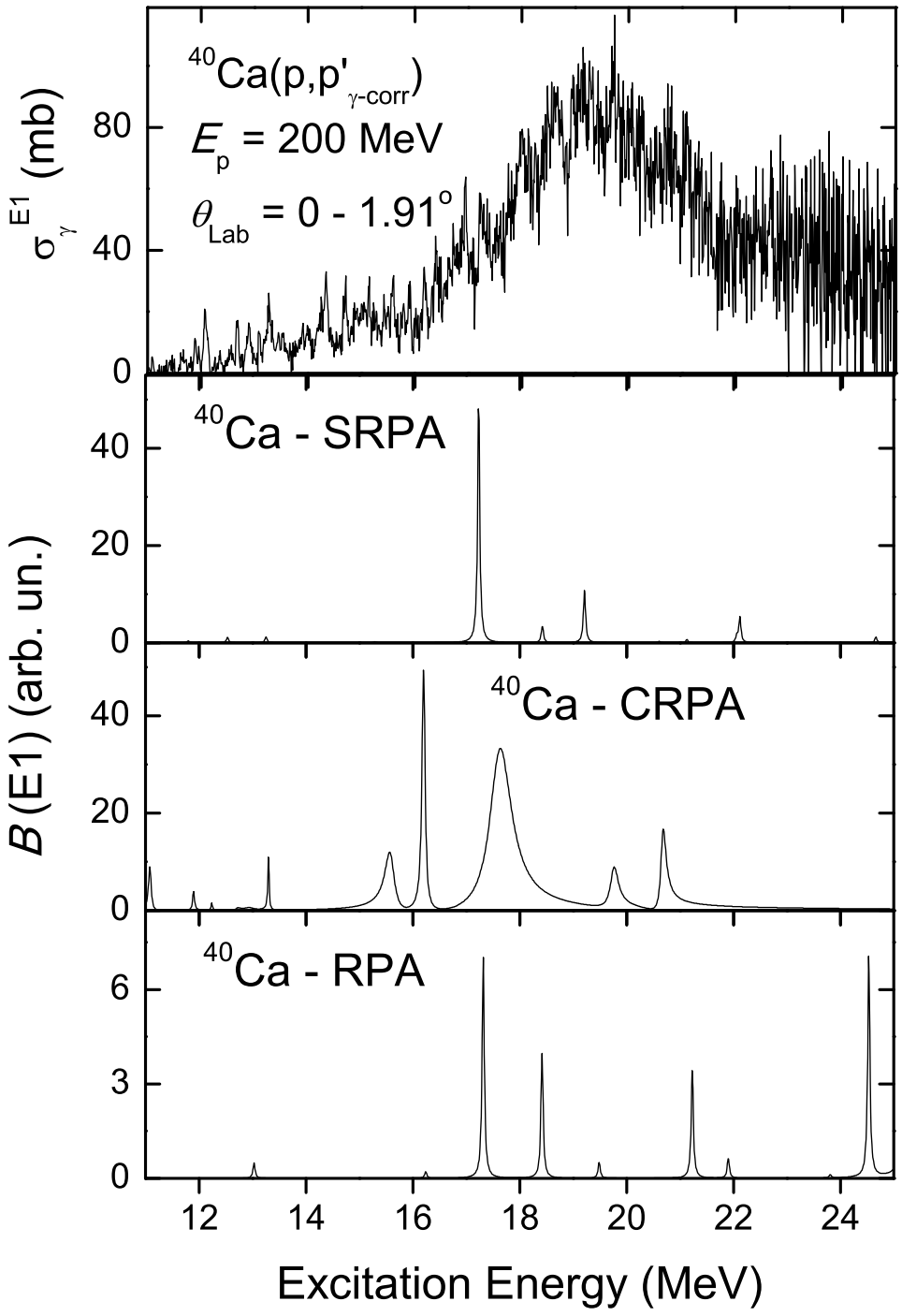

Figure 4.17: From top to bottom: the experimental ^{40}Ca(p,p$'_{\gamma-\mathrm{corr}}$) spectrum; strength distribution functions within the framework of the relativistic second random phase approximation (SRPA) (Section 2.4.3); the continuum random phase approximation (CRPA) (Section 2.4.5), and the random phase approximation (RPA) (Section 2.4.1).

the CRPA with the SLy4 interaction exhibits significant amount of fine structure with a good prediction of the centroid energies. In addition, a broad structure around the centroids was observed for both ^{40}Ca and ^{48}Ca.

Although a comparison of the strength distribution functions is necessary for relating gross properties of the resonance such as its overall shape, a class-to-class comparison between experimentally extracted characteristic energy scales and those of the various theoretical model calculations is paramount for assessing the effectiveness of each of these theoretical models. This will also allow for an understanding of the role of the corresponding interactions and ultimately identify the origin of the various factors that contribute to the total width of the observed resonances.

4.4 Extraction of the characteristic energy scales by means of Wavelet analysis

Wavelet analysis has been performed on all available theoretical model calculations and compared with the experimental data. For ease of comparison, the models were arranged according to the similarity of their formalisms (see Section 2.4). The models in which the relativistic quasi-particle is considered as the building block, notably the relativistic quasi-particle time blocking approximation (RQTBA) and the relativistic quasi-particle random phase approximation (RQRPA) were compared together with experimental data. Thereafter, the models built on the random phase approximation (i.e. QRPA, SRPA, CRPA, RPA) were also compared with the experimental data, in order to account for the the role of Landau damping, collisional damping and possible contribution from the escape width.

In the following, the continuous Wavelet transform analysis is applied to the (p,p$'_{\gamma-corr}$) spectra of the four calcium isotopes acquired at $E_{\mathrm{p}} = 200$ MeV and

$\theta_{\mathrm{Lab}} = 0 \pm 1.91^{o}$. Similarly, the Wavelet analysis was also carried out on all the theoretical calculations and the obtained characteristic energy scales are compared on a class-to-class basis which is defined by the range of the extracted scale energies. In order to obtain these characteristic scales, a power spectrum of the Wavelet signal which corresponds to the absolute values of the Wavelet coefficients is constructed on the scale axis.

4.4.1 RQTBA and RQRPA

The experimental ^{40,42,44,48}Ca(p,p$'_{\gamma-\mathrm{corr}}$) spectra and corresponding plots of the absolute value of the Wavelet coefficients as a function of the excitation energy (known as the coefficient plots) are shown in Figs. 4.18 - 4.21. The RQTBA (see Section 2.4.7) spectra and corresponding coefficient plots are also shown. In the coefficient plots, the scales present in both the experimental as well as the theoretical spectra are illustrated with different colours of which the red indicates a strong scale corresponding to a high absolute value of Wavelet coefficient and blue indicating the lowest absolute values of Wavelet coefficients. On the right hand side are the corresponding plots of power spectra. The characteristic energy scales are indicated in the power spectra with bumps whereby a huge bump indicates a prominent scale.

In Figs. 4.22 - 4.25 the experimental ^{40,42,44,48}Ca(p,p$'_{\gamma-\mathrm{corr}}$) spectra and their corresponding power spectra are plotted alongside those of the theoretical calculations of the RQTBA and RQRPA. The position of the characteristic energy scales are indicated in red arrows. The extracted characteristic energy scales (ΔE) are classified as follows:

- Class I: $\Delta E < 300$ keV,
- Class II: 300 keV $\leq \Delta E < 1000$ keV and
- Class III: $\Delta E \geq 1000$ keV.

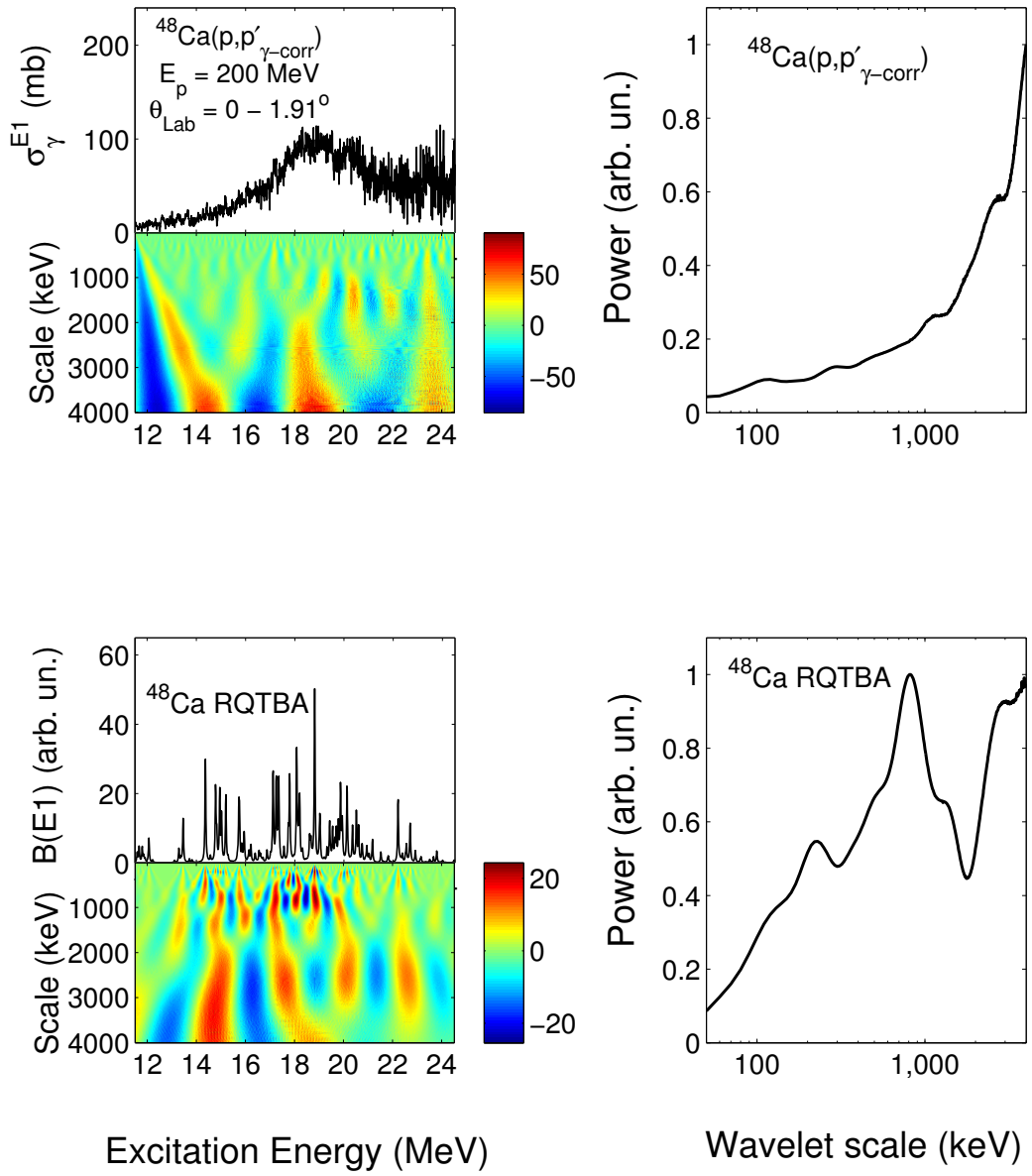

Figure 4.18: *Top panel*: Experimental ^{48}Ca(p,p$'_{\gamma-\mathrm{corr}}$) spectrum on top of the its Wavelet coefficients plot on the left hand side while the corresponding power spectrum is shown on the right hand side; *Bottom panel*: The ^{48}Ca - RQTBA strength distribution function plotted on top of its coefficients plot. The corresponding power spectrum is also shown on the right hand side.

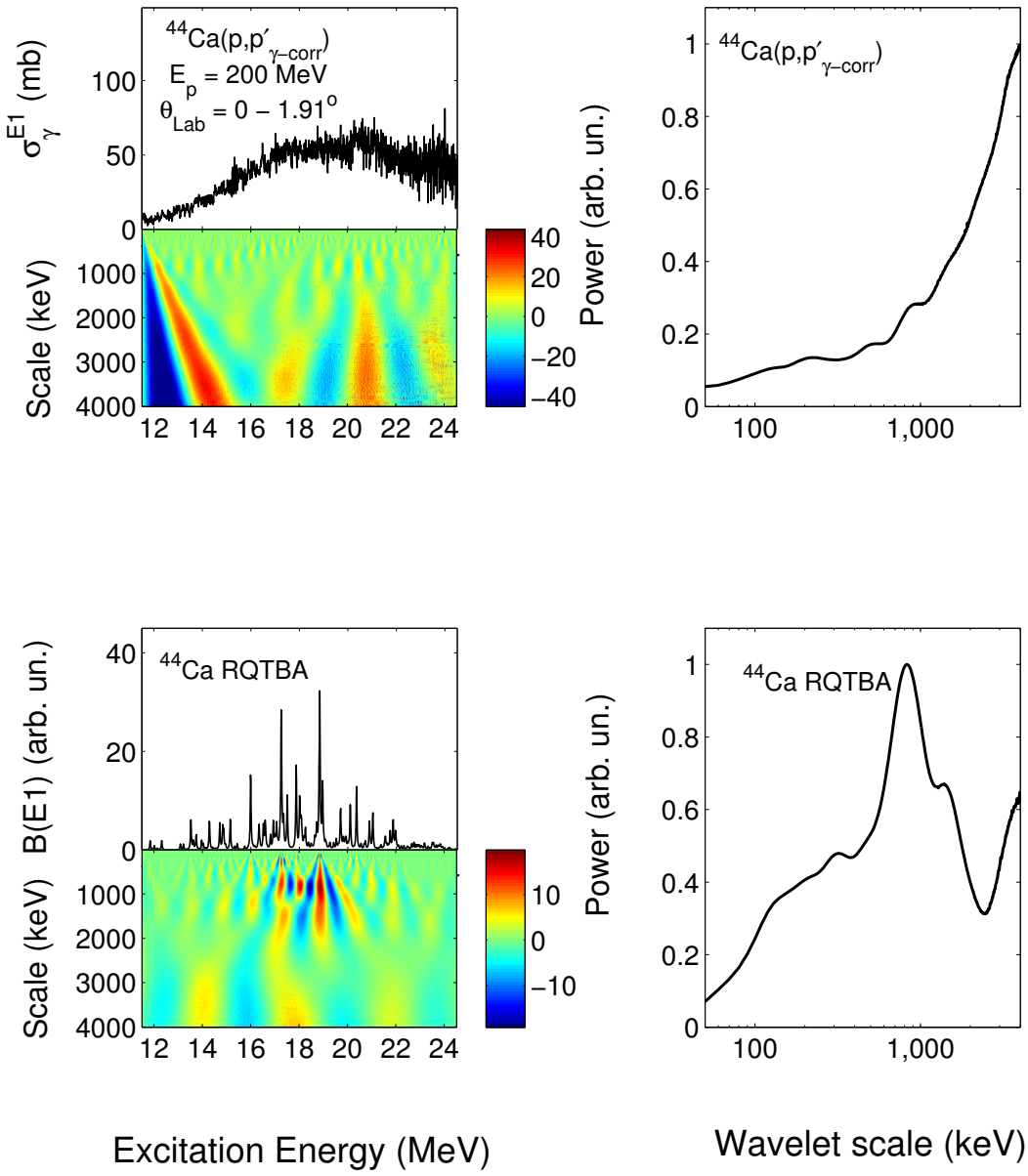

Figure 4.19: *Top panel*: Experimental ^{44}Ca(p,p$'_{\gamma-\mathrm{corr}}$) spectrum on top of the its Wavelet coefficients plot on the left hand side while the corresponding power spectrum is shown on the right hand side; *Bottom panel*: The ^{44}Ca - RQTBA strength distribution function plotted on top of its coefficients plot. The corresponding power spectrum is also shown on the right hand side.

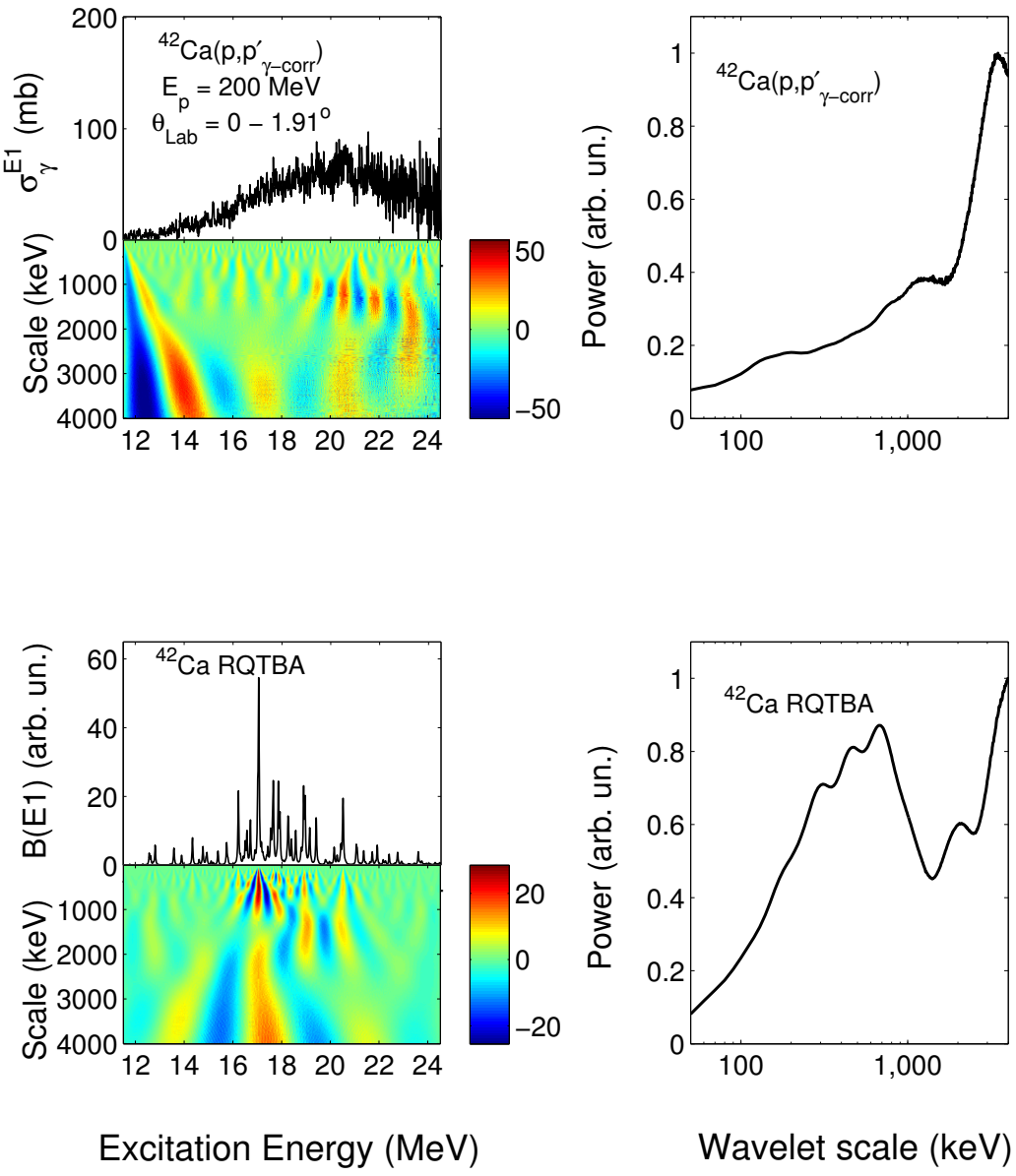

Figure 4.20: *Top panel*: Experimental ^{42}Ca(p,p$'_{\gamma-\mathrm{corr}}$) spectrum on top of the its Wavelet coefficients plot on the left hand side while the corresponding power spectrum is shown on the right hand side; *Bottom panel*: The ^{42}Ca - RQTBA strength distribution function plotted on top of its coefficients plot. The corresponding power spectrum is also shown on the right hand side..

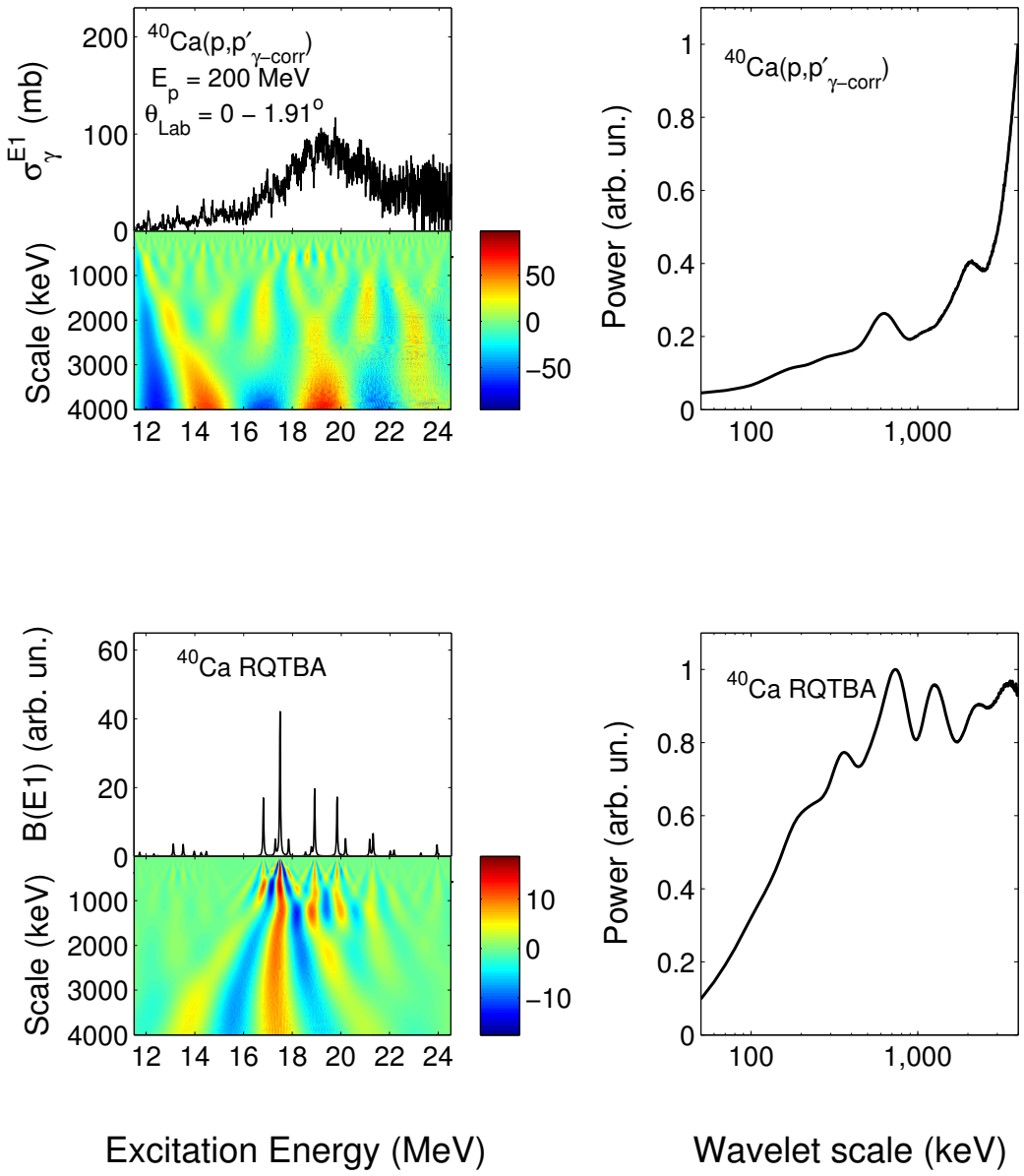

Figure 4.21: *Top panel*: Experimental ^{40}Ca(p,p$'_{\gamma-\mathrm{corr}}$) spectrum on top of the its Wavelet coefficients plot on the left hand side while the corresponding power spectrum is shown on the right hand side; *Bottom panel*: The ^{40}Ca - RQTBA strength distribution function plotted on top of its coefficients plot. The corresponding power spectrum is also shown on the right hand side.

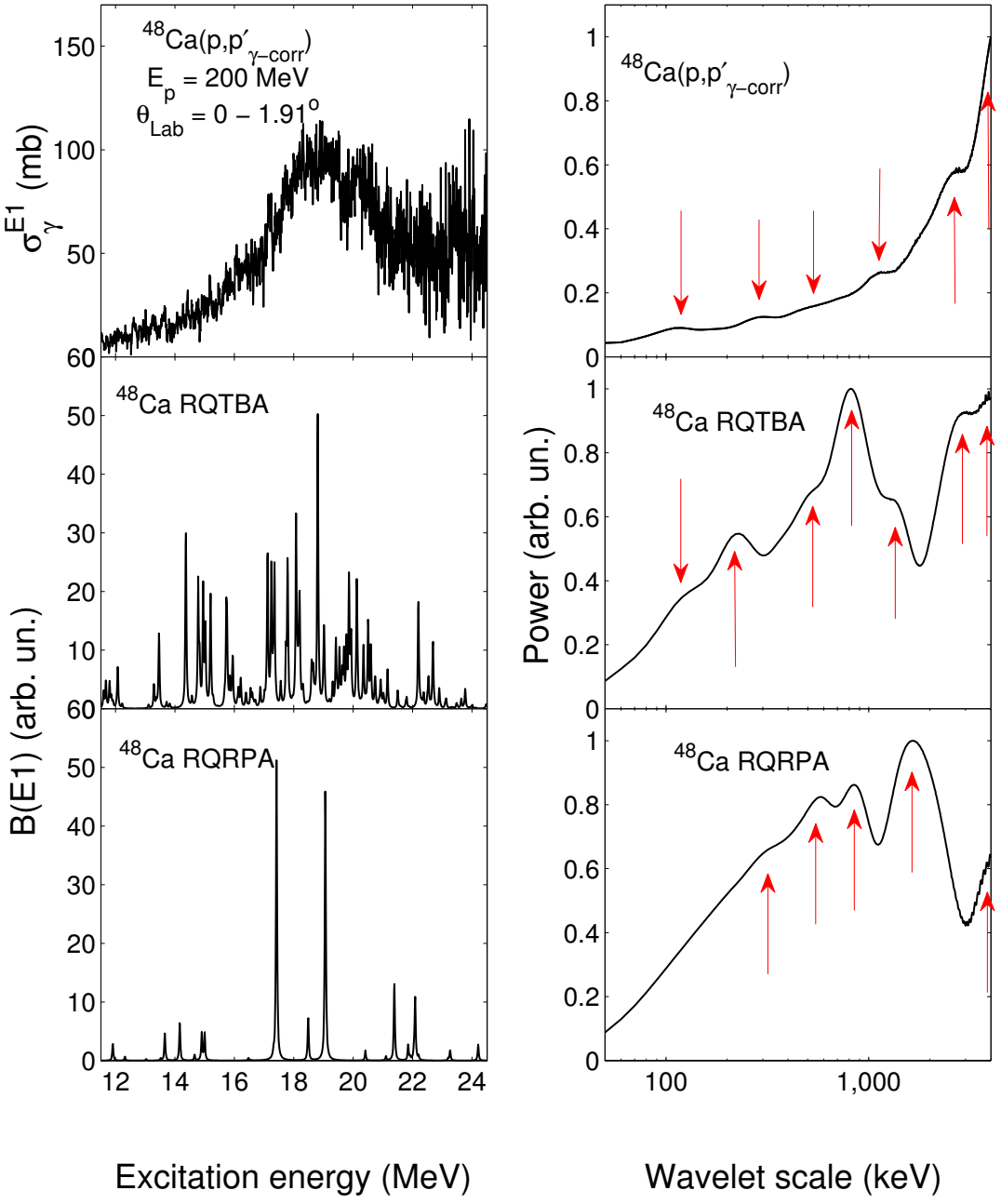

Figure 4.22: From top to bottom: On the left hand side is the ^{48}Ca(p,p$'_{\gamma-\mathrm{corr}}$) spectrum; the ^{48}Ca - RQTBA spectrum and, the ^{48}Ca - RQRPA spectrum. On the right hand side are the corresponding power spectra with the characteristic scales pointed out with red arrows.

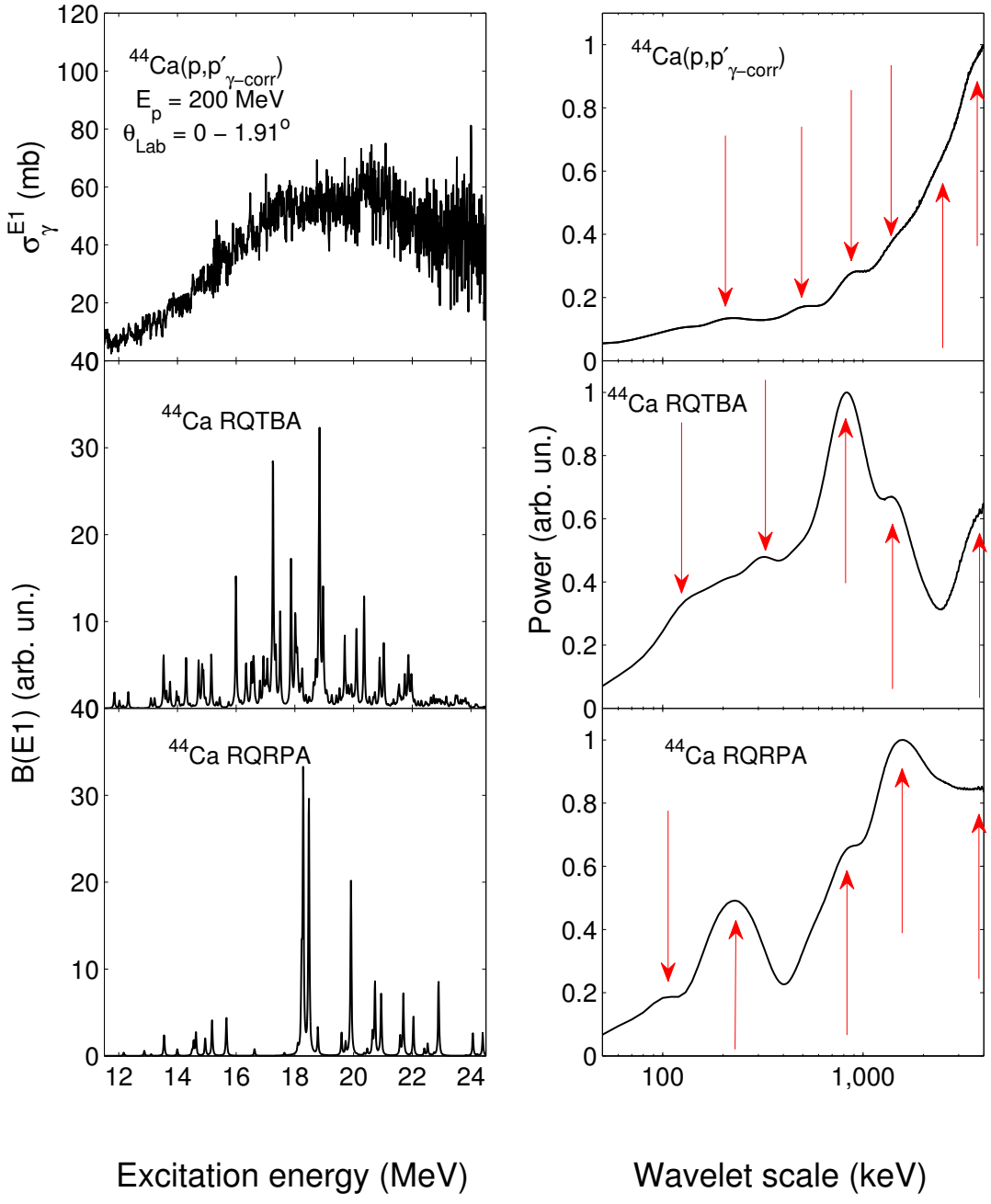

Figure 4.23: From top to bottom: On the left hand side is the ^{44}Ca(p,p′$_{\gamma-\mathrm{corr}}$) spectrum; the ^{44}Ca - RQTBA spectrum and, the ^{44}Ca - RQRPA spectrum. On the right hand side are the corresponding power spectra with the characteristic scales pointed out with red arrows.

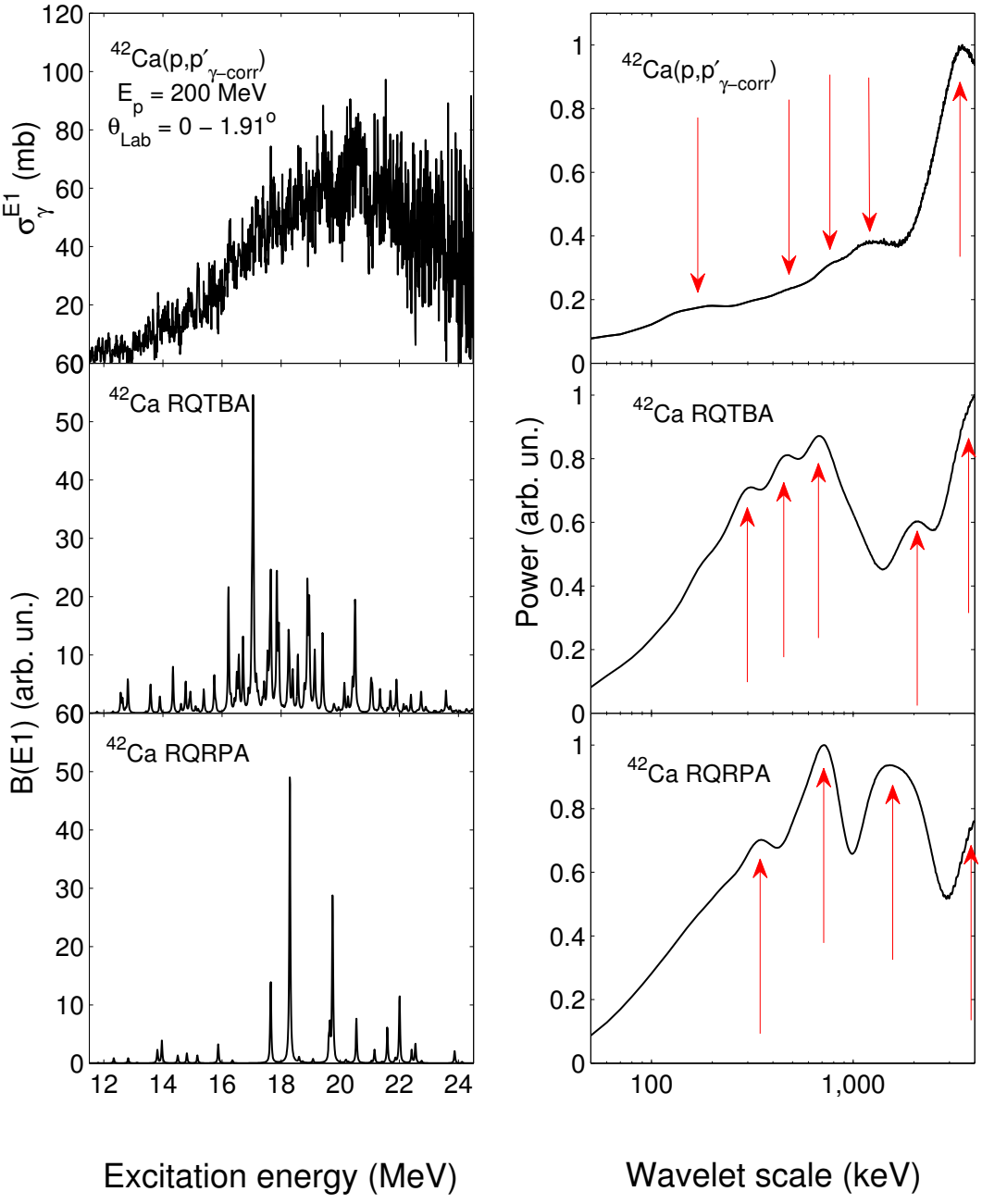

Figure 4.24: From top to bottom: On the left hand side is the ^{42}Ca(p,p$'_{\gamma-\mathrm{corr}}$) spectrum; the ^{42}Ca - RQTBA spectrum and, the ^{42}Ca - RQRPA spectrum. On the right hand side are the corresponding power spectra with the characteristic scales pointed out with red arrows.

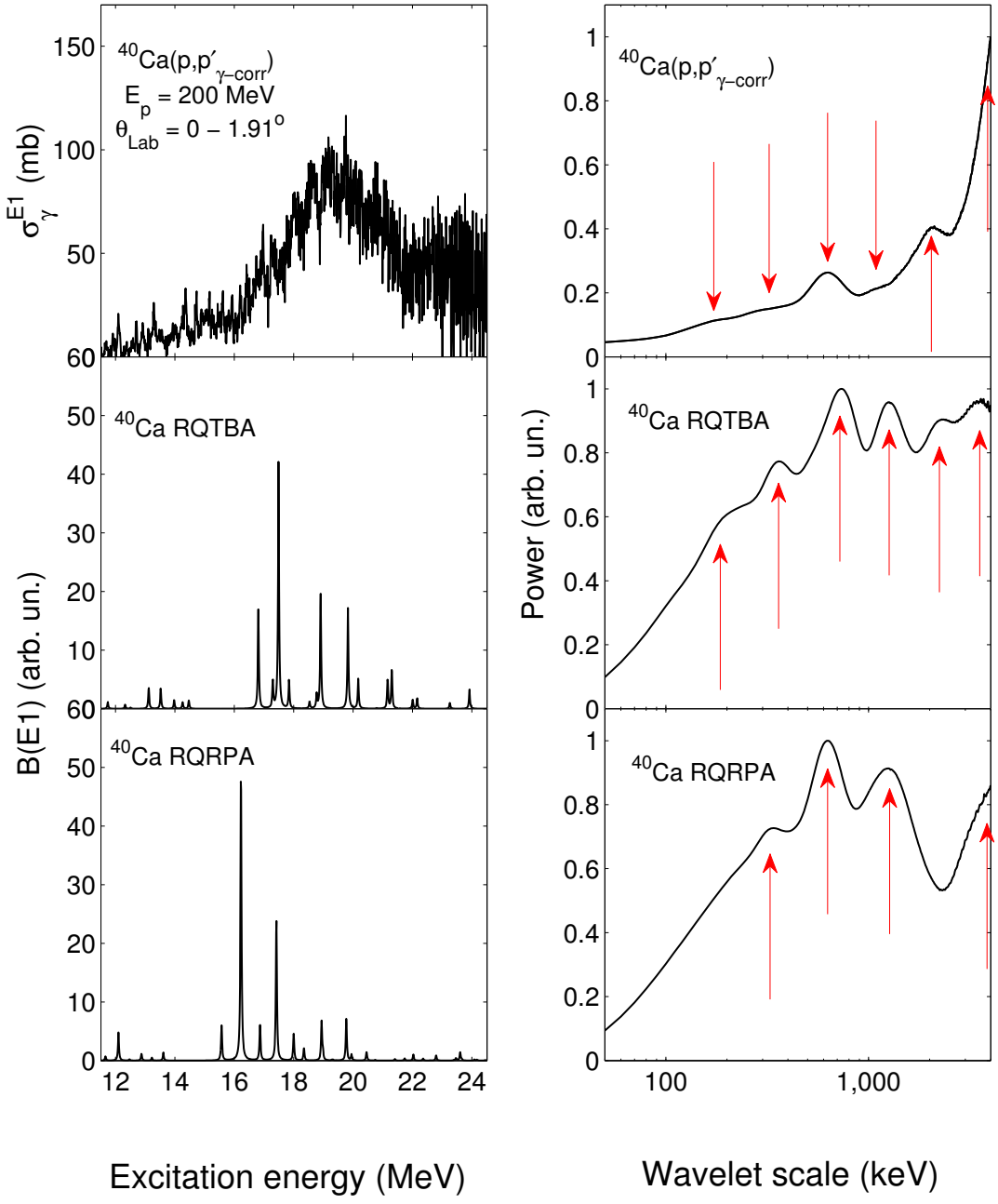

Figure 4.25: From top to bottom: On the left hand side is the ^{40}Ca(p,p$'_{\gamma-\mathrm{corr}}$) spectrum; the ^{40}Ca - RQTBA spectrum and, the ^{40}Ca - RQRPA spectrum. On the right hand side are the corresponding power spectra with the characteristic scales pointed out with red arrows.

Table 4.2: Characteristic energy scale values extracted from the experimental ($p,p'_{\gamma-corr}$) and theoretical calculations of the RQTBA and RQRPA.

^{48}**Ca**	**Class I**	**Class II**	**Class III**
Experiment	**130** —	**320** 630 —	**1390** **2880** 3820
RQTBA	140 **230**	— 530 **820**	1360 **2770** 3870
RQRPA —	—	320 **530** **850**	**1640** — 3860
^{44}**Ca**	**Class I**	**Class II**	**Class III**
Experiment	— **180**	**300** — **800**	1770 2710 3770
RQTBA	— 140	**320** — **830**	**1470** — 3790
RQRPA	100 **230**	— — **860**	**1600** – 3830
^{42}**Ca**	**Class I**	**Class II**	**Class III**
Experiment	— 190	490 — 800	**1610** — **3650**
RQTBA	— –	**310** **470** **690** —	— **2200** 3840
RQRPA	— —	**330** **720** —	**1560** — 3860
^{40}**Ca**	**Class I**	**Class II**	**Class III**
Experiment	— 180 290	— **640** —	1280 **2250** 3770
RQTBA	— 200	**360** **720** —	**1270** **2330** **3700**
RQRPA	— —	**340** **630** —	**1260** — 3770

The obtained ΔE values are summarised in Table 4.2. In order to differentiate the prominent scales identified as fully formed bumps from the shoulder bumps corresponding to the less prominent scales, the former were written in bold font in the tables.

As seen in Table 4.2, the 3 classes of scales are present in the experimental data of all four calcium isotopes. They are also all present in the RQTBA calculations except for the class I scales in ^{42}Ca. The RQRPA calculations reproduce pretty

well the Class II and Class III scales of the experimental data across the calcium isotope chain. They, however, fail to reproduce the Class I scales for ^{48}Ca, ^{42}Ca and ^{40}Ca. In the case of ^{44}Ca where the Class I is present and well reproduced, the Class II scales are only partially reproduced. A class-to-class comparison of the results shows that the RQTBA reproduced all the scales present in the experimental data of the calcium isotopes except for the 2710 keV scale in ^{44}Ca which is not prominent. The RQRPA on the other hand, reproduced at least 2 of 3 scales present in Classes II and III for all the isotopes. In the case of ^{44}Ca where the Class I scales occurred, 2 scales are present as against only 1 in the experimental data. It can therefore be deduced that while the RQRPA does well in reproducing the Class II and Class III scales, the RQTBA performs better in reproducing the characteristic energy scales present in the experimental data of ^{48}Ca, ^{44}Ca, ^{42}Ca and ^{40}Ca. It is however important to note that although the scales are reproduced, there are slight differences in their energy values between the experimental data and the theoretical calculations.

4.4.2 RPA-based Models

The continuous Wavelet transform analysis has also been carried out on theoretical calculations performed within the framework of the Quasi-particle Random Phase Approximation (QRPA) with the Gogny D1S interaction for all four isotopes. In the case of ^{48}Ca and ^{40}Ca the Second Random Phase Approximation (SRPA) with the UCOM interaction, the Continuum Random Phase Approximation (CRPA) with the SLy4 interaction and the Random Phase Approximation (RPA) with the GLSG interaction (see Section 2.4) calculations were also included. The results together with those of the experimental data are shown in Figs. 4.26 - 4.29. The extracted characteristic energy scale values from the QRPA calculations for all the calcium isotopes, together with those of the SRPA, CRPA and RPA in the cases of ^{48}Ca and ^{40}Ca are summarised in Tables 4.3 - 4.5.

A comparison between the scales extracted from the experimental data and those

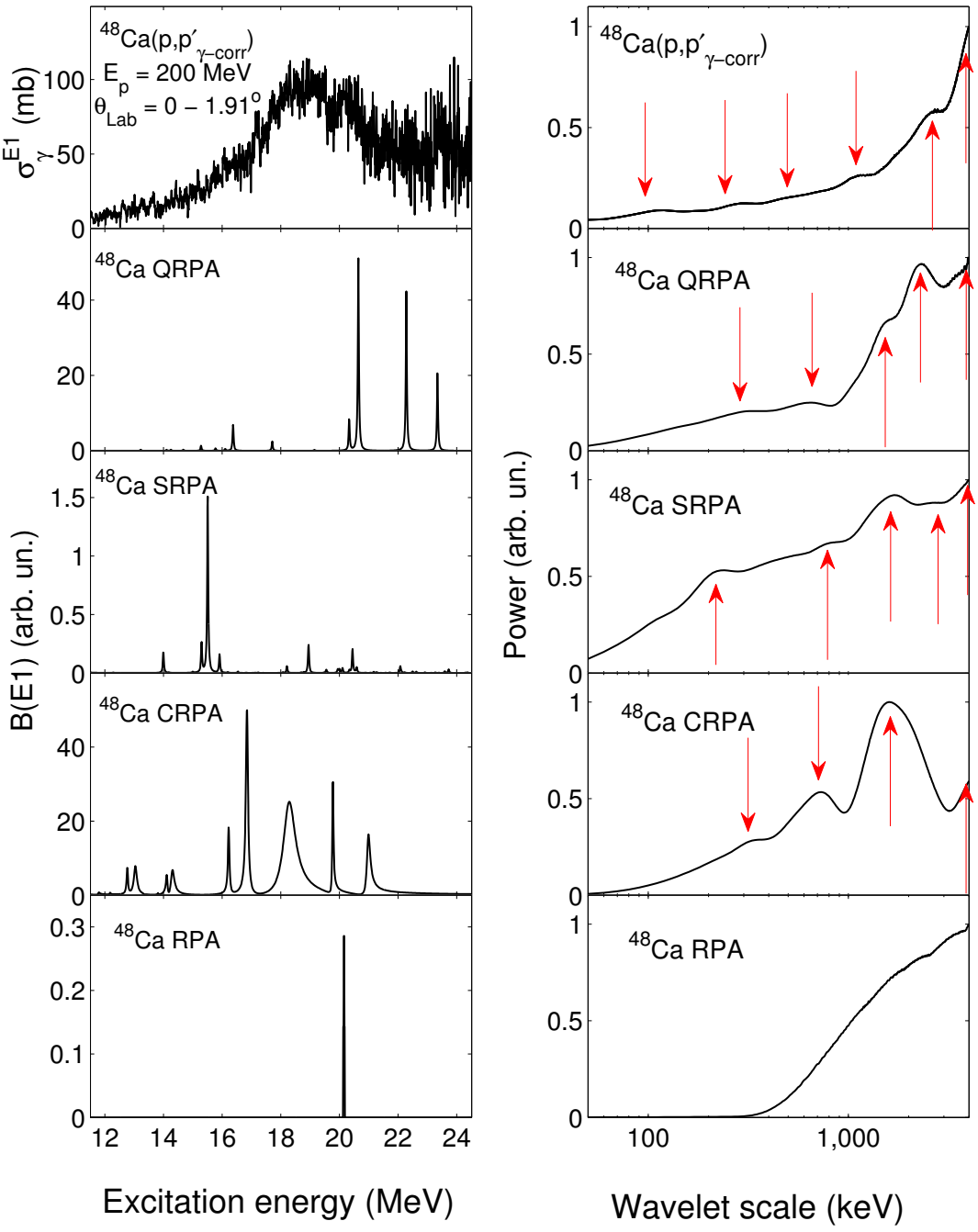

Figure 4.26: From top to bottom: On the left hand side is the experimental ^{48}Ca(p,p$'_{\gamma-\mathrm{corr}}$) spectrum, spectra of the theoretical models of the ^{48}Ca - QRPA; ^{48}Ca - SRPA, ^{48}Ca - CRPA, and ^{48}Ca - RPA. On the right hand side are their corresponding power spectra with the characteristic energy scales pointed out with red arrows.

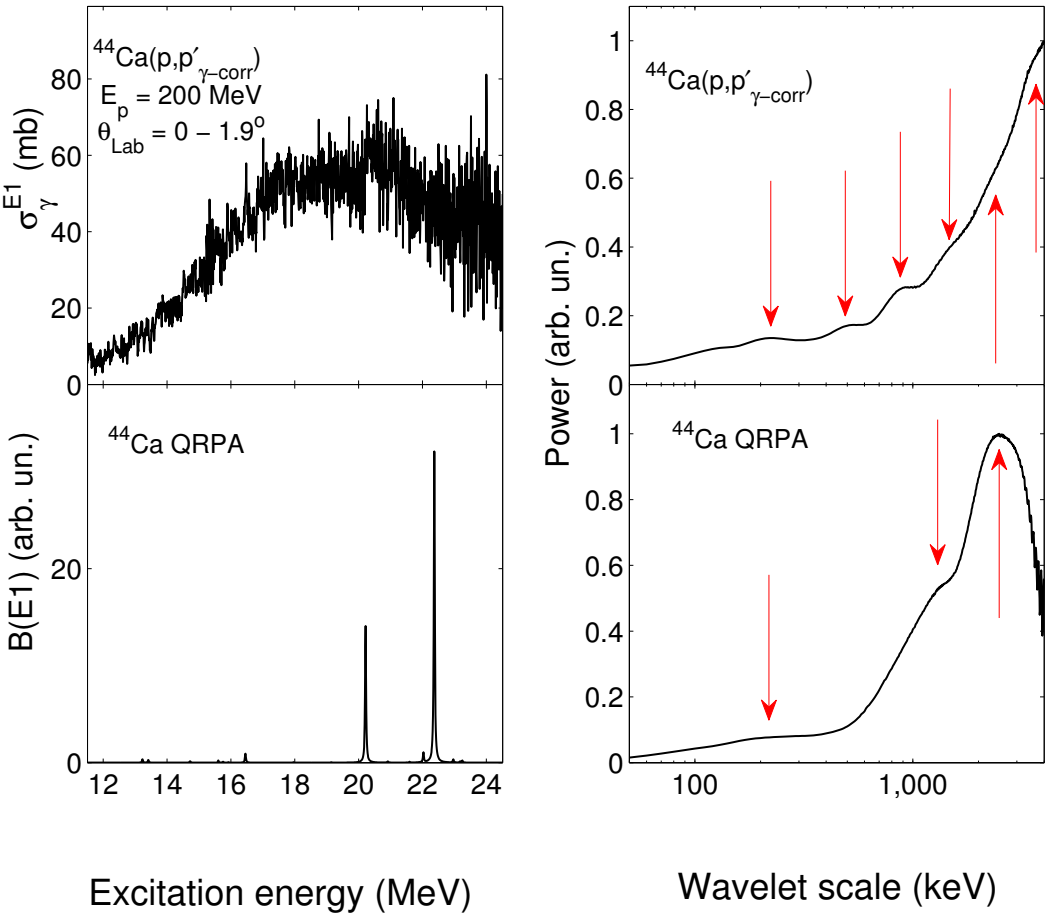

Figure 4.27: *Top to bottom*: On the left hand side is the experimental ^{44}Ca(p,p$'_{\gamma-\mathrm{corr}}$) spectrum and *bottom panel*: is the spectrum of the theoretical models of the ^{44}Ca - QRPA. On the right hand side are their corresponding power spectra with the characteristic energy scales pointed out with red arrows.

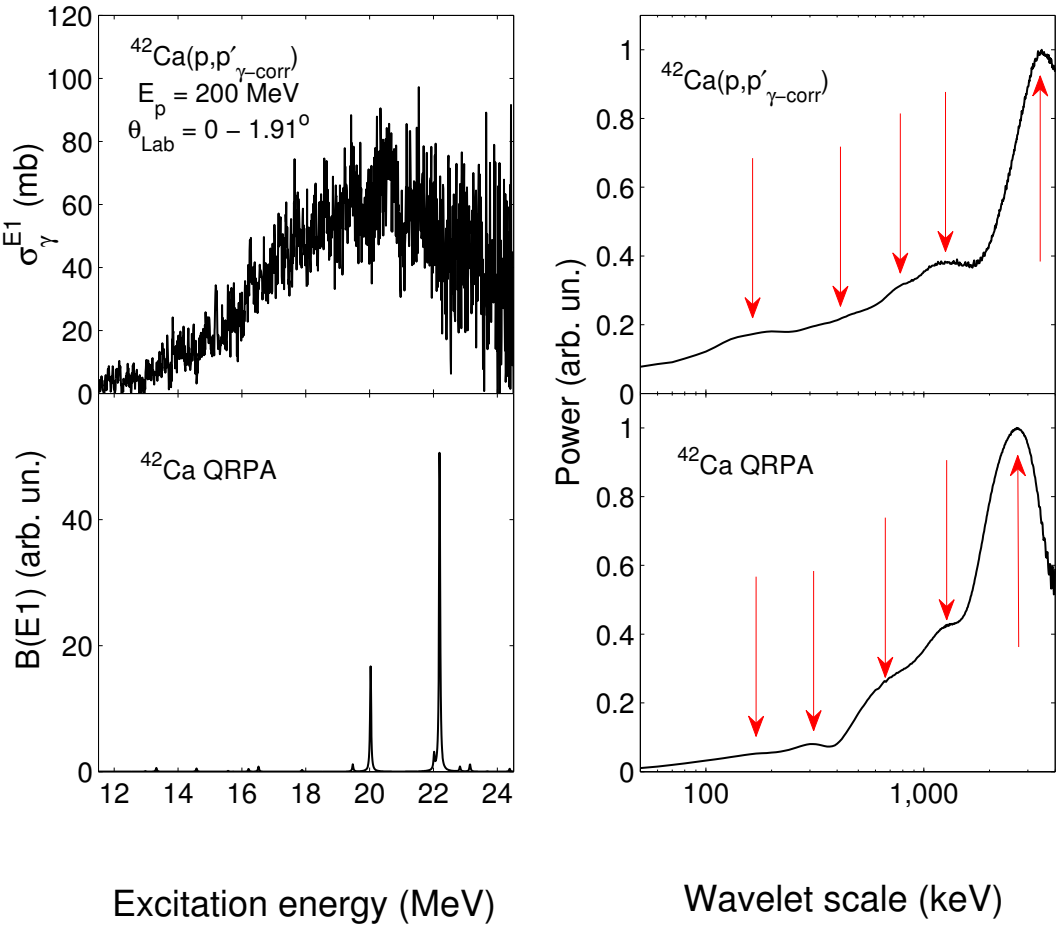

Figure 4.28: *Top to bottom*: On the left hand side is the experimental ^{42}Ca(p,p$'_{\gamma-\mathrm{corr}}$) spectrum and *bottom panel*: is the spectrum of the theoretical models of the ^{42}Ca - QRPA. On the right hand side are their corresponding power spectra with the characteristic energy scales pointed out with red arrows.

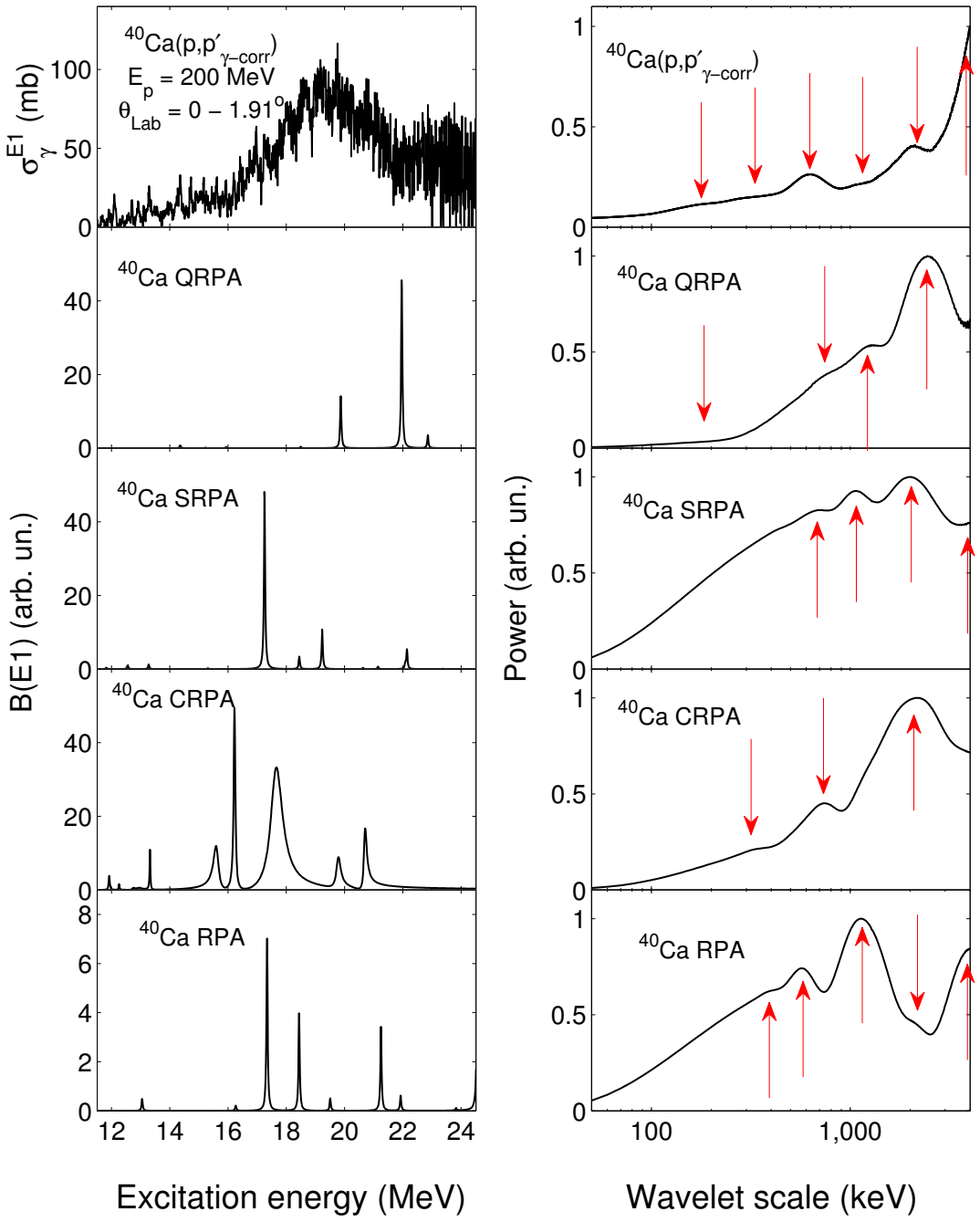

Figure 4.29: From top to bottom: On the left hand side is the experimental ^{40}Ca(p,p$'_{\gamma-\mathrm{corr}}$) spectrum; spectra of the theoretical models of the ^{40}Ca - QRPA; ^{40}Ca - SRPA; ^{40}Ca - CRPA, and ^{40}Ca - RPA. On the right hand side are their corresponding power spectra with the characteristic energy scales pointed out with red arrows.

Table 4.3: Extracted characteristic energy scales of the ^{48}Ca(p,p$'_{\gamma-\mathrm{corr}}$) experimental data and those of the theoretical calculations of the ^{48}Ca - QRPA, ^{48}Ca - SRPA, ^{48}Ca - CRPA and ^{48}Ca - RPA.

^{48}Ca	**Class I**	**Class II**	**Class III**
Experiment	**130** —	**320** 630 —	**1390** **2880** 3820
QRPA	— —	310 **670** —	1480 **2300** 3700
SRPA	— **220**	— 790 —	**1670** 2790 3810
CRPA	— —	**340** **720** —	**1620** — 3840
RPA	— —	— — —	— — —

Table 4.4: Extracted characteristic energy scales of the ^{42,44}Ca(p,p$'_{\gamma-\mathrm{corr}}$) experimental data and those of the theoretical calculations of the ^{44}Ca - QRPA and ^{42}Ca - QRPA.

^{44}Ca	**Class I**	**Class II**	**Class III**
Experiment	— **180**	**300** — **800**	1770 2710 3770
QRPA	— 210	— — —	1320 **2940** —
^{42}Ca	**Class I**	**Class II**	**Class III**
Experiment	— 190	490 — 800	**1610** — **3650**
QRPA	— 160	**340** 730 —	1210 **2870** —

Table 4.5: Extracted characteristic energy scales of the ^{40}Ca(p,p$'_{\gamma-\mathrm{corr}}$) experimental data and those of the theoretical calculations of the ^{40}Ca - QRPA, ^{40}Ca - SRPA, ^{40}Ca - CRPA and ^{40}Ca - RPA.

^{40}Ca	**Class I**	**Class II**	**Class III**
Experiment	— 180 290	— **640** —	1280 **2250** 3770
QRPA	— 180 —	370 760 —	**1210** **2560** —
SRPA	— —	— 660 —	**1060** **2000** 3910
CRPA	— —	340 **740** —	— **2060** —
RPA	— —	340 **580** —	**1120** 2240 3840

of the QRPA shows that for the semi-magic nuclei of ^{44}Ca and ^{42}Ca for which only QRPA calculations are available, the Class I scales are well reproduced. While the Class II scales are not reproduced in ^{44}Ca, they are well reproduced in ^{42}Ca. For the Class III category, one of the two scales present in the experimental data of ^{42}Ca is well reproduced while the second scale differs in energy value from the experimental scale by about 1 MeV. In the case of ^{44}Ca two of the three scales present in the experimental data are well reproduced in the QRPA calculations. In the case of ^{48}Ca, the Class II and Class III scales are well reproduced while the Class I scales do not occur at all with the QRPA. In the case of ^{48}Ca in particular, all the high energy scales are excellently reproduced. These two classes of scales are also well reproduced with the SRPA to account for collisional damping while in the case of the RPA, the IVGDR is contained in a single state located around 20 MeV as seen in Fig. 4.26 (bottom panel). In the case of ^{40}Ca, the QRPA and the SRPA excellently reproduce the Class II scales while the RPA excellently reproduce the Class II and Class III scales.

On the account of the escape width, the results of the CWT with the CRPA shows that the Class II scales are all reproduced for both ^{48}Ca and ^{40}Ca while the Class III scales are only partially reproduced with two out of the three for

^{48}Ca and only one of the three in the case of ^{40}Ca.

It can therefore be concluded that Landau damping mainly accounts for the Class II and Class III scales present in the experimental data of ^{48}Ca, ^{44}Ca, ^{42}Ca and ^{40}Ca with some contributions from the escape width especially for scale energies ranging between 300 keV and 1 MeV corresponding to the Class II scales.

It is important to note that the Class I scales are poorly accounted for by the RPA-based models in general. In fact, they do not occur at all in most of these calculations. This observation also applies to the RQRPA. The RQTBA is the only model that reproduces the Class I scales satisfactorily. This raises the question of the origin of the Class I scales in the experimental data of the calcium isotopes under study.

4.5 Extraction of experimental level density of the $J^\pi = 1^-$ states

The experimental ^{40,42,44,48}Ca(p,p$'_{\gamma-\mathrm{corr}}$) data also allows for the extraction of the level density of the spin-parity states $J^\pi = 1^-$, by means of fluctuation analysis. This provides an avenue for testing theoretical microscopic and phenomenological models by comparing predicted level density results to the experimental results over the same excitation energy range within the giant dipole resonance region.

4.5.1 Fluctuation analysis method

In the following, a description of the fluctuation analysis method applied to the ^{40,42,44,48}Ca(p,p$'_{\gamma-\mathrm{corr}}$) spectra acquired at $E_\mathrm{p} = 200$ MeV and $\theta_\mathrm{Lab} = 0 \pm 1.91°$, is given as outlined in Section 2.6.4.

In order to effectively extract the experimental level spacing from which the level

density can be calculated using Eq. (2.103), a background subtraction procedure based on the Discrete Wavelet Transform as discussed in Section 4.1.2.1 is adopted, the description of which is given as follows:

- The Ca(p,p$'_{\gamma-\mathrm{corr}}$) spectra are decomposed into approximations (A$_j$) and details (D$_j$) which correspond to the large-scale or low-frequency components and the small-scale or high-frequency components of the signals, respectively. At any level j of the decomposition, the original spectrum can be reconstructed by summing the approximation terms up with the corresponding details components [Pol14]. The spectrum decomposition process is illustrated in Figs. 4.30 - 4.33, for ^{48}Ca, ^{44}Ca, ^{42}Ca and ^{40}Ca, respectively. Here, the Bior6.8 type of Discrete Wavelet Transform (DWT) was used to determine the background. The choice of Bior6.8 is informed by its significant number of vanishing moments.

- The background-subtracted spectrum which contains the information on the fluctuations in the region of the IVGDR is then analysed. In a bid to eliminate fluctuations due to finite statistics, the spectrum is first folded with a Gaussian function whose width (σ) is comparable to half the energy resolution of the experimental data to yield the spectrum $g(E_\mathrm{x})$. In order to remove gross structure from the data, the spectrum is also folded with a Gaussian function whose width ($\sigma_>$) is about twice the energy resolution of the experimental data to yield the spectrum $g_>(E_\mathrm{x})$. A dimensionless stationary spectrum, $d(E_\mathrm{x})$ is then obtained as the ratio of $g_>(E_\mathrm{x})$ to $g(E_\mathrm{x})$:

$$d(E_\mathrm{x}) = \frac{g_>(E_\mathrm{x})}{g(E_\mathrm{x})}, \tag{4.3}$$

  whose value is sensitive to the fine structure and distributed around the average value of 1. The smoothing function parameters are optimised by varying them and searching for a region where the autocorrelation function is independent of slight changes in the value of $\sigma_>$.

A quantitative measure of the fluctuations is provided by the autocorrelation function (Section 2.6.4.1) whose experimental value is approximately given by Eq. (2.101). A schematic illustration of the above described processes from the original ^{40,42,44,48}Ca(p,p$'_{\gamma-\mathrm{corr}}$) spectra to the corresponding $g_{>}(E_{\mathrm{x}})$, $g(E_{\mathrm{x}})$, $d(E_{\mathrm{x}})$ and the experimental autocorrelation function spectra are illustrated in Figs. 4.34 - 4.37.

4.5.2 Results of extracted level densities

The experimental autocorrelation function given by Eq. (2.101) is proportional to the mean level spacing ($\langle D \rangle$), the sum of the normalised variances (α), the experimental energy resolution (ΔE) and the expression in the square brackets denoted F($\Delta E, \sigma, \sigma_{>}$). Since only 1^{-} states are considered to be excited within the excitation energy range of 13 - 20 MeV considered, α is determined as the sum of the variances of the Wigner and Porter-Thomas distributions (Section 2.6.4) as: $\alpha = \alpha_{\mathrm{D}} + \alpha_{\mathrm{PT}} = 2.273$.

From Eq. (2.101), the factor F reduces to:

$$F(\Delta E, \sigma, \sigma_{>}) = 1 + \frac{1}{y} - \frac{2\sqrt{2}}{\sqrt{y^2+1}}, \quad for \quad \epsilon = 0, \tag{4.4}$$

where

$$y = \frac{\sigma_{>}}{\sigma}. \tag{4.5}$$

The interval between 13 and 20 MeV was split into 1 MeV-long segments in each of which the mean level spacing was determined. A summary of the parameters used in evaluating the level density of the calcium isotopes is given in Table 4.6. Rearranging Eq. (2.101), one obtains:

$$\langle D \rangle = \frac{2\Delta E\sqrt{\pi}}{2.273 \times 0.3495} \times (C(\epsilon = 0) - 1), \tag{4.6}$$

where C($\epsilon = 0$) - 1 corresponds to the variance of d(E_x) which is to be determined over each 1 MeV-long energy interval considered. Hence, for the four calcium

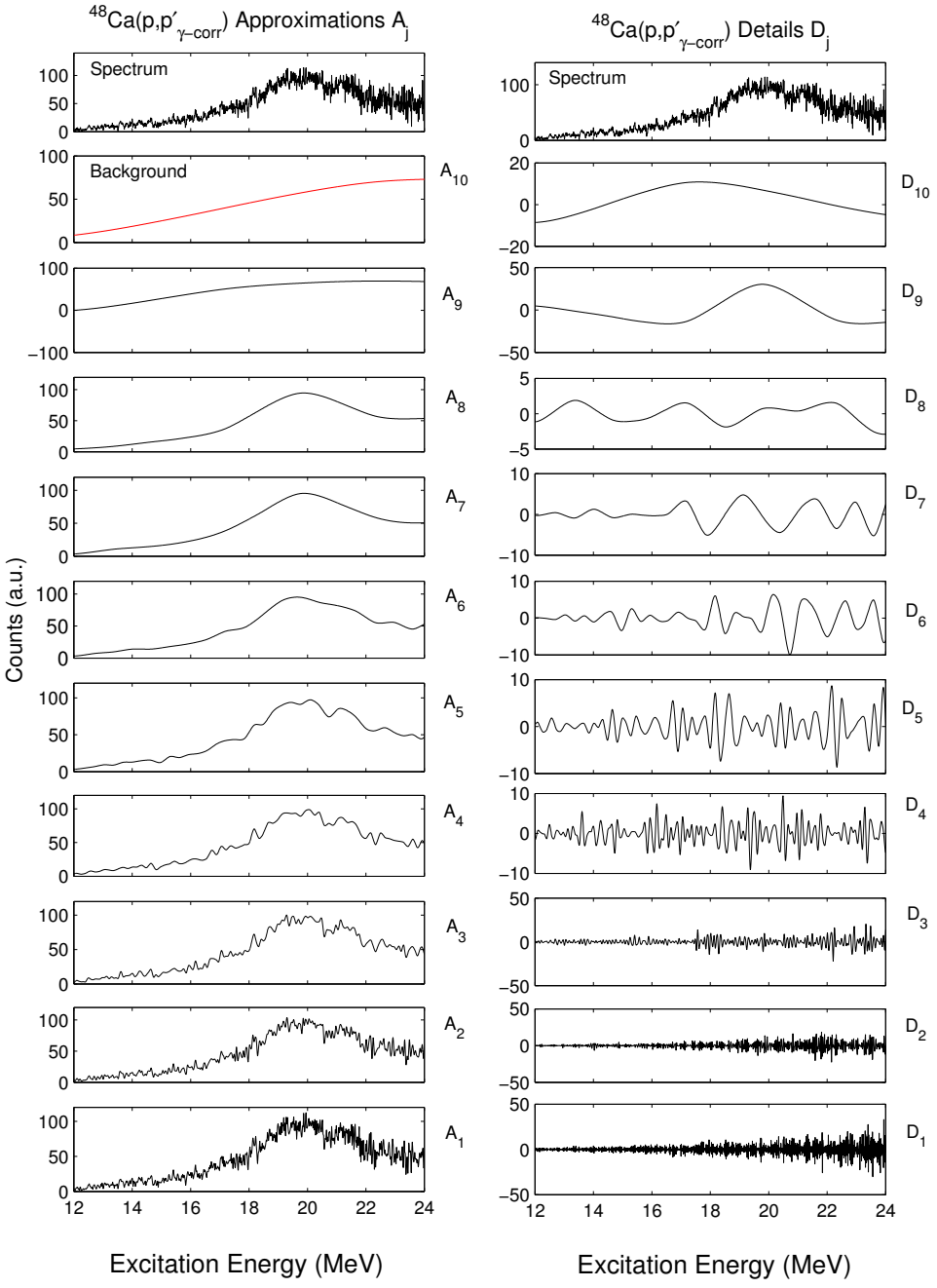

Figure 4.30: Decomposition of the ^{48}Ca(p,p′$_{\gamma-\mathrm{corr}}$) spectrum (*top panel)* which was measured at $E_\mathrm{p} = 200$ MeV and $\theta_\mathrm{Lab} = 0^o$ into approximation A_j and details D_j using the Bior6.8 type of DWT. The approximation A_{10} (in red) is adopted as the Bior6.8 background.

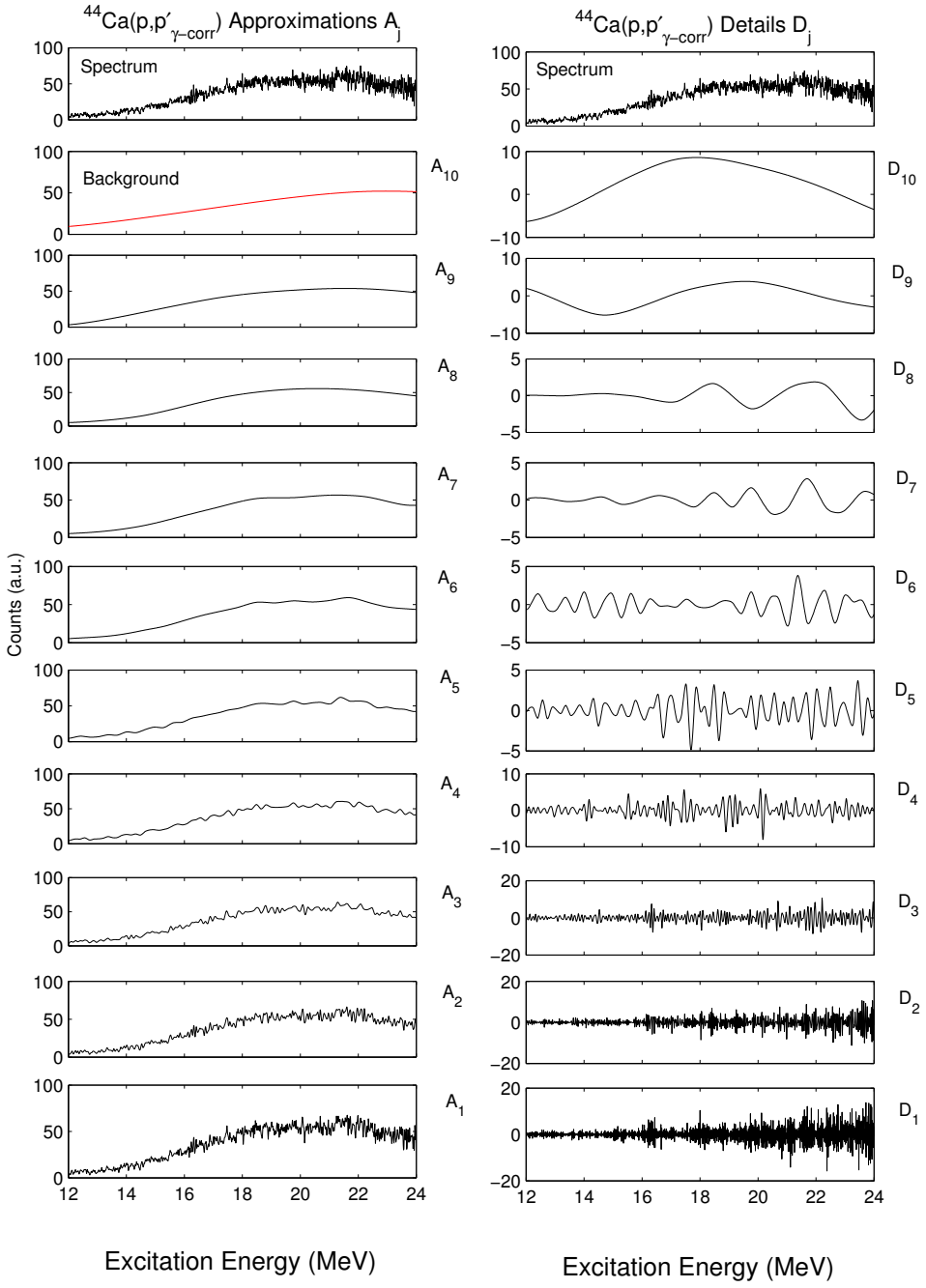

Figure 4.31: Decomposition of the ^{44}Ca(p,p$'_{\gamma-\mathrm{corr}}$) spectrum (*top panel)* which was measured at $E_\mathrm{p} = 200$ MeV and $\theta_\mathrm{Lab} = 0^o$ into approximation A_j and details D_j using the Bior6.8 type of DWT. The approximation A_{10} (in red) is adopted as the Bior6.8 background.

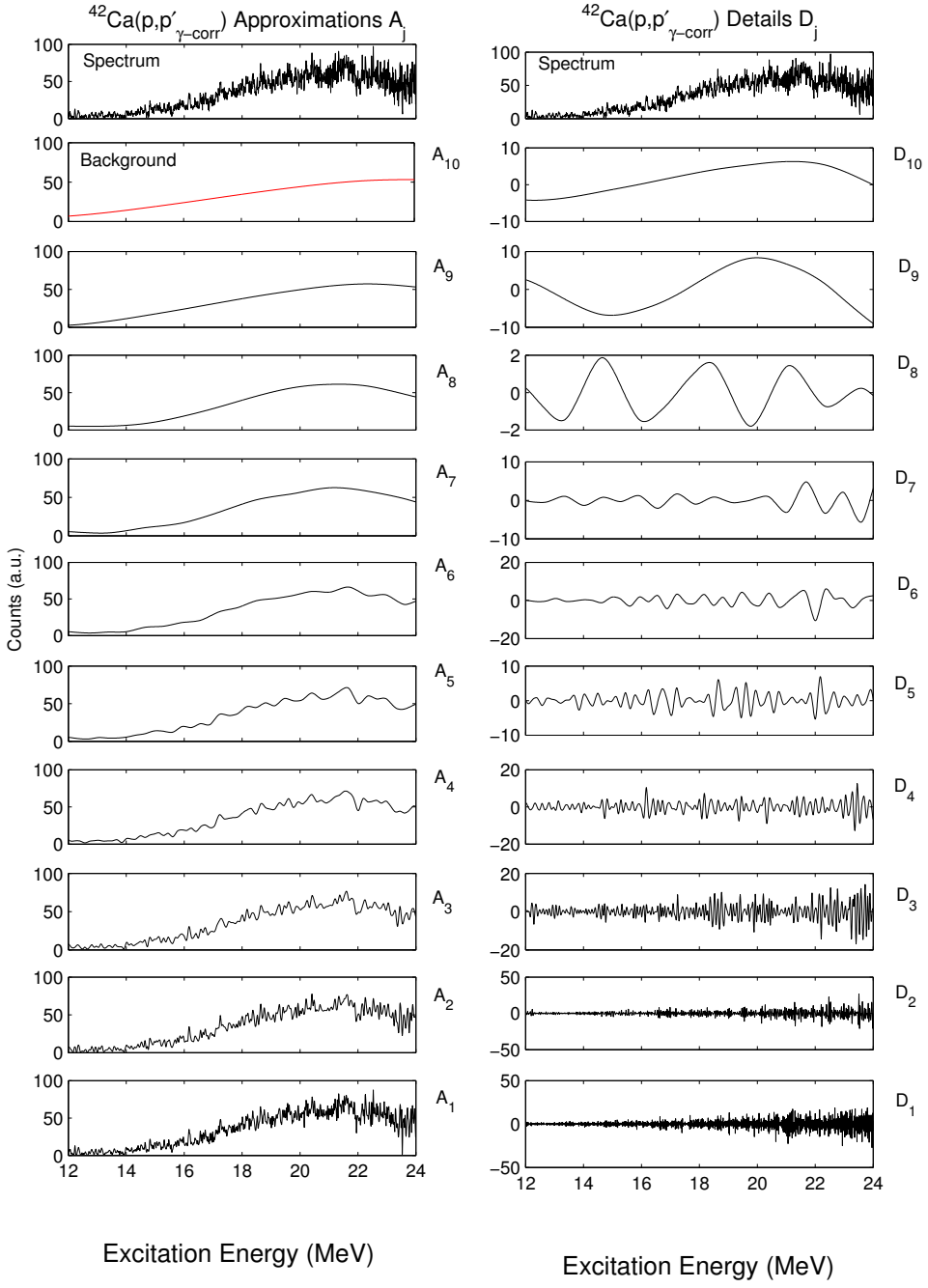

Figure 4.32: Decomposition of the ^{42}Ca(p,p$'_{\gamma-\mathrm{corr}}$) spectrum (*top panel)* which was measured at $E_\mathrm{p} = 200$ MeV and $\theta_\mathrm{Lab} = 0^o$ into approximation A_j and details D_j using the Bior6.8 type of DWT. The approximation A_{10} (in red) is adopted as the Bior6.8 background.

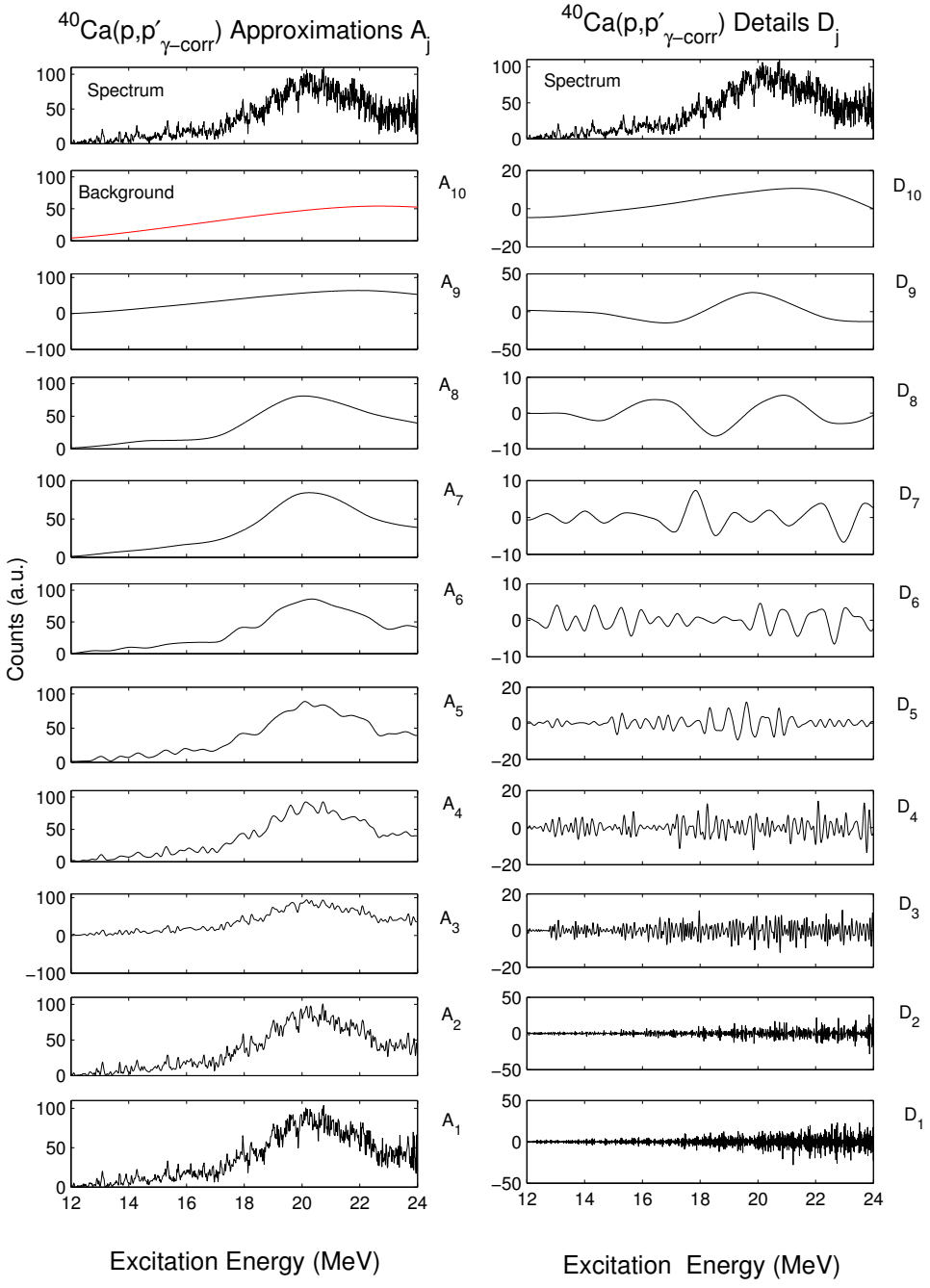

Figure 4.33: Decomposition of the ^{40}Ca(p,p$'_{\gamma-\mathrm{corr}}$) spectrum (*top panel)* which was measured at $E_\mathrm{p} = 200$ MeV and $\theta_\mathrm{Lab} = 0^o$ into approximation A_j and details D_j using the Bior6.8 type of DWT. The approximation A_{10} (in red) is adopted as the Bior6.8 background.

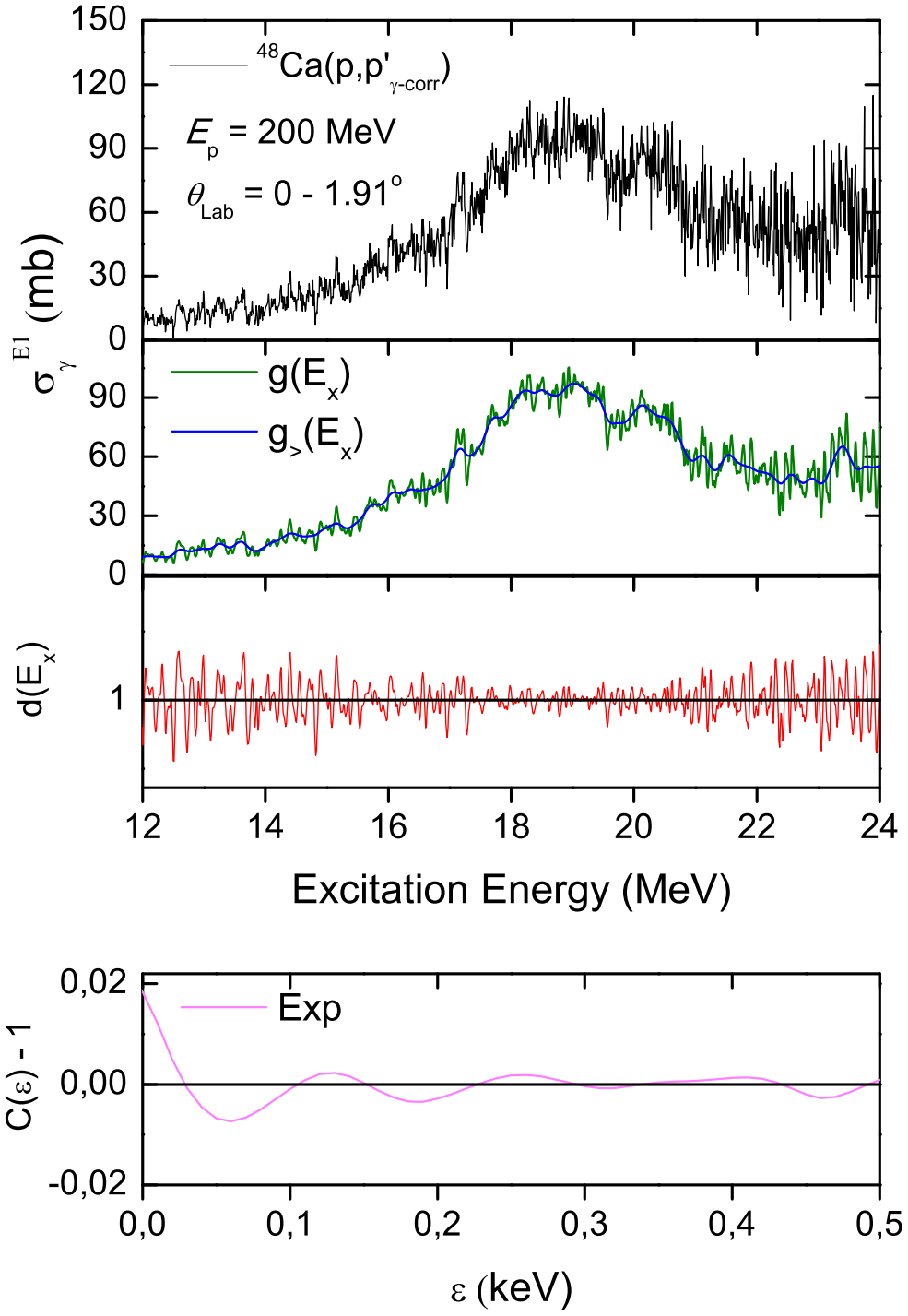

Figure 4.34: From top to bottom: The background subtracted ^{48}Ca(p,p$'_{\gamma-\mathrm{corr}}$) spectrum acquired at E_p = 200 MeV and $\theta_\mathrm{Lab} = 0^o$; $g(E_\mathrm{x})$ and $g_>(E_\mathrm{x})$ are the smoothed spectra; $d(E_\mathrm{x})$ is the stationary spectrum; and, the experimental auto-correlation function in pink colour (*bottom panel*).

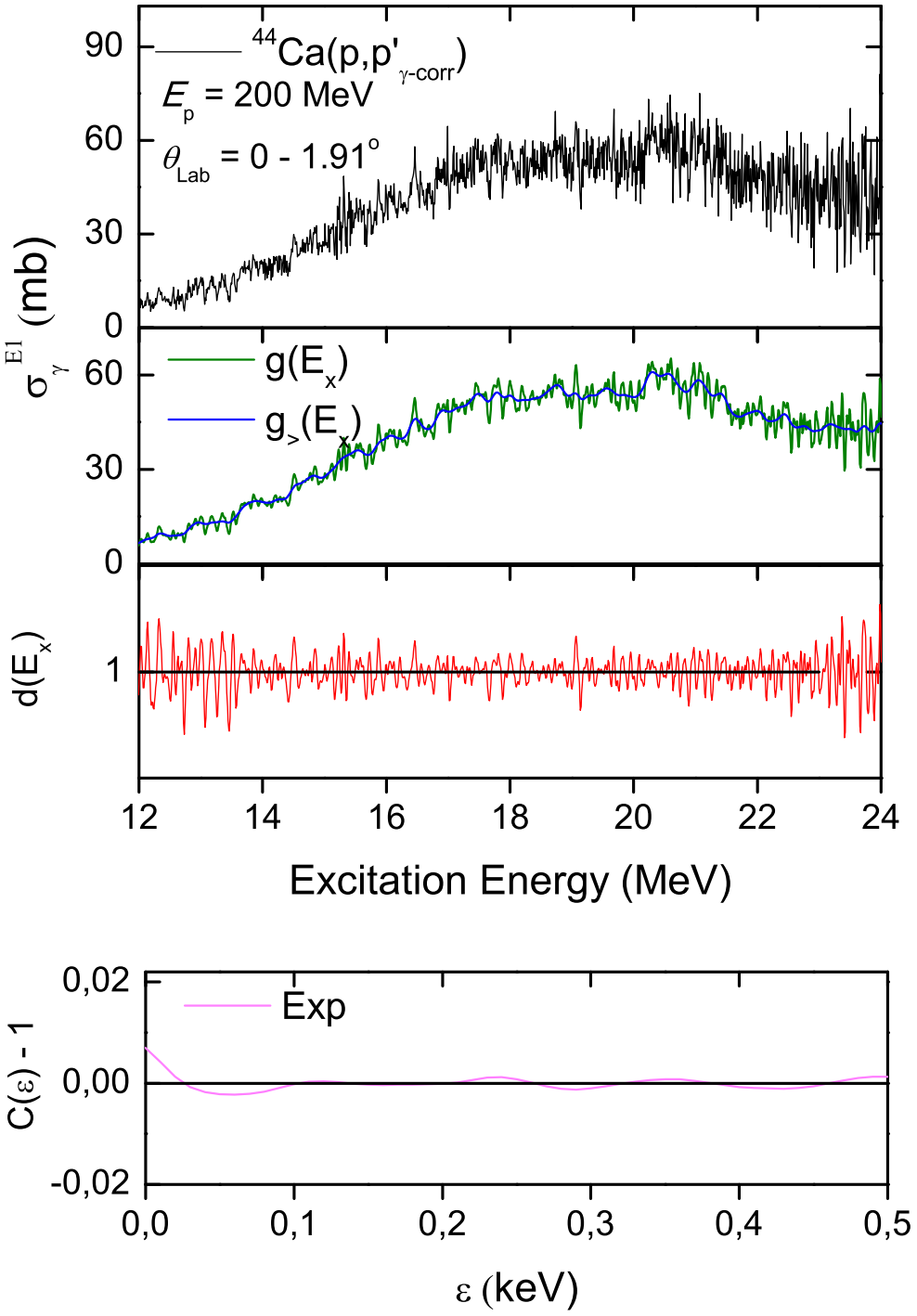

Figure 4.35: From top to bottom: The background subtracted ^{44}Ca(p,p$'_{\gamma-\mathrm{corr}}$) spectrum acquired at E_p = 200 MeV and $\theta_\mathrm{Lab} = 0^o$; $g(E_\mathrm{x})$ and $g_>(E_\mathrm{x})$ are the smoothed spectra; $d(E_\mathrm{x})$ is the stationary spectrum; and, the experimental auto-correlation function in pink colour (*bottom panel*).

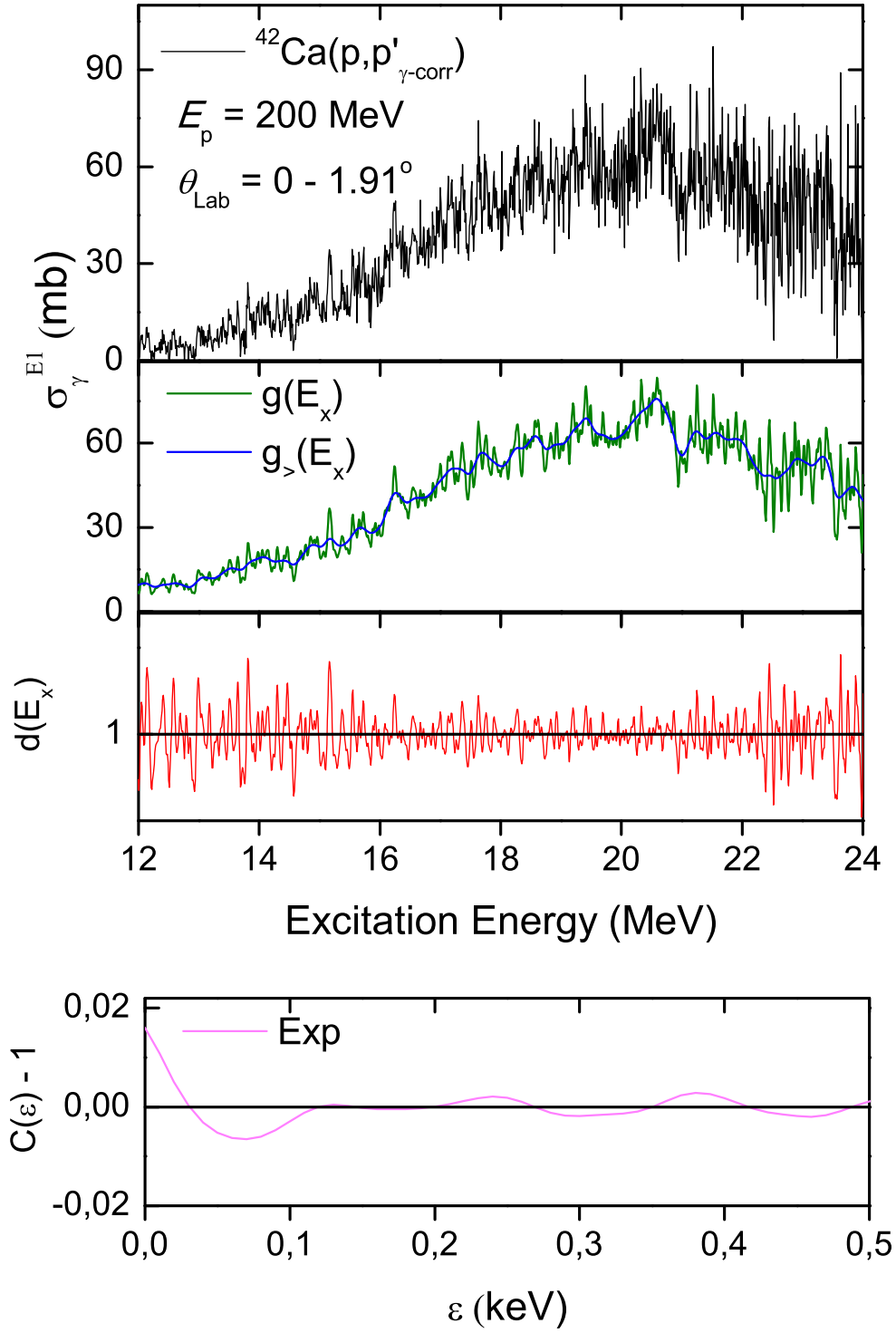

Figure 4.36: From top to bottom: The background subtracted ^{42}Ca(p,p$'_{\gamma-\mathrm{corr}}$) spectrum acquired at E_p = 200 MeV and $\theta_\mathrm{Lab} = 0^o$; $g(E_\mathrm{x})$ and $g_>(E_\mathrm{x})$ are the smoothed spectra; $d(E_\mathrm{x})$ is the stationary spectrum; and, the experimental auto-correlation function in pink colour (*bottom panel*).

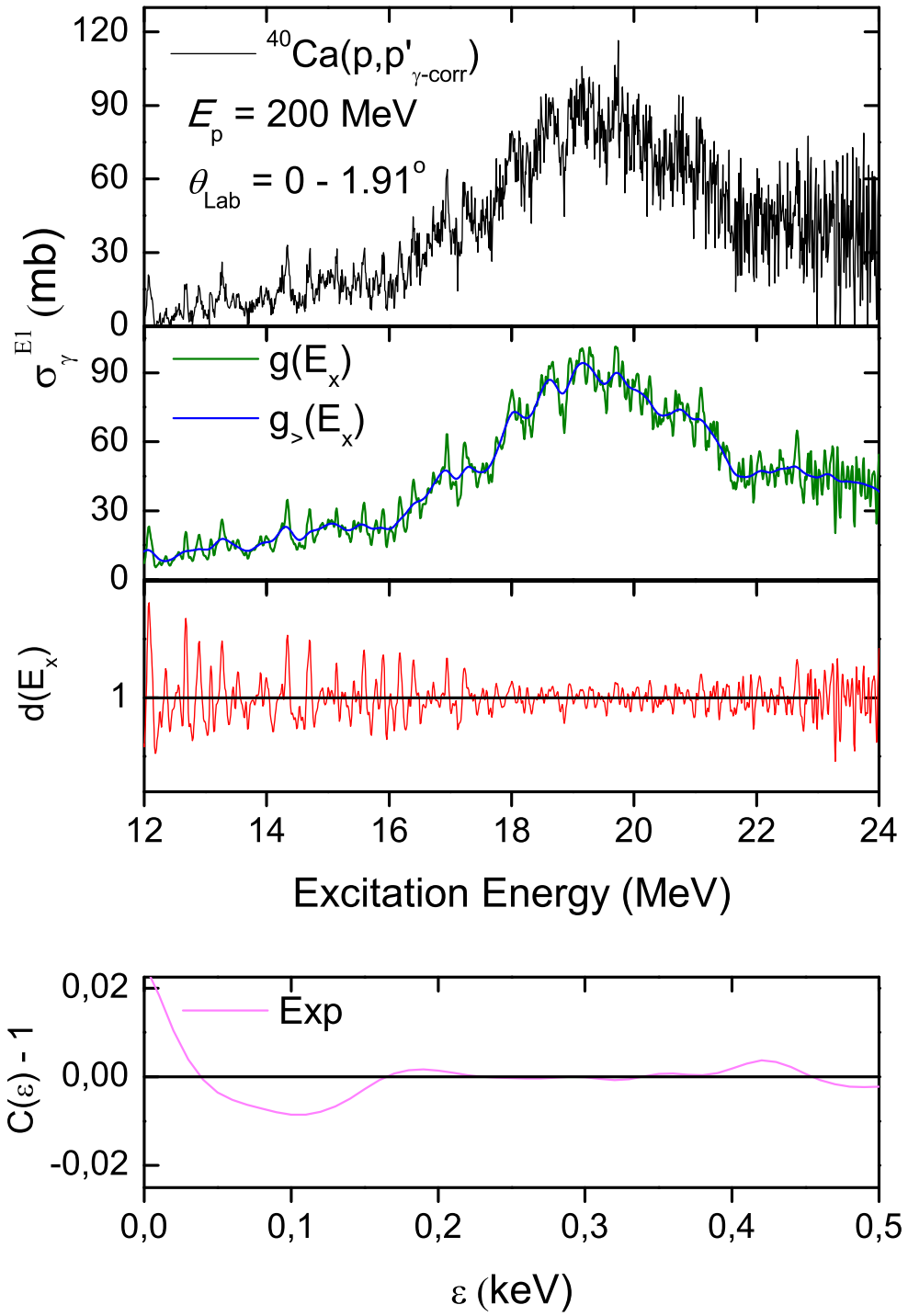

Figure 4.37: From top to bottom: The background subtracted ^{40}Ca(p,p$'_{\gamma-\mathrm{corr}}$) spectrum acquired at E_p = 200 MeV and $\theta_\mathrm{Lab} = 0^o$; $g(E_\mathrm{x})$ and $g_>(E_\mathrm{x})$ are the smoothed spectra; $d(E_\mathrm{x})$ is the stationary spectrum; and, the experimental auto-correlation function in pink colour (*bottom panel*).

Table 4.6: Level density evaluation input parameters for the calcium isotopes.

Calcium Isotope	ΔE (MeV)	σ (keV)	$\sigma_>$ (keV)	y	F($\Delta E, \sigma, \sigma_>$)
^{40}Ca	0.047	24	60	2.5	0.3495
^{42}Ca	0.04	20	50	2.5	0.3495
^{44}Ca	0.033	17	43	2.5	0.3495
^{48}Ca	0.04	20	50	2.5	0.3495

isotopes, Eq. (4.6) reduces to:

$$\begin{aligned} \langle D \rangle_{^{40}Ca} &= 0.210 \times (C(\epsilon = 0) - 1) \\ \langle D \rangle_{^{42}Ca} &= 0.170 \times (C(\epsilon = 0) - 1) \\ \langle D \rangle_{^{44}Ca} &= 0.147 \times (C(\epsilon = 0) - 1) \\ \langle D \rangle_{^{48}Ca} &= 0.170 \times (C(\epsilon = 0) - 1). \end{aligned} \tag{4.7}$$

The obtained results of level density were plotted together with the theoretically predicted values of level density based on the Hartree-Fock Bogolyubov (HFB) [Hil06], the Hartree-Fock-Bardeen-Cooper-Schrieffer (HF-BCS) [Dem01] and two phenomenological models of the back-shifted Fermi gas model (BSFG) [Rau97, Egi05] in Figs. 4.38 - 4.41 for ^{48}Ca, ^{44}Ca, ^{42}Ca and ^{40}Ca, respectively. Also, the extracted values of level densities at the excitation energies of 13, 17 and 20 MeV together with the predictions of the BSFG of Ref. [Rau97] are summarised in Table 4.7.

4.5.3 Error estimation in the evaluation of the experimental level density

Errors associated with the evaluation of the experimental level density originate from the following sources [Usm11b]:

(i) the choice of the DWT wavelet function;

(ii) the choice of the width of the smoothing Gaussian function; and,

Table 4.7: Extracted values of level densities from the ^{40,42,44,48}Ca(p,p$'_{\gamma-\mathrm{corr}}$) spectra and the prediction of the BSFG of Ref. [Rau97] at the excitation energies of 13, 17 and 20 MeV.

Ca-isotope	E_{X}(MeV)	Experimental value	BSFG of Ref. [Rau97]
^{48}Ca	13	164.03 ± 62.9	131.40
	17	528.66 ± 246.6	1037.25
	20	1516.30 ± 703.2	4234.90
^{44}Ca	13	436.32 ± 160.9	208.69
	17	3373.69 ± 2026	1493.82
	20	2892.68 ± 1813.9	5666.304
^{42}Ca	13	273.38 ± 87.74	153.97
	17	914.65 ± 252.87	1032.46
	20	2009.48 ± 727.35	3753.96
^{40}Ca	13	82.33 ± 21.32	55.03
	17	310.42 ± 39.94	362.18
	20	953.28 ± 213	1318.14

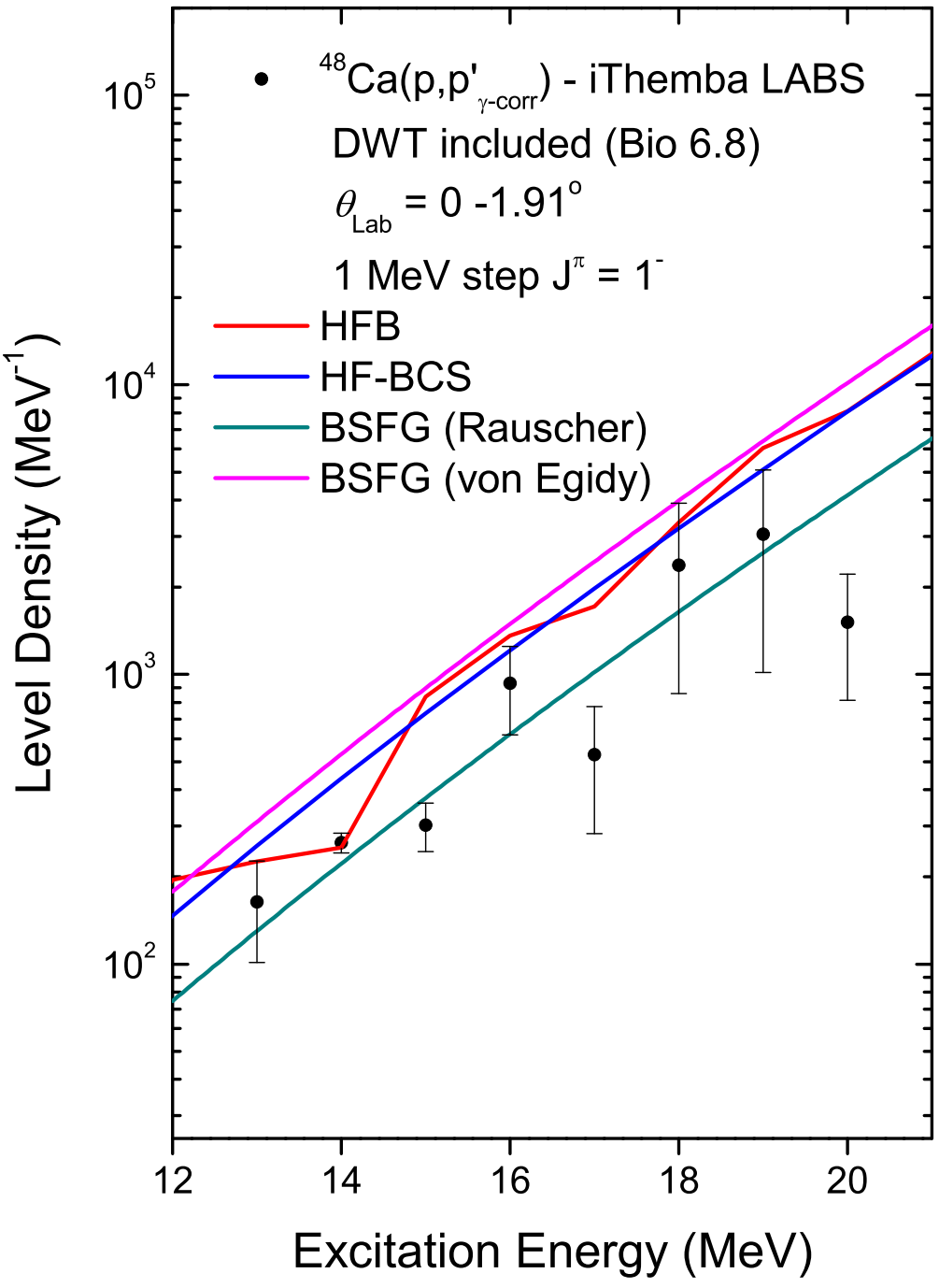

Figure 4.38: A plot of the experimental level density of ^{48}Ca together with the parametrisations of the HFB (red line), HF-BCS (blue line), BSFG of Ref. [Rau97] (dark cyan line) and the BSFG of Ref. [Egi05] (magenta line).

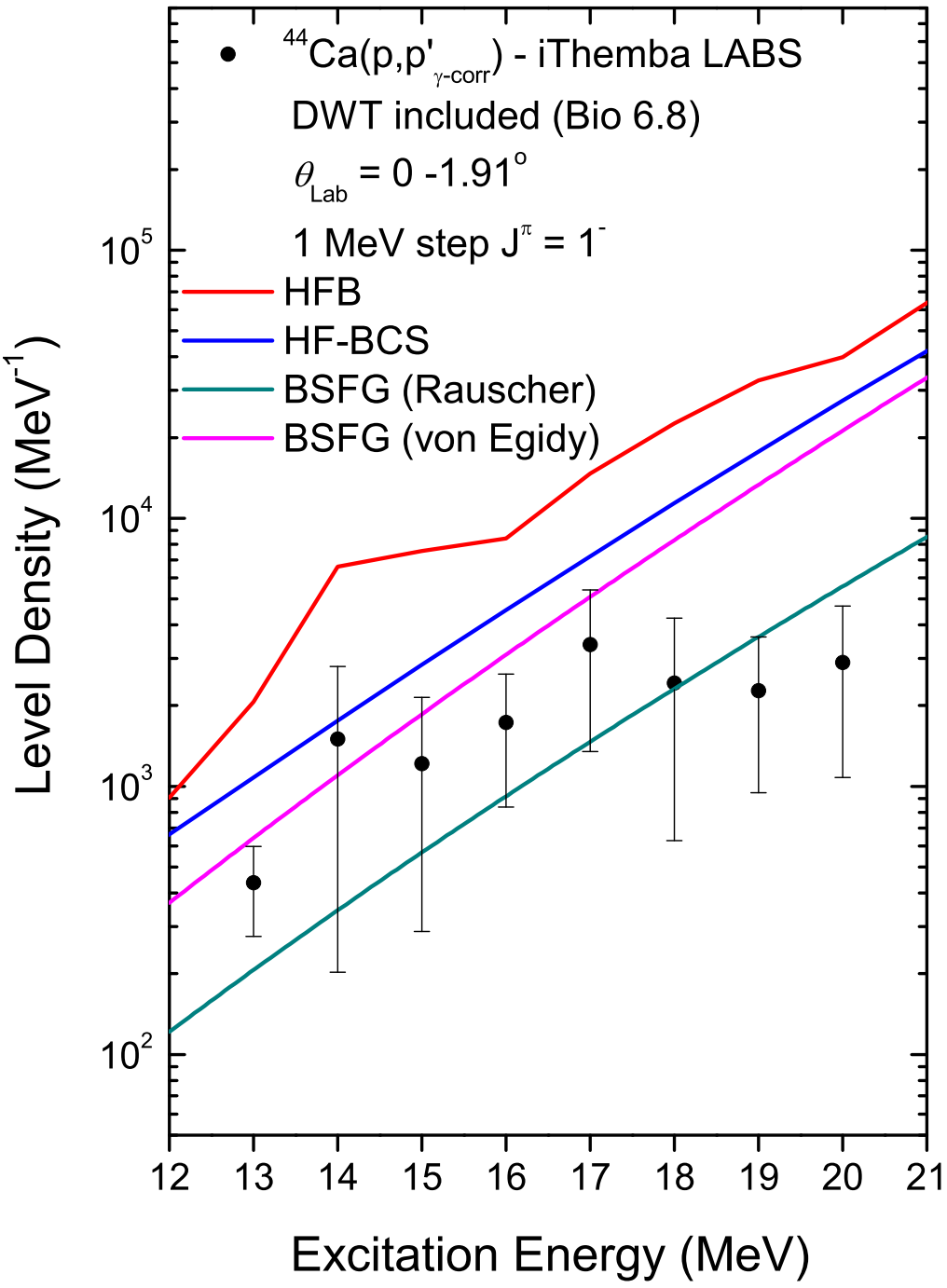

Figure 4.39: A plot of the experimental level density of ^{44}Ca together with the parametrisations of the HFB (red line), HF-BCS (blue line), BSFG of Ref. [Rau97] (dark cyan line) and the BSFG of Ref. [Egi05] (magenta line).

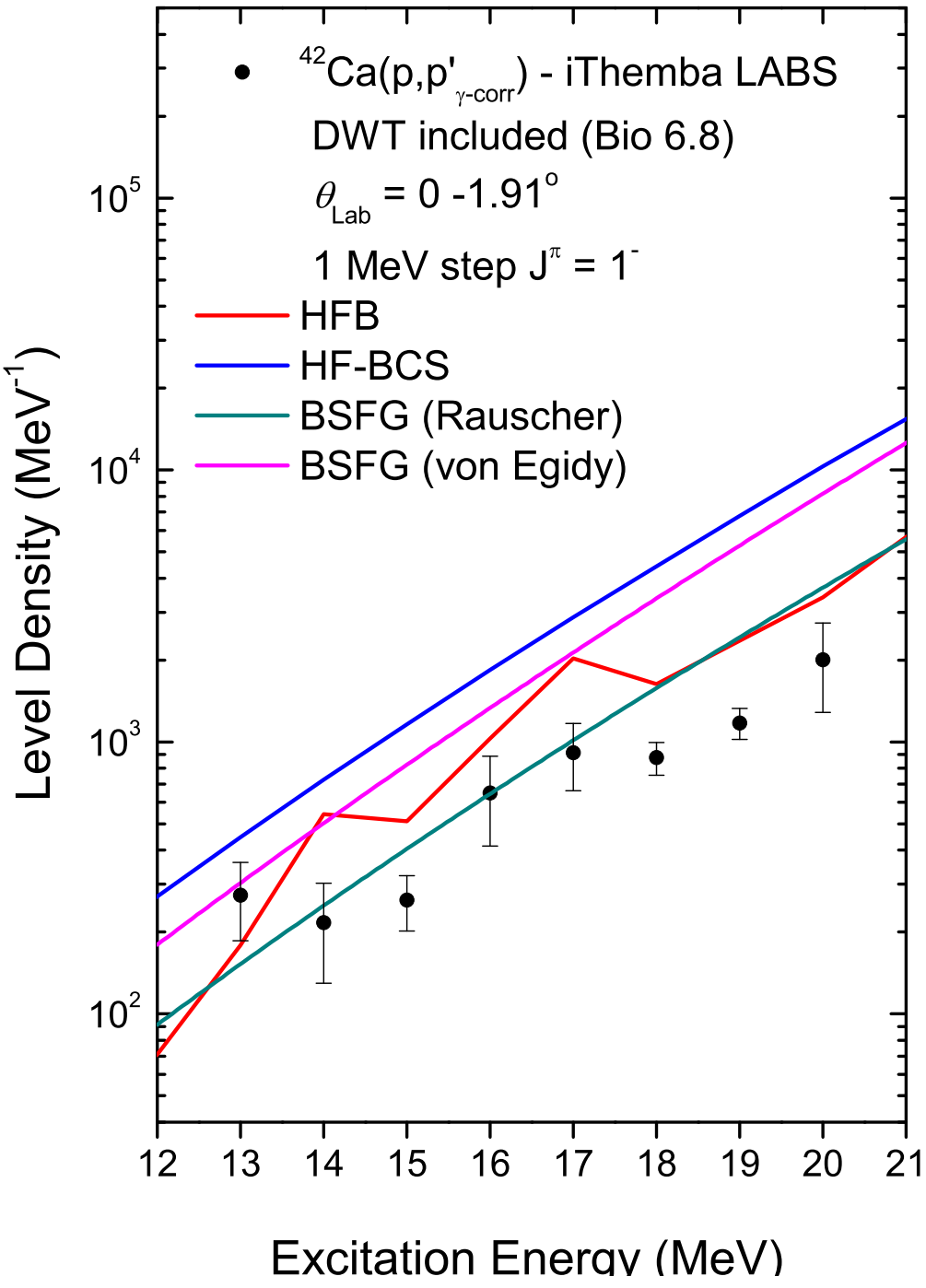

Figure 4.40: A plot of the experimental level density of ^{42}Ca together with the parametrisations of the HFB (red line), HF-BCS (blue line), BSFG of Ref. [Rau97] (dark cyan line) and the BSFG of Ref. [Egi05] (magenta line).

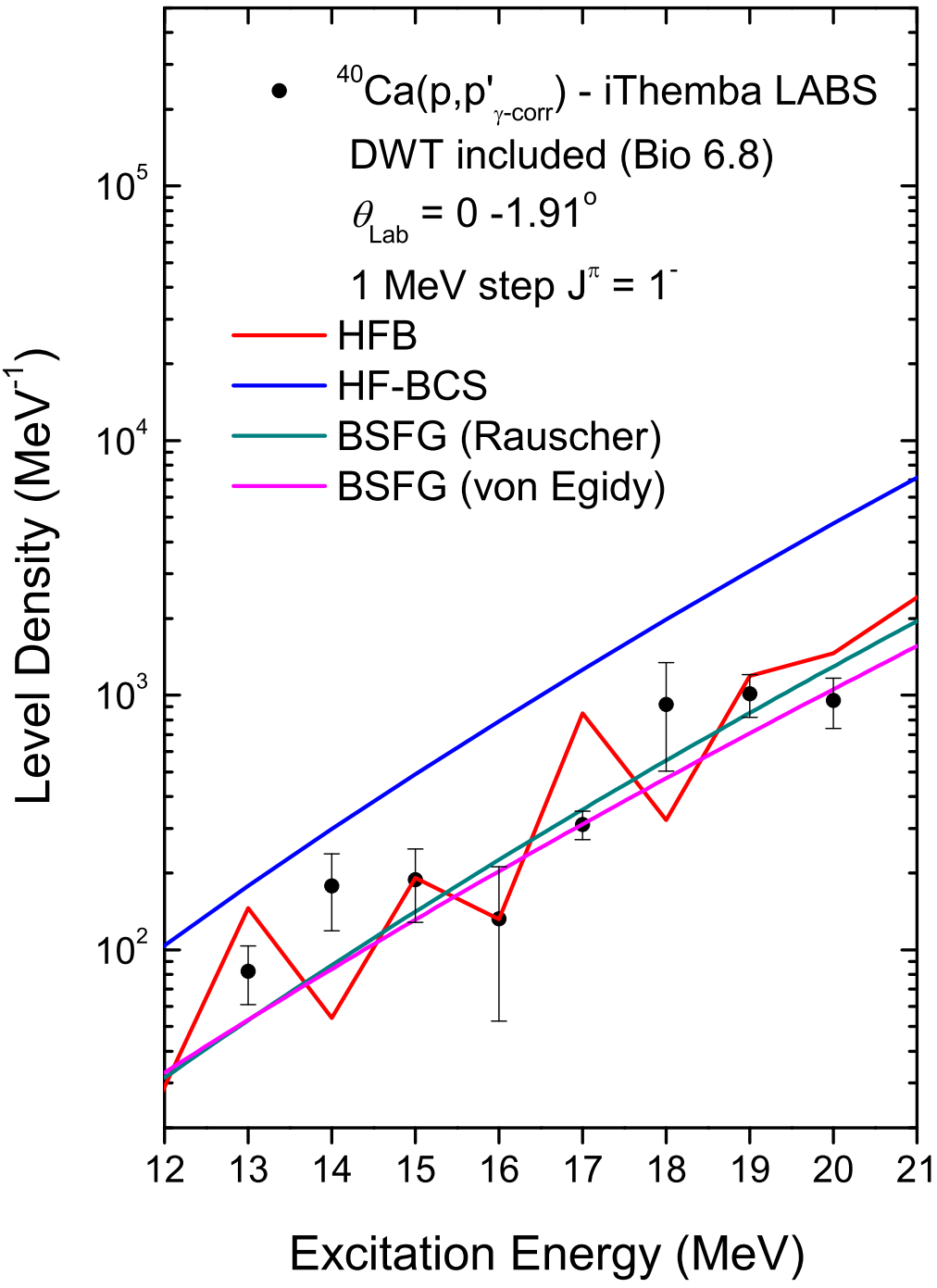

Figure 4.41: A plot of the experimental level density of ^{40}Ca together with the parametrisations of the HFB (red line), HF-BCS (blue line), BSFG of Ref. [Rau97] (dark cyan line) and the BSFG of Ref. [Egi05] (magenta line).

(iii) the choice of the length of the energy interval.

Error emanating from the choice of the DWT background model was investigated by using Bior5.5 and comparing to the result obtained using Bior6.8. It was observed that the error contribution was significant at the lower end of the excitation energy range considered while it reduces significantly and tends to vanish with increasing excitation energy. For all four calcium isotopes, this type of error contributed about 5% of the measured level density value. In order to account for uncertainties due to the choice of the widths of the smoothing functions, the ratio $\frac{\sigma_>}{\sigma}$ was varied between 2.5 - 3.5 [Pol14] and the error contribution was observed to be below 1% of the measured value. Too short intervals were not considered in order to avoid errors in the autocorrelation function owing to the finite range of data points. Similarly, too long intervals were avoided as the exponential dependence of the level spacing is substituted in the analysis with a linear expression [Usm11b, Pol14]. In a bid to account for the uncertainty due to the choice of the length of the energy segments, various energy intervals were also considered ranging between 800 keV to up to 2 MeV and the error contributions varied from isotope to isotope as discussed below.

4.5.4 Discussion

As seen in Figs. 4.38 - 4.41 the experimental level density results of all the calcium isotopes under study are compared with the parametrisations of microscopic models of the HFB and HF-BCS and those of phenomenological models of the BSFG.

In the case of ^{48}Ca, the results of level density extracted from the experimental data show an energy dependence similar to those of the parametrisations of the HF-BCS and both parametrisations of the BSFG. In terms of magnitude, however, the BSFG of Ref. [Rau97] best describes the experimental results. The BSFG of Ref. [Egi05] and the HF-BCS overestimate it by factors of $\sim$ 3 and 2, respectively. The HFB model fails to reproduce the experimental data both

in energy dependence and magnitude. The sharp decrease in level density at 17 MeV and 20 MeV can be attributed to statistical fluctuations resulting from decrease in count rate as can be observed in Fig.4.34. The error contributions to the measured experimental level density values varied significantly between 17 MeV and 20 MeV. The bulk of the error contribution emanated from the change in energy interval.

For ^{44}Ca just like in the case of ^{48}Ca, the experimental level density has an energy dependence comparable to those of the parametrisations of the HF-BCS and the two BSFG for excitation energies of 13 - 17 MeV. The BSFG model of Ref. [Egi05], however, best describes the experimental level density in terms of magnitude over that energy range. While the BSFG model of Ref. [Rau97] underestimates the experimental level density by about a factor of 1.5 the HF-BCS rather overestimates it by a factor of ~ 2.5. Again, the HFB model fails to predict the experimental level density in both magnitude and energy dependence. For the excitation energy range of 18 - 20 MeV, the BSFG model of Ref. [Rau97] best describe the experimental level density as compared to the other models. The error contribution in this case as in the case of ^{48}Ca is mostly accounted for by the change in energy intervals.

The experimental level density of ^{42}Ca agrees excellently with the predictions of the BSFG model of Ref. [Rau97] compared to other models which severely overestimate it. In this case the error contribution due to change in energy intervals is not as significant as in the cases of ^{48}Ca and ^{44}Ca. The error contribution at 13 MeV is mostly due to the choice of the DWT function for the background subtraction.

In the case of ^{40}Ca the parametrisations of the HFB model although have comparable magnitudes with the experimental values of level density, there is a considerable difference in their energy dependences. The HF-BCS predicted values

are significantly higher than the experimentally extracted values of level density. Again, the parametrisations of the 2 BSFG models give the best description of the experimental level density over the excitation energy range of 13 - 20 MeV, both of which are also of comparable magnitude over that energy region. Here, the error contribution which is mostly due to change in energy intervals, has its lowest value at 16 MeV and highest value at 18 MeV.

Also, as seen in the Table 4.7, the experimental level density values of the doubly magic nuclei of ^{40,48}Ca are lower than those of the semi-magic nuclei of ^{42,44}Ca at the selected excitation energies of 13, 17 and 20 MeV.

It can be concluded from the present study that the level density of the $J^{\pi} = 1^{-}$ states extracted from high energy resolution (p,p$'_{\gamma-\mathrm{corr}}$) spectra of ^{40,42,44,48}Ca are well described by the parametrisations of the BSFG model of Ref. [Rau97] over the excitation energy of 13 - 20 MeV. In the case of ^{44}Ca, the experimental results are in better agreement with the parametrisations of the BSFG of Ref. [Egi05] between 13 - 17 MeV. It is however important to note that in most cases there were slight differences between the magnitude of the experimentally extracted level density and those of the theoretical model that best described it.

Chapter 5

Conclusion and recommendations

In the present study, the ability of high energy resolution proton inelastic scattering measurements to extract important nuclear structure information from atomic nuclei was once again tested.

High energy-resolution zero-degree (p,p′) experiments were carried out on the neutron-rich ^{42}Ca, ^{44}Ca and ^{48}Ca and excellent energy resolution of $\sim \Delta E =$ 33 keV was achieved. Fine structure was observed in the region of the isovector giant dipole resonance (IVGDR) which lies in the energy range 11 - 25 MeV. For the sake of systematic investigation, data of the IVGDR of ^{40}Ca acquired under similar experimental conditions were included in this study.

Double differential cross-sections were extracted from the experimental data from which equivalent photo-absorption cross-section were derived by means of the virtual photon production technique. Excellent agreement was found between the extracted equivalent photo-absorption cross-sections and the photo-absorption cross-sections of ^{40}Ca, ^{42}Ca, ^{44}Ca and ^{48}Ca, measured from photo-neutron reactions already reported in the literature.

By means of Gaussian and Lorentzian fits of the obtained experimental data,

the centroids and widths of the IVGDR of these isotopes were extracted and the obtained results were found to be in good agreement with the predictions of the macroscopic models in which these parameters are expressed in terms of the atomic mass number of the nuclei.

Furthermore, the characteristic energy scales of the IVGDR of these isotopes were extracted from the obtained high energy resolution data and compared to those of theoretical calculations conceived within the framework of the Relativistic Quasi-particle Time Blocking Approximation (RQTBA), the Relativistic Quasi-particle Random Phase Approximation (RQRPA), the Quasi-particle Random Phase Approximation (QRPA), the Second Random Phase Approximation (SRPA), the Continuum Random Phase Approximation (CRPA) and the ordinary Random Phase Approximation (RPA). Of all these models, the RQTBA best described the experimental data for all the four isotopes of calcium in terms of reproducibility of the energy scales present in them as well as in terms of the amount of fine structure exhibited and the prediction of the centroid energies, compared to the other models.

In terms of the origin of the observed scales in the experimental data of the calcium isotopes, the results of the QRPA calculations for all 4 calcium isotopes together with those of the SRPA, CRPA and RPA in the cases of the doubly-magic ^{48}Ca and ^{40}Ca led to the conclusion that Landau damping accounts for scales observed in Classes II and III with some contribution from the escape width especially for the Class II scales. The role of Landau damping has also been reported for the isoscalar giant quadrupole resonance of ^{40}Ca with similar theoretical model calculations [Usm11a]

The Class I scales failed to be reproduced with most of the theoretical models employed in the present study. This raises the question of the origin of the Class I scales present in ^{40,42,44,48}Ca extracted from high energy resolution (p,p$'$)

measurements.

The experimental level density results show very good agreement with the parametrisations of the theoretical phenomenological models of the Back-shifted Fermi Gas (BSFG) over those of the theoretical microscopic models of the Hartree-Fock Bogolyubov (HFB) and the Hartree-Fock-Bardeen-Cooper-Schrieffer (HF-BCS). However, the BSFG of Ref. [Rau97] gave a better prediction of the experimental level density for all four calcium isotopes over the one of Ref. [Egi05].

5.1 Recommendations

In order to gain more insights into the origin of the low energy scales observed in the experimental data of ^{40}Ca, ^{42}Ca, ^{44}Ca and ^{48}Ca, more sophisticated theoretical calculations would be required as they were only well reproduced with the RQTBA model calculations.

Moreover, similar study on ^{46}Ca in the future would allow for an update of the database of the complete chain of the stable calcium isotopes with ground state $J^{\pi} = 0^{+}$.

References

[Abo02] S. N. Abolmasov, A. A. Bizyukov, Y. Kawai, A. Y. Kashaba, V. I. Maslov, and K. N. Sereda, Japanese Journal of Applied Physics **41** (2002) 5415.

[Ada84] S. Adachi and N. Van Giai, Physics Letters **B 149** (1984) 447.

[Ahr75] J. Ahrens, H. Borchert, K. H. Czock, H. B. Eppler, H. Gimm, H. Gundrum, M. Kröning, P. Riehn, G. Sita Ram, A. Zieger, and B. Ziegler, Nuclear Physics **A 251** (1975) 479.

[Aib03] H. Aiba, M. Matsuo, S. Nishizaki, and T. Suzuki, Physical Review **C 68** (2003) 054316.

[Aib99] H. Aiba and M. Matsuo, Physical Review **C 60** (1999) 034307.

[Ass81] Y. Assafiri and M. Thompson, Nuclear Physics **A 357** (1981) 429.

[Aue75] N. Auerbach and N. Yeverechyahu, Annals of Physics **95** (1975) 35.

[Bag65] J. E. E. Baglin and B. M. Spicer, Nuclear Physics **54** (1965) 549.

[Bal47] G. C. Baldwin and G. S. Klaiber, Physical Review **71** (1947) 3.

[Bal48] G. C. Baldwin and G. S. Klaiber, Physical Review **73** (1948) 1156.

[Ber14] C. Bertulani (2014) Private communication.

[Ber75] B. L. Berman and S. C. Fultz, Reviews of Modern Physics **47** (1975) 713.

[Ber77a] R. Bergère, *Photonuclear Reactions I*, Lecture Notes in Physics-Springer **61** (1977).

[Ber77b] W. Bertozzi, M. V. Hynes, C. P. Sargent, C. Creswell, P. C. Dunn, A. Hirsch, M. Leitch, B. Norum, F. N. Rad, and T. Sasanuma, Nuclear Instruments and Methods **141** (1977) 457.

[Ber83] G. F. Bertsch, P. F. Bortignon, and R. A. Broglia, Reviews of Modern Physics **55** (1983) 287.

[Ber85] C. A. Bertulani and G. Baur, Nuclear Physics **A 442** (1985) 739.

[Ber88] C. A. Bertulani and G. Baur, Physics Reports **163** (1988) 299.

[Ber91] G. Bertsch, **Computational Nuclear Physics I**, K. Langanke, J. E. Maruhn, S. E. Koonin (Eds.), *Springer-Verlag* (1991).

[Ber93a] C. A. Bertulani and A. M. Nathan, Nuclear Physics **A 554** (1993) 158.

[Ber93b] M. Berz, K Joh, J. A. Nolen, B. M. Sherrill, A. F. Zeller, Physical Review **C 47** (1993) 537.

[Bev03] P. R. Bevington and D. K. Robinson, *Data Reduction and Error Analysis for Physical Sciences* Third Edition, McGraw-Hill Higher Education (2003).

[Bir16] J. H. Birkhan, PhD thesis, Technische Universität Darmstadt, Germany (2016) Unpublished.

[Blo63] B. Block and H. Feshbach, Annals of Physics **23** (1963) 47.

[Blo71] H. G. Blosser, G. M Crawley, R. Deforest, E. Kashy, and B. H. Wildenthal, Nuclear Instruments and Methods **91** (1971) 61.

[Blu08] W. Blum, W. Riegler and L. Rolandi, *Particle detection with drift chambers*, Springer Science & Business Media (2008).

[Boh51] D. Bohm and D. Pines, Physical Review **82** (1951) 625.

[Boh98] A. Bohr and B. R. Mottelson, *Nuclear Structure*, World Scientific (1998).

[Bot37] W. Bothe and W. Z. Gentner, Zeitschrift für Physik **71** (1937) 236.

[Bow83] J. D. Bowman, H. W. Baer, R. Bolton, M. D. Cooper, F. H. Cverna, N. S. P. King, M. Leitch, H. S. Matis, E. Erell, J. Alster, A. Doron, M. A. Moinster, E. Balckmore, and E. R. Siciliano, Physical Review Letters **50** (1983) 1195.

[Box58] G. E. P. Box and M. E. Muller, The Annals of Mathematical Statistics **29** (1958) 610.

[Bro14] Brookhaven National Laboratory, *National Nuclear Data Center (NNDC)*. Accessed in (2014). www.nndc.bnl.gov.

[Bro59] G. E. Brown and M. Bolsterli, Physical Review Letters **3** (1959) 472.

[Bru97] R. Brun and F. Rademakers, ROOT - An Object Oriented Data Analysis Framework, Proceedings AIHENP'96 Workshop, Lausanne, Sep. 1996, Nuclear Instruments and Methods in Physics Research **A 389** (1997) 81. See also http://root.cern.ch/.

[But90] J. M. Butler, D. Eartly, D. Green, H. Haggerty, S. Hansen, S. Igarashi, H. Jöstlein, J. Li, R. Li, E. Malamud, H. Mao, P. Martin, N. Oshima, R. Yamada, P. Xie, T. Marshall, S. Kunori, M. Fortner, J. Green, D. Hedin, T. Kramer, P. Lee, A. Tseng, S. Willis, Y. Antipov, B. Baldin, D. Denisov, S. Denisov, V. Glebov and N. Mokhov, Nuclear Instruments and Methods in Physics Research **290** (1990) 122.

[CAE02] CAEN Electronic Instrumentation, Mod.V820/V830, 32ch. Latching/-Multievent Latching Scalar, Technical Information Manula Revision **no. 3** (2002). Available at http://www.tunl.duke.edu/documents/public/electronics/CAEN/caen_v820-v830.pdf.

[CAE10] CAEN Electronic Instrumentation, 32-Channel Multivent QDC, Products Catalog **V792N** (2010). Avalaible at http://www.caen.it/csite/CaenProd.jsp?parent=11&idmod=286.

[CAE12] CAEN Electronic Instrumentation, Mod.V1190-VX1190 A/B 128/64 Ch Multihit TDC, Technical Information Manual Revision **no. 13** (2012). Available at www.caen.it/servlet/checkCaenManualFile?Id=8657.

[Cal98] A. R. Calderbank, I. Daubechies, W. Sweldens, and B. L. Yeo, Applied and Computational Harmonic Analysis **5** (1998) 332.

[Car01] J. Carter, H. Diesener, U. Helm, G. Herbert, P. von Neumann-Cosel, A. Richter, G. Schrieder, and S. Strauch, Nuclear Physics **A 696** (2001) 317.

[Cha98] E. Chabanat, P. Bonche, P. Haensel, J. Meyer, and R. Schaeffer, Nuclear Physics **A 635** (1998) 231.

[Cla96] H. L. Clark, D. H. Youngblood, and Y. W. Lui, Physical Review **C 54** (1996) 72.

[Coh59] B. L. Cohen, Review of Scientific Instruments **30** (1959) 415.

[Con02] J. L. Conradie, P. Andersen, P. J. Celliers, E. A. de Kock, J. L. G. Delsink, J. G. de Villiers, J. S. du Toit, D. T. Fourie, P. Fördelman, M. N. Fredericks, M. E. Hogan, M. F. Jakoet, D. T. L. Jones, I. H. Kohler, Y. E. Manjoo, E. M. Murphy, A. O'Ryan, J. V. Pilcher, D. Prince, P. F. Rohwer, M. J. van Niekerk, H. du Plessis, S. Schroeder, J. F. Sharpey-Schafer, T. N. Symons, T. N. van der Walt, and C. Vermeulen, Proceedings of the 8th European Particle Accelerator Conference (EPAC), 3 - 7 June in Paris, France (2002) 560.

[Con10] J. L. Conradie, L. Anthony, A. H. Botha, J. G. de Villiers, J. L. G. Delsink, W. Duckitt, D. T. Fourie, M. E. Hogan, C. Lussi, I. H. Kohler,

A. Crombie, H. Mostert, R. McAlister, S. S. Ntshangase, J. V. Pilcher, P. F. Rohwer, M. Sakildien, N. Stodart, R. W. Thomae, M. J. van Niekerk, and P. A. van Schalkwyk, Proceedings of 19th International Conference on Cyclotrons and their Applications (CYCLOTRONS 2010), 6 - 10 September, Lanzhou, China (2010) 43.

[Cos94] P. von Neumann-Cosel, H. Diesener, U. Helm, G. Herbert, V. Huck, A. Richter, G. Schrieder, A. Stascheck, A. Stiller, J. Ryckebusch, J. Carter, A. A. Cowley, R. W. Fearick, J. J. lawrie, S. J. Mills, R. T. Newman, J. V. Pilcher, F. D. Smit, Z. Z. Vilakazi, and D. M. Whittal, Nuclear Physics **A 569** (1994) 373.

[Dan50] S. M. Dancoff, Physical Review **78** (1950) 382.

[Dau92] I. Daubechies, *Ten Lectures on Wavelets*, Society for Industrial and Applied Mathematics (1992).

[Dav97] B. F. Davis, U. Garg, W. Reviol, M. N. Harakeh, A. Bacher, G. P. A. Berg, C. C. Foster, E. J. Stephenson, Y. Wang, J. J anecke, K. Pharm, D. Roberts, H. Akimune, M. Fujiwara, and J. Lisantti, Physical Review Letters **79** (1997) 609.

[Dem01] P. Demetriou and S. Goriely, Nuclear Physics **A 696** (2001) 95.

[Die01a] H. Diesener, U. Helm, P. von Neumann-Cosel, A. Richter, G. Schrieder, A. Stascheck, A. Stiller, and J. Carter, Nuclear Physics **A 696** (2001) 272.

[Die01b] H. Diesener, U. Helm, V. Huck, P. von Neumann-Cosel, C. Rangacharyulu, A. Richter, G. Schrieder, A. Stascheck, S. Strauch, J. Ryckebusch, and J. Carter, Nuclear Physics **A 696** (2001) 293.

[Die94] H. Diesener, U. Helm, G. Herbert, V. Huck, P. von Neumann-Cosel, C. Rangacharyulu, A. Richter, G. Schrieder, A. Stascheck, A. Stiller, J. Ryckebusch and J. Carter, Physical Review Letters **72** (1994) 1994.

[Dil73] W. Dilg, W. L. Schantl, H. Vonah, and M. Uhl, Nuclear Physics **A 217** (1973) 269.

[Dro08] M. Drosg, *LARELKIN Two-body relativistic kinematics code Version*, Nuclear Data Services, International Atomic Energy Agency (IAEA) (2008). See https://www-nds.iaea.org/public/libraries/larelkin/.

[Dro86] S. Drozdz, V. Klemt, J. Speth, and J. Wambach, Nuclear Physics **A 451** (1986) 11.

[Egi05] T. von Egidy and D. Bucurescu, Physical Review **C 72** (2005) 044311.

[Ego16] I. A. Egorova and E. Litvinova, Physical Review **C 94** (2016) 034322.

[Eng81] H. A. Enge, Nuclear Instruments and Methods in Physics Research **187** (1981) 1.

[Era86] R. A. Eramzhyan, B. S. Ishkhanov, I. M. Kapitonov, and V. G. Neudatchin, Physics Reports **136** (1986) 229.

[Eri60] T. Ericson, Advances in Physics **9** (1960) 425.

[Eri63] T. Ericson, Annals of Physics **23** (1963) 390.

[Ero03] V. A. Erokhova, M. A. Elkin, A. V. Izotova, B. S. Ishkhanov, I. M. Kapitonov, E. I. Lileeva, and E. V. Shirokov, Bulletin of Russian Academy of Sciences, Physics **67** (2003) 1636.

[Fal70] S. Fallieros and B. Goulard, Nuclear Physics **A 147** (1970) 593.

[Fed99] A. Fedorova and M. Zeitlin, Proceedings of the 1999 Particle Accelerator Conference, March 29 - April 2, New York City (1999) 2900.

[Fes54] H. Feshbach, C. E. Porter, and V. F. Weisskopf, Physical Review **96** (1954) 448.

[Fes67] H. Feshbach, A. K. Kerman, and R. H. Lemmer, Annals of Physics **41** (1967) 230.

[Fes74] H. Feshbach, Reviews of Modern Physics **46** (1974) 1.

[Fir95] R. B. Firestone, V. S. Shirley, C. M. Baglin, S. Y. F. Chu, and J. Zipkin, *Table of Isotopes CD-ROM Edition, Version 1.0, March 1996*, Wiley, New York (1996).

[Fis01] K. G. Fissum, W. Bertozzi, J. P. Chen, D. Dale, H. C. Fenker, J. Gao, A. Gavalya, S. Gilad, C. R. Leathers, N. Liyanage, R. O. Michaels, E. A. J. M. Offermann, J. Segal, J.A. Templon, R. Wechsler, B. Wojtsekhowski, and J. Zhao, Nuclear Instruments and Methods in Physics Research **A 474** (2001) 108.

[Fra85] M. A. Franey and W. G. Love, Physical Review **C 31** (1985) 488.

[Fri89] D. L. Friesel, T. J. P. Ellison, T. Sloan and M. Ball, Proceedings of the 12th International Conference on Cyclotrons and their Applications, Berlin, Germany (1989) 380. Available at http://accelconf.web.cern.ch/AccelConf/c89/papers/f7-02.pdf.

[Fuj02] H. Fujita, Y. Fujita, G. P. A. Berg, A. D. Bacher, C. C. Foster, K. Hara, K. Hatanaka, T. Kawabata, T. Noro, H. Sakaguchi, Y. Shimbara, T. Shinada, E. J. Stephenson, H. Ueno, and M. Yosoi, Nuclear Instruments and Methods in Physics Research **A 484** (2002) 17.

[Gil65] A. Gilbert and A. G. W. Cameron, Canadian Journal of Physics **43** (1965) 1446.

[Gle65] N. K. Glendenning and M. Veneroni, Physics Letters **14** (1965) 228.

[Gle66] N. K. Glendenning and M. Veneroni, Physical Review **144** (1966) 839.

[Gle83] N. K. Glendenning, *Direct Nuclear Reactions*, World Scientific (1983).

[Goe82] K. Goeke and J. Speth, Annual Review of Nuclear and Particle Science **32** (1982) 65.

[Gol48] M. Goldhaber and E. Teller, Physical Review **74** (1948) 1046.

[Gol84] A. Goldberg, Nuclear Physics **A 420** (1984) 636.

[Gou67] B. Goulard and S. Fallieros, Canadian Journal of Physics **45** (1967) 3221.

[Gru08] C. Grupen and B. Shwartz, *Particle detectors (Second Edition)*, Cambridge University Press (2008).

[Haa10] M. Haahr, *Gaussian Random Number Generator* (2010) https://www.random.org/gaussian-distributions/

[Har02] M. N. Harakeh and A. van der Woude, *Giant Resonances: Fundamental High-Frequency Modes of Nuclear Excitation*, Oxford University, Oxford (2002).

[Har77] M. N. Harakeh, K. van der Borg, T. Ishimatsu, H. P. Morsch, A. van der Woude and F. E. Bertrand, Physical Review Letters **38** (1977) 676.

[Har81] P. D. Harty and M. N. Thompson, Australian Journal of Physics **34** (1981) 505.

[Hil00] S. Hilaire, *Lecture on Nuclear Data and Nuclear Reactors: Physics, Design and Satefy*, ICTP Lecture Notes Series, March 13 - April 14, Trieste, Italy (2000).

[Hil06] S. Hilaire and S. Goriely, Nuclear Physics **A 779** (2006) 63.

[Hil97] S. Hilaire, PhD thesis, Institut National Polytechnique de Grenoble, Grenoble, FRANCE (1997) Unpublished.

[Hil98] S. Hilaire, J. P. Delaroche, and A. J. Konig, Nuclear Physics **A 632** (1998) 417.

[Hla05] T. T. Hlatshwayo, MSc thesis, University of Zululand (2005) Unpublished.

[Ike80] H. Ikegami, S. Morinobu, I. Katayama, M. Fujiwara, and S. Yamabe, Nuclear Instruments and Methods **175** (1980) 335.

[Jac02] N. Jachowicz, K. Heyde, J. Ryckebusch, and S. Rombouts, Physical Review **C 65** (2002) 025501.

[Jac62] J. D. Jackson, *Classical Electrodynamics*, Wiley New York (1962).

[Jac75] R. Jäckle and H. Pilkuhn, Nuclear Physics **A 247** (1975) 521.

[Jin14] M. Jingo, PhD thesis, University of the Witwatersrand, Johannesburg (2014) Unpublished.

[Joh66] M. B. Johnson, L. W. Owen, and G. R. Satchler, Physical Review **142** (1966) 748.

[Jon76] B. Jonson, E. Hagberg, P. G. Hansen, P. Hornshøj, and P. Tidemand-Petersson, *Proceedings of the 3rd international conference on nuclei far from stability*, 19-26 May, Cargèse, Corsica, France (1976) 277.

[Jon85] D. T. L. Jones, Proceedings of the 5. Neutron Dosimetry, September 17 - 21, Munich, Germany, International Nuclear Information System (INIS), IAEA **18** (1985) 17.

[Kai10] G. Kaiser, *A friendly guide to wavelets*, Springer Science & Business Media (2010).

[Kal04] Y. Kalmykov, PhD thesis, Technische Universität Darmstadt, Germany (2004) Unpublished.

[Kal06] Y. Kalmykov, T. Adachi, G. P. A. Berg, H. Fujita, K. Fujita, Y. Fujita, K. Hatanaka, J. Kamiya, K. Nakanishi, P. von Neumann-Cosel, V. Yu. Ponomarev, A. Richter, N. Sakamoto, Y. Sakemi, A. Shevchenko, Y.

Shimbara, Y. Shimizu, F. D. Smit, T. Wakasa, J. Wambach, and M. Yosoi, Physical Review Letters **96** (2006) 012502.

[kee87] G. J. O'keefe, M. N. Thompson, Y. I. Assafiri, R. E. Pywell and K. Shoda, Nucl. Phys. **A 469** (1987) 239.

[Khe10] N. Y. Kheswa, P. Papka, E. Z. Buthelezi, R. M. Lieder, R. Neveling, and R. T. Newman, Nuclear Instruments and Methods in Physics Research **A 613** (2010) 389.

[Kim15] Y. Kim and P. Papakonstantinou, **ArXiv:1509.02259v1** 8 Sept.(2015).

[Kni98] D. Knight, *Humphry Davy: Science and Power*, Cambridge University Press (1998).

[Kno99] G. F. Knoll, *Radiation Detection and Measurement (3rd Edition)*, Wiley (1999).

[Kum66] H. Kümmel, J. H. E. Mattauch, W. Thiele and A. H. Wapstra, Nuclear Physics **81** (1966) 129.

[Lac00] D. Lacroix, A. Mai, P. von Neumann-Cosel, A. Richter, and J. Wambach, Physics Letters **B 479** (2000) 15.

[Lal97] G. A. Lalazissis, J. Köning, and P. Ring, Physical Review **C 55** (1997) 540.

[Lev52] R. E. le Levier and D. S. Saxon, Physical Review **87** (1952) 40.

[Lit07] E. Litvinova, P. Ring, and V. I. Tselyaev, Physical Review **C 75** (2007) 064308.

[Lit08] E. Litvinova, P. Ring and V. Tselyaev, Physical Review **C 78** (2008) 014312.

[Lit09] E. Litvinova, P. Ring, V. Tselyaev, and K. Langanke, Physical Review **C 79** (2009) 054312.

[Lit15] E. Litvinova, Physical Review **C 91** (2015) 034332.

[Lov81] W. G. Love and M. A. Franey, Physical Review **C 24** (1981) 1073.

[Lyn68] J. E. Lynn, *The Theory of Neutron Resonance Reactions*, Clarendon Press (1968).

[Mad83] V. A. Madsen and W. Tobocman, Physical Review **139** (1965) B864.

[Mal99] S. Mallat, *A Wavelet Tour of Signal Processing*, Academic Press (1999).

[Mar83] S. A. Martin, A. Hardt, J. Meissburger, G. P. A. Berg, U. Hacker, W. Hürlimann, J. G. M. Römer, T. Sagefka, A. Retz, O. W. B. Schult, K. L. Brown, and K. Halbach, Nuclear Instruments and Methods in Physics Research **214** (1983) 281.

[Mel56] M. A. Melkanoff, S. A. Moszkowski, J. Nodvik, and D. S. Saxon, Physical Review **101** (1956) 507.

[Mes62] A. Messiah, *Quantum mechanics, 2 vols*, New York (1962).

[MID15] MIDAS (Maximum Integrated Data Acquisition System), Paul Sherrer Institute (2015), https://midas.psi.ch.

[Mig44] A. Migdal, USSR Academy of Science - Journal of Physics **8** (1944) 331.

[Mis94] V. Mishra, N. Boukharouba, C. E. Brient, S. M. Grimes, and R. S. Pedroni, Physical Review **C 49** (1994) 750.

[Mla06] R. M. Mlambo, M. W. Swanepoel, J. J. Nieto-Camero, and J. E. Symons, International Conference on Quality Assurance and New Techniques in Radiation Medicine (QANTRM), November 13 - 15, Vienna, Austria, IAEA Book of Extended Synopses (IAEA-CN-146) (2006) 134.

[Moh12] P. J. Mohr, B. N. Taylor, and D. B. Newell, Journal of Physical and Chemical Reference Data **41** (2012) 043109.

[Mos78] J. M. Moss, D. R. Brown, D. H. Youngblood, C. M. Rozsa and J. D. Bronson, Physical Review **C 18** (1978) 741.

[Mye69] W. D. Myers and W. J. Swiatecki, Annals of Physics **55** (1969) 395.

[Mye74] W. D. Myers and W. J. Swiatecki, Annals of Physics **84** (1974) 186.

[Nat91] National Accelerator Centre (NAC) Faure, 1991 Annual Report, NAC/AR/92-01 (1992) 27.

[Nem62] P. E. Nemirovsky and Y. V. Adamchuk, Nuclear Physics **39** (1962) 551.

[Nev01] R. Neveling, PhD thesis, Stellenbosch University, Stellenbosch (2001) Unpublished.

[Nev11] R. Neveling, H. Fujita, F. D. Smit, T. Adachi, G. P. A. Berg, E. Z. Buthelezi, J. Carter, J. L. Conradie, M. Couder, R. W. Fearick, S. V. F ortsch, D. T. Fourie, Y. Fujita, J. Görres, K. Hatanaka, M. Jingo, A. M. Krumbholz, C. O. Kureba, J. P. Mira, S. H. T. Murray, P. von Neumann-Cosel, S. O'Brien, P. Papka, I. Poltoratska, A. Richter, E. Sideras-Haddad, J. A. Swartz, A. Tamii, I. T. Usman, and J. J. van Zyl, Nuclear Instruments and Methods in Physics Research **A 654** (2011) 29.

[Nev14] R. Neveling, F. D. Smit, H. Fujita, and R. T. Newman, K600 Manual, iThemba LABS, Cape Town (2014) Unpublished.

[New56] T. D. Newton, Canadian Journal of Physics **34** (1956) 804.

[New96] R. T. Newman, PhD thesis, University of Cape Town, Cape Town (1996) Unpublished.

[Nud14] Nudat2.6, National Nuclear Data Center (nndc) Brookhaven National Laboratory. Accessed in (2014). http://www.nndc.bnl.gov/nudat2/.

[Oak15] Oak Ridge National Laboratory (ORNL), ORNL Isotope Production Program, Official Website: http://www.ornl.gov/

science-discovery/nuclear-science/research-areas/isotopes. Accessed in (2015).

[Oik77] S. Oikawa and K. Shoda, Nucl. Phys. **A 277** (1977) 301.

[Paa03] N. Paar, P. Ring, T. Nikšić, and D. Vretenar, Physical Review **C 67** (2003) 034312.

[Pan85] J. Pan and W. J. Tompkins, IEEE Transactions on Biomedical Engineering **BME-32** (1985) 230.

[Pap07] P. Papakonstantinou, Europhysics Letters **78** (2007) 12001.

[Pap09] P. Papakonstantinou and R. Roth, Physics Letters **B 671** (2009) 356.

[Per05] S. Péru, J. F. Berger, and P. F. Bortignon, The European Physics Journal **A 26** (2005) 25.

[Per08] S. Péru and H. Goutte, Physical Review **C 77** (2008) 044313.

[Pit71] R. Pitthan and Th. Walcher, Physics Letters **B 36** (1971) 563.

[Pol11] I. Poltoratska, PhD thesis, Technische Universität Darmstadt, Germany (2011) Unpublished.

[Pol14] I. Poltoratska, R. W. Fearick, A. M. Krumbholz, E. Litvinova, H. Matsubara, P. von Neumann-Cosel, V. Yu. Ponomarev, A. Richter, and A. Tamii, Physics Review **C 89** (2014) 054322.

[Pon14] V. Y. Ponomarev *Private communication* (2014).

[Pyw80] R. E. Pywell, M. N. Thompson K. Shoda, M. Sugawara, T. Saito, H. Tsubota, H. Miyase, J. Uegaki, T. Tamae, H. Ohashi and T. Urano, Australian Journal of Physics **33** (1980) 685.

[Rau97] T. Rauscher, F-K. Thielemann, and K-L. Kratz, Physical Review **C 56** (1997) 1613.

[Ray07] J. Raynal, Nuclear Energy Agency (NEA) (2007). Available at http://www.oecd-nea.org/tools/abstract/detail/nea-1209.

[Rod67] L. S. Rodberg and R. M. Thaler, *Introduction to the quantum theory of scattering*, Academic Press (1967).

[Rot05] R. Roth, H. Hergert, P. Papakonstantinou, T. Neff, and H. Feldmeier, Physical Review **C 72** (2005) 034002.

[Rot10] R. Roth, T. Neff and H. Feldmeier, Progress in Particle and Nuclear Physics **65** (2010) 50.

[Row68] D. J. Rowe, Reviews of Modern Physics **40** (1968) 153.

[Sai15] Saint-Gobain Crystals, Material safety datasheet (2015). Avalaible at http://www.caen.it/csite/CaenProd.jsp?parent=11&idmod=286.

[Sat66] G. R. Satchler, Nuclear Physics **77** (1966) 481.

[Sch82] P. Schwandt, H. O. Meyer, W. W. Jacobs, A. D. Bacher, S. E. Vigdor, M. D. Kaitchuck, and T. R. Donoghue, Physical Review **C 26** (1982) 55.

[She04] A. Shevchenko, J. Carter, R. W. Fearick, S. V. Förtsch, H. Fujita, Y. Fujita, Y. Kalmykov, D. Lacroix, J. J. Lawrie, P. von Neumann-Cosel, R. Neveling, V. Yu. Ponomarev, A. Richter, E. Sideras-Haddad, F. D. Smit, and J. Wambach, Physical Review Letters **93** (2004) 122501.

[She05] A. Shevchenko, PhD thesis, Technische Universität Darmstadt, Germany (2005) Unpublished.

[She08] A. Shevchenko, J. Carter, G. R. J. Cooper, R. W. Fearick, Y. Kalmykov, P. von Neumann-Cosel, V. Y. Ponomarev, A. Richter, I. Usman and J. Wambach, Physical Review **C 77** (2008) 024302.

[She09] A. Shevchenko, O. Burda, J. Carter, G. R. J. Cooper, R. W. Fearick, S. V. Förtsch, H. Fujita, Y. Fujita, Y. Kalmykov, D. Lacroix, J. J. Lawrie,

P. von Neumann-Cosel, R. Neveling, V. Yu. Ponomarev, A. Richter, E. Sideras-Haddad, F. D. Smit, and J. Wambach, Physical Review **C 79** (2009) 044305.

[She96] Y. Sheng, *The transforms and applications handbook*, Boca Raton, Fl: CRC (1996).

[Sif09] M. Sifuzzaman, M. R. Islam, and M. Z. Ali, *Application of Wavelet Transform and its Advantages Compared to Fourier Transform*, Vidyasagar University, Midnapore, West-Bengal, India (2009).

[Spe81] J. Speth and A. van der Woude, Reports on Progress in Physics **44** (1981) 719.

[Ste13] G. F. Steyn, C. Vermeulen, A. H. Botha, J. L. Conradie, J. P. A. Crafford, J. L. G. Delsink, J. Dietrich, H. du Plessis, D. T. Fourie, Z. Kormány, M. J. van Niekerk, P. F. Rohwer, N. P. Stodart, and J. G. de Villiers, Nuclear Instruments and Methods in Physics Research **A 727** (2013) 131.

[Ste50] H. Steinwedel and J. H. D. Jensen, Zeitschrift für Naturforschung **5** (1950) 413.

[Str00] S. Strauch, P. von Neumann-Cosel, C. Rangacharyulu, A. Richter, G. Schrieder, K. Schweda, and J. Wambach, Physical Review Letters **85** (2000) 2913.

[Tae07] J. Taelman, S. van Huffel, and A. Spaepen, Proceedings of the 29th Annual International Conference of the IEEE Engineering in Medicine and Biology Society, August 23 - 26, Lyon, France (2007) 682.

[Tam45] I. E. Tamm, Journal of Physics, Academy of Science of the USSR **9** (1945) 449.

[Tho61] D. J. Thouless, Nuclear Physics **22** (1961) 78.

[Tor75] Y. Torizuka, K. Itoh, Y. M. Shin, Y. Kawozoe, H. Matsuka, and G. Takeda, Physical Review **C 11** (1975) 1174.

[Tsa78] S-F. Tsai, Physical Review **C 17** (1978) 1862.

[Tse07] V. I. Tselyaev, Physical Review **C 75** (2007) 024306.

[Usm11a] I. Usman, Z. Buthelezi, J. Carter, G. R. J. Cooper, R. W. Fearick, S. V. Förtsch, H. Fujita, Y. Fujita, Y. Kalmykov, P. von Neuman-Cosel, R. Neveling, P. Papakonstantinou, A. Richter, R. Roth, A. Shevchenko, E. Sideras-Haddad, and F.D. Smit, Physics Letters **B 698** (2011) 191.

[Usm11b] I. Usman, Z. Buthelezi, J. Carter, G. R. J. Cooper, R. W. Fearick, S. V. Förtsch, H. Fujita, Y. Kalmykov, P. von Neuman-Cosel, R. Neveling, I. Poltoratska, A. Richter, A. Shevchenko, E. Sideras-Haddad, and F.D. Smit, Physical Review **C 84** (2011) 054322.

[Val61] J. G. Valatin, Physical Review **122** (1961) 1012.

[Vil06] J. G. de Villiers, PhD thesis, University of the Witwatersrand, Johannesburg (2006) Unpublished.

[Vra14] V. Vrankovic and D. George, Paul Sherrer Institute (PSI), Switzerland. Accessed in (2014). Available at http://magnet.web.psi.ch/Analysis/track.html.

[Wak02] T. Wakasa, K. Hatanaka, Y. Fujita, G. P. A. Berg, H. Fujimura, H. Fujita, M. Itoh, J. Kamiya, T. Kawabata, K. Nagayama, T. Noro, H. Sakaguchi, Y. Shimbara, H. Takeda, K. Tamura, H Ueno, M. Uchida, M. Uraki, and M. Yosoi, Nuclear Instruments and Methods in Physics Research **A 482** (2002)79.

[Wam88] J. Wambach, Reports on Progress in Physics **51** (1988) 989.

[Wei34] C. F. v. Weizsäcker, Zeitschrift für Physik **88** (1934) 612.

[Wig65] E. P. Wigner, in C. E. Porter (Ed.) *Statistical theories of spectra: Fluctuation*, Academic Press, New York (1965).

[Wil34] E. J. Williams, Physical Review **45** (1934) 729.

[Wil56] D. H. Wilkinson, Physica **22** (1956) 1039.

[Win79] A. Winther and K. Alder, Nuclear Physics **A 319** (1979) 518.

[Wit00] K. Wittenburg, American Institute of Physics Conference Proceedings **546** (2000) 3.

[Wol14] Wolfram Research Inc., Mathematica's Element Data function from Wolfram Research, Inc. Accessed in (2014). Available at http://periodictable.com/Elements/020/data.html.

[Woo54] R. D. Woods and D. S. Saxon, Physical Review **95** (1954) 577.

[Yan83] C. Yannouleas, M. Dworzecka, and J. J. Griffin, Nuclear Physics **A 397** (1983) 239.

[Yan86] C. Yannouleas and S. Jang, Nuclear Physics **A 455** (1986) 40.

[Yan87] C. Yannouleas, Physical Review **C 35** (1987) 1159.

[Zeg99] R. G. T. Zeggers, PhD Thesis, University of Groningen, Netherlands (1999)(Unpublished).

Appendix A

Description of the Box-Muller transform approach

In this approach, a pair of random deviates is generated from the same distribution starting with a pair of random numbers.

Considering a pair of independent random variables, x_1 and x_2 of the same rectangular density function on the interval [0,1] with mean 0 and variance 1. The probability density of x_1 is given as:

$$f(x_1) = \frac{1}{\sqrt{2\pi}} e^{-\frac{x_1^2}{2}}. \tag{A.1}$$

Likewise,

$$f(x_2) = \frac{1}{\sqrt{2\pi}} e^{-\frac{x_2^2}{2}}. \tag{A.2}$$

The joint density of x_1 and x_2 is given as:

$$f(x_1, x_2) = \frac{1}{2\pi} e^{-\frac{\left(x_1^2 + x_2^2\right)}{2}} = \frac{1}{\sqrt{2\pi}} e^{-\frac{x_1^2}{2}} . \frac{1}{\sqrt{2\pi}} e^{-\frac{x_2^2}{2}} = f(x_1) f(x_2). \tag{A.3}$$

The probability density is constant on all circles such that $\theta = \arctan\left(\frac{x_2}{x_1}\right)$ is uniformly distributed over [0,2π]. Similarly, the square of the radius vector, defined as: $r^2 = x_1^2 + x_2^2$, has a χ^2 distribution with 2 degrees of freedom.

Let

$$U_1 = e^{-\frac{\left(x_1^2+x_2^2\right)}{2}} \tag{A.4}$$

and

$$U_2 = \frac{\theta}{2\pi} \tag{A.5}$$

If U_1 has a rectangular density on [0,1], $-2lnU_1$ has a χ^2 distribution with 2 degrees of freedom such that:

$$x_1 = rcos\theta \qquad \text{and} \qquad x_2 = rsin\theta. \tag{A.6}$$

From Eqs. (A.4) and (A.5),

$$r = \sqrt{-2lnU_1} \qquad \text{and} \qquad \theta = 2\pi U_2. \tag{A.7}$$

Substituting Eqs. (A.7) into Eqs. (A.6),

$$x_1 = \sqrt{-2lnU_1}cos\left(2\pi U_2\right) \qquad \text{and} \qquad x_2 = \sqrt{-2lnU_1}sin\left(2\pi U_2\right), \tag{A.8}$$

as given in Ref. [Box58].